


Springer Geology

Tatiana Chaplina *Editor*



Processes in GeoMedia— Volume V

 Springer

Springer Geology

Series Editors

Yuri Litvin, Institute of Experimental Mineralogy, Moscow, Russia

Abigail Jiménez-Franco, Barcelona, Spain

Soumyajit Mukherjee, Earth Sciences, IIT Bombay, Mumbai, Maharashtra, India

Tatiana Chaplina, Institute of Problems in Mechanics, Russian Academy of Sciences, Moscow, Russia

The book series Springer Geology comprises a broad portfolio of scientific books, aiming at researchers, students, and everyone interested in geology. The series includes peer-reviewed monographs, edited volumes, textbooks, and conference proceedings. It covers the entire research area of geology including, but not limited to, economic geology, mineral resources, historical geology, quantitative geology, structural geology, geomorphology, paleontology, and sedimentology.

More information about this series at <https://link.springer.com/bookseries/10172>

Tatiana Chaplina
Editor

Processes in GeoMedia—Volume V

 Springer

Editor

Tatiana Chaplina

Ishlinsky Institute for Problems in Mechanics

Moscow, Russia

ISSN 2197-9545

ISSN 2197-9553 (electronic)

Springer Geology

ISBN 978-3-030-85850-6

ISBN 978-3-030-85851-3 (eBook)

<https://doi.org/10.1007/978-3-030-85851-3>

© The Editor(s) (if applicable) and The Author(s), under exclusive license to Springer Nature Switzerland AG 2022

This work is subject to copyright. All rights are solely and exclusively licensed by the Publisher, whether the whole or part of the material is concerned, specifically the rights of translation, reprinting, reuse of illustrations, recitation, broadcasting, reproduction on microfilms or in any other physical way, and transmission or information storage and retrieval, electronic adaptation, computer software, or by similar or dissimilar methodology now known or hereafter developed.

The use of general descriptive names, registered names, trademarks, service marks, etc. in this publication does not imply, even in the absence of a specific statement, that such names are exempt from the relevant protective laws and regulations and therefore free for general use.

The publisher, the authors and the editors are safe to assume that the advice and information in this book are believed to be true and accurate at the date of publication. Neither the publisher nor the authors or the editors give a warranty, expressed or implied, with respect to the material contained herein or for any errors or omissions that may have been made. The publisher remains neutral with regard to jurisdictional claims in published maps and institutional affiliations.

This Springer imprint is published by the registered company Springer Nature Switzerland AG
The registered company address is: Gewerbestrasse 11, 6330 Cham, Switzerland

Contents

Verification Second-Order Sea Wave Models	1
A. S. Zapevalov and A. V. Garmashov	
Internal Gravity Waves Fields Dynamics in Vertically Stratified Horizontally Inhomogeneous Medium	11
V. V. Bulatov and Yu. V. Vladimirov	
Far Internal Gravity Waves Fields Generated by a Sources Distributed on a Moving Plane	17
V. V. Bulatov and Yu. V. Vladimirov	
A Two-Story Tornado in a Lab	25
I. V. Naumov, B. R. Sharifullin, S. G. Skripkin, M. A. Tsoy, and V. N. Shtern	
Conditions of the Effective Mixing in a T-Type Micromixer at Low Reynolds Numbers	35
A. Yu. Kravtsova, P. E. Ianko, M. V. Kashkarova, A. V. Bilsky, Y. V. Kravtsov, and I. V. Naumov	
The Problem of Exact Solutions Construction for Potential Steady Surface Waves in the Case of a Liquid of Finite Depth	43
A. V. Kistovich	
Anisotropic Permeability of Geomaterials: Lab Test and Borehole Environment Model	49
Larisa Nazarova, Nikita Golikov, Leonid Nazarov, and Galina Nesterova	
Calculation of Dynamic and Energy Characteristics in the Region of Western Crimea Based on the Observational Data from Hydrological Surveys in 2007–2009 in the Numerical Model of the Black Sea Dynamics Using the Kalman Filter Algorithm	59
Demyshev Sergei and Evstigneeva Natalia	
One-Dimensional Coherent Convective Structures from Heat Sources	71
A. V. Kistovich	

Features of the Spread Oil Spill in Arctic Conditions	79
V. P. Pakhnenko	
Study of Undercurrents in the Black Sea Northeastern Part by Using Numerical Simulation and Observation Data	93
S. G. Demyshev, N. V. Markova, and O. A. Dymova	
Modeling Group Structure of the Sea Surface Waves	101
P. Shumeyko and A. Yu. Abramovich	
Identification of the Time-Variable Power of a Point Pollution Source in the Azov Sea Based on the Variational Assimilation Algorithm	109
Kochergin Vladimir Sergeevich and Kochergin Sergey Vladimirovich	
Increase in Illumination of 253.7 nm in a Cylindrical PTFE Cavity	117
Mikhail A. Kotov, Andrey N. Shemyakin, Nikolay G. Solovyov, and Mikhail Yu. Yakimov	
Determination of the Matter Fluxes on the Sea Bottom Using a Variational Assimilation Algorithm and Remote Sensing Data	131
Kochergin Vladimir Sergeevich and Kochergin Sergey Vladimirovich	
Determination of the Vertical Velocity in Hydrodynamic Model Using Nested Grids	139
Kochergin Vladimir Sergeevich and Kochergin Sergey Vladimirovich	
Analysis of the Meteorological and Hydrophysical Factors of Massive Wash-Outs of Marine Litter to the Shore of Sambian Peninsula (The Baltic Sea)	145
S. V. Fetisov, I. P. Chubarenko, and E. E. Esiukova	
The Shores of the Northern Pacific Contact Zones	157
E. I. Ignatov, V. V. Afanas'ev, and V. Uba	
Formation of Temperature Anomalies in the Laptev Sea (2000– 2020 Years)	169
M. V. Kraineva and E. N. Golubeva	
On Possibility of Applying Aircraft Scanning Laser Locator for Solving Problems of Operational Oceanology	179
V. N. Nosov, S. B. Kaledin, S. G. Ivanov, E. A. Zevakin, L. V. Serebrinikov, A. S. Savin, and V. I. Timonin	
The Methodology for Enhancement in Determining the Area of Total Underwork of the Rock Mass	189
S. B. Kulibaba and E. N. Esina	

Kinematic Model of the Development of the Bottom of the Powell Basin (Weddell Sea)	197
A. A. Schreider, A. E. Sazhneva, M. S. Kluyev, A. L. Brekhovskikh, F. Bohoyo, J. Galindo-Zaldivar, C. Morales, and E. I. Evsenko	
Investigation of Influence of the Screw Propeller Working Towards the Flow on Parameters of Near Water Aerosol	209
V. N. Nosov, S. G. Ivanov, V. I. Pogonin, S. B. Kaledin, E. A. Zevakin, and N. A. Zavyalov	
Gold of Riftogenic Structures of the East Ural Uplift	217
A. V. Kolomoets and P. V. Pankratiev	
Aeolian Morpholithogenesis on the Shores of the Northern Pacific	223
V. V. Afanas'ev and A. I. Levitsky	
Variants of Visualization of the Marine Forecast on the Examples of the Crimean Basin of the Black Sea	233
N. Voronina	
Destruction of Rocky Coastes of Cold Seas	243
V. V. Afanas'ev and A. V. Uba	
Bottom Sediments of the Kazantip Nature Reserve Coastal Water Area (Azov Sea) as an Indicator of the Water Area Wellbeing	253
E. A. Tikhonova, O. V. Soloveva, and N. V. Burdiyan	
The Assessment of the Multifunctional Center Construction Impact on the Surrounding Buildings Within Megapolis Limits	263
D. L. Neguritsa, G. V. Alekseev, E. A. Medvedev, A. A. Tereshin, and K. M. Slobodin	

Verification Second-Order Sea Wave Models



A. S. Zapevalov  and A. V. Garmashov 

Abstract Second-order nonlinear models are currently one of the main tools for studying and forecasting sea waves. The models will include bound components resulting from the interaction of free waves. Like any mathematical model, they are created for certain conditions. The widespread use of such models requires their verification. The criterion for correctness in this work is the correspondence between the measured and calculated values of the asymmetry and kurtosis coefficients. The analysis uses data from direct measurements of sea waves. The measurements were carried out on the Black Sea, on a stationary oceanographic platform of the Marine Hydrophysical Institute of the Russian Academy of Sciences. It is shown that nonlinear second-order models describe well the average tendencies of changes in the coefficients of skewness and kurtosis with a change in the steepness of the wave. At the same time, the values of the coefficients of asymmetry and kurtosis vary widely with a fixed value of steepness. Steepness is not the only parameter that determines the deviations of the surface elevation distributions from the Gaussian distribution. The considered class of nonlinear wave models does not fully describe the variety of real situations that arise in the sea, which imposes restrictions on their use in engineering calculations.

Keywords Sea surface · Statistical moments · Nonlinear random wave · Second-order random model

1 Introduction

Second-order random wave models are not new; indeed, they have been a research topic for almost 60 years (Hasselmann 1962; Longuet-Higgins 1963; Tayfun 1980) and remain so today (Jha and Winterstein 2000; Tayfun and Alkhalidi 2016; Gao et al. 2020). But, they have not entered common engineering practice, which applies either random linear (Gaussian) waves, or regular waves (Hou et al. 2006). The complexity

A. S. Zapevalov (✉) · A. V. Garmashov
Marine Hydrophysical Institute RAS, Sevastopol, Russian Federation
e-mail: sevzepter@mail.ru

of constructing wave models is determined by the fact that the wave field depends on a large number of factors, the significance of which varies in different situations.

In a linear wave field, surface elevations are described by the Gaussian distribution. The field of sea surface waves is weakly nonlinear. In the absence of strong currents, the statistical properties of waves are described by decomposing the wave profile in a series with respect to the wave steepness (Longuet-Higgins 1963)

$$\varepsilon = \sqrt{m_2}k_p, \quad (1)$$

where m_2 is the second statistical moment (variance) of the surface elevations; k_p is spectrum peak wavenumber. The steepness ε is a small parameter, for sea waves the condition is usually fulfilled $0 < \varepsilon < 0.1$.

The nonlinearity leads to the evolution of the spectrum and also leads to the deviation of the wave statistics from the statistics of the Gaussian distribution, which is manifested in the senior cumulants of the waves (cumulants of the third order and higher) (Annenkov and Shrira 2013). The deviations of the senior cumulants from zero are considered as indicators of the nonlinearity of the waves. Due to the fact that the nonlinearity is weak, the deviations of the distribution of sea surface elevations from the Gauss distribution are small (Jha and Winterstein 2000; Babanin and Polnikov 1995; Zapevalov et al. 2011). However, weak nonlinearity plays an important role in the formation of the wave field, including the formation of the group structure and in the occurrence of abnormally large waves (Xiao et al. 2013; Ruban 2013a, 2013b).

Nonlinear wave models are usually tested by mathematical simulation using data from laboratory experiments (Gao et al. 2020). Obviously, this approach does not allow us to evaluate these models with confidence. It is necessary to verify the models according to the data of direct measurements of sea surface waves, which is the goal of our work.

2 Second-Order Random Model

A nonlinear model describing the elevation of the sea surface is usually represented as the sum of two components (Gao et al. 2020)

$$\eta(x, t) = \eta_1(x, t) + \eta_2(x, t). \quad (2)$$

The first component describes a linear wave field. The change in the elevation of the surface at a fixed point is given as a superposition of an infinite number of sinusoidal waves

$$\eta_1(x, t) = \sum_{n=1}^{\infty} a_n \cos \psi_n, \quad (3)$$

where x and t are the spatial and temporal coordinates, respectively, a_n is the amplitude, $\psi_n = k_n x - \omega_n t + \phi_n$, k_n and ω_n the wave number and angular frequency, ϕ_n is the phase. The random phase values are evenly distributed over the range from 0 to 2π . The amplitude is related to the frequency wave spectrum by the equation a_n

$$\frac{1}{2} a_n^2 = S(\omega_n) d\omega. \quad (4)$$

The JONSWAP spectrum or its modification is usually used to calculate the amplitudes (Socquet-Juglard et al. 2005). The JONSWAP empirical spectrum was constructed from research carried out in the North Sea as part of the Joint North Sea Wave Project (JONSWAP). It was obtained for sea waves in conditions of limited fetch. The JONSWAP spectrum has the form (Hasselmann et al. 1973)

$$S(\omega) = \frac{\alpha g^2}{\omega^5} \exp\left(-\frac{5}{4} \left(\frac{\omega_p}{\omega}\right)^4\right) \gamma^\Phi, \quad (5)$$

where α is the dimensionless parameter, g is the gravitational acceleration, ω_p is the peak spectral frequency, the so-called peak gain, $\gamma = 3.3$ is the so-called peak enhancement coefficient, $\Phi = \exp\left(-\frac{(\omega - \omega_p)^2}{2\nu^2\omega^2}\right)$, ν is the parameter that determines the width of the spectral peak: if $\omega \leq \omega_p$ then $\nu = 0.07$, if $\omega > \omega_p$ then $\nu = 0.09$.

By virtue of the central limit theorem, in a linear wave field, the sea surface elevations are distributed according to the Gauss law

$$P_G(\eta_1) = \frac{1}{\sqrt{2\pi m_2}} \exp\left(-\frac{\eta_1^2}{2m_2}\right). \quad (6)$$

In deep water, gravitational waves obey the dispersion equation $\omega^2 = gk$.

Usually, the nonlinear component is represented as (Jha and Winterstein 2000; Tayfun and Alkhalidi 2016; Gao et al. 2020; Agarwal and Manuel 2009).

$$\eta_2(x, t) = \sum_{m=1}^{\infty} \sum_{n=1}^{\infty} \{a_n a_m [B_{mn}^- \cos(\psi_m - \psi_n) + B_{mn}^+ \cos(\psi_m + \psi_n)]\}, \quad (7)$$

where B_{mn}^- and B_{mn}^+ are the second order transfer functions. Functions B_{mn}^- and B_{mn}^+ are calculated from the Laplace equation for the velocity potential with nonlinear boundary conditions. The nonlinear model (7) includes second-order bound components that appear as a result of the interaction of free waves.

The probability density functions (PDF) of sea surface elevations of a nonlinear wave field are constructed under the assumption that the wave spectrum is narrow-band. The width of the spectrum is defined as

$$\nu = \sqrt{\frac{M_0 M^2}{M_1^2} - 1} \quad (8)$$

where the spectral moments are

$$M_j = \int \omega^j S(\omega) d\omega. \quad (9)$$

The spectrum is considered to be narrowband if the condition $\nu^2 \ll 1$ is met (Tayfun 1980; Longuet-Higgins 1975).

Consider the PDF of sea surface elevations $P(\eta)$ constructed within the framework of a second-order nonlinear wave field model. The function $\eta(x, t)$ is normalized in such a way that its variance is equal to one, the mean value is equal to zero. All considered PDFs were obtained in the approximation of a narrow-band wave spectrum.

The probabilistic description of nonlinear waves with a narrow-band spectrum can be simplified to a form in which each realization of the surface displacement appears as an amplitude-modulated Stokes wave with an average frequency and a random phase. It is assumed that the PDF is one-parameter, depending only on the steepness ε .

Within the framework of these assumptions a probability density function was constructed in the form (Socquet-Juglard et al. 2005)

$$P_S(\eta, \varepsilon) = \frac{1 - 7\varepsilon^2/8}{\sqrt{2\pi(1 + 3G + 2G^2)}} \exp\left(-\frac{G^2}{2\varepsilon^2}\right), \quad (10)$$

where

$$G = \sqrt{1 + 2\varepsilon\eta} - 1. \quad (11)$$

An analytically simpler approximation for a narrow-band spectrum is proposed for the PDF in the form (Tayfun and Alkhalidi 2016)

$$P_T(\eta, \varepsilon) \cong \frac{\alpha}{\sqrt{2\pi}} \frac{\exp(-\varepsilon^2 G^2/2)}{G + 1}, \quad (12)$$

where α is the normalization coefficient. The approximation (12) is valid in the domain $\eta > -1/(2\varepsilon)$.

The changes in the PDF with increasing wave steepness, constructed in the framework of a nonlinear wave field model, are shown in Fig. 1. Within the range $|\eta| < 1$, the deviations of PDF from the Gaussian distribution are small; at $\varepsilon = 0.01$ they practically coincide. The function

$$R(\eta, \varepsilon) = P(\eta, \varepsilon) / P_G(\eta) \tag{13}$$

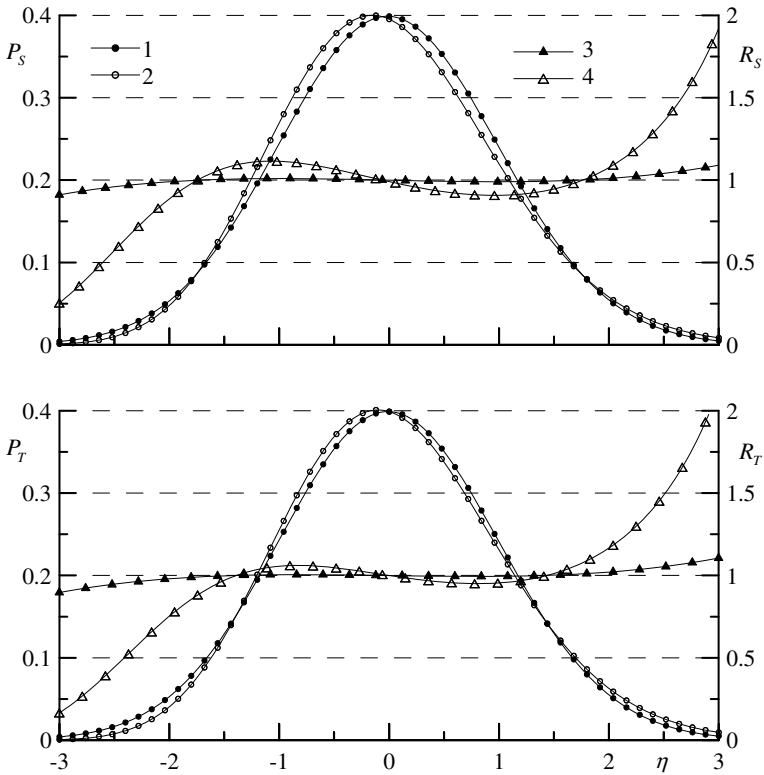


Fig. 1 PDF and deviations from the Gaussian distribution. Curves 1 and 2 are PDF at $\varepsilon = 0.01$ and $\varepsilon = 0.1$, curves 3 and 4 are functions R at $\varepsilon = 0.01$ and $\varepsilon = 0.1$, respectively

3 Comparison with Field Measurement Data

The measurements were carried out in the winter period of 2018–2019 on the stationary oceanographic platform of the Marine Hydrophysical Institute. The platform is located on the Black Sea near the southern coast of Crimea. The depth at its location is 30 m. For the characteristic wind waves and swells of the Black Sea, this depth corresponds to the condition of “deep water”. The fulfillment of this condition means that the influence of the bottom on surface waves can be neglected.

A string resistive waveguide was used to measure surface elevations. Its sensitive element is a sensor made of nichrome wire (Toloknov and Korovushkin 2010).

Measurements taken in winter cover a wide range of meteorological conditions. The data analyzed here were obtained in December 2018 (first series of measurements) and in January 2019 (second series of measurements). Wave and meteorological measurements were carried out simultaneously. The averaging period was 20 min.

In the first series of measurements, the wind speed varied in the range of 0–26 m/s, and the significant wave height (the average height of one third of the highest waves) varied in the range from 0.23 m to 2.26 m. In the second series of measurements, the wind speed varied in the range of 0–25 m/s, and the significant height varied in the range from 0.14 m to 1.71 m.

When verifying PDF approximations, it is required that they reproduce the first three or four statistical moments with sufficient accuracy (Tayfun and Alkhalidi 2016). Consider the extent to which the second-order wave model satisfy this requirement. The moment of the statistical distribution of elevations of order n is described by the expression

$$m_n = \int_{-\infty}^{\infty} \eta^n P(\eta) dx . \quad (14)$$

For further analysis, we will use the skewness and kurtosis coefficients.

$$\lambda_3 = m_3 / m_2^{3/2} , \quad (15)$$

$$\lambda_4 = m_4 / m_2^2 - 3 . \quad (16)$$

The results of determining the skewness coefficient of sea surface elevations, as well as the regressions constructed from two series of measurements, are shown in Fig. 2. The same figure also shows the results of model calculations of the dependence $\lambda_3 = \lambda_3(\varepsilon)$. For the first series of measurements, the average steepness is 0.025, and the minimum and maximum steepness are 0.004 and 0.088, respectively. In the second series of measurements, the average steepness is 0.026, and the minimum and maximum steepness are 0.005 and 0.086, respectively.

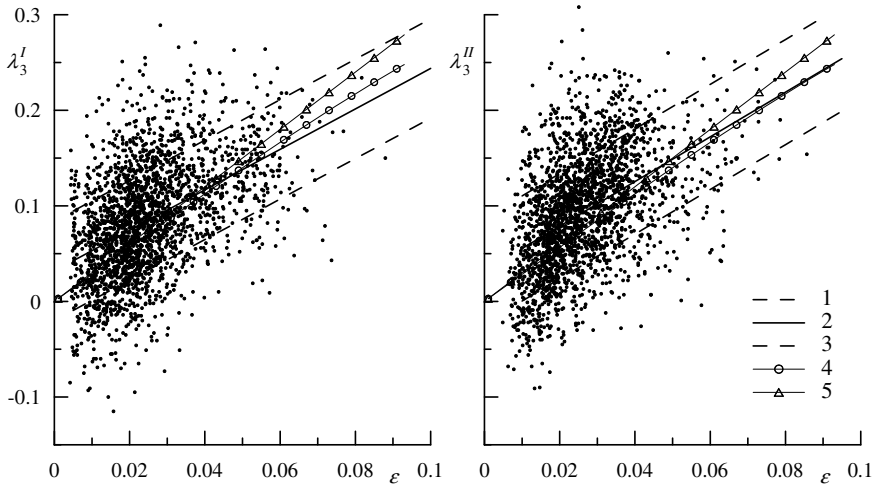


Fig. 2 Dependence of the skewness coefficients λ_3 on the steepness ε . The points are measured data. Curves 1, 2, and 3 are regressions and standard deviations from them, curves 4 and 5 are dependences constructed according to models (12) and (10)

The regression dependencies for the first and second series of measurements are described by the equations

$$\lambda_3^I = 0.02 + 2.12\varepsilon \pm 0.047, \quad (17)$$

$$\lambda_3^{II} = 0.032 + 2.32\varepsilon \pm 0.06, \quad (18)$$

where the superscript indicates the number of the measurement series.

The regressions $\lambda_4 = \lambda_4(\varepsilon)$ shown in Fig. 3. They have the form

$$\lambda_4^I = -0.011 + 1.24\varepsilon \pm 0.105, \quad (19)$$

$$\lambda_4^{II} = -0.035 + 1.837\varepsilon \pm 0.099. \quad (20)$$

Let's compare the theoretical dependencies with the regressions constructed from the data of two series of measurements. From Figs. 2 and 3, it follows that the statistical coefficients constructed from models and dependencies practically coincide with the regressions. Thus, the representation of the nonlinear component in the form (6) well describes the average deviations of the wave distributions from the Gaussian distribution.

However, it should be noted that the estimates of the skewness and kurtosis coefficients determined at a fixed steepness value are widely distributed. This means that

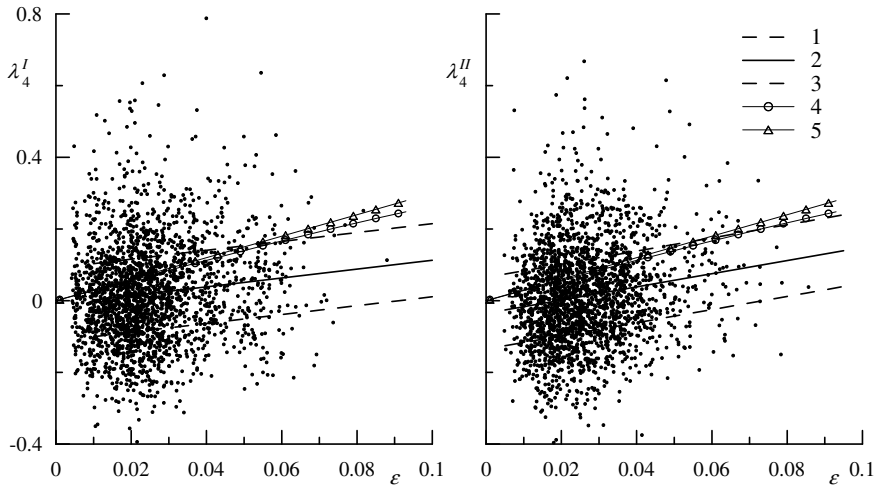


Fig. 3 Dependence of the kurtosis coefficients λ_4 on the steepness ϵ . The points are measured data. Curves 1, 2, and 3 are regressions and standard deviations from them, curves 4 and 5 are dependences constructed according to models (12) and (10)

steepness is not the only parameter that determines the type of distribution of sea surface elevations.

The correlation coefficients between the steepness and the skewness coefficient are 0.46–0.48, with a standard deviation of 0.05–0.06. The correlation coefficients between the steepness and the kurtosis coefficient are 0.11–0.12, i.e. the dependence of λ_4 on ϵ is weak. The standard deviation is ~ 0.1 .

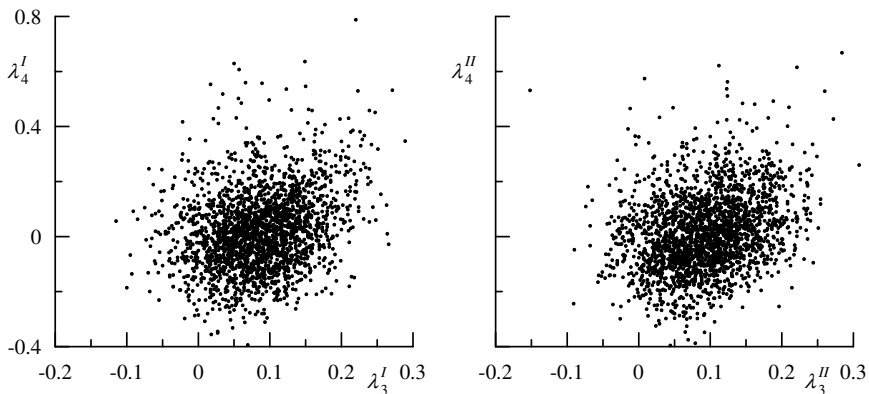


Fig. 4 Statistical dependence of λ_4 on λ_3

The one-parameter wave model assumes that there is a certain relationship between the coefficients λ_3 and λ_4 . Figure 4 shows that there is no such dependence. The correlation coefficient between λ_3 and λ_4 is 0.27.

4 Conclusion

The verification of the second-order nonlinear models involving bound components resulting from the interaction of free waves is carried out. It is shown that the second-order nonlinear models describe well the average trends of changes in the distributions of sea surface elevations when the wave steepness changes. It is also shown that the considered class of nonlinear wave models does not fully describe the variety of real situations arising in the sea. This imposes restrictions on their use in engineering calculations.

Acknowledgements This work was carried out in the context of the State project 0555-2021-0003 “Development of operational oceanology methods based on interdisciplinary studies of the processes of formation and evolution of the marine environment and mathematical modeling using remote and contact measurement data”.

References

- Agarwal P, Manuel L (2009) On the modeling of nonlinear waves for prediction of long-term offshore wind turbine loads. *J Offshore Mech Arct Eng* 131(4):041601
- Annenkov SY, Shrira VI (2013) Large-time evolution of statistical moments of wind-wave fields. *J Fluid Mech* 726:517–546
- Babanin AV, Polnikov VG (1995) On the non-Gaussian nature of wind waves. *Phys Oceanogr* 6(3):241–245
- Gao Z, Sun Z, Liang S (2020) Probability density function for wave elevation based on Gaussian mixture models. *Ocean Eng* 213:107815
- Hasselmann K (1962) On the non-linear energy transfer in a gravity-wave spectrum. *J Fluid Mech* 481–500
- Hasselmann K, Barnett TP, Bouws E, Carlson H, Cartwright DE, Enke K, Ewing JA, Gienapp H, Hasselmann DE, Kruseman P, Meerburg A, Mller P, Olbers DJ, Richter K, Sell W, Walden H (1973) Measurements of wind-wave growth and swell decay during the joint north sea wave project (JONSWAP). *Ergänzungsheft zur Deutschen Hydrographischen Zeitschrift Reihe A8(12):1–95*
- Hou Y, Song G, Zhao X, Song J, Zheng Q (2006) Statistical distribution of nonlinear random water wave surface elevation. *Chin J Ocean Limnol* 24(1):1–5
- Jha AK, Winterstein SR (2000) Nonlinear random ocean waves: prediction and comparison with data. In: *Proceedings of 19th international offshore mechanics and arctic engineering*, ASME, Paper No. ETCE/OMAE 2000-6125
- Longuet-Higgins MS (1963) The effect of non-linearities on statistical distribution in the theory of sea waves. *J Fluid Mech* 17(3):459–480
- Longuet-Higgins MS (1975) On the joint distribution of the periods and amplitudes of sea waves. *J Geophys Res* 80(18):2688–2694

- Ruban VP (2013) On the modulation instability of surface waves on a large-scale shear flow. *J Exp Theor Phys Lett* 97(4):188–193
- Ruban VP (2013b) Rogue waves at low Benjamin-Feir indices: numerical study of the role of nonlinearity. *J Exp Theor Phys Lett* 97(12):686–689
- Socquet-Juglard H, Dysthe K, Trulsen K, Krogstad H, Liu J (2005) Probability distributions of surface gravity waves during spectral changes. *J Fluid Mech* 542(1):195–216
- Tayfun MA (1980) Narrow-band nonlinear sea waves. *J Geophys Res* 85(C3):1548
- Tayfun MA, Alkhalidi MA (2016) Distribution of surface elevations in nonlinear seas. In: *Offshore technology conference Asia*
- Toloknov YN, Korovushkin AI (2010) Sistema sbora gidrometeorologicheskoy informatsii hydrometeorological information collection system. *Sistemy kontrolya okruzhayushchey sredy* 10:50–53 (in Russian)
- Xiao W, Liu Y, Wu G, Yue DKP (2013) Rogue wave occurrence and dynamics by direct simulations of nonlinear wave-field evolution. *J Fluid Mech* 720:357–392
- Zapevalov AS, Bol'shakov AN, Smolov VE (2011) Simulating of the probability density of sea surface elevations using the Gram–Charlier series. *Oceanology* 51(3):406–413

Internal Gravity Waves Fields Dynamics in Vertically Stratified Horizontally Inhomogeneous Medium



V. V. Bulatov  and Yu. V. Vladimirov 

Abstract The paper considers the problem of the harmonic internal gravity waves dynamics in a vertically stratified horizontally inhomogeneous medium. It is assumed that the scale of the horizontal variability of the medium density exceeds the characteristic lengths of internal gravity waves. The solution is constructed using a modified version of the spatio-temporal ray method. An asymptotic solution is constructed that allows one to calculate the amplitude and phase characteristics of wave fields. The solutions obtained make it possible to calculate the internal gravity waves fields for arbitrary disturbances sources.

Keywords Stratified medium · Internal gravity waves · Asymptotics · Ray method

Horizontal heterogeneity and non-stationarity have a significant impact on the propagation of internal gravity waves (IGW) in stratified natural environments (Ocean, Atmosphere) (Fabrikant and Stepanyants 1998; Miropol'skii and Shishkina 2001; Mei et al. 2017; Morozov 2018). If the ocean depth and its density are changing slowly as compared to the characteristic length (period) of IGW, which is well done in the real ocean, then for solving the mathematical modeling of IGW dynamics we may use the space–time ray-optics method (geometrical optics method) and its generalizations (Bulatov and Vladimirov 2012, 2019; Kravtsov and Orlov 1999). The requirement of slowness as compared with characteristic lengths (periods) of internal gravity waves, changing horizontal (time) parameters of the medium is a mandatory condition for using the geometrical optics method. This condition, however, may not be used to formulate sufficient applicability conditions for this method. It's evident that making an error estimation of the geometrical optics method requires more accurate analytical approaches than the space–time ray–path method, but because of

V. V. Bulatov (✉) · Yu. V. Vladimirov
Ishlinsky Institute for Problems in Mechanics RAS, Vernadskogo ave. 101-1, 119526 Moscow, Russia
e-mail: internalwave@mail.ru

Yu. V. Vladimirov
e-mail: vladimyura@yandex.ru

significant computational difficulties it is not realistic. The analytical methods available at this time for researching the IGW dynamics in stratified, non-uniform and non-stationary mediums are severely limited and do not allow us to estimate a faulty proportion of the geometrical optics method for real-world ambients. In most cases there are no accurate analytical solutions, and the well-known rigorous solutions can only instruct about a possible error rate for typical situations. The same instructions about a possible error rate for the space–time ray-path method can be obtained by comparing the resulting asymptotics with approximated, but more general than the ray-path, solutions of basic wave problems. Thus, the correctness of using the space–time ray-path method and its results should be considered in the frame of consistency of theoretical results with the field measurement data (Mei et al. 2017; Morozov 2018; Kravtsov and Orlov 1999; Froman and Froman 2002; Broutman and Rottman 2004).

In this paper we consider harmonic internal gravity waves. For determination of a small perturbations of pressure $p = \exp(i\omega t)P(z, x, y)$ and velocity components $U_j = \exp(i\omega t)u_j(z, x, y)$, $j = 1, 2, 3$ we obtain (Bulatov and Vladimirov 2012, 2019; Bulatov 2014; Matyushin 2019; Bulatov et al. 2019)

$$\begin{aligned}
 -\omega^2 \left(\frac{\partial^2 u_3}{\partial z^2} + \delta^{-2} \Delta u_3 \right) + \delta^{-2} \frac{g}{\rho_0} \left(\delta^{-1} u_1 \frac{\partial \rho_0}{\partial x} + \delta^{-1} u_2 \frac{\partial \rho_0}{\partial y} + u_3 \frac{\partial \rho_0}{\partial z} \right) &= 0, \\
 \delta^{-1} \Delta u_1 + \frac{\partial^2 u_3}{\partial z \partial x} &= 0, \quad \delta^{-1} \Delta u_2 + \frac{\partial^2 u_3}{\partial z \partial y} = 0, \\
 \delta^2 \frac{\partial}{\partial z} \left(\frac{\partial D}{\partial z} \alpha^{-1} \right) - \Delta D &= -\frac{\partial}{\partial z} (\alpha^{-1} \nabla D \nabla \chi), \\
 \delta^2 \frac{\partial D}{\partial z} + \nabla D \nabla \chi &= 0, \quad \text{for } z = 0, -H
 \end{aligned} \tag{1}$$

$$\chi(z, x, y) = g\omega^{-2} \ln \rho_0, \quad \alpha(z, x, y) = \omega^{-2} N^2(z, x, y) - 1, \quad D = P/\rho_0$$

$$\Delta = \partial^2/\partial x^2 + \partial^2/\partial y^2, \quad \nabla = \left(\frac{\partial}{\partial x}, \frac{\partial}{\partial y} \right), \quad N^2(z, x, y) = g \frac{\partial \ln \rho_0}{\partial z}$$

where $\rho_0(z, x, y)$ —undisturbed density, $N^2(z, x, y)$ —buoyancy frequency, g —gravity acceleration, $D(z, x, y) = P(z, x, y)/\rho_0(z, x, y)$, $\delta \gg 1$. The large parameter δ characterizes the ratio of the horizontal and vertical scales of density variability in real ocean (Miropol'skii and Shishkina 2001; Mei et al. 2017; Morozov 2018). The asymptotic solution of systems (1) shall be found in the form (Miropol'skii and Shishkina 2001; Kravtsov and Orlov 1999; Froman and Froman 2002; Bulatov 2014)

$$u_i(z, x, y) = \sum_{m=0}^{\infty} (i\delta)^{-m} u_{mj}(z, x, y) \exp(i\delta L(x, y)), \quad j = 1, 2, 3$$

$$P(z, x, y) = \sum_{m=0}^{\infty} (i\delta)^{-m} P_m(z, x, y) \exp(i\delta L(x, y))$$

Functions $L(x, y), P_m, u_{jm}, j = 1, 2, 3, m = 0, 1, \dots$ are subject to definition. Using relations: $u_{10} = -i|\nabla L|^{-2} L'_x \frac{\partial u_{30}}{\partial z}, u_{20} = -i|\nabla L|^{-2} L'_y \frac{\partial u_{30}}{\partial z}$ we can get:

$$\Pi u_{30} = 0, \Pi = \frac{\partial^2}{\partial z^2} + |\nabla L|^2 ((N(z, x, y)/\omega)^2 - 1)$$

$$u_{30}(0, x, y) = u_{30}(H, x, y) = 0,$$

This spectral problem has a calculation setup of eigenfunctions ϕ_{0n} and eigenvalues $\Omega_n(x, y, \omega) \equiv |\nabla L_n|$, which are assumed to be known (Miropol'skii and Shishkina 2001; Bulatov and Vladimirov 2012, 2019; Bulatov 2014) From here on the index n will be omitted while assuming that further calculations belong to an individually taken mode. For determination of the function $L(x, y)$ we have the eikonal equation: $\nabla^2 L = \Omega^2(x, y, \omega)$. For solving this equation we have the rays systems: $x'_\sigma = e \Omega(x, y, \omega)^{-1}, y'_\sigma = b \Omega(x, y, \omega)^{-1}, b'_\sigma = \Omega(x, y, \omega)'_y, e'_\sigma = \Omega(x, y, \omega)'_x$, where $e = \partial L / \partial x, b = \partial L / \partial y, d\sigma$ is the length element of the ray, σ —ray coordinate. The function $u_{30}(z, x, y)$ is defined to the accuracy of multiplication by the some arbitrary function. The solution to problem (1) can be sought in the form: $D(z, x, y) = \sum_{n=1}^{\infty} A_n(z, x, y) \Phi_n(z, x, y) \exp(i\delta L_n(x, y))$. Functions $\Phi_n(z, x, y)$ are determined from the vertical spectral problem

$$\begin{aligned} \frac{\partial}{\partial z} \left(\frac{\partial \Phi_n(z, x, y)}{\partial z} \alpha^{-1} \right) + \Omega_n^2(x, y, \omega) \Phi_n(z, x, y) &= 0 \\ \frac{\partial \Phi_n(z, x, y)}{\partial z} &= 0, \text{ for } z = 0, -H \end{aligned} \quad (2)$$

Functions $A_n(z, x, y)$ can be represented as (index n is omitted hereafter): $A(z, x, y) = A_0(x, y) + \sum_{m=1}^{\infty} (i\delta)^{-m} A_m(z, x, y)$. Then, to determine the function $A_0(x, y)$, one can obtain the transfer equation

$$2\Lambda \nabla S \nabla A_0 + \Lambda A_0 \Delta S + A_0 (\nabla \Lambda + \mathbf{I}) = 0$$

$$\Lambda = \int_{-H}^0 \Phi^2(z, x, y) dz, \mathbf{I} = \frac{1}{2} \int_{-H}^0 \frac{\nabla \chi}{\alpha} \frac{\partial \Phi^2}{\partial z} dz$$

Along rays this equation has a solution

$$A_0^2(\sigma) \Lambda(\sigma) \Omega(\sigma) da(\sigma) = A_0^2(\sigma_0) \Lambda(\sigma_0) \Omega(\sigma_0) da(\sigma_0) T$$

$$T = \exp\left(-\int_{-\sigma_0}^{\sigma} \mathbf{I} \nabla S(\Lambda \Omega)^{-1} d\sigma\right)$$

where $da(\sigma) = R(\sigma)d\sigma$ —ray tube width, $R(\sigma)$ —geometric ray divergence (Kravtsov and Orlov 1999; Froman and Froman 2002; Bulatov 2014). It can be shown that the exponential factor T is $\Omega(\sigma)/\Omega(\sigma_0)$. Therefore, the solution for the $A_0(\sigma)$ is simplified: $A_0^2(\sigma)\Lambda(\sigma)da(\sigma) = A_0^2(\sigma_0)\Lambda(\sigma_0)da(\sigma_0)$. Then the expression for \mathbf{I} can be represented as

$$\begin{aligned} \mathbf{I} &= \int_{-H}^0 \frac{\nabla \chi}{\alpha} \Phi \frac{\partial \Phi}{\partial z} dz = -\frac{1}{2\Omega^2} \int_{-H}^0 \frac{\partial}{\partial z} \left(\left(\alpha^{-1} \frac{\partial \Phi}{\partial z} \right)^2 \right) \nabla \chi dz = \\ &= \frac{1}{2\Omega^2} \int_{-H}^0 \frac{\partial}{\partial z} (\nabla \chi) \left(\left(\alpha^{-1} \frac{\partial \Phi}{\partial z} \right)^2 \right) \nabla \chi dz = \\ &= \frac{1}{2\omega^2 \Omega^2} \int_{-H}^0 \nabla N^2(z, x, y) \left(\left(\alpha^{-1} \frac{\partial \Phi}{\partial z} \right)^2 \right) dz \end{aligned}$$

It is possible to obtained

$$-\Lambda \nabla \ln \Omega = \frac{1}{2\omega^2 \Omega^2} \int_{-H}^0 \nabla N^2(z, x, y) \left(\left(\alpha^{-1} \frac{\partial \Phi}{\partial z} \right)^2 \right) dz \quad (3)$$

Apply to Eq. (2) the operator ∇

$$\begin{aligned} \frac{\partial}{\partial z} \left(\frac{\partial \mathbf{F}}{\partial z} \alpha^{-1} \right) + \Omega^2 \mathbf{F} &= -\frac{\partial}{\partial z} \left(\frac{\partial \Phi}{\partial z} \nabla(\alpha^{-1}) \right) - \Phi \nabla \Omega^2, \mathbf{F} = \nabla \Phi \\ \frac{\partial \mathbf{F}}{\partial z} &= 0, \text{ for } z = 0, -H \end{aligned} \quad (4)$$

From (3)–(4) we get

$$\nabla \Omega^2 \int_{-H}^0 \Phi^2(z, x, y) dz = \int_{-H}^0 \frac{\partial}{\partial z} \left(\omega^{-2} \alpha^{-2} \frac{\partial \Phi}{\partial z} \nabla N^2 \right) \Phi dz$$

As a result we can get

$$\mathbf{I} = -\Lambda \nabla \ln \Omega$$

The conservation law can be written as well in the form suitable for finding the function A_0 :

$$\begin{aligned} \frac{A_0^2(x(\sigma, \alpha), y(\sigma, \alpha))}{\Omega^2(x(\sigma, \alpha), y(\sigma, \alpha))} d a(x(\sigma, \alpha), y(\sigma, \alpha)) &= \\ &= \frac{A_0^2(x_0(\alpha), y_0(\alpha))}{\Omega^2(x_0(\alpha), y_0(\alpha))} d a(x_0(\alpha), y_0(\alpha)) \end{aligned}$$

where $d a(x(\sigma, \alpha), y(\sigma, \alpha)) = J(x(\sigma, \alpha), y(\sigma, \alpha)) d\alpha$ is the unit ray tube width, J —Jacobian from ray coordinates to Cartesian coordinates. Note that the wave energy flash is proportional to $A_0^2 \Omega^{-1} d a$, thus, in this case, there survives the value equal to the wave energy flash divided by the wave vector modulus (Miropol'skii and Shishkina 2001; Bulatov and Vladimirov 2012, 2018, 2019; Bulatov 2014). In real oceanic conditions, an arbitrary source of disturbances can be represented as a superposition of harmonic waves

$$(U_i, p) = \int \omega \sum_{m=0}^{\infty} (i\delta)^{-m} (u_{jm}, P_m) \exp(i\omega t - i\delta L_m(\omega, x, y)) d\omega, j = 1, 2, 3$$

In this paper we have built asymptotics notations of the solutions on IGW propagation in the non-uniform medium in the horizontal direction. Numerical calculations for typical oceanic parameters indicate essential influence of the factors of horizontal non-uniformity of natural parameters on real IGW dynamics. All obtained analytical results of this paper were generally obtained for arbitrary density distributions and other parameters of non-uniform stratified natural mediums, and moreover, the basic physical mechanisms of forming the investigated phenomena of IGW dynamics in non-uniform stratified mediums were examined in the frame of the available field data. The popularity of suggested approaches to analyze the IGW dynamics could be supported by the fact of existing a wide scope of interesting physical problems which are quite adequately defined by these approaches, because the multiplicity of issues of the kind is related to the variety of non-uniform stratified mediums (Morozov 2018; Matyushin 2019; Lecoanet et al. 2015; Voelker et al. 2019; Wang et al. 2017). The importance of such methods for analyzing the wave field is attributed to not only their visualization, universal applicability and effectiveness in solving various problems, but also to a possibility that they become a semi-empirical basis for other method of approximations in the propagation theory for wave packets of other physical nature. Therefore, to understand the physics of many linear and non-linear wave processes within non-uniform media we have to study the full complex of hydrodynamic effects going with the propagation of IGW in a stratified medium, moreover, it so happened that the analytical constructions of the sort can be easily observed under the real ocean conditions (Mei et al. 2017; Morozov 2018).

Acknowledgements The work is carried out with financial support from the Russian Foundation for Basic Research, project 20-01-00111A.

References

- Broutman D, Rottman J (2004) A simplified Fourier method for computing the internal wave field generated by an oscillating source in a horizontally moving, depth-dependent background. *Phys Fluids* 16:3682–3689
- Bulatov VV, Vladimirov YV (2012) *Wave dynamics of stratified mediums*. Nauka, Moscow
- Bulatov VV, Vladimirov YV (2014) Asymptotical analysis of internal gravity wave dynamics in stratified medium. *Appl Math Sci* 8:217–240
- Bulatov VV, Vladimirov YV (2018) Internal gravity waves in horizontally inhomogeneous ocean. In: Velarde MG et al (eds) *The ocean in motion*. Springer oceanography. Springer International Publishing AG, Berlin, pp 109–126
- Bulatov VV, Vladimirov YV (2019) *A general approach to ocean wave dynamics research: modelling, asymptotics, measurements*. OntoPrint Publishers, Moscow
- Bulatov VV, Vladimirov YV, Vladimirov IY (2019) Far fields of internal gravity waves from a source moving in the ocean with an arbitrary buoyancy frequency distribution. *Russian J Earth Sci* 19:ES5003
- Fabrikant AL, Stepanyants YA (1998) *Propagation of waves in shear flows*. World Scientific Publishing, London
- Froman N, Froman P (2002) *Physical problems solved by the phase-integral method*. Cambridge University Press, Cambridge
- Kravtsov Y, Orlov Y (1999) *Caustics, catastrophes and wave fields*. Springer, Berlin
- Lecoanet D, Le Bars M, Burns KJ, Vasil GM, Brown BP, Quataert E, Oishi JS (2015) Numerical simulations of internal wave generation by convection in water. *Phys Rev E – Stat Nonlinear Soft Matter Phys* 9:1–10
- Matyushin PV (2019) Process of the formation of internal waves initiated by the start of motion of a body in a stratified viscous fluid. *Fluid Dyn* 54:374–388
- Mei CC, Stiassnie M, Yue DK-P (2017) *Theory and applications of ocean surface waves*. Advanced series of ocean engineering, vol 42. World Scientific Publishing, Singapore
- Miropol'skii YZ, Shishkina OV (2001) *Dynamics of internal gravity waves in the ocean*. Kluwer Academic Publishers, Boston
- Morozov TG (2018) *Oceanic internal tides. Observations, analysis and modeling*. Springer, Berlin
- Voelker GS, Myers P G, Walter M, Sutherland BR (2019) Generation of oceanic internal gravity waves by a cyclonic surface stress disturbance. *Dyn Atm Oceans* 86:16–133
- Wang H, Chen K, You Y (2017) An investigation on internal waves generated by towed models under a strong halocline. *Phys Fluids* 29:065104

Far Internal Gravity Waves Fields Generated by a Sources Distributed on a Moving Plane



V. V. Bulatov  and Yu. V. Vladimirov 

Abstract The problem of the internal gravity waves far fields generated by a moving non-local source of disturbances is considered. The integral representation of the solution has the form of a sum of wave modes. The perturbation method was used to study the characteristics of the corresponding dispersion relations that determine the behavior of far wave fields. The asymptotics of solutions for individual wave modes are obtained, which make it possible to calculate wave fields far from arbitrary non-local sources of disturbances. A general scheme of mathematical modeling of the internal gravity waves far fields generated by a moving non-local sources is proposed.

Keywords Stratified medium · Internal gravity waves · Source distribution · Far fields

Perturbations of various physical nature are important mechanisms of generation of internal gravity waves (IGW) in stratified media (ocean, atmosphere of the Earth); they include natural sources (moving disturbances of the atmospheric pressure, flows over uneven bottom topography, leeward perturbations of flows near mountains, tidal generation) and anthropogenic influence (marine technological structures, collapse of turbulent mixing regions, underwater explosions) (Lighthill 1978; Miropol'skii and Shishkina 2001; Mei et al. 2017; Morozov 2018). Generation and propagation of IGW in real oceanic conditions are essentially nonlinear. It is possible to linearize the system describing the wave dynamics under some reasonable assumptions. A combination of model concepts and semi-empirical, and possibly, even experimental data may become interesting (Adcroft and Campin 2011; Elizarova 2009; Bulatov and Vladimirov 2012, 2019). Solutions of linear equations of IGW generated by local sources of disturbances were studied in detail in Lighthill (1978); Miropol'skii and Shishkina 2001; Gray et al. 1983; Kallen 1987; Borovikov and

V. V. Bulatov (✉) · Yu. V. Vladimirov
Ishlinsky Institute for Problems in Mechanics RAS, Vernadskogo ave. 101-1, 119526 Moscow, Russia
e-mail: internalwave@mail.ru

Yu. V. Vladimirov
e-mail: vladimyura@yandex.ru

Bulatov 1995). Therefore, knowing such solutions, it is possible to write a solution for non-local sources distributed vertically and horizontally. The following approach is also possible. Let us assume that there is a nonlocal source of disturbances that leaves behind a turbulent wake (a region of eddies or a mixing zone) that generates IGW by means of a specific mechanism. We locate an imaginary plane parallel to the trajectory of motion of the source of perturbations; the initial data on the plane can be determined both experimentally and by numerical simulations. Then it is possible to solve the problem of the propagation of IGW in a linear formulation using the data on the plane as the boundary conditions. Much real information can be stored under these a priori conditions (Elizarova 2009; Robey 1997; Voisin 2007; Wang et al. 2017a, 2017b). A linear theory based on these conditions can give quite satisfactory results far from the regions of nonlinearity. This approach seems to be quite reasonable, since good results should be expected from the linear theory far from the turbulence regions, mixing zones, eddy formations, and other nonlinear phenomena (Bulatov and Vladimirov 2012, 2019, 2020). In this paper, we consider an example illustrating this approach, which makes it possible to calculate properties of IGW far from nonlocal sources of perturbations, the distribution of which is given on a certain plane in a layer of stratified medium.

Vertical component W of velocity of linear IGW, which are generated by a point source of perturbations moving in an inviscid, incompressible, stratified medium of depth H with velocity V on plane $y = 0$ in the Boussinesq approximation satisfies equation (Lighthill 1978; Miropol'skii and Shishkina 2001; Bulatov and Vladimirov 2012, 2019)

$$LW(x + Vt, y, z, z_0) = 0, \quad L = \frac{\partial^2}{\partial t^2} \left(\Delta + \frac{\partial^2}{\partial z^2} \right) + N^2(z) \Delta \quad (1)$$

$$\Delta = \frac{\partial^2}{\partial x^2} + \frac{\partial^2}{\partial y^2}, \quad N^2(z) = -\frac{g}{\rho_0(z)} \frac{d\rho_0(z)}{dz},$$

$$W = \delta(x + Vt) \delta(z - z_0) \quad (y = 0), \quad (2)$$

$$W = 0 \quad (z = 0, -H), \quad (3)$$

where $N^2(z)$ is squared Brunt–Väisälä frequency (buoyancy frequency), g is acceleration due to gravity, and $\rho_0(z)$ is unperturbed density of the stratified medium. Solution $U(x + Vt, y, z)$ with arbitrary boundary condition at $y = 0$ of the following form $U(x + Vt, 0, z) = f(x + Vt, z)$ is determined by the corresponding convolution

$$U(x + Vt, y, z) = \int_{-H}^0 dz_0 \int_{-\infty}^{\infty} W(x + Vt - \lambda, y, z - z_0) f(\xi, z_0) d\lambda \quad (4)$$

Uniqueness of the solution is provided by the radiation condition, which can be set as follows. We consider function $\eta(t, x, y, z)$ that satisfies Eq. (1), boundary conditions (3), and boundary condition at $y = 0$ written as

$$\eta = \delta(x + Vt)\delta(z - z_0)\exp(\varepsilon t) (y = 0) \text{ at } \varepsilon > 0. \tag{5}$$

If we seek function η as: $\eta = \exp(\varepsilon t)\xi(x + Vt, y, z)$ and introduce additional condition for decreasing $\xi \rightarrow 0 (y \rightarrow \infty)$, then ξ is determined uniquely. Then, solution W of problem (1)–(3) is determined as the limit: $W(x + Vt, y, z) = \lim_{\varepsilon \rightarrow 0} \xi$. Solution of problem (1), (3), (5) can be reasonably sought by separating variables. Let w be a solution of Eq. (1) satisfying boundary conditions (3), and boundary condition at $y = 0$

$$w = \exp(i(\mu x + \Omega t))\delta(z - z_0) (y = 0), \quad \Omega = \omega - i\varepsilon. \tag{6}$$

Then, solution of problem (1), (3), (5) at $t > 0$ is written in terms of w as:

$$\eta(t, x, y, z) = \frac{1}{4\pi^2 i} \int_{-\infty}^{\infty} d\mu \int_{-\infty - i\varepsilon}^{\infty - i\varepsilon} \frac{w d\omega}{\omega - \mu V}.$$

We shall seek for the solution to problem (1), (3), (6) using the method of separation of variables and consider the spectral problem

$$\Omega^2 \frac{\partial^2 \phi}{\partial z^2} + (\mu^2 + \nu^2)(N^2(z) - \Omega^2)\phi = 0, \tag{7}$$

$$\phi = 0 (z = 0, -H),$$

where, μ is a free parameter, ν is a spectral parameter. This problem has a set of eigen values $\pm \nu_n(\mu)$ and eigen functions $\phi_n(z, \mu)$; these functions are complete and orthonormal with the weight $(N^2(z) - \Omega^2)$ (Lighthill 1978; Miropol'skii and Shishkina 2001; Bulatov and Vladimirov 2012, 2019). Therefore, the following expansion is possible: $\delta(z - z_0) = \sum_n (N^2(z_0) - \Omega^2) F_n(z, z_0, \mu)$, $F_n(z, z_0, \mu) = \phi_n(z, \mu)\phi_n(z_0, \mu)$. If we assume that ν_n is a root with positive imaginary part, solution of problem (1), (3), (5) will be written as:

$$w = \sum_n (N^2(z) - \Omega^2) \exp(i(\mu x + \Omega t + \nu_n y)) F_n(z, z_0, \mu).$$

Then, we can present solution of problem (1), (3), (4) as:

$$\eta(t, x, y, z) =$$

$$= \sum_n \int_{-\infty}^{\infty} \frac{(N^2(z) - (\mu V - i\varepsilon)^2)}{2\pi} \exp(\varepsilon t + i v_n(\mu) y + i \mu(x + Vt)) F_n(z, z_0, \mu) d\mu$$

where $v_n(\mu)$ are eigen numbers of spectral problem:

$$(\mu V - i\varepsilon)^2 \frac{\partial^2 \phi_n}{\partial z^2} + (\mu^2 + v_n^2(\mu))(N^2(z) - (\mu V - i\varepsilon)^2) \phi_n = 0, \quad (8)$$

$$\phi_n = 0 \quad (z = 0, -H).$$

Let us consider properties of functions $v_n(\mu)$ assuming that $\varepsilon = 0$. This function is either real or imaginary depending on the sign of $v_n^2(\mu)$. If $\mu V > N_{\max}$, where N_{\max} is the maximum value of the Brunt-Väisälä frequency, then v_n^2 is negative: $v_n^2 = -\gamma_n^2(\mu)$ and we have to take values $v_n = i\gamma_n(\mu)$. A transition to small $\varepsilon > 0$ does not change the sign of the imaginary part of v_n . If $\mu V < N_{\max}$, then v_n^2 is positive and can be determined from equation: $\omega_n(\kappa) = \mu V$, where $\kappa = \sqrt{\mu^2 + v^2}$, and $\omega_n(\kappa)$ is determined from the solution of the main spectral problem of internal gravity waves (Lighthill 1978; Miropol'skii and Shishkina 2001; Morozov 2018) (we neglect rotation of the Earth)

$$\frac{\partial^2 \phi_n(z, k)}{\partial z^2} + k^2 \left(\frac{N^2(z)}{\omega_n^2(k)} - 1 \right) \phi_n(z, k) = 0,$$

$$\phi_n = 0 \quad (z = 0, -H).$$

The main properties of functions $\mu = \mu_n(v)$ are studied in detail in Bulatov and Vladimirov (2012, 2019), Gray et al. (1983), Borovikov and Bulatov (1995). These functions monotonously increase at $v \rightarrow \infty$ and tend to a finite limit equal to $N_{\max}/V \equiv M$. Function $\mu_n(v)$ monotonously increases at $v \rightarrow \infty$ and tends to a finite limit equal to M . Therefore, the inverse function monotonously increases and tends to infinity at $\mu \rightarrow M$. At the given values of μ the sign of $v_n(\mu)$ is found from the condition that coefficient at $\exp(\pm i v_n(\mu) y)$ decreases when $y \rightarrow +\infty$. If we consider domain $y < 0$, we select the opposite sign. Let us calculate the imaginary addition to $v_n(\mu)$. We present $v_n(\mu)$ as $v_n = v_{n0} + i\varepsilon v_{n1}$, then using the theory of perturbations we can get from Eq. (7) that

$$v_{n1} = -\frac{1}{v_{n0}} \left(\frac{1}{\mu V (v_{n0}^2 + \mu^2)} + \mu V (v_{n0}^2 + \mu^2) \int_{-H}^0 \phi_n^2(z, \mu) dz \right).$$

Therefore, at $y > 0$ we select the minus sign for the coefficient at $\exp(\pm i v_n(\mu) y)$, and positive sign if the values of y are negative. Let us now consider the case when

$\mu > M$. In this case $v_n^2(\mu)$ is negative and correspondingly $v_n(\mu)$ is purely imaginary; its absolute value is not smaller than M , which follows from the existence of solution to the Sturm–Liouville problem: $\frac{d^2\phi}{dx^2} + q(x)\phi = 0$, only if $q(x)$ is not smaller than 0 at all x . At $\mu > M$ we get that $N^2(z) - \mu^2 V^2 < 0$ at all z , therefore, $\mu^2 + v_n^2(\mu) > 0$ at $\mu > M$. Therefore, $v_n^2(\mu) < -M^2$ at all $\mu > M$. Hence, the contribution of the imaginary part of function $v_n(\mu)$ is an exponentially small value. Inverse function $v = v_n(\mu)$ increases and tends to infinity at $\mu \rightarrow M$. At small μ , the following expansion is possible: $v_n(\mu) = \alpha_n \mu + j_n \mu^3 + \dots$, where $\alpha = q_n$, $j_n = \beta_n q_n^4$, q_n , β_n are coefficients of expansion $\mu_n(v) = q_n^{-1} v - \beta_n v^3 + \dots$ at zero. At $\varepsilon = 0$ and $\mu < M$. Equation (6) determines two families of dispersion curves $v = \pm v_n(\mu)$; among these two branches we select the one whose imaginary part is positive at $\varepsilon < 0$. This branch can be easily chosen using the method of perturbations; therefore, we take $v = -v_n(\mu)$. Now we can make a transition to the limit at $\varepsilon \rightarrow 0$, and as a result get a solution of problem (1)–(3) in the form

$$W = \frac{1}{2\pi} \sum_n (I_n^0 + I_n^+ + I_n^-),$$

$$I_n^0 = \int_{-M}^M A_n(z, z_0, \mu) \exp(i\mu(x + Vt) - i v_n(\mu)y) d\mu,$$

$$I_n^- = \int_{-\infty}^{-M} A_n(z, z_0, \mu) \exp(i\mu(x + Vt) - \gamma_n(\mu)y) d\mu,$$

$$I_n^+ = \int_M^{\infty} A_n(z, z_0, \mu) \exp(i\mu(x + Vt) - \gamma_n(\mu)y) d\mu,$$

$$A_n(z, z_0, \mu) = (N^2(z_0) - \mu^2 V^2) F_n(z, z_0, \mu).$$

We assume in integrals I_n^0 that $v_n(\mu)$ is a monotonously increasing function of μ determined from (6). Integrals I_n^\pm are exponentially small at $y \gg 1$. Therefore, at $y \gg 1$ (at large distances from plane $y = 0$) we get

$$W = \sum_n W_n,$$

$$W_n = \frac{1}{2\pi} \int_{-M}^M A_n(z, z_0, \mu) \exp(i\mu(x + Vt) - i v_n(\mu)y) d\mu.$$

This expression differs from integral presentations of individual wave modes considered in Bulatov and Vladimirov (2012, 2019), Gray et al. (1983), Borovikov

and Bulatov (1995) by the coefficient at the exponent. Therefore, asymptotics of the components of W_n at $y \gg 1$ can be found similarly. At $x + Vt < q_n y$ (where $q_n = \sqrt{V^2 c_n^{-2} - 1}$, and c_n is the maximum group velocity of wave mode n), W_n exponentially decreases. At $x + Vt > q_n y$, asymptotics of W_n can be found using the stationary phase method:

$$W_n \approx 2 \frac{N^2(z_0) - (\mu_n^*)^2 V^2}{\sqrt{2\pi y |v_n''(\mu_n^*)|}} \cos(\Phi_n) F_n(z, z_0, \mu_n^*), \quad (9)$$

$$\Phi_n = \mu_n^*(x + Vt) - v_n(\mu_n^*)y + \pi/4$$

where μ_n^* is a solution of equation $\frac{x+Vt}{y} = \frac{\partial v_n(\mu)}{\partial \mu}$. At $x + Vt \rightarrow q_n y$, stationary points $\mu = \pm \mu_n^*$ merge, and then near the wave front of individual mode $x + Vt = q_n y$, asymptotics of W_n at $y \gg 1$ are expressed from the Airy function (Bulatov and Vladimirov (2012, 2019); Borovikov and Bulatov 1995):

$$W_n \approx \frac{N^2(z_0) F_n(z, z_0, 0)}{q_n \sqrt[3]{\beta_n q_n y}} Ai\left(\frac{x + Vt - q_n y}{q_n \sqrt[3]{\beta_n q_n y}}\right), \quad (10)$$

$$Ai(\tau) = \frac{1}{2\pi} \int_{-\infty}^{\infty} \cos(\tau u - u^3/3) du.$$

Let us qualitatively describe propagation of far field of IGW from a nonlocal source of perturbations: at $x + Vt < q_1 y$, the wave field is negligibly small, at $x + Vt = q_1 y$, the front of the first wave mode arrives to the fixed point of observations; in the vicinity of the front the field is described by formulas (4), (10) through the Airy function convolution; at $q_1 y < x + Vt < q_2 y$, the far wave field consists of one wave packet, which is determined by convolution from formulas (4), (9); at $x + Vt = q_2 y$, the second wave packet arrives to the point of observations; in the vicinity of this packet, the wave field is also described by Airy functions (4), (10); at $q_1 y < x + Vt < q_3 y$, the wave field consists of two terms determined by the corresponding convolutions (4), (9); at $x + vt = q_3 y$, the third wave packet arrives to the point of observations; the total wave field consists of three terms, and so on. Numerical simulations for realistic distributions of buoyancy frequency observed in the ocean show that the main contribution to the far wave field of IGW is done only by a few first wave modes. Therefore, in the majority of the practically important oceanographic problems the applicable accuracy of simulations of far wave fields can be provided by not more than 3–5 wave modes (Bulatov and Vladimirov 2012, 2019, 2020; Borovikov and Bulatov 1995).

The asymptotics of the solutions obtained in this paper make it possible to calculate wave fields far from arbitrary nonlocal sources of perturbations. A general scheme for modeling the far fields of IGW from moving nonlocal sources of disturbances can

be presented as follows. Main characteristics of the wave field parameters (velocity components, density, pressure) are determined from the numerical solution of the complete system of hydrodynamic equations. Their distribution can be specified on a given plane. If we assume that a linear model of wave dynamics of stratified media is adequate, far fields of IGW can be calculated from formulas (4), (9), (10) far from the sources of perturbations. The results of calculations show that under real hydrological conditions of the ocean, only the first few wave modes make the main contribution to the far fields. Therefore, the results obtained in this work make it possible not only to efficiently calculate far wave fields, but also to carry out a qualitative assessment of the solutions obtained.



Acknowledgements The work is carried out with financial support from the Russian Foundation for Basic Research, project 20-01-00111A.

References

- Adcroft A, Campin J-M (2011) MITgcm user manual. MIT, Cambridge
- Borovikov VA, Bulatov VV, Vladimirov YV (1995) Internal gravity waves excited by a body moving in a stratified fluid. *Fluid Dyn Res* 5:325–336
- Bulatov VV, Vladimirov YV (2012) Wave dynamics of stratified mediums. Nauka, Moscow
- Bulatov VV, Vladimirov YV (2019) A general approach to ocean wave dynamics research: modelling, asymptotics, measurements. OntoPrint Publishers, Moscow
- Bulatov V, Vladimirov Y (2020) Generation of internal gravity waves far from moving non-local source. *Symmetry* 12(11):1899
- Elizarova TG (2009) Quasi-gas dynamic equations. Springer, Berlin
- Gray EP, Hart RW, Farrel RA (1983) The structure of the internal Mach front generated by a point source moving in a stratified fluid. *Phys Fluids* 26:2919–2931
- Kallen E (1987) Surface effects of vertically propagation waves in a stratified fluid. *J Fluid Mech* 148:111–125
- Lighthill J (1978) Waves in fluids. Cambridge University Press, Cambridge
- Mei CC, Stiassnie M, Yue DK-P (2017) Theory and applications of ocean surface waves. Advanced series of ocean engineering, vol 42. World Scientific Publishing, Singapore
- Miropol'skii YZ, Shishkina OV (2001) Dynamics of internal gravity waves in the ocean. Kluwer Academic Publishers, Boston
- Morozov TG (2018) Oceanic internal tides. Observations, analysis and modeling. Springer, Berlin
- Robey H (1997) The generation of internal waves by a towed sphere and its wake in a thermocline. *Phys Fluids* 9:3353
- Voisin B (2007) Lee waves from a sphere in a stratified flow. *J Fluid Mech* 574:273–292
- Wang H, Chen K, You Y (2017) An investigation on internal waves generated by towed models under a strong halocline. *Phys Fluids* 29:065104
- Wang J, Wang S, Chen X, Wang W, Xu Y (2017) Three-dimensional evolution of internal waves rejected from a submarine seamount. *Phys Fluids* 29:106601

A Two-Story Tornado in a Lab



I. V. Naumov , B. R. Sharifullin, S. G. Skripkin, M. A. Tsoy,
and V. N. Shtern 

Abstract Looking for a flow pattern optimal for the growth of a culture in vortex bioreactors, we found a curious structure, which mimics strong vortices observed in the atmosphere and the ocean, and can be referred to as “two-story tornado”. The rotating lid drives circulation of two immiscible fluids in a sealed vertical cylinder. As the rotation speed exceeds a threshold, the spiraling in flow above the interface induces the spiraling out flow below the interface. This paradoxical phenomenon indicates that the radial velocity jumps at the interface, i.e., there is a slip between these moving fluids. As the rotation speed further increases, the tornado-like motion develops in both fluid and a dual vortex breakdown occurs. This experimentally discovered and practically important slip phenomenon yet requires an explanation.

Keywords Vortex flow · Tornado · Flow visualization · Immiscible fluids · Vortex breakdown

1 Introduction

It has long been known that vortex motion is one of the basic states of a moving medium. Despite the centuries-old history of hydrodynamics, dating back to the works of da Vinci, Torricelli and Newton, many of its mysteries still remain unsolved. These primarily concern vortex flows. Natural vortex flows have different structures and scales in the thickness of their medium and near the free surface, where they coexist and interact with waves of different natures. Some vortex structures, such as eddies on the surfaces of seas and oceans, tornadoes, or waterspouts over the water surface, can be observed with the naked eye (Fig. 1), while spiral galaxies, large-scale atmospheric vortices, currents in the ocean (Fig. 2), and vortex motion in the vessels of biological organisms require special recording equipment.

Although the existence of various types of vortices in contact with a free surface, such as a vertical Rankine vortex (whirlpool) or Helmholtz half-rings behind a blunt

I. V. Naumov (✉) · B. R. Sharifullin · S. G. Skripkin · M. A. Tsoy · V. N. Shtern
Kutateladze Institute of Thermophysics SB RAS, Novosibirsk, Russia
e-mail: naumov@itp.nsc.ru



Fig. 1 Photos of natural vortices (from open-access internet sites)



Fig. 2 Pictures of large natural vortices (from open-access internet sites)

body has been known for a long time, important issues of the generation of vortices, their metamorphoses, and their influence on the transfer of matter require further analysis and understanding.

In technical applications, the creation of successful vortex mixing methods is promising direction for the optimization of chemical, pharmaceutical, biological, and other processes. These methods depend on the properties of the vortex motion and change with varying structure and rotation strength of the flow. In both natural and technical applications, the vortex core can suddenly expand, and the axial velocity can reverse its direction. This phenomenon, referred to as vortex breakdown (VB), has been the subject of more than a thousand publications since 1957 (Peckham and Atkinson 1957).

The lasting interest of researchers is due to important applications and the seemingly mysterious nature of VB. In an airplane with delta-shaped wings, VB causes sudden changes in lift and drag. In vortex burners, VB stabilizes the flame and reduces harmful emissions. VB weakens the tornado by expanding its funnel. In biological and chemical vortex reactors (Fig. 3), VB improves the mixing of ingredients (Shtern 2018).

A suitable model of a bio-reactor is a vertical cylindrical container filled with two immiscible fluids, the movements of which are caused by the rotation of the upper disk. Simple geometry and isolation from external disturbances make this model very

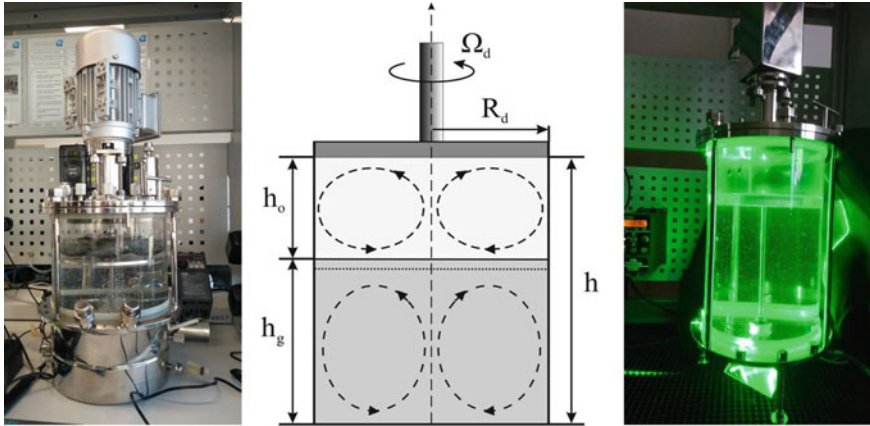


Fig. 3 Photos of a bioreactor (left) and the experimental set up (right). A schematic of meridional motion (center)

convenient for experimental and numerical studies. In particular, the model makes it easier to study the nature of VB and other striking phenomena, which this movement is rich in: sliding between liquids (Naumov et al. 2018a), hysteresis (Naumov et al. 2020a) and the appearance of multiple circulation cells (Naumov et al. 2018b).

2 Problem Formulation and Methods

Our studies of the vortex motion near the interface between two liquids were carried out in a cylindrical container made of optical grade Plexiglas. The container had a radius $R = 48$ mm and a height $h = 2.5R$. The container was filled with two immiscible liquids: (a) a 67% aqueous solution of glycerin (heavy liquid, density $\rho_g = 1070$ kg/m³ and kinematic viscosity $\nu_g = 3$ mm²/s) and (b) sunflower oil (light liquid with $\rho_o = 920$ kg/m³ and $\nu_o = 49$ mm²/s). The density and kinematic viscosity of the working fluids used in the experiment were determined at room temperature (22.6 °C) and were kept constant during observations.

A significant difference in the density of the upper and lower liquids provided the stable interface. The vortex motion of liquids was generated by the upper disk ($R_d = 47$ mm), which rotated with an angular velocity Ω_d , while the other walls of the container were stationary. Rotation of the disk was set by a stepper motor, and its intensity was characterized by the Reynolds number $Re = \Omega_d R^2 / \nu_o$, where ν_o is the kinematic viscosity of the fluid in contact with the rotating disk.

Polyamide beads, of density 1030 kg/m³ and diameter around 10 μ m, serve as seeding light-scattering particles (tracers) for both PIV measurements and visualization of flow pattern. The previous studies (Naumov et al. 2019; Carrión et al. 2020) and current study show that the experimental (with tracers) and numerical (with no

tracer) velocity profiles and flow patterns well agree in the upper fluid (oil). This agreement indicates that the presence of the tracer particles does not significantly disturb the flow. The amount of particles and the averaging procedure in tracking visualization are sufficient for detecting of dual vortex breakdown (DVB). Distortions due to the cylindrical sidewall do not significantly affect velocities near the axis where DVB's are detected while sometimes causing errors up to 5% in the radial velocity at the periphery. However, these errors do not significantly affect the velocity profiles presented in this paper.

The technique of tracer visualization has been improved and adapted to the experimental conditions for the optical diagnostics of vortex flow with the development of bubble-type vortex breakdown. This technique appears efficient for investigations of slow processes, where the displacement of tracers in the flow is extremely small and it is necessary to increase the exposure time to catch a vortex flow pattern. The main problem is the noise accumulation while drawing a track for a long exposure time. To overcome this problem, we use a short exposure time, subtract a pre-measured average intensity value, and apply the floating averaging window in order to obtain a sufficient track length and optimal contrast for the upper and lower liquids (Naumov et al. 2020b; Carrión et al. 2020).

3 Two-Story Tornado Discussion

Let us dwell in more detail on the phenomenon, which for the sake of brevity we will call a “vortex domino” (VD). With a certain selection of fluids and the ratio of their volumes, VB occurs almost simultaneously in both fluids with an increase in rotation (Naumov et al. 2019; Naumov and Sharifullin 2020). The result is a meridional flow structure that resembles a one–one domino tile (hence the name “vortex domino”, Fig. 4).

Near the lid, centrifugal force pushes the adjacent fluid from the axis to the periphery, generating a meridional circulation: the upper fluid descends near the side wall to the interface. There it spirally converges to the cylinder axis, where it returns to the vicinity of the lid. This centrifugal circulation (CC) causes anti-centrifugal circulation (AC) in the lower fluid: convergence to the axis near the interface, immersion near the axis to the bottom, a spiral divergence to the side wall, and rise along the wall to the interface. Such a two-toroid vortex structure (already favorable for mixing) exists at the slowest rotation.

As the rotation speeds up, dramatic and important changes in the flow topology occur. In the lower fluid, a new CC cell appears near the interface as a result of the competition between mass centrifugal forces (pushing the fluid to the periphery) and viscous friction forces (pushing the fluid to the axis). This cell emerges at the intersection of the axis with the interface and expands downward and radially, dividing the original AC cell into the lower (bottom) and upper (adjacent to the interface) ring-like parts. Then the CC cell occupies almost the entire volume of the lower fluid, the bottom AC cell collapses, and the upper AC cell takes the form of a thin ring located

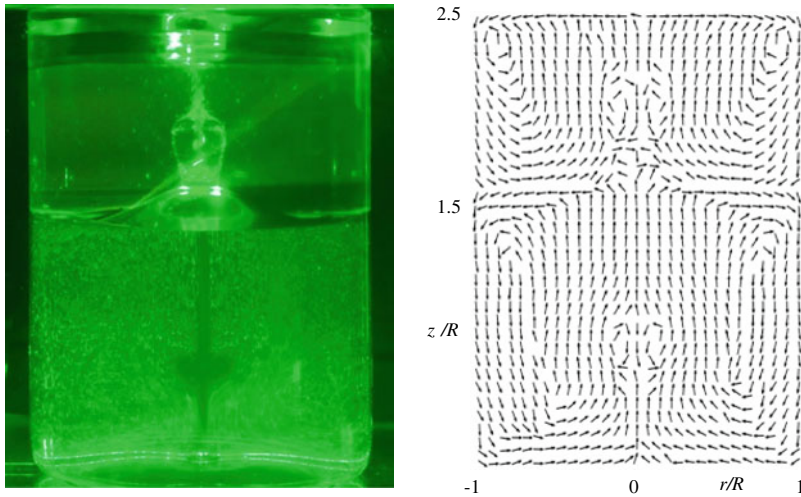


Fig. 4 Vortex breakdown “domino” photo (left) and normalized measured PIV vector field (right) from Naumov et al. 2020b

at the intersection of the interface and the side wall. Further, at the intersection of the interface with the axis in the lower fluid, a new AC cell appears which merges with the AC ring, forming a thin AC layer (Naumov et al. 2018b). This layer, adjacent to the entire interface from below, serves as a kind of liquid bearing, separating the centrifugal circulations of the upper and lower fluids (Fig. 3, center).

Surprisingly, it was found that numerical simulations contradict this experimental scenario of changing the flow structure (Naumov et al. 2018a; Carrión et al. 2020). The calculated and experimental results are in agreement in the upper liquid, but diametrically opposed in the lower one. In contrast to experiments in simulations, a new CC cell develops near the bottom and grows upward, reaching the interface at the axis (Naumov et al. 2018a).

Further investigation showed that sliding occurs in the experiments: the radial velocity at the interface undergoes a jump, changing its magnitude and even its direction. While in the calculations, the condition of velocity continuity was used. This explains the difference in results.

Although the experimental and numerical scenarios for the formation of centrifugal circulation in the lower fluid are radically different, the final result is almost the same: tornado-like swirling jets develop in both fluids, and the entire flow takes on the structure of a miniature two-story tornado. It was found that (with a certain selection of liquids and the ratio of their volumes) with an increase in the rotation speed, the vortex breakdown occurs in the upper fluid (Naumov et al. 2019), in the lower fluid (Naumov and Sharifullin 2020), or almost simultaneously in both (Naumov et al. 2020b; Carrión et al. 2020). The result is the meridional flow structure that resembles a one–one domino tile.

An important and paradoxical experimental fact is that a spiral flow of a lighter upper fluid converging above the interface creates a diverging (!) spiral motion of the denser lower fluid under the interface. Figure 5 illustrates this phenomenon showing the flow patterns for $Re = 50$ (with no paradox) and $Re = 250$ (with the paradox). With a further increase in disk rotation, a significant deformation of the interface occurs (Fig. 6), which facilitates the transfer of angular momentum through the interface. Converging spirals are still observed above the interface, and diverging spirals are observed below the interface. However in the near-axis region, concentric circles appear with their radius equal to the radius of the hump of the interface. Such a structure is observed until the appearance of pulsations, the destruction of the interface, and the mixing of both liquids as the rotation further intensifies (for $Re > 1200$).

Unlike the known slip mechanisms (in a rarefied gas, on a rough surface, or created by surfactants), in this new case, sliding is caused by centrifugal force. The detected slip is of fundamental importance, since all calculations of two-fluid rotating flows, obtained under the condition of continuity, now require revision.

Despite the experimental and numerical scenarios being radically different, the final result is almost the same: a thin AC layer is formed separating the large-scale CC regions in the upper and lower fluids. A slight difference is that the CC areas do not touch each other in the experiment, but they touch at one point (at the axis) in the calculation.

During experimental studies, different liquids (alcohol, water, glycerin and mixtures thereof) were used with their density difference from 0.5% to 30% with repeating results of the evolution of the vortex motion. In an aerial-vortex bioreactor, a similar movement is observed where the air vortex drives the circulation of

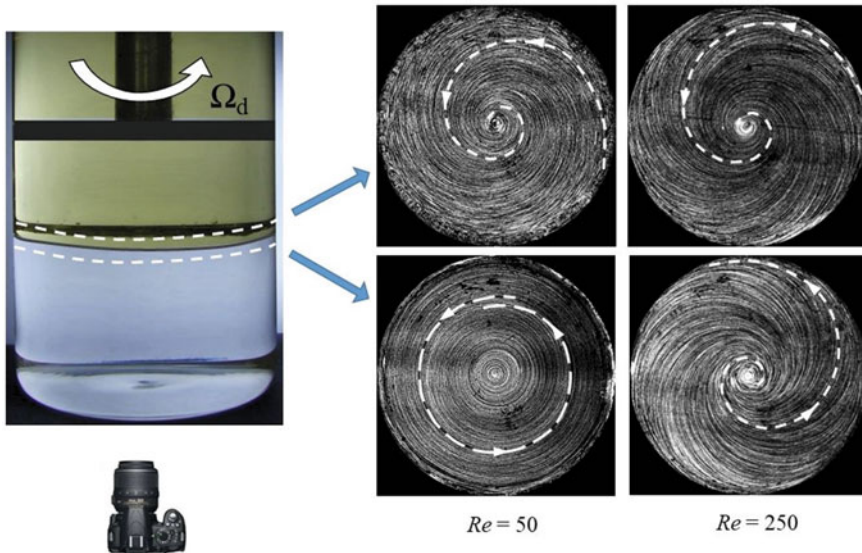


Fig. 5 Spiral motion above and below the interface at $Re = 250$

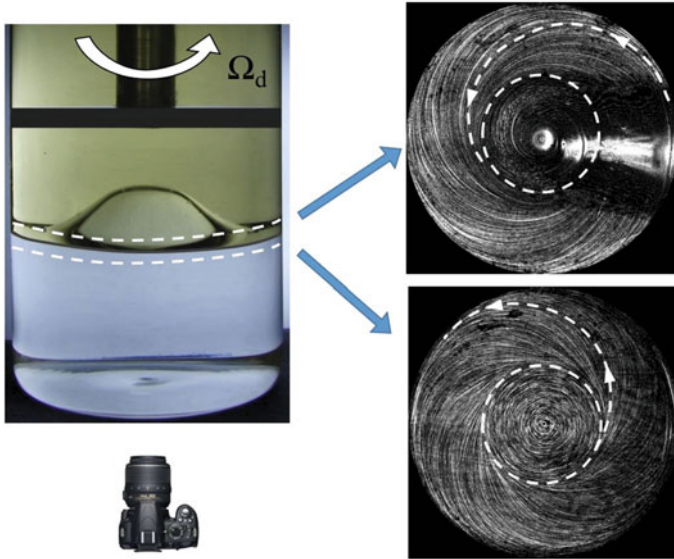


Fig. 6 Spiral motion above and below the interface at $Re = 500$

a working liquid. The difference in densities between air and liquid in this case is more than 1000 times.

It should be noted that vortex flows of immiscible liquids, in addition to technological processes, are also present in nature. Figure 7 shows the stable stratification of fluids of different density and salinity observed at the confluence of the waters of the North and Baltic seas, as well as the Mediterranean Sea and Atlantic Ocean.



Fig. 7 Examples of immiscible configurations of the aquatic environment. On the left is North and Baltic Sea, on the right is Mediterranean Sea and Atlantic Ocean (from open-access internet sites)

Thus, the presented mechanism of the development of a vortex pattern can be extrapolated to natural phenomena, when on the water surface, suddenly in the eye of the observer, vortices are formed.

4 Physical Mechanism of Double Vortex Breakdown

Now let us dwell in more detail on the “vortex domino” effect—the simultaneous emergence of AC cells and reversals of the axial velocity near the centers of both fluids (Fig. 8b). This dual vortex breakdown occurs with an increase in the rotation, but is not directly related to the deformation of the interface. In the upper fluid, the meridional circulation transfers the angular momentum from the rotating lid downward along the side wall and then to the axis near the interface. In the lower fluid, the CC transfers angular momentum from the rotating upper fluid downward along the side wall and then to the axis near the bottom wall. In both fluids, the converging motion causes the “ice skater effect”—an increase in angular velocity when fluid particles approach the axis. Figuratively speaking, a tornado-like swirling jet arises in both fluids, and the entire flow takes on the structure of a miniature two-story tornado (Fig. 8a).

Pressure near the axis of a vortex is less than the pressure at the periphery (to balance the centrifugal force). Therefore, an increase in the angular velocity leads to the appearance of zones of significantly reduced pressure near the intersection of the axis with the bottom wall (in the lower fluid) and with the interface (in the

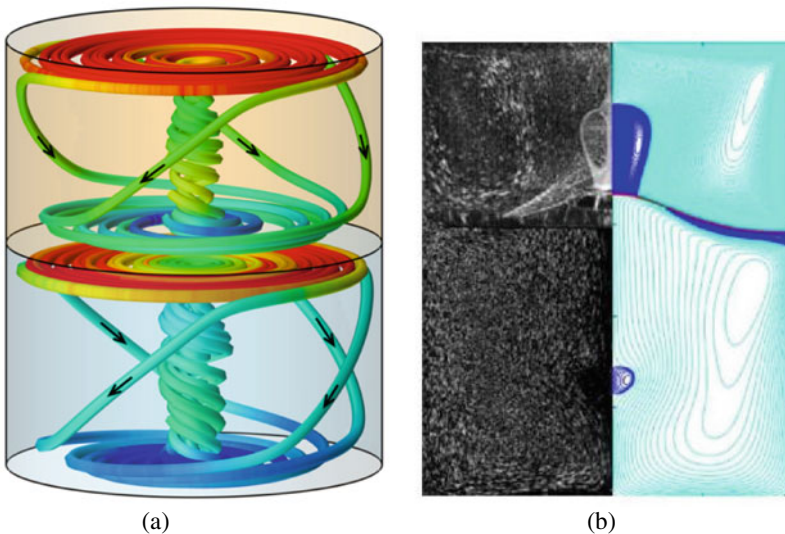


Fig. 8 Two-story tornado. **a** Tracks of fluid particles. **b** The pattern of the meridional motion in experiment (left) and numerical simulation (right) at $Re = 700$

upper fluid). The low pressure in these zones sucks in the surrounding fluid and thereby reduces and partially reverses the velocity on the axis. As a result, AC cells are formed near the centers of both fluids. That is, a dual VB occurs and the structure shown in Fig. 8 appears.

The multiplicity of cells and their arrangement in the “vortex domino” enhance mixing that is beneficial for biological and chemical processes. However, with a further increase in the rotation, the AC cells disappear, and an extended unfavorable stagnation zone arises near the axis. Thus, our study determines not only the optimal flow structure, but also the optimal rotation speed.

5 Conclusions

A curious structure, which can be referred to as “two-story tornado” was found in a vertical cylindrical container filled with two immiscible fluids, the movements of which are caused by the rotation of the upper disk. The results obtained can be of interest:

- (a) For technological applications where the observed multiplicity of cells and their arrangement in the “vortex domino” enhance the mixing and saturation of the working medium with nutrients and oxygen, which is beneficial for biological processes. Our research indicates how to achieve this: the culture is placed in a lower liquid, which is driven by an upper fluid (liquid or gas), propelled by the rotation of the lid. The culture is not destroyed because it does not touch the rotating solid parts of the reactor.
- (b) For fundamental research, since the discovered effect of centrifugal slip requires a revision of the results of calculations of two-fluid rotating flows, obtained under the condition of continuity of velocity and stresses at the interface between the fluids.
- (c) For modeling elements of the atmosphere–ocean system, since it leads to the formation (miniature in the laboratory) of a two-story tornado and helps explain the formation of vortex motion at the interfaces between two media of different densities (for example, seawater of different salinity or gas conglomerates of different densities in space).

Acknowledgements This work was supported by the Russian Science Foundation, project No. 19-19-00083.

References

- Carrión L, Naumov IV, Sharifullin BR, Herrada MA, Shtern VN (2020) Formation of dual vortex breakdown in a two-fluid confined flow. *Phys Fluids* 32:104107
- Naumov IV, Herrada MA, Sharifullin BR, Shtern VN (2018a) Slip at the interface of a two-fluid swirling flow. *Phys Fluids* 30:074101
- Naumov IV, Herrada MA, Sharifullin BR, Shtern VN (2018b) Hysteretic growth and decay of a waterspout column. *Phys Rev Fluids* 3:024701
- Naumov IV, Glavny VG, Sharifullin BR, Shtern VN (2019) Formation of a thin circulation layer in a two-fluid rotating flow. *Phys Rev Fluids* 4:054702
- Naumov IV, Sharifullin BR, Shtern VN (2020a) Vortex breakdown in the lower fluid of a two-fluid swirling flow. *Phys Fluids* 32:014101
- Naumov IV, Sharifullin BR, Kravtsova AY, Shtern VN (2020b) Velocity jumps and the Moffatt eddy in two-fluid swirling flows. *Exp Thermal Fluid Sci* 116:110116
- Naumov IV, Sharifullin BR, Tsoy MA, Shtern VN (2020c) Dual vortex breakdown in a two-fluid confined flow. *Phys Fluids* 32:061706
- Peckham DH, Atkinson SA (1957) Preliminary results of low speed wind tunnel tests on a Gothic wing of aspect ratio 1.0. Technical report, Aeronautical Research Council, CP-508, TN NO. 254
- Shtern V (2018) Cellular flows. Topological metamorphoses in fluid mechanics. Cambridge University Press, Cambridge

Conditions of the Effective Mixing in a T-Type Micromixer at Low Reynolds Numbers



A. Yu. Kravtsova , P. E. Ianko, M. V. Kashkarova, A. V. Bilsky, Y. V. Kravtsov, and I. V. Naumov 

Abstract Using the laser-induced fluorescence method, the conditions for effective mixing of liquids in a rectangular micromixer are established. It is revealed that values of the mixing coefficient more than 0.5 are achieved in a range of Reynolds numbers from 3 to 186 due to a change in the ratio of input flow rates.

Keywords Micromixer · Mixing efficiency · Microchannel · LIF technique

1 Introduction

The effective mixing of liquids in micromixers is still an urgent problem for many industries application, including chemical, microbiological, pharmaceutical, etc. One of the most used micromixers is the mixer T-shaped configuration with two inlets and one outlet. Significant results of the investigation of hydrodynamic flow in case of equal flow rates have been achieved in this issue. It is established that at equal input flow rates and $Re < 5$, a stationary vortex-free motion is obtained in the output channel of a T-shaped micromixer. With this movement, mixing is achieved by molecular diffusion, so that the mixing efficiency remains low. It is determined that with an increase in the Reynolds number, horseshoe-shaped vortices (Dean vortices) appear in the mixer, which arise due to the development of secondary currents caused by the action of centrifugal force in connection with the rotation of the flows into the outlet channel. The occurrence of such vortices is noted at $Re > 20$ (Minakov et al. 2012). With a further increase in the number of Re , the intensity of the vortices increases. However, with equal input flow rates, until the Reynolds number reaches 150, each vortex is within the same fluid and does not cross the boundary interface. The mixing efficiency in such a stationary vortex symmetric flow is still low. It is found that at $Re > 150$, the Dean vortices lose their symmetry: they rotate by an angle of 45° relative to the central plane (Engler et al. 2004; Dreher et al. 2009; Poole et al. 2013, etc.). As a result, S-shaped vortices are formed. The contact surface of liquids

A. Yu. Kravtsova · P. E. Ianko · M. V. Kashkarova · A. V. Bilsky · Y. V. Kravtsov · I. V. Naumov (✉)
Kutateladze Institute of Thermophysics SB RAS, Novosibirsk, Russia
e-mail: naumov@itp.nsc.ru

with such a stationary asymmetric vortex flow increases and, accordingly, the mixing efficiency increases sharply. For increases more than $Re = 240$ the flow becomes to be unsteady. The mixing efficiency becomes very high, peaking at $Re = 400$. During the transition to turbulence (when the Reynolds number increases to 600), the S-shaped vortex structure is destroyed, the flow becomes quasi-periodic and breaks up into many large vortices. This leads to a decrease in the contact area of the mixing liquids and a sharp decrease in the mixing efficiency (Minakov et al. 2012).

Thus, to date, the main factors of effective mixing of liquids with an equal flow rates in T-type micromixers have been determined. The most important of them is the achievement of a relatively high Reynolds number in the output channel—from 150 to 400 and the transition to unsteady flow regimes. At the same time, taking into industrial production interests, it would be advantageous to determine the conditions for good mixing and at lower Reynolds numbers. As a possible direction for solving this problem, it is proposed to study the mixing of liquids at different input flow rates. A limited number of works are known in this area. Rahimi et al. (2015) presented the results of a study of mixing liquids efficiency at different input flow rates in T-shaped channels of circular cross-section for two Reynolds numbers: $Re = 49$ and $Re = 498$. Detailed data by these authors are given only for $Re = 498$. For the smaller of the shown numbers, the materials are not presented by these authors. Taking into industrial production interests and the limited number of publications on the study of this search direction, we believe that the issues of mixing liquids in T-shaped micromixers at low Reynolds numbers need further studding.

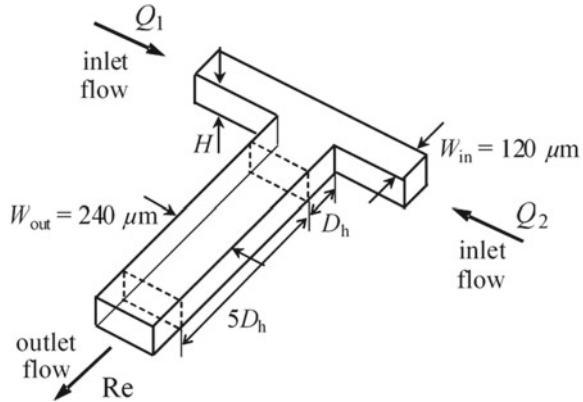
The aim of the work is to definition the conditions for effective mixing of liquids in a T-shaped micromixer at low Reynolds numbers.

2 Experimental Setup and Measurement Technique

Experimental investigation of the flow hydrodynamics in a micron-sized channel was carried out. The working section is a T-shaped microchannel made of optically transparent SU-8 material with dimensions of $120 \times 120 \times 240$ microns (height H , width of the input channel W_{in} and width of the output channel W_{out}) (Fig. 1). The KD Scientific dual-outlet syringe pump supplies the continuous fluid flow to the microchannel inputs. The liquid flow rate at the inputs varies from 0.39 ml/h to 202 ml/h. The Reynolds number (Re), calculated from the bulk flow velocity in the output channel (U_0), its characteristic hydraulic diameter ($D_h = 160 \mu\text{m}$), and the kinematic flow viscosity (ν), varied from 3 to 186. Since the geometry of the T-microchannel is symmetric, it is assumed for certainty that the input flow rate on the left channel is less than on the right, i.e. $Q_1 < Q_2$. The ratio of input flow rates is determined by the coefficient R : $R = Q_1 / Q_2$.

To visualize the flow regimes in the microchannel, the laser-induced fluorescence (LIF) method is used, inverted in a Carl Zeiss Axio Observer microscope. Z1. Distilled water is supplied to one inlet of the channel and a solution of rhodamine 6G dye is supplied to the second one. The concentration of the rhodamine 6G solution

Fig. 1 Sketch of microchannel



is 362 mg/l. The flow inside the working area is illuminated by an Nd: YAG laser (wavelength 532 nm, pulse energy 25 MJ) for a short period of time equal to 10 ns which are obtained it possible to images for instantaneous flow structures. The light emitted by the rhodamine 6G dye in the red wavelength range is recorded by a CCD camera (8 bits, the resolution of the matrix is 2048×2048 pixels) (Kravtsova et al. 2019a, 2019b). The resulting images is the instantaneous concentration fields.

To calculate the quantitative parameters of mixing was obtained. To analyze the flow mixing, a series of experimental images were obtained using LIF and processed using the software ActualFlow (<http://polis-instruments.ru/downloads>). These images provide qualitative and quantitative information to compare concentration uniformity under different conditions. Several steps have been taken to obtain quantitative information on flow mixing.

The first step was the acquisition of images with natural light and at some constants of concentration of liquid Rhodamine 6G solution in the entire measuring range. A certain set of specified concentrations of solutions was chosen to cover the entire range of concentrations in the measurement area during the experiment. For each concentration value and data 100 images were taken.

The next step was to average the obtained images for each series. This procedure allowed reducing the effects of camera noise and instability of the laser pulse energy. The background image obtained with natural light was subtracted from the calculated average images.

The resulting set of images at various concentrations of solution and distilled water in the stream was used to plot the concentration as a function of brightness at each specific point of the image. A calibration curve for the whole image was plotted using the least squares method, based on the average intensity values for each image. This curve was supplemented with correction factors for each image point, designed to eliminate the effect of different illumination of the flow areas and obtained by averaging the ratio of the average image brightness to the brightness at the point over all calibration images. The calibration curve was approximated by the polynomial function to the second power for Rhodamine 6G solution. The polynomial function

had the form $c = 0.0001 \cdot I_0^2 - 0.035 \cdot I_0 + 5.49$, where I_0 was the image brightness, representing the dependence of the dye concentration in the flow, c .

Then, we restored the concentration field from instantaneous images of the stream according to the calibration in several works. The next step was the reconstruction of the concentration fields from images obtained during the averaging of instant gray-scale data, based on the calibration function (PLIF Reconstruction, <http://polis-instruments.ru/downloads>).

Using the average concentration fields, the concentration profiles in each cross-section channel were constructed and the mixing efficiency was estimated according to procedure described in Dankwerts (Dankwerts 1952):

$$I_M = 1 - \sigma/\sigma_0,$$

$\sigma^2 = \frac{1}{N} \sum_{i=1}^N (c_i - \bar{c})^2$, where \bar{c} is the average value of concentration, c_i is the concentration value in each point on the concentration profile, and N is the number of points over which the mixing efficiency was calculated) and $\sigma_0^2 = \bar{c}(c_{\max} - \bar{c})$, the latter being the maximal root mean square deviation for mixing the liquid with concentration from 0 to c_{\max} (here c_{\max} is the maximal concentration of Rhodamine 6G dye (362 mg/l)). Thus, the liquids were completely mixed at $I_M = 1$ and segregated at $I_M = 0$.

3 Results

The concentration fields are used to identify the features of the liquids flow in the micromixers and to diagnose flow regimes, as well as to estimate the mixing coefficients of liquids. At now, for some each of the flow regimes the mixing coefficients it is already obtained by previous authors. According to the results of a data of additional special experiments it is possible defined the mechanisms that determine a specified efficiency of mixing liquids in specified flow regimes. Therefore, the task of the study may ultimately be reduced to determining the conditions for the formation of a particular flow regime with the already known efficiency of mixing liquids, on a specific experimental setup. So, as the accepted regime map is not, we present the conditions for the occurrence of several fluid flow regimes in the outlet channel of a T-type micromixer at low Reynolds numbers and different input flow rate ratios (Table 1).

It is determined that for stationary flow regimes when $Re < 10$ and $0.05 < R < 1$, the mixing efficiency is quite low, less than 0.32. At such values of the number Re , horseshoe-shaped vortices do not yet occur (Minakov et al. 2012; Rahimi et al. 2015). Therefore, in these conditions, the mixing of liquids is achieved only by molecular diffusion and its efficiency remains low. Stationary flow regime with partial penetration of the one of the inlets flows into the opposite input channel occurs in range Reynolds number from 47 to 186. The moment of liquid penetration into

Table 1 Fluid flow regimes and the ranges of Reynolds number and input flow rate ratios corresponding to them

Regimes	Re	R
Stationary flow regime with a domination of one of the inlet flows in outlet channel	$Re < 10$	$0.05 < R < 1$
Stationary flow regime with partial penetration of the one of the inlet flows into the opposite input channel	$47 < Re < 186$	$\sim R^2, R < 0.15$
Stationary asymmetric flow regime	$47 < Re < 186$	$0.15 < R < 1$
Streaks stationary flow regime	$Re = 186$	$0.15 < R < 1$

the opposite inlet channel depends on two factors simultaneously: the value of the Reynolds number and the ratio of the inlet flow rates. It is obtained the relation between the Reynolds number and the ratio of input flow rates for thus case. It is described by a polynomial function of the second degree of inlet flow rate ratio, $\sim R^2$. At a very small ratio of input flow rates is due to the absolute dominance of one of the inlet flows in the mixing channel the mixing efficiency is low. In this regard, unfavorable conditions for mixing are again formed, since mainly one liquid enters the outlet channel.

Stationary asymmetric flow regime occurs for $47 < Re < 186$ and $0.15 < R < 1$. In these regimes the mixing efficiency is more or equal to mixing efficiency for $R = 1$ (Fig. 2).

In streaks stationary flow regimes, the mixing efficiency increases more than 0.5 with change in the R. The number of streaks increases which reflects the flow layering. In this regard, the number of boundaries between the two liquids also increases and, accordingly, the mixing efficiency increases (Engler et al. 2004).

In accordance with the data obtained and the estimations performed, the high values of the mixing coefficient are observed in the stationary asymmetric flow regimes and streaks stationary flow regimes (Fig. 2). They vary from 0.5 to 0.85.

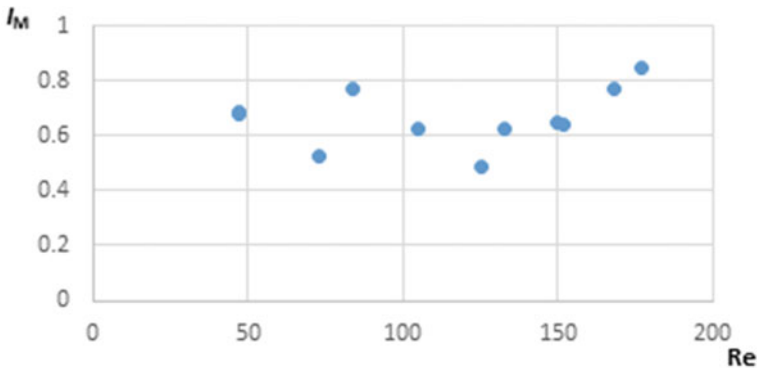


Fig. 2 The maximal mixing coefficient for stationary flow regimes in case of range inlet flow rate ratios

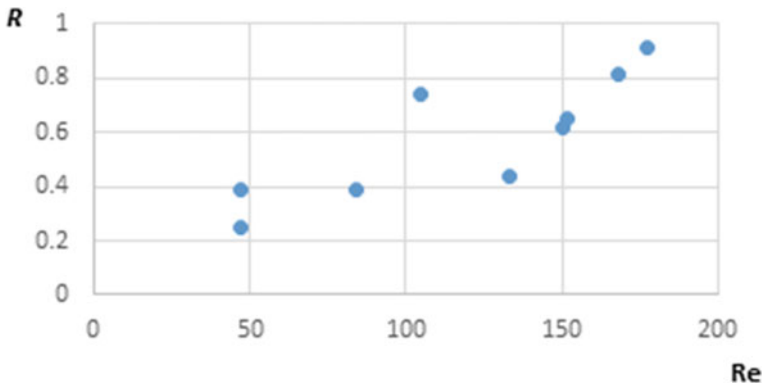


Fig. 3 The ratio of input flow rates (R) versus the Reynolds number (Re), at which the maximum values of the mixing coefficient

The maximum estimated values of the mixing coefficient amount to 0,87 for the Reynolds number $Re = 177$ and $R = 0.9$. It is important to emphasize that when the number of Re increases from 47 to 177, the maximum estimated values of the mixing coefficient were not observed in the entire interval R ($0.15 < R < 1$) established for the stationary asymmetric flow, but only in narrow range. The visualization of flow regimes may be found in work (Kravtsova 2020).

The ratio of input flow rates at which the maximum estimated values of the mixing coefficient are marked enlarges with the increase in the Reynolds number in the change R from 0.15 to 1 (Fig. 3). It should be noted that in the stationary asymmetric flow, the displacement of the vortices known in the literature beyond the limits of a single liquid and, thus, the increase in the mixing efficiency of liquids is predetermined. Thus, a significant increase in mixing efficiency can be achieved in the range of Reynolds numbers from 3 to 186 only by changing the ratio of input flow rates in the range from 0.2 to 0.9.

4 Conclusion

According to series of experiments, it was found that for small Reynolds numbers, the most effective mixing of liquids in a T-shaped micromixer is achieved in a narrow range of Re and R numbers: as the Reynolds numbers increase from 47 to 177 and the input flow ratio enlarges in parallel from 0.25 to 0.9.

Acknowledgements This work was supported by Russian Science Foundation (grant № 19-79-10217).

References

- Dankwerts PV (1952) The definition and measurements of some characteristics of mixtures. *Appl Sci Res* 279–296. [https://doi.org/10.1016/0032-5910\(73\)80031-2](https://doi.org/10.1016/0032-5910(73)80031-2).
- Dreher S, Kockmann N, Wolas P (2009) Characterization of laminar transient flow regimes and mixing in T-shaped micromixers. *Heat Transfer Eng* 30(1):91–100. <https://doi.org/10.1115/ICNMM2007-30041>
- Engler M, Kockmann N, Kiefer T, Woias P (2004) Numerical and experimental investigations on liquid mixing in static micromixers. *Chem Eng J* 101:315–322. <https://doi.org/10.1088/0960-1317/20/1/015029>
- Kravtsova AY (2020) Visualization of flow regimes in symmetric microchannel in case of different inlet flowrate ratios for fixed outlet Reynolds number. *J Eng Thermophys* 29(4):1–6
- Kravtsova AY, Ianko PE, Kashkarova MV, Bilsky AV (2019) Estimation of the flows mixing efficiency inside T-micromixer with an external perturbation for low Reynolds numbers. *J Phys Conf Ser* 1382:(012159)-6. <https://doi.org/10.1088/1742-6596/1382/1/012159>.
- Kravtsova AY, Ianko PE, Kashkarova MV, Bilsky AV (2019) Investigation of the perturbation flow in a T-microchannel using the LIF technique. *J Visual* 22(5):851–855. <https://doi.org/10.1007/s12650-019-00574-5>
- Minakov AV, Rudyak VY, Gavrilov AA, Dekterev AA (2012) Mixing in a T-shaped micromixer at moderate Reynolds numbers. *Thermophys Aeromech* 19(3):385–395. <https://doi.org/10.1134/S0869864312030043>
- Poole RJ, Alfateh M, Gauntlett AP (2013) Bifurcation in a T-channel junction: effects of aspect ratio and shear-thinning. *Chem Eng Sci* 104:839–848. <https://doi.org/10.1016/j.ces.2013.10.006>
- Rahimi M, Akbari M, Parsamoghdam M, Alsairafi A (2015) CFD study on effect of channel confluence angle on fluid flow pattern in asymmetrical shaped microchannels. *Comput Chem Eng* 73:172–182. <https://doi.org/10.1016/j.compchemeng.2014.12.007>

The Problem of Exact Solutions Construction for Potential Steady Surface Waves in the Case of a Liquid of Finite Depth



A. V. Kistovich 

Abstract The problem of exact solution construction for the potential steady surface waves propagating along the surface of the finite depth liquid is considered. It is shown that such solution cannot be done in the class of real functions.

Keywords Potential surface waves · Stream function · Exact solution

1 Introduction

The problem of describing potential surface waves has been a classic problem of hydrodynamics for two centuries. The currently well-known results of studies by Boussinesq (1871), Stokes (1847), Rayleigh (1876) and many other researchers, which form the basis of the theory of surface waves, provide only approximate solutions to the existing problem. For this reason, obtaining accurate solutions is still an urgent problem. Most approaches to solving this problem are based on the assumption of the exponential damping of perturbations of all physical fields generated by the passage of a surface wave as it moves deeper into the liquid (for the case of its infinite depth). In Kistovich et al. (2021) it was shown that such an assumption entails the absence of an exact solution in the class of real functions. At the same time, it remains possible for a fluid of finite depth to search for a solution in the form $A \exp(kz) + B \exp(-kz)$ where A and B are some functions of the horizontal coordinate. In the presented paper, it is shown that with such an approach, it is also impossible to construct an exact solution to the problem in the class of real functions.

A. V. Kistovich (✉)

Ishlinsky Institute for Problems in Mechanics of the Russian Academy of Science, Moscow, Russia

e-mail: kavmendeleev@mail.ru

2 Problem Statement

A two-dimensional problem of wave propagation along the free surface of an ideal incompressible fluid of finite depth h is considered. In the coordinate system (x, z) , whose vertical axis z is directed against the gravity vector \mathbf{g} , the pressure is described by the function $p(\xi, z)$ ($\xi = x - ct$, c is the wave propagation velocity), the velocity field \mathbf{v} has only two components v_x and v_z . The deviation of the free surface from the undisturbed state $z = 0$ is given by the function $\zeta(\xi)$. The system of equations of motion and the boundary conditions have the form.

$$\begin{aligned} \rho(-cv'_\xi + (\mathbf{v}\nabla)\mathbf{v}) &= -\nabla p + \rho\mathbf{g}, & \nabla \cdot \mathbf{v} &= 0, & \nabla \times \mathbf{v} &= 0. \\ p|_{z=\zeta} &= p_a, & v_z - v_x \zeta'_\xi|_{z=\zeta} &= -c \zeta'_\xi, & v_z|_{z=-h} &= 0 \end{aligned} \quad (1)$$

Here p_a is atmospheric pressure, ρ is the liquid's density.

Representing the pressure in a liquid as the sum of atmospheric, hydrostatic, and wave pressures $p = p_a + \rho g(\zeta - z) + \tilde{p}$, introducing a stream function ψ such that $v_x = \psi'_z$, $v_z = -\psi'_x \equiv -\psi'_\xi$, and using the potential nature of the waves transforms the system (1) to the form

$$\begin{aligned} \Delta\psi &= 0, & \frac{\partial}{\partial \xi}((\psi - \zeta)|_{z=\zeta}) &= 0, & \psi'_\xi|_{z=-h} &= 0 \\ \frac{\partial}{\partial \xi} \left(\left(\frac{1}{2}(\psi'^2_\xi + \psi'^2_z) - \psi'_z + \beta\zeta \right) \Big|_{z=\zeta} \right) &= 0, & \beta &= \frac{g}{c^2k}, \end{aligned} \quad (2)$$

where coordinates ξ and z , the depth of the liquid h and the shape of the surface wave $\zeta(\xi)$ are normalized by a certain wave number k ; the stream function ψ is normalized by c/k , and the pressure is normalized by $\rho g/k$.

3 Solution of the Problem

Solution (2) is presented in the classical form

$$\psi = F(\xi)\exp(z - \zeta) + H(\xi)\exp(-z + \zeta). \quad (3)$$

Substituting (3) in (2) leads to the following system of equations, which are numbered separately for the convenience of further presentation

$$F'' - 2\zeta'F' + (1 + \zeta'^2 - \zeta'')F = 0. \quad (4)$$

$$H'' + 2\zeta'H' + (1 + \zeta'^2 + \zeta'')H = 0. \quad (5)$$

$$F + H = \zeta, \quad (6)$$

$$(F' - \zeta' F + H' + \zeta' H)^2 + (F - H)^2 + 2(\beta \zeta - F + H) = 0. \quad (7)$$

$$(F' - \zeta' F) \exp(-h - \zeta) + (H' + \zeta' H) \exp(h + \zeta) = 0. \quad (8)$$

Here, Eqs. (4, 5) are consequences of the Laplace equation for the stream function; Eqs. (6, 7) follow from the kinematic and dynamic boundary conditions on the free surface, respectively; Eq. (8) describes the boundary condition on the bottom. The integration constants in (6, 7) are zero because in the absence of motion ($F = H = 0$), no perturbations of the free surface can take place (i.e. $\zeta = 0$). The stroke indicates differentiation by variable ξ .

To analyze the system (4-8), the difference is made from Eq. (4) multiplied by H and Eq. (5) multiplied by F

$$\frac{\partial}{\partial \xi} (F' H - H' F - 2F H \zeta') = 0.$$

The integration of this relation leads to the result

$$F' H - H' F - 2F H \zeta' = 0.$$

The integration constant is zero according to the above reasons. As a result, the dependence is valid

$$F = A H \exp(2\zeta), \quad (9)$$

where A is some constant value.

Substitution of (9) into (6) allows to define the functions F and H by expressions

$$F = \frac{A \zeta \exp(2\zeta)}{1 + A \exp(2\zeta)}, \quad H = \frac{\zeta}{1 + A \exp(2\zeta)} \quad (10)$$

The subsequent substitution of (10) in the boundary condition at the bottom of (8) determines the constant A and leads to the final result for the functions F and H

$$F = \frac{\zeta \exp(h + \zeta)}{2 sh(h + \zeta)}, \quad H = -\frac{\zeta \exp(-h - \zeta)}{2 sh(h + \zeta)}. \quad (11)$$

In turn, the substitution of (11) in (3) defines the stream function explicitly

$$\psi = \frac{\zeta sh(h + z)}{sh(h + \zeta)}. \quad (12)$$

In addition, substituting (11) in (4) and (5) leads to the same relation

$$(1 - \zeta \operatorname{cth}(h + \zeta)) \left(\zeta'' - 2 \operatorname{cth}(h + \zeta) \zeta'^2 \right) + \zeta (1 - \zeta'^2) = 0. \quad (13)$$

Finally, substituting (11) into (7) forms the equation

$$(1 - \zeta \operatorname{cth}(h + \zeta))^2 \zeta'^2 + \zeta^2 \operatorname{cth}^2(h + \zeta) + 2\zeta (\beta - \operatorname{cth}(h + \zeta)) = 0. \quad (14)$$

If we denote Eq. (13) with a symbol U , and Eq. (14) with a symbol V , then the combination of the form $\operatorname{cth}(h + \zeta) (dV/d\xi - 2(1 - \zeta \operatorname{cth}(h + \zeta))U)$ leads to the condition of compatibility of Eqs. (13) and (14)

$$\begin{aligned} & \operatorname{cth}^2(h + \zeta)(1 - \zeta \operatorname{cth}(h + \zeta))^2 \zeta'^2 + \zeta^2 \operatorname{cth}^2(h + \zeta) + \\ & + (1 - \operatorname{cth}^2(h + \zeta))(1 - \zeta \operatorname{cth}(h + \zeta))^2 + \beta \operatorname{cth}(h + \zeta) - 1 = 0. \end{aligned} \quad (15)$$

The transition in (15) to the limit at $\zeta \rightarrow 0$ leads to the relations

$$\beta = \operatorname{cth}(h) \sim c^2 = \frac{g}{k} \operatorname{th}(kh). \quad (16)$$

The second relation in (16) is presented in dimensional form. Substituting expression (16) for β (15) generates the final form of the compatibility condition

$$\begin{aligned} & \operatorname{cth}^2(h + \zeta)(1 - \zeta \operatorname{cth}(h + \zeta))^2 \zeta'^2 + \zeta^2 \operatorname{cth}^2(h + \zeta) + \\ & + (1 - \operatorname{cth}(h + \zeta))^2 (1 - \zeta \operatorname{cth}(h + \zeta))^2 + \operatorname{cth}(h) \operatorname{cth}(h + \zeta) - 1 = 0. \end{aligned} \quad (17)$$

Due to the fact that in Eq. (17) the value of

$$\zeta^2 \operatorname{cth}^2(h + \zeta) + (1 - \operatorname{cth}(h + \zeta))^2 (1 - \zeta \operatorname{cth}(h + \zeta))^2 + \operatorname{cth}(h) \operatorname{cth}(h + \zeta) - 1$$

takes at $h > 0, \zeta > 0$ only positive values, which means that Eq. (17) has no valid solutions for positive deviations of the surface from its unperturbed state $z = 0$.

According to the law of conservation of mass, the wave surface must contain both elevations and depressions relative to the undisturbed level $z = 0$. Thus, the obtained result indicates that there are no solutions to problems (1, 2) in the class of real functions when using the classical representation (3). Therefore, the expected exact solution (1, 2, and 3) lies in the complex domain.

In the limiting case of an infinitely deep liquid, the correlations obtained here translate into the results presented in Kistovich et al. (2021), with an exact solution in the form of complex-valued waves. The work was carried out with the financial support of the project of the Russian Federation represented by the Ministry of Education and Science of Russia № 075-15-2020-802.

References

Boussinesq J (1871) *Compte Rendus* 72:755–759

Kistovich AV, Chaplina TO, Pokazeev KV (2021) *Advanced studies in ocean physics*. Springer Nature Switzerland AG 2021. Springer Oceanography. <https://doi.org/10.1007/978-3-030-72269-2>

Rayleigh L (1876) On waves. *Philos Mag* 5(I)(4): 257–279

Stokes GG (1847) On the theory of oscillatory waves. *Trans Cambridge Philos Soc* 8:441–455

Anisotropic Permeability of Geomaterials: Lab Test and Borehole Environment Model



Larisa Nazarova , Nikita Golikov , Leonid Nazarov ,
and Galina Nesterova 

Abstract Theoretical substantiation and lab tests of the method for synthesis of a relationship describing angular anisotropy of the effective permeability in borehole environment based on the inverse coefficient problem solution in terms of the data on percolation tests of regularly non-uniform cylindrical specimens with a central hole are set forth in the paper. With a view to provide the algorithmic support of GIS data inversion in the course of determination of poroperm properties of production intervals the researchers developed and implemented by the hybrid numerical method to realize the multiphysical model of the evolution of geomechanical and electrohydrodynamic fields under filtration of multiphase fluid in the borehole environment with consideration for anisotropy of permeability induced by difference in components of the external stress fields. The numerical experiments enabled to establish that in the overbalanced drilling the configuration of invaded zone depends on the proportion between horizontal stress components outside of the well influence zone.

Keywords Mass transfer · Poroperm properties · Lab test · Anisotropic permeability · Pressure · Inverse problem

1 Introduction

To solve the problems on advance degassing of coal seams and coalmine methane utilization design (Seidle 2011), investigation of geothermal systems (Salimzadeh et al. 2018), construction of underground gas storages (Caglayan et al. 2020), inversion of geophysical borehole surveying data with the view to establish production intervals and to assess poroperm properties of rocks (Hsu and Robinson 2019; Ahmed 2019; Yeltsov et al. 2014; Garcia and Heidari 2021) and other actual problems

L. Nazarova (✉) · L. Nazarov
Chinakal Institute of Mining, Siberian Branch of the Russian Academy of Sciences, 54 Krasny Prospekt, 630091 Novosibirsk, Russia

N. Golikov · G. Nesterova
Trofimuk Institute of Petroleum Geology and Geophysics, Siberian Branch of the Russian Academy of Sciences, 3 Prospekt Koptyuga, 630090 Novosibirsk, Russia

requires the development of multiphysical models and their appropriate verification. Such models comprising the conservation law and state equations also involve empirical relationships between parameters of the physical field arising in borehole environment, such as petrophysical formulas of electroconductivity of a heterogenic medium, relationship of phase permeability versus fluid concentration, the reservoir rock poroperm properties—stress relationship. The last factor as well as probable difference between components of the external stress field and disturbance of rock mass stability caused by boring operations can provoke the permeability anisotropy in the vicinity of a borehole. Subsequently, the borehole environment can not be described in terms of one dimensional models (Yeltsov et al. 2012; Nazarova and Nazarov 2018), so 2D and 3D models should be used, but they imply the proper parametric base resting on respective experiments, where specific features of poroperm properties distribution are considered.

The paper reports the data on percolation tests of regularly heterogeneous cylindrical specimens with central hole. The specimens made of a synthetic geomaterial are used to work out a process for determination of the effective permeability—polar angle relationship based on solution of the inverse coefficient problem. The researchers propose 2D multiphysical model describing evolution of geomechanical and electrohydrodynamic fields in the borehole environment under multiphase filtration.

2 Anisotropic Permeability by Lab Test Data and Inverse Problem Solution

2.1 Experimental Design

Cylindrical specimens (height $h = 110$ mm, external radius $R = 75$ mm, central channel diameter $2a = 8$ mm) were assembled of six components of the same shape (Fig. 1a), but different permeability. The components were made of the conditioned cryogel consisted of three calibrated sand fractions (0.5, 1, and 1.5 mm) under the original technological process (Nazarova et al. 2019). Permeability values of specimen components assessed under the standard procedure (RF Standard 26450.2–85 1985), appeared $k_0 = 24$ mD, $k_1 = 29$ mD, and $k_2 = 35$ mD.

Specimen 1 in isolating rubber collar 2 was placed in sealed metal chamber 3 (Fig. 1b), the rest free space stuffed with coarse-grain sand 4 (fraction 5 mm) exhibited high permeability (more than 3 Darcy) and did not notably affect the filtration characteristics of the test system. The air was pumped under constant pressure p_m through central hole 5. The air flowrate Q_{mn} was recorded at a stationary mode with relative precision of 2% at side surface of the specimen segment (central angle $2\beta = 30^\circ$, Figs. 1a and 2), which position was determined by angle φ_n (the flowmeter was connected through adapter 6). Measurement results at $p_m = 1.05, 1.10, \dots, 1.25$ bar and $\varphi_n = 30^\circ, 45^\circ, \dots, 150^\circ$ are reported in Table 1.

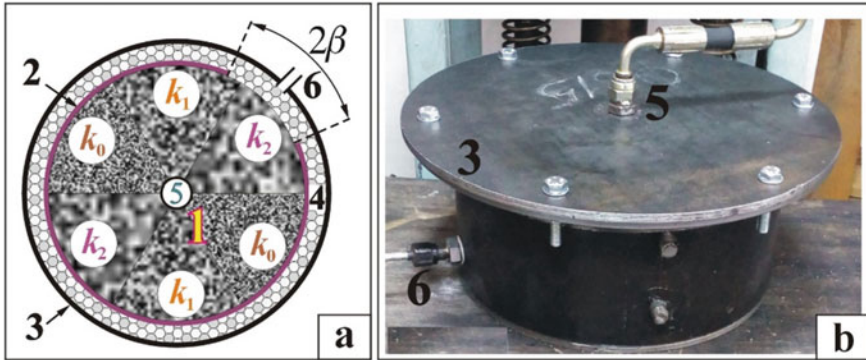


Fig. 1 Specimen structure (a) and test bench (b)

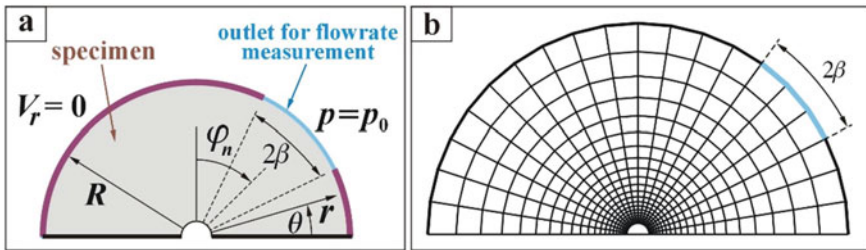


Fig. 2 Model of the experiment and boundary conditions (a), computational grid (b)

Table 1 Flowrate Q_{mn} (ml/min) at different input pressure p_m and angle φ_n

m	p_m (bar)	φ_n (deg)								
		30°	45°	60°	75°	90°	105°	120°	135°	150°
1	1.05	50	54	59	62	64	64	65	64	61
2	1.10	101	111	120	128	131	132	133	131	124
3	1.15	127	138	150	159	163	165	166	164	155
4	1.20	156	170	185	196	201	203	204	202	190
5	1.25	213	232	252	267	274	277	279	275	260

2.2 Model of the Percolation Experiment

Evolution of hydrodynamic fields in the test specimen in polar coordinates (r, θ) (Fig. 2a) is described by the system including (Kochin et al. 1964):

Continuity equation

$$\frac{\partial(\omega\rho)}{\partial t} + \operatorname{div}(\rho\vec{V}) = 0; \quad (1)$$

Darcy's law

$$\vec{V} = -\frac{K}{\eta} \operatorname{grad} p \quad (2)$$

and state equation

$$p = p_0\rho/\rho_0 \quad (3)$$

where ω —porosity, p —pressure, ρ and η —density and viscosity of gas, ρ_0 —gas density at atmospheric pressure p_0 , $\vec{V} = (V_r, V_\theta)$ —seepage velocity, permeability K is the piecewise constant function versus polar angle

$$K(\theta) = \begin{cases} k_0 & 0 \leq \theta \leq \pi/3, \pi \leq \theta \leq 4\pi/3 \\ k_1 & \pi/3 \leq \theta \leq 2\pi/3, 4\pi/3 \leq \theta \leq 5\pi/3 \\ k_2 & 2\pi/3 \leq \theta \leq \pi, 5\pi/3 \leq \theta \leq 2\pi \end{cases}$$

System (1)—(3) reduces to non-linear parabolic equation

$$\frac{\partial p}{\partial t} = b \operatorname{div}(Kp \operatorname{grad} p) \quad (4)$$

($b = \rho_0/\omega\eta p_0$) for which the following boundary conditions are formulated (Fig. 2a):

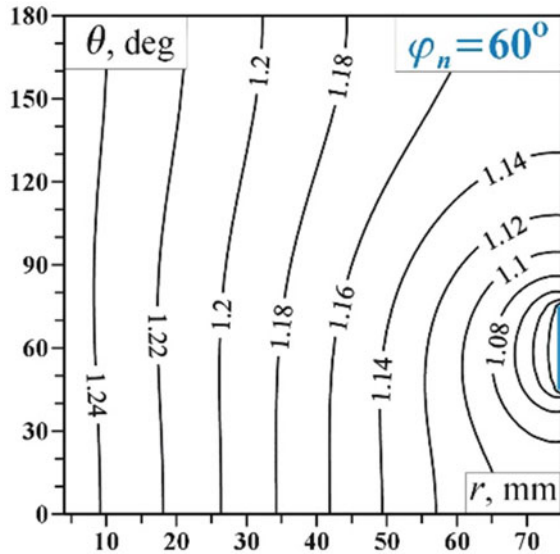
$$\begin{aligned} p(a, \theta, t) &= p_m; \\ (R, \theta, t) &= p_0 \quad \text{at} \quad |\theta - \varphi_n| \leq \beta; \\ V_r(R, \theta, t) &= 0 \quad \text{at} \quad |\theta - \varphi_n| > \beta. \end{aligned} \quad (5)$$

The flowrate through the sector at side surface of the specimen determined by angle φ_n (Figs. 1 and 2a) is calculated by formula

$$Q(t) = hR \int_{\varphi_n - \beta}^{\varphi_n + \beta} V_r(R, \theta, t) d\theta, \quad (6)$$

where radial velocity V_r is found from (2).

Fig. 3 Contour lines of p/p_0



System (4), (5) was solved by the finite-difference method of alternating directions (Samarskii 2001) at nonuniform grid (Fig. 2b). It is important to point out that stationary distribution of hydrodynamic field parameters does not depend on b value.

Pressure distribution (Fig. 3) in the specimen at the steady-state filtration mode at $\varphi_n = 60^\circ$ and $p_m = 1.25$ bar indicates the existence of depressed zones of comparatively low gradient far from the sector where the flowrate was measured.

2.3 Test Data Interpretation

The inverse problem statement runs as follows: using the measurement data on flow rates Q_{mn} (Table 1) it is required to find continuous function describing dependence of the effective permeability versus angle θ . Suppose that $K(\theta) = A + (B - A)\theta/\pi$ ($0 \leq \theta \leq \pi$) and introduce the objective function

$$\Psi(A, B) = \sqrt{45 \sum_{m=1}^5 \sum_{n=1}^9 [Q(A, B, p_m, t) - Q_{mn}]^2} / \sum_{m=1}^5 \sum_{n=1}^9 Q_{mn}$$

where Q —stationary flowrate, computed from (4), (6) at some A, B, p_m , and φ_n values. The minimum of function Ψ , which was determined by the modified conjugate-gradient method (Nazarov et al. 2013), provides solution of the inverse problem, viz., values of A and B coefficients.

Fig. 4 Level lines of objective function Ψ

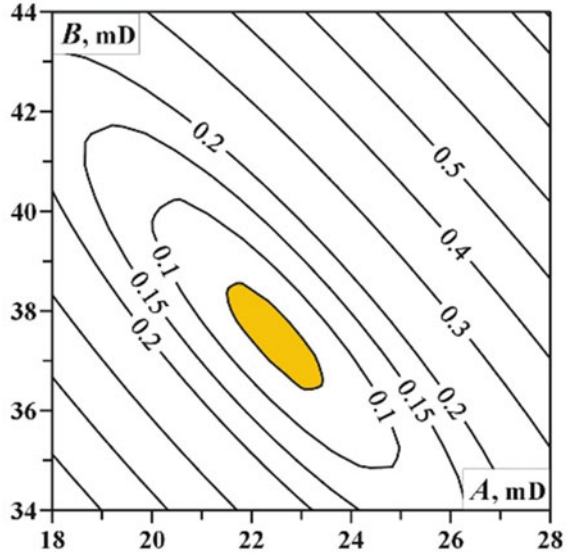


Figure 4 demonstrates level lines of the objective function, the toned area is equivalency domain $\Psi \leq 0.05$. It is obvious that Ψ is unimodal, so the stated inverse problem is uniquely solvable. Within up to 10% accuracy the target coefficients: $A = 22\text{--}23$ mD and $B = 37\text{--}38$ mD are in good compliance with permeability values k_0 , k_1 , and k_2 of separate sections of the test specimen.

3 Mass Transfer in Borehole Environment

Poroperm properties anisotropy is governed by both specific structural features of a seam and non-homogeneous stress state in well environment. Due consideration should be given to this peculiarity in modeling intended to describe mass transfer processes in the vicinity of borehole.

Let at time moment $t = 0$ a horizontal formation filled with a multiphase fluid and bounded with impermeable interfaces beds is penetrated to its entire thickness h by a vertical borehole of radius a . In the overbalanced drilling case when the initial reservoir pressure p_s is lower than bottom hole pressure p_b , a flashed zone and mud cake tend to come into being. The poroelastic model describing quasistatic deformation of a reservoir under two-phase fluid filtration includes:

Equilibrium equation

$$\sigma_{ij,j} = 0; \tag{7}$$

Hooke's law

$$\sigma_{ij} = \lambda \varepsilon_{ij} + 2\mu \varepsilon_{ij} - p \quad (8)$$

Cauchy's relations

$$\varepsilon_{ij} = 0.5(u_{i,j} + u_{j,i}) \quad (9)$$

continuity equation for each phase

$$\frac{\partial(\omega S_n)}{\partial t} + \text{div } \vec{V}_n = 0 \quad (10)$$

Darcy's law

$$\vec{V}_n = -\frac{K k_n}{\eta_n} \text{grad } p \quad (11)$$

salt transfer equation

$$\frac{\partial(\omega C S_1)}{\partial t} + \text{div}(C \vec{V}_1) = 0; \quad (12)$$

as well as empirical dependences of porosity ω versus pressure p

$$\omega = \omega_0 + \beta p; \quad (13)$$

permeability K versus effective stress (Nazarova and Nazarov 2018; Nazarova et al. 2019)

$$K = K_0 \exp(-\gamma \sigma_f) \quad (14)$$

and growth rate of mud cake thickness D versus flow rate Q (Yeltsov et al. 2012)

$$2\pi ah \frac{\partial D}{\partial t} = \psi Q, \quad (15)$$

where u_i , ε_{ij} , and σ_{ij} —components of displacement vector, strain and stress tensors; $i, j = r, \theta$; (r, θ) —cylindrical coordinates; δ_{ij} —Kronecker delta; λ, μ —Lame parameters; $\sigma_f = \sigma_{ii}/3 - p$; S_n —saturation of phase n (here $n = 1$ corresponds to drilling mud filtrate, $n = 2$ —oil, $S_1 + S_2 = 1$); C —salinity; $k_n = S_n^{\alpha_n}$ —relative phase permeability, α_n —empirical parameters; \vec{V}_n —seepage velocity; η_n —viscosity; β

and γ —fluid and reservoir rock compressibilities $\psi = \xi/(1 - \xi)(1 - \omega_m)$; ω_m —porosity of mud cake; ξ —clayey content in drill mud;

$$Q = ah \int_0^{2\pi} \left(\vec{V}_1(a, \theta, t) \right)_r d\theta.$$

System (7)–(15) is solved in domain $\{a \leq r \leq R, 0 \leq \theta \leq \pi\}$, with formulation of initial

$$p(r, \theta, 0) = p_s, \quad S_1(r, \theta, 0) = S_0, \quad C(r, \theta, 0) = C_0, \quad D(0) = 0 \quad (16)$$

and boundary

$$\begin{aligned} \sigma_{rr}(a, \theta) = p_b, \quad \sigma_{rr}(R, \theta) = (q_1 \cos^2 \theta + q_2 \sin^2 \theta) \sigma_V \\ \sigma_{r\theta}(a, \theta) = \sigma_{r\theta}(R, \theta) = 0 \end{aligned} \quad (17)$$

$$\begin{aligned} p(a, \theta, t) = p_b, \quad p(R, \theta, t) = p_b, \\ S_1(a, \theta, t) = S_m, \quad S_1(R, \theta, t) = S_0, \\ C(a, \theta, t) = C_m, \quad C(R, \theta, t) = C_m \end{aligned} \quad (18)$$

conditions (line $\theta = 0, \pi$ —symmetry axis), where R is size of well influence zone ($a \ll R$), S_0, C_0 —water saturation and salinity in an intact reservoir, S_m and C_m are water saturation and salinity of drill mud, q_1 and q_2 are lateral pressure coefficients corresponding to maximum σ_{\max} and minimum σ_{\min} horizontal stresses in the external field; $\sigma_V = \rho_1 g H$ is lithostatic stress at reservoir occurrence depth H , ρ_1 is average overlying rock density.

The stated boundary-value problem, implemented by the hybrid numerical method (Nazarova et al. 2020), enabled to develop the rapid computing algorithm at every time moment in the same grid (similar to grid in Fig. 2b); system (7)–(9) and (17) was solved by the finite element method (original code (Nazarova and Nazarov 2009), while (10)–(16), (18) was solved by the finite-difference method of alternating directions) (Samarskii 2001).

Let exemplify the effect of “induced” anisotropy of permeability on distribution of electrohydrodynamic fields in borehole environment. The computation was based on the following model parameters matching to an actual production interval of an operating well, Kogalym oil deposit, West Siberia (Yeltsov et al. 2014): $H = 2518$ m, $\rho_1 = 2500$ kg/m³, $g = 9.81$ m/s², $\lambda = \mu = 20$ GPa, $a = 0.1$ m, $R = 2$ m, $K_0 = 34$ mD, $\eta_1 = 0.001$ Pa · s, $\eta_2 = 0.004$ Pa · s, $\alpha_1 = 2$, $\alpha_2 = 3$, $\beta = 10^{-9}$ 1/Pa, $\gamma = 10^{-10}$ 1/Pa, $\xi = 0.45$, $\omega_m = 0.2$, $q_1 = 0.7$, $q_2 = 0.62$, $p_s = (1 + q_1 + q_2) \sigma_V / 3$ (Khristianovich 1989), $p_b = 1.05 p_s$, $C_0 = 1$ g/l, $C_m = 20$ g/l, $S_0 = 0.3$, $S_m = 0.9$.

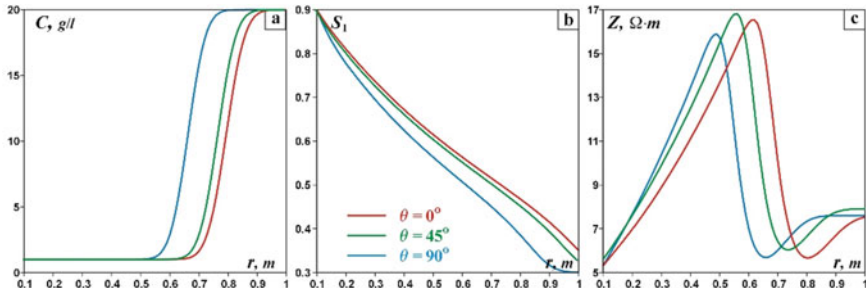


Fig. 5 Distribution of salinity C (a), water saturation S_1 (b) and true resistivity Z (c)

Figure 5 demonstrates distribution of water saturation S_1 , salinity C and true resistivity Z , calculated from Archie formula (Archie 1942) in modification (Yeltsov et al. 2012)

$$Z = \frac{A}{\omega^2 C (S_0 + S_1)^2},$$

(A —empiric constant) at time moment $t = 2$ days. It is obvious that minor difference between horizontal stress components in the external field leads to qualitative alteration in distribution of information-bearing parameters applicable to inverse logging data. In particular, drill mud penetration values in direction of σ_{max} action are 15–20% higher than similar magnitudes in orthogonal direction.

This factor should be taken into account to inverse the evidence obtained by advanced borehole geoelectrical methods (Yeltsov et al. 2014; Garcia et al. 2019; Bennis and Torres-Verdin 2019).

Acknowledgements The work was carried out with partial financial support of the Russian Foundation for Basic Research (Project No. 19-05-00689) and Programs of Federal Scientific Investigations: Identification Numbers AAAA-A17-117122090002-5 and 0331-2019-0015.

References

Ahmed TH (2019) Reservoir engineering handbook, 5th edn. Gulf Professional Publishing, Oxford
 Archie GE (1942) The electrical resistivity log as an aid in determining some reservoir characteristics. Trans AIME 146:54–62
 Bennis M, Torres-Verdin C (2019) Estimation of dynamic petrophysical properties from multiple well logs using machine learning and unsupervised rock classification. In: SPWLA 60th annual logging symposium, the Woodlands, Texas, USA. Expanded abstract: paper number: SPWLA-2019-KKKK
 Caglayan D, Weber N, Heinrichs HU, Linßen J, Robinius M, Kukla PA, Stolten D (2020) Technical potential of salt caverns for hydrogen storage in Europe. Int J Hydrogen Energy 45:6793–6805

- Garcia AP, Heidari Z (2021) A new multiphysics method for simultaneous assessment of permeability and saturation-dependent capillary pressure in hydrocarbon-bearing rocks. *SPE J* 26(1):155–171
- Garcia P, Heidari Z, Torres-Verdin C (2019) Multi-frequency interpretation of electric resistivity and dielectric permittivity measurements for simultaneous assessment of porosity, water saturation, and wettability (expanded abstract) In: SPWLA 60th annual logging symposium, the Woodlands, Texas, USA. Paper number: SPWLA-2019-III
- Hsu CS, Robinson PR (2019) *Petroleum science and technology*. Springer, New York
- Khristianovich SA (1989) Fundamentals of seepage theory. *Sov Min Sci* 25:397–412
- Kochin NE, Kibel IA, Roze NV (1964) *Theoretical hydromechanics*. Wiley, Chichester
- Nazarov LA, Nazarova LA, Karchevskii AL, Panov AV (2013) Estimation of stresses and deformation properties in rock mass based on inverse problem solution using measurement data of free boundary displacement. *J Appl Ind Math* 7(2):234–240
- Nazarova LA, Nazarov LA (2009) Dilatancy and the formation and evolution of disintegration zones in the vicinity of heterogeneities in a rock mass. *J Mining Sci* 45(5):411–419
- Nazarova LA, Nazarov LA (2018) Geomechanical and hydrodynamic fields in producing formation in the vicinity of well with regard to rock mass permeability-effective stress relationship. *J Mining Sci* 54(4):541–549
- Nazarova LA, Nazarov LA, Skulkin AA, Golikov NA (2019) Stress-permeability dependence in geomaterials from laboratory testing of cylindrical specimens with central hole. *J Mining Sci* 55(5):708–714
- Nazarova LA, Skulkin AA, Golikov NA, Nazarov LA (2020) Experimental investigation of poroperm properties of geomaterials in non-uniform stress field. *J Mining Sci* 56(5):706–712
- RF Standard 26450.2–85 (1985) *Rocks. Method for determination of absolute gas permeability coefficient by stationary and non-stationary filtration*
- Salimzadeh S, Paluszny A, Nick HM, Zimmerman RW (2018) A three-dimensional coupled thermo-hydro-mechanical model for deformable fractured geothermal systems. *Geothermics* 71:212–224
- Samarskii AA (2001) *The theory of difference schemes*. Marcel Dekker Inc., New York
- Seidle J (2011) *Fundamentals of coalbed methane reservoir engineering*. PennWell Books, Tulsa
- Yeltsov IN, Nesterova GV, Kashevarov AA (2012) Invasion zone modeling using water- and oil-based muds. *J Appl Mech Technical Phys* 53(4):552–558
- Yeltsov IN, Nesterova GV, Sobolev AY, Epov MI, Nazarova LA, Nazarov LA (2014) Geomechanics and fluid flow effects on electric well logs: multiphysics modeling. *Russ Geol Geophys* 55(5–6):775–783

Calculation of Dynamic and Energy Characteristics in the Region of Western Crimea Based on the Observational Data from Hydrological Surveys in 2007–2009 in the Numerical Model of the Black Sea Dynamics Using the Kalman Filter Algorithm



Demyshev Sergei and Evstigneeva Natalia

Abstract Hydrophysical fields and arrays of kinetic and potential energy budget components, continuous in time and space, were reconstructed on the basis of a thermohydrodynamic model and observational measurements of temperature and salinity in 2007 and 2009 in the region of western Crimea. To implement the procedure of assimilation of data observations, we used a four-dimensional analysis, based on a Kalman filter, taking into account the heterogeneity and non-isotropy of error estimates of temperature and salinity. We used a real atmospheric forcing and a high resolution (a horizontal grid $\sim 1.6 \times 1.6$ km and 30 vertical layers from 1 to 1200 m). The change of kinetic energy was determined mainly by wind action, vertical friction and the work of pressure forces; change in potential energy—by advection of potential energy. The calculated fields of currents were characterized by mesoscale eddy formations and jet currents. A horizontal velocity shear (resulting from the negative work of the wind force) and current flow around the coastline under the action of weak winds could be possible mechanisms of the generation of coastal mesoscale and submesoscale eddies in the coastal zone.

Keywords Black Sea · Numerical modeling · Assimilation of observational data · Mesoscale and Submesoscale Eddies · Jet currents

1 Methodology and Sources

One of the urgent tasks of modern oceanology is to reconstruct three-dimensional structure of thermohydrodynamic fields using data of hydrological measurements in a numerical model. Its solution allows to adequately determine the areas of generation of meso- and submesoscale features of coastal circulation (eddies, frontal zones,

D. Sergei · E. Natalia (✉)

Marine Hydrophysical Institute RAS, Sevastopol, Russian Federation

e-mail: naevstigneeva@yandex.ru

jet currents, etc.), which is necessary for the construction and exploitation of coastal structures, mining and forecasting the impact on the marine environment of accidental releases of pollutants and the formation of stagnant zones.

Previously conducted numerical experiments have shown the effectiveness of using hydrodynamic models with the block of assimilation of operational observational data. The problem of complex use of measurement data of temperature, salinity and current velocity at POLYMODE polygons, when they were assimilated into a model on the basis of the Kalman filter, was considered in Knysh et al. (2012). The method of optimal interpolation was used to assimilate observational data of level anomalies in the Atlantic Ocean into the HYCOM ocean hydrodynamic model in Tanajura et al. (2014). A problem of variational assimilation of sea surface temperature data in the model of the Black Sea dynamics for the reconstruction of surface flows was formulated in Agoshkov et al. (2013). A new version of the oceanographic data assimilation system, developed at the Hydrometeorological Center of Russia, was presented in Zelenko et al. (2016). An assimilation was carried out according to the analysis–forecast–analysis scheme, the components of which were the procedures for preparing the observational data obtained in the online mode, the variational data analysis scheme and the model of general ocean circulation. Algorithms of variational assimilation of temperature and level data at the liquid boundary were formulated in Agoshkov et al. (2020), the results of numerical experiments on the use of the algorithms in the Baltic Sea circulation model were also presented.

The approach, proposed in this research, was based on a modern numerical model of dynamics (Demyshev 2011) and the Kalman filter procedure, which took into account the non-isotropy and inhomogeneity of the error estimates of the temperature and salinity fields (Knysh et al. 1980; Knysh 1981).

Expedition surveys in the coastal zone of the Black Sea are constantly conducted by Marine Hydrophysical Institute (MHI), in which data on the vertical and spatial distribution of hydrophysical characteristics is received. Hydrological surveys in September 2007 and in April–May 2009 in the region of western Crimea (Fig. 1), were selected for the analysis in the research.

The aim of this paper is to restore the hydrophysical fields and fields of energy characteristics, using the hydrodynamic model and experimental data at the R/V “Experiment” in the autumn of 2007 and at the R/V “Saphir” in the spring of 2009. The study of possible physical mechanisms of formation of mesoscale eddies, jet currents in the region of western Crimea on the basis of the analysis of the obtained hydrophysical and energy fields, the study of the formation of circulation features for different seasons of the year (on the example of surveys of the autumn and winter seasons) is also of interest.

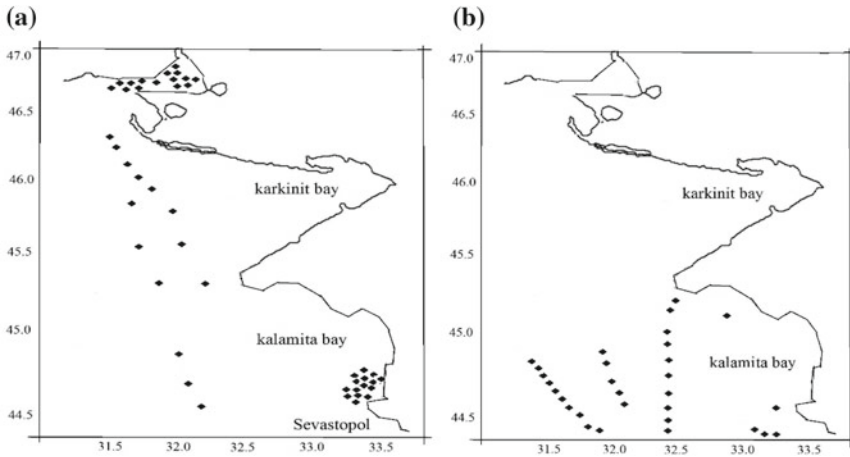


Fig. 1 Scheme of stations at R/V “Experiment” from 16th to 22nd of September, 2007 (a) and at R/V “Sapfir” from 29th of April to 2nd of May, 2009 (b)

2 Statement of the Problem and Parameters of the Numerical Experiments

The numerical model of the sea dynamics, based on the full equations of ocean thermohydrodynamics in the Boussinesq approximation, hydrostatics and incompressibility of sea water in the form of a Gromeka-Lamb, the boundary conditions on the surface, on the bottom and on solid side walls were described in detail in Demyshev (2011). The calculated area was placed between 28.7 and 33.8° E and 44.4 and 46.8° N (a detailed bottom relief with a resolution of ~1.6 km was taken into account). We used a horizontal grid of 1.6 × 1.6 km (302 × 196 points). A time step was equal to 30 s. Horizontal components of the current velocity, temperature and salinity were calculated for 30 horizons. Vertical velocity component was determined in accordance with the accepted finite—difference approximation (Demyshev 2011). The turbulent viscosity and horizontal diffusion were chosen in the form of a harmonic operator, the values of the coefficients were equal to $\nu_H = 5 \cdot 10^5 \text{ cm}^2/\text{s}$, $H = 5 \cdot 10^5 \text{ cm}^2/\text{s}$. The coefficients of turbulent momentum exchange and vertical diffusion were calculated in accordance with the Philander–Pakanovsky approximation (Pacanowski and Philander 1981).

At the southern border (corresponding to the parallel 44.4°N), the following conditions were set. The components of the current velocity, temperature and salinity (the Dirichlet conditions) were specified in the boundary regions, where water flowed into the domain ($v > 0$); conditions $\partial u/\partial n = 0$, $\partial v/\partial n = 0$ and radiation conditions for T and S were specified in the boundary regions, where water flowed out of the domain.

($v < 0$).

The period of integration of the model equations in the autumn season was 10 days (from 14 to 24th of September, 2007). The integration period of the model equations in the spring season was 6 days (from 28th of April to 4th of May, 2009).

The discharges of rivers was taken into account. The data of the regional atmospheric model “ALADIN” (ALADIN international team 1997) for the autumn season and the data of the Greek Center for atmospheric forecasts “SKIRON” (<http://forecast.uoa.gr/forecastnew.php>) for the spring season, were used in the experiments. It was determined that wind acting from the south-west, as well as winds from the north and north-east (with a maximum speed 8 m/s) prevailed in September 2007. Winds blowing from the north-east and south-west (with a maximum speed 18 m/s) were observed in April–May of 2009.

The data of hydrological surveys at the R/V “Experiment” in September 2007 and at the R/V “Saphir” in April–May 2009, taken from the MHI data bank (Suvorov et al. 2003), were used in the work. The measurements were carried out on the basis of CTD probes SHIK-1 and SHIK-2 (offshore measuring complexes). The maximum depth, to which the sounding was carried out, varied from 5 to 500 m. 44 stations were completed in the period from September 16 to 22, 2007 and 30 stations were completed in the period from April 29 to May 2, 2009 during the expeditions.

3 Analysis of the Energy Characteristics of the Circulation in the Autumn Season of 2007 and in the Spring Season of 2009

Finite-difference analogs of the equations of density change of kinetic and potential energy were written out, on the basis of which the energy characteristics were calculated in Demyshev (2004). Further in the text, the term “energy” referred to the energy density, i.e., the energy of a single volume.

The symbolic record of the kinetic energy budget equation (KE) had the form:

$$E_t + Adv(P + E) = \Pi \Leftrightarrow E + F_{Bfr}^\tau(E) - Diss_{Ver}(E) - Diss_{Hor}(E) + D_{Fic}(E),$$

where $Adv(P)$ was the work of the pressure force, $Adv(E)$ was kinetic energy advection, $\Pi \Leftrightarrow E$ was buoyancy force work, $F_{Bfr}^\tau(E)$ was the change of KE due to the work of the wind force and due to the bottom friction, $Diss_{Ver}(E)$ and $Diss_{Hor}(E)$ was energy dissipation due to vertical and horizontal internal friction, $D_{Fic}(E)$ was the redistribution of kinetic energy in the basin and its loss due to friction against the side walls.

The change of potential energy (PE) was described by the following equation:

$$\begin{aligned} \Pi_t + Adv(\Pi) = -\Pi \Leftrightarrow E + Diff_{Hor}(\Pi) + Diff_{Ver}^{Fluxes}(\Pi) + Diff_{Ver}^{KV}(\Pi) + \\ + Diff_{Ver}^{Bot-Sur}(\Pi) + Diff_{Ver}^{Add}(\Pi), \end{aligned}$$

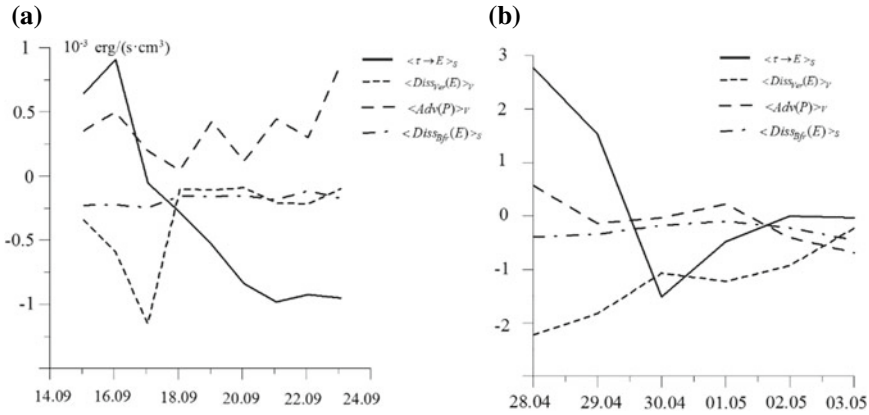


Fig. 2 Temporal change of integral energy terms in the kinetic energy budget equation in the volume-averaged computational domain **a**: in the autumn season of 2007, **b**: in the spring season of 2009

where $Adv(\Pi)$ was a potential energy advection, $Diff_{Hor}(\Pi)$ was a change in PE due to horizontal turbulent diffusion, $Diff_{Ver}^{Fluxes}(\Pi)$ was a change in PE due to buoyancy fluxes and vertical internal diffusion, $Diff_{Ver}^{Bot-Sur}(\Pi)$ was a change in PE due to the difference between the bottom and surface density, $Diff_{Ver}^{KV}(\Pi)$ was a change in PE due to inhomogeneity of the vertical turbulent diffusion coefficient in depth, $Diff_{Ver}^{Add}(\Pi)$ was an additional term due to the nonlinear dependence of density on temperature and salinity.

Figure 2a and b illustrated the temporal change of the integral energy terms, averaged over the volume of the calculated domain, in the budget equation of the KE for the autumn season of 2007 and the spring season of 2009. The angle brackets indicated the integration operation.

In the autumn season of 2007 the main contribution to the KE was made by the work of the pressure force $\langle Adv(P) \rangle_v$ (Fig. 2a), by the wind force $\langle \tau \rightarrow E \rangle_s$ in the period from 15 to 17 September, the maximum value of velocity reached 11 m/s (September 17). The loss of energy was due to vertical internal friction, the change in KE due to friction on the bottom $\langle Diss_{Bfr}(E) \rangle_s$ and term $\langle \tau \rightarrow E \rangle_s$.

In the spring season of 2009 the main inflow to the KE was from the wind, which reached 18 m/s from 28 to 30th of April, and from the work of the pressure force $\langle Adv(P) \rangle_v$ (Fig. 2b). The loss of energy was due to vertical internal friction $\langle Diss_{Ver}(E) \rangle_v$ and $\langle Diss_{Bfr}(E) \rangle_s$.

It was noted that the greater the variability of the inflow from the wind, the greater the dissipation of kinetic energy was in both the autumn and spring seasons. The contributions of the buoyancy force, kinetic energy advection and energy dissipation due to horizontal internal friction were insignificant. The main qualitative difference between the energy balance in the autumn and spring seasons was in the work of the pressure force. It was significant in the autumn; its influence was small in the spring.

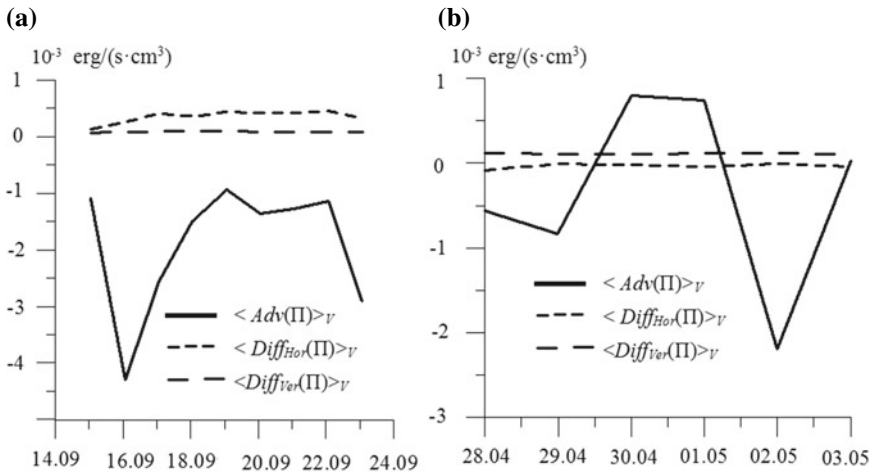


Fig. 3 Temporal change of the integral energy terms averaged over the calculated area in the equation of the potential energy budget **a** In the autumn season of 2007, **b** In the spring season of 2009

The change in the potential energy (Fig. 3a, b) was mainly determined by the advection of the potential energy. A small contribution of horizontal and vertical turbulent diffusions was also noted.

The main contribution was made by the term that characterized the density difference at the surface and at the bottom of the sea, when calculating the total vertical diffusion in the potential energy budget equation, in both the autumn and spring seasons. It was compensated by a term, depending on the change in the diffusion co-efficient with a depth.

4 Analysis of the Calculated Fields of Currents and the Terms of the Kinetic Energy Budget Equations in the Autumn Season of 2007

Figure 4a–c illustrated the fields of currents at the depth of 5 m for 15th, 20th, and 23rd of September, 2007 (every third arrow was shown).

The currents in the upper layer were directed mainly to the east and south-east from 14 to 18th of September. Mesoscale anticyclonic eddy was generated near the Kalamita bay at the depth of 5–36 m (Fig. 4a). The values of current velocity increased to 45 cm/s at the depth of 1–5 m near the Tarkhankut, submesoscale cyclonic eddy in the 10–20 m layer near Evpatoria was generated. The beginning of the formation of eddies, caused by with the meandering of the Rim Current (RC), has been noted since 17th of September, below the depth of 10 m.

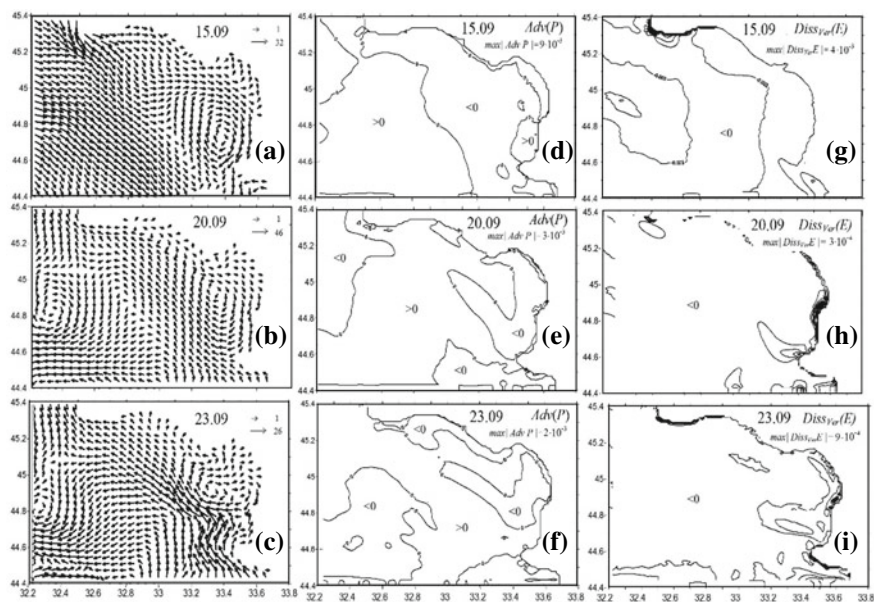


Fig. 4 Fields of currents (cm/s), $Adv(P)$ ($\text{erg}/(\text{s}\cdot\text{cm}^3)$) and $Diss_{Ver}E$ ($\text{erg}/(\text{s}\cdot\text{cm}^3)$) at the depth of 5 m on 15th, 20th and 23rd of September, 2007

From 19 to 24th of September direction of currents in the upper layer was the western and north-western, the meander element of RC was observed between 32.2 and 32.6° E. As an illustration, we present the fields of currents for September 20 (Fig. 4b).

On 22nd and 23rd of September a current at the depth of 1–36 m in the region of western Crimea was directed to the north and north-west. An anticyclonic eddy was observed in the Kalamita bay. Figure 4c illustrated those features.

Submesoscale eddies with diameters of less than 5 km with an existence time of 1–2 days were also obtained in the upper layer (for example, in Fig. 6a) during the calculating period.

The most energetically significant components of the budget (the fields of work of the pressure force, vertical friction and wind) were selected for analysis from the analysis of the graphs shown in Figs. 2 and 3.

The fields of work of the pressure force at the depth of 5 m for 15th, 20th and 23rd of September, 2007, were presented in Fig. 4d–f, which were characterized by significant variability and alternating areas with positive and negative values. The process of increasing the kinetic energy due to the work of the pressure force was observed in the zones corresponding to the positive values of $Adv(P)$. The maximum values of work of the pressure force were obtained in the central part of the region. The maximum value of module was $9\cdot 10^{-3}$ $\text{erg}/(\text{s}\cdot\text{cm}^3)$ on 15th of September and it decreased to $2\cdot 10^{-3}$ $\text{erg}/(\text{s}\cdot\text{cm}^3)$ on 23rd of September.

The predominance of the contribution of the work of the pressure force (Fig. 2) to the increase in the kinetic energy may be due to the fact that the work of the pressure force mainly depended on the difference in the bottom relief (the pressure anomaly can be represented as $P = -g \cdot \int_z^H \rho dz$). There was a depth dump, where the depth varies from 100 to 1300 m, between the meridians 31 and 33.5°E.

A comparison of the spatial distributions of $Adv(P)$ and the fields of currents showed that there was a correspondence between the location of the positive values of the work of pressure forces and the zones of generation of mesoscale circulation features (anticyclonic eddy in the Kalamita bay, intensive flow in the region of western Crimea).

The fields of $Diss_{ver}(E)$ (energy dissipation due to vertical internal friction) at the depth of 5 m for 15th, 20th and 23rd of September, 2007 were presented on Fig. 4g-i. According to Fig. 2, the inflow of energy from the wind was compensated by vertical friction. The central part of the region was characterized by intensive work of vertical dissipation, the maximum value of modules of $Diss_{ver}(E)$ was $4 \cdot 10^{-3}$ erg/(s·cm³) on 15th of September, the values decreased along the coast. The variability of the $Diss_{ver}(E)$ was insignificant after 20th of September, the values of modules did not exceed $3 \cdot 10^{-3}$ erg/(s·cm³).

5 Analysis of Calculated Fields of Currents and Terms of the Kinetic Energy Budget Equations in the Spring Season of 2009

Figure 5a, b showed the fields of currents at the depth of 5 m for 30th of April and 3rd of May, 2009 (every third arrow was shown).

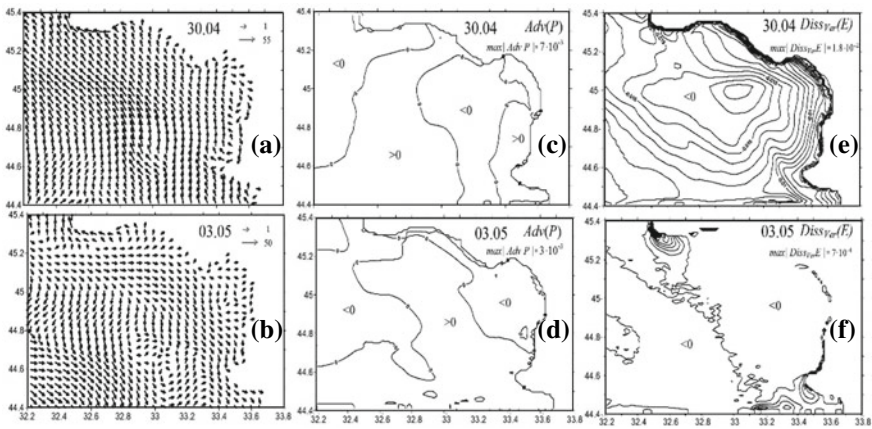


Fig. 5 Fields of currents (cm/s), $Adv P$ (erg/(s·cm³)) and $Diss_{ver}E$ (erg/(s·cm³)) at the depth of 5 m on 30th of April and 3rd of May, 2009

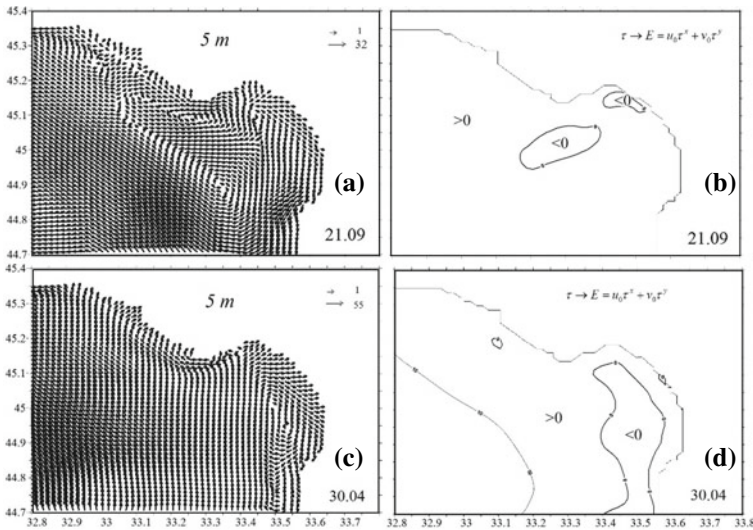


Fig. 6 Field of currents (cm/s) at the depth of 5 m on 21st of September, 2007 (a), field $\tau \rightarrow E = u_0\tau^x + v_0\tau^y$ (erg/(s·cm²)) on 21st of September (b), field of currents (cm/s) at the depth of 5 m on 30th of April, 2009 (c), field $\tau \rightarrow E$ (erg/(s·cm²)) on 30th of April, 2009 (d)

The currents in the upper layer were directed to the west and north-west (Fig. 5a) from 28th April to 1st of May. Its maximum values were 65 cm/s on 30th of April. It was noted that the depth reversal of the current velocity vector took place according to the Ekman theory. Mesoscale anticyclonic eddy was observed near the Kalamita bay at the depth of 5 m, mesoscale anticyclonic eddy formations were generated near Sevastopol at the depth of 10–36 m. We noted that eddy formations in the current field were weaker at high values of wind velocity (more than 11 m/s) on 28th and 29th of April.

The currents in the upper layer were directed to the east and south-east (Fig. 5b) from 2nd of May to 4th of May, the maximum speed of the currents obtained 51 cm/s on 2nd May. Cyclonic mesoscale eddy formations were obtained in the Kalamita bay and in the region between 32.6 and 33°E at the depth of 10–20 m. Eddy formations of different signs of rotation with a radius of less than 10 km were formed below the depth of 10 m.

The fields of work of the pressure force at the depth of 5 m for 30th of April and 3rd of May, 2009 were presented in Fig. 5c, d. Areas with both positive and negative values were noted. Maximum module value was $7 \cdot 10^{-3}$ erg/(s·cm²) on 30th of April, $3 \cdot 10^{-3}$ erg/(s·cm²)—on 3rd of May (observed in the central part of the region). Positive values of the work of pressure force prevailed in the areas of formation of circulation features (anticyclonic eddy in the Kalamita bay, intense flow along the western coast of the Crimea).

The fields of $Diss_{ver}(E)$ at the depth of 5 m for 30th of April and 3rd of May 2009 were presented on Fig. 5e, f. The central region was characterized by intensive

work of vertical dissipation on 30th of April, the maximum value for the module was $1.8 \cdot 10^{-2}$ erg/(s·cm²), along the coast the values decreased. Significant losses of the KE were explained by the intensification of the processes of mixing and vertical exchange due to the action of winds with a speed of more than 10 cm/s. The module values of $Diss_{ver}(E)$ did not exceed $7 \cdot 10^{-4}$ erg/(s·cm²) on 3rd of May.

The spatial distributions of the term $\tau \rightarrow E = u_0\tau^x + v_0\tau^y$ that determined the contribution to the kinetic energy from the wind, which was obtained by integrating vertically the budget equation of the wind energy for both seasons, were also analyzed. The fields of currents at the depth of 5 m in the autumn season of 2007 and in the spring season of 2009 were presented on Fig. 6a, c. Figure 6b, d showed the corresponding fields of $\tau \rightarrow E$.

The inflow of energy from the wind prevailed in almost the entire region, except for the Kalamita bay. There was a horizontal shift in the velocity field in the zone, where the work of the wind force was negative (the wind and currents on the surface were directed in opposite directions). Consequently, a possible mechanism for the formation of an anticyclonic eddy in the Kalamita bay could be the shear instability of the current.

It was also noted from the analysis of fields of currents and fields of $\tau \rightarrow E = u_0\tau^x + v_0\tau^y$ that eddies with radius of less than 10 km formed in the autumn season of 2007 and in the spring season of 2009 along the coast in zones corresponding to the minimum values of $\tau \rightarrow E$. A possible mechanism of formation was the flow of the current around the coastline under the influence of weak winds.

To summarize the conclusions: the dynamic and energy characteristics of the coastal circulation in the region of western Crimea were calculated on the basis of the hydrodynamic model (~1.6 km horizontally and 30 horizons vertically) and the temperature and salinity observations, obtained during the hydrological surveys at the R/V “Experiment” in 2007 and at the R/V “Saphir” in 2009, taking into account the real atmospheric forcing.

Change of kinetic energy was determined mainly by wind action, vertical friction, and the pressure force in both the autumn and spring seasons; change in potential energy was determined by the advection of potential energy. The greater the variability of the inflow from the wind, the greater the dissipation of kinetic energy was.

According to the results of the calculation in the autumn season, the following features of the circulation were noted: an anticyclonic eddy with a radius of about 15 km in the upper water layer in the Kalamita bay, an anticyclonic eddy with a radius of about 15 km in the entire water layer, caused the Rim Current. The current intensification at the depth of 1–36 m layer in the region of western Crimea was noticed on 22nd and 23rd of September. Small-scale anticyclonic and cyclonic eddies could be generated in the upper layer along the coast during the calculation.

According to the results of the calculation in the spring season, the following features of the circulation were obtained: mesoscale eddy in the upper water layer near the Kalamita bay, in the layer of 10–36 m, submesoscale eddy formations near Sevastopol.

The regions of formation of mesoscale eddies and jet currents were characterized by intensive work of the pressure force, which was about several times higher than the other terms of the equation of the kinetic energy budget. The possible mechanism of the formation of an anticyclonic eddy in the Kalamita bay in the autumn and spring seasons was an effect of the shear instability of the currents. Small-scale eddies (with a radius of less than 10 km) were formed in both the autumn and winter seasons as a result of the influence of inhomogeneities of the coast line on the current under the action of weak winds.

Acknowledgements The analysis of hydrophysical fields, reconstructed taking into account the data of hydrological surveys of 2007–2009, was carried out with the financial support of the Russian Foundation for Basic Research and the city of Sevastopol within the framework of the scientific project No. 18-45-920019. The study of possible physical mechanisms for the generation of meso- and submesoscale circulation features on the basis of the analysis of energy fields was carried out within the framework of the state assignment on topic No. 0555-2021-0004 (code “Oceanological processes”).

References

- Knysh VV, Korotaev GK, Mizyuk AI, Sarkisyan AS (2012) Assimilation of hydrological observation data for calculating currents in seas and oceans. *Izv Atmos Ocean Phys* 48:57–73. <https://doi.org/10.1134/S0001433812010057>
- Tanjura CAS, Costa FB, Silva RR, Ruggiero GA et al (2014) Assimilation of sea surface height anomalies into HYCOM with an Optimal Interpolation Scheme over the Atlantic Ocean. *Rev Brazilian Geofis* 31:257–270. <https://doi.org/10.22564/rbgf.v31i2.293>
- Agoshkov VI, Parmuzin EI, Shutyaev VP (2013) Observational data assimilation in the problem of Black Sea circulation and sensitivity analysis of its solution. *Izv Atmos Ocean Phys* 49:592–602. <https://doi.org/10.1134/S0001433813060029>
- Zelenko AA, Vil'fand RM, Resnyanskii YuD, Strukov BS et al (2016) An ocean data as-similation system and reanalysis of the world ocean hydrophysical fields. *Izvestiya. at-Mospheric and Oceanic Physics*. 52(4):443–454. <https://doi.org/10.1134/S0001433816040149>
- Agoshkov VI, Zalesny VB, Sheloput TO (2020) Variational assimilation of data in problems of modeling hydrophysical fields in open water areas. *Izvestiya RAN. Phys Atmos Ocean* 56(3):293–308. <https://doi.org/10.1134/S0001433820030020>
- Demyshv SG (2011) Prognostic numerical analysis of currents in the black sea with high horizontal resolution. *Phys Oceanogr* 21(1):33–44. <https://doi.org/10.1007/s11110-011-9102-x>
- Knysh VV, Moiseenko VA, Sarkisyan AS, Timchenko IE (1980) Complex use of measurements at the hydrophysical ocean polygons in four-dimensional analysis. *Reports of AS USSR*. 252(4):832–836
- Knysh VV (1981) Hydrothermodynamic models of the ocean in the algorithm of multielement four-dimensional analysis of hydrophysical fields: dissertation for the degree of Doctor of Physics and Mathematics. Sevastopol, 396 p. (in Russian)
- Pacanowski RC, Philander SGH (1981) Parameterization of vertical mixing in numerical models of tropical oceans. *J Phys Oceanogr* 11(11):1443–1451
- ALADIN international team (1997) The ALADIN project: mesoscale modelling seen as a basic tool for weather forecasting and atmospheric research. *World Meteorol Organ Bulle* 46(4):317–324. http://www.umr-cnrm.fr/aladin/IMG/pdf/ALADIN_PROJECT-pdf_-_Adobe_Acrobat_Professional.pdf. Accessed 23 Nov 2020

- NonHydrostatic SKIRON/Eta modelling system. <http://forecast.uoa.gr/forecastnew.php>. Accessed 18 Apr 2019
- Suvorov AM, Andryushchenko EG, Godin EA, Ingerov AV et al (2003) The bank of oceanological data of the MHI NASU: content and structure of databases, database man-agreement system. Environ Monit Syst 130–137. (in Russian)
- Demyshev SG (2004) Energy of the Black Sea climatic circulation. Part I. Discrete equations for the rate of change of kinetic and potential energies. Meteorol Hydrol 9:65–80

One-Dimensional Coherent Convective Structures from Heat Sources



A. V. Kistovich 

Abstract The problem of the periodic convective patterns is considered from the point of view of interacting cells coherent structures. It should be especially emphasized that all interactions are taking into account, including those between remote cells. For one-dimensional structure, the interaction coefficients are defined exactly for infinite coherent structure. In the case of finite number of cell the approximate values of interaction coefficients were received.

Keywords Convective structure · Elementary cell · Interaction coefficient · Interaction energy

Introduction

Convective phenomena in liquids are the subject of intensive experimental and theoretical research. In natural and laboratory conditions, various types of convective structures are observed, among which coherent structures are distinguished, the determination of the characteristics of which provides important information about the general properties of convective flows. Such structures include flows that arise in the modes of roller convection from a flat horizontal heat source (White 1988), and systems of horizontal convective cells that form near a vertical flat source in a stratified fluid (Nekrasov et al. 1976). A striking example of coherent structures is a system of spatially periodic jets emerging from a horizontal linear heat source in a medium with salt stratification (Popov et al. 1980).

In this paper, an attempt is made to describe such properties of the mentioned structures, which do not depend on the specific implemented mode of convection.

A. V. Kistovich (✉)

Ishlinsky Institute for Problems in Mechanics of the Russian Academy of Science, Moscow, Russia

e-mail: kavmendeleeevo@mail.ru

The convective structures observed experimentally (White 1988; Nekrasov et al. 1976; Popov et al. 1980) are conditionally divided into two groups: structures with one-dimensional and two-dimensional symmetries. They require separate consideration. The following is an analysis of the properties of one-dimensional structures.

1 One-Dimensional Structures

First, we consider an infinite convective structure that periodically repeats itself in one direction. Such types of structures include horizontal shafts in a liquid with a weak dependence of viscosity on temperature (White 1988), convective cells that arise near a heated wall in a stratified liquid (Nekrasov et al. 1976), and floating jets from a horizontal heated cylinder (Popov et al. 1980). A schematic representation of such a structure is shown in Fig. 1.

Each square of the depicted structure denotes a separate convective cell, which is called an *elementary cell* in the case when it cannot be divided into two or more periodically repeating structural units, with which the entire area of convection can be densely filled by means of translation.

It is believed that the elementary cells are indistinguishable from each other, have their own *internal energy* $u^{(1)}$ and can interact with each other.

Let $\epsilon^{(1)}$ denote the *total energy of interaction* of the elementary cell with all other cells of the infinite structure. The symbol μ_i denotes the coefficient of interaction between the j -th and $j + i$ -th cells, where j is an **arbitrary** number. The meaning of the interaction coefficient is determined by the value $\mu_i \epsilon^{(1)}$, which describes the value of the interaction energy between the j -th and $j + i$ -th cells. In contrast to the Ising model (Baxter 1989), the proposed model takes into account not only the interactions with the nearest neighbors, but with all the cells forming a convective structure.

The value $w^{(1)}$, which denotes the total energy of a unit cell in a one-dimensional structure, is defined as the sum of its internal energy and the energy of interaction with all other cells

$$w^{(1)} = u^{(1)} + \epsilon^{(1)}. \tag{1}$$

On the other hand, the use of the concept of the interaction coefficient μ_i allows us to determine the total energy by the ratio

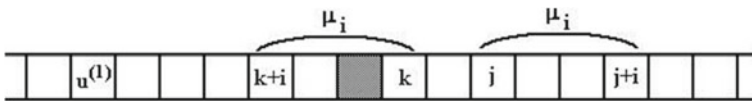


Fig. 1 One-dimensional structure

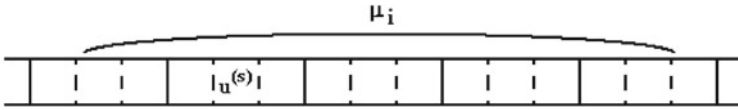


Fig. 2 Partitioning into s -cells

$$w^{(1)} = u^{(1)} + 2\varepsilon^{(1)} \sum_{i=1}^{\infty} \mu_i. \tag{2}$$

Then from (1) and (2) it necessarily follows

$$2 \sum_{i=1}^{\infty} \mu_i \equiv 1. \tag{3}$$

The resulting expression is one of the fundamental relations of a one-dimensional convective structure.

The structure under study can also be considered in another way, by dividing it into a system of periodically repeating s -cells, as shown in Fig. 2.

Each s -cell consists of s elementary cells that border each other in pairs. If we forget about the internal structure of the s -cell, the resulting picture looks no different from the one shown in Fig. 1. It is clear that the internal energy of the s -cell $u^{(s)}$ and its total energy of interaction $\varepsilon^{(s)}$ with the other s -cells differs from the corresponding characteristics of the unit cell. At the same time, there are values that are the same for both structures—these are the interaction coefficients μ_i .

The energy of interaction between the m -th and $m+n$ -th s -cells can be determined by summing up the interactions between the elementary cells that make up them

$$\mu_n \varepsilon^{(s)} = \varepsilon^{(1)} \sum_{j=0}^{s-1} \sum_{i=0}^{s-1} \mu_{ns+j-i}. \tag{4}$$

At the same time, the total energy $w^{(s)}$ of the s -cell in the structure is determined by the expression

$$w^{(s)} = s w^{(1)} - \varepsilon^{(1)} \sum_{i=1}^{s-1} (s-i) \mu_i, \tag{5}$$

which is the result of summing the total energies of the s elementary cells that make up the s -cell, minus the internal interactions that are twice taken into account when summing.

The main assumption is that both the total energy and the energy of the interaction of the coherent structure under study are renormalizable, that is, the relations are fulfilled

$$w^{(s)} = \lambda_s w^{(1)}, \quad \varepsilon^{(s)} = \lambda_s \varepsilon^{(1)}, \quad (6)$$

where λ_s is renormalization coefficient.

Substituting (6) into (4) and (5) converts them to the form

$$\lambda_s \mu_n = \sum_{j=0}^{s-1} \sum_{i=0}^{s-1} \mu_{ns+j-i}, \quad \lambda_s = s - \frac{\gamma}{1+\gamma} \sum_{i=1}^{s-1} (s-i) \mu_i, \\ s = 1, 2, \dots; \quad n = 1, 2, \dots; \quad \lambda_1 \equiv 1 \quad (7)$$

where $\gamma = \varepsilon^{(1)}/u^{(1)}$.

Exclusion from (7) of the λ_s renormalization coefficient, taking into account the ratio

$$\sum_{j=0}^{s-1} \sum_{i=0}^{s-1} \mu_{ns+j-i} \equiv \sum_{i=1}^{s-1} (s-i)(\mu_{ns+i} + \mu_{ns-i}) + s\mu_{ns},$$

generates the basic system of interaction equations of a one-dimensional system

$$s(1+\gamma)(\mu_n - \mu_{ns}) = \sum_{i=1}^{s-1} (s-i)[(1+\gamma)(\mu_{ns+i} + \mu_{ns-i}) + \gamma\mu_n\mu_i], \\ s = 1, 2, \dots; \quad n = 1, 2, \dots; \quad (8)$$

which must be supplemented with the normalization Eq. (3).

The system of Eqs. (8) determines the compatibility of the system (7).

2 The Solution to the Problem has the Form

Let there be a set of renormalization coefficients

$$\lambda_1 \equiv 1, \lambda_2, \lambda_3, \dots, \lambda_N, \dots, \lambda_s, \dots,$$

moreover, if s is a prime number, then λ_s is chosen arbitrarily.

If $s = \prod_{i=1}^{m(s)} \sigma_i$ is a composite number, where σ_i is a prime number, and $m(s)$ is the number of prime divisors of s , then the renormalization coefficients satisfy the condition: $\lambda_s = \prod_{i=1}^{m(s)} \lambda_i$ (i.e., $\lambda_4 = \lambda_2^2$, $\lambda_6 = \lambda_2 \lambda_3$, etc.). Then the interaction coefficients μ_k are determined by the relations

$$\mu_1 = 1 - \frac{\lambda_2}{2}, \quad \mu_2 = -\frac{1}{2} + \lambda_2 - \frac{\lambda_3}{2}, \quad \dots, \quad \mu_k = -\frac{\lambda_{k-1}}{2} + \lambda_k - \frac{\lambda_{k+1}}{2}. \quad (9)$$

If we impose additional conditions following from the physical meaning of the coefficients μ_i, λ_i , namely

$$\mu_i > \mu_j, \quad j > i; \quad \lambda_j > \lambda_i, \quad j > i; \quad \mu_i, \lambda_i > 0, \quad \forall i, \quad (10)$$

then all the necessary conditions are satisfied by the solution

$$\lambda_n = n^\gamma, \quad \mu_n = -\frac{\lambda_{n-1}}{2} + \lambda_n - \frac{\lambda_{n+1}}{2} = -\frac{(n-1)^\gamma}{2} + n^\gamma - \frac{(n+1)^\gamma}{2} \quad (11)$$

for any γ from the interval $(0, 1)$.

Any field or laboratory experiment is carried out in finite volumes of space with finite dimensions and a finite number of convective cells. In relation to the above approach, this fact imposes the requirement of a sufficiently rapid decline in the interaction coefficients μ_n with an increase in the index n , in the case when comparisons are made with the experimental results. This provides, to a certain extent, an adequate description of the state of the internal cells of the convective structure, but does not eliminate the boundary effects associated with the final dimensions of the convection region.

Figure 3 shows the relative errors in estimating the interaction energy of a cell in a structure of finite dimensions compared to an infinite ideal structure.

The error value is calculated using the formula

$$\varepsilon(\gamma, N) = 1 - 2 \sum_{i=1}^N \mu_i(\gamma), \quad (12)$$

where γ is a parameter that determines the set of interaction coefficients, $2N + 1$ is the number of cells in the convective structure. Selecting an odd number of cells has little effect on the result, but it makes it some easier to record the error $\varepsilon(\gamma, N)$.

The result shown in Fig. 3 shows that with a small number of cells in the experimentally observed structure, it is necessary, when attempting a theoretical description, to limit the possible value of the parameter γ to $(0, \approx 0.5)$.

The state of the convective structure is considered in the quasi-stationary limit, that is, it is assumed that in a certain time neighborhood of the selected moment of observation of the convective structure, its characteristics (distributions of the fields

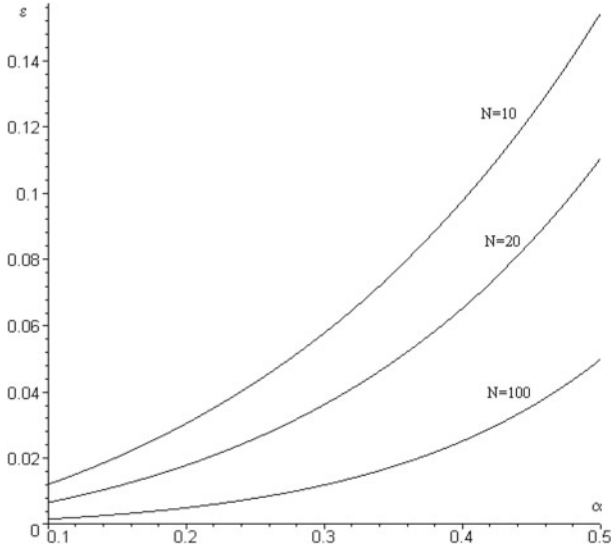


Fig. 3 Relative error $\varepsilon(\gamma, N)$

of velocity, temperature, pressure, density, etc.) change weakly. Let's denote by the symbol W the energy stored in the structure. In the case of a finite number of N cells, this energy is determined by the ratio

$$W(\gamma, N) = N u_N^{(1)}(\gamma) + \varepsilon_N^{(1)}(\gamma) \sum_{i=1}^N (N - i) \mu_i(\gamma). \quad (13)$$

Here $u_N^{(1)}(\gamma)$ is the internal energy of the cell, $\varepsilon_N^{(1)}(\gamma)$ is the total energy of the interaction of the cell in the structure. Strictly speaking, the expression (13) does not take into account the boundary effects associated with the finite dimensions, which determines the single energy $\varepsilon_N^{(1)}(\gamma)$ for any convective cell. For this reason, the expression (13) is certainly an approximation.

The total energy of the convective structure is determined by the ratio

$$W = \int_V (c_v \Delta T + \rho \mathbf{v}^2 / 2 + p + gz(\beta \Delta S - \alpha \Delta T)) dV. \quad (14)$$

Here ΔT , ΔS are the fields of temperature and salinity perturbations; ρ is the density of the medium; \mathbf{v} is the velocity field; p is the pressure, minus the hydrostatic part; g is the gravitational acceleration directed against the z axis; α , β are the coefficients of temperature expansion and salt contribution to the density, respectively; c_v is the heat capacity at a constant volume; V is the volume occupied by the convective structure.

In the absence of convection ($\Delta T = \Delta S = p = \mathbf{v} = 0$), there are no cells, as there is no interaction between them. For this reason, the value of $\int_V c_v \Delta T dV$ is related to the internal energy of the structure, that is,

$$\int_V c_v \Delta T dV = N u_N^{(1)}(\gamma). \quad (15)$$

(Since the physical coefficients α and β do not appear explicitly in the following calculations, their coincidence with the mathematical parameters indicated by the same symbols does not cause any discrepancies.)

The remaining part of the total energy (14) is interpreted as the total energy of the interaction of cells. Let us ask the question: can the total energy of a convective structure described by the parameters (γ, N) be attributed to another structure with the parameters (δ, M) ?

If this is possible, then the relation arises

$$W(\delta, M) = M u_M^{(1)}(\delta) + \varepsilon_M^{(1)}(\delta) \sum_{i=1}^M (M - i) \mu_i(\delta), \quad (16)$$

similar to the expression (14). In this case $W(\gamma, N) \equiv W(\delta, M)$.

The internal energies of these structures also coincide (according to the definition given above), thus

$$N u_N^{(1)}(\gamma) = M u_M^{(1)}(\delta). \quad (17)$$

Here we assume that for a fixed total energy of the convective structure W , the ratio of the internal energy of an individual cell to its energy of interaction with the entire structure is a constant value, that is,

$$u_N^{(1)}(\gamma) / \varepsilon_N^{(1)}(\gamma) = u_M^{(1)}(\delta) / \varepsilon_M^{(1)}(\delta) = \kappa. \quad (18)$$

Then, based on the relations (13)–(18), the condition follows

$$\frac{1}{N} \sum_{i=1}^N (N - i) \mu_i(\gamma) = \frac{1}{M} \sum_{i=1}^M (M - i) \mu_i(\delta), \quad (19)$$

determining the possibility of implementing two similar but different convective structures at a given total energy W .

Below, in Table 1, are the values of the interaction coefficients that correspond to the structures $N = 4, \gamma = 0.145$; $N = 6, \gamma = 0.339$; $N = 8, \gamma = 0.430$. These structures satisfy the relation (19).

Table 1 Interaction coefficients

	μ_1	μ_2	μ_3	μ_4
$\gamma = 0.145$	0.447	0.019	0.009	0.005
$\gamma = 0.339$	0.368	0.039	0.019	0.011
$\gamma = 0.430$	0.326	0.045	0.023	0.014

3 Conclusions

It is seen that the structure with the largest number of cells ($N = 8$) is characterized by increased interaction with remote cells than the structure with the number $N = 4$ of cells. It has a large correlation radius, and therefore is more stable with respect to perturbations. This indicates a tendency for the convective flow to break up into cellular structures. This is confirmed, for example, by the experiments described in Popov et al. (1980), when a heated horizontal cylinder floats not a “wall” of warm liquid, but a system of heated jets periodically distributed along the heat source.

In the case of roll convection in a horizontal rectangular cuvette, the configuration for which, as follows from the above, the number of convective rolls will be the largest will be more stable. Since the diameter of the convective roll is equal to the depth of the liquid layer, the obvious result follows from this fact is that the convective rolls will line up along the short wall of the cuvette, since in this case their number will be maximum.

At the same time, without knowing the critical value of the energy W_* , at which the convective motion begins, it is impossible to make an unambiguous choice in favor of the implementation of a particular structure. The work was carried out with the financial support of the project of the Russian Federation represented by the Ministry of Education and Science of Russia № 075-15-2020-802.

References

- Baxter RJ (1989) Exactly solved models in statistical mechanics. Academic, London
- Nekrasov VN, Popov VA, Chashechkin YuD (1976) Formation of the periodic structure of a convective flow under lateral heating of a stratified liquid//Izvestia AS USSR. Atmos Ocean Phys 12(11):1191–1200 (In Russian)
- Popov VA, Chashechkin YD (1980) Free convection near a horizontal cylinder in a stratified liquid. J Technical Phys 50(10):2189–2200 (In Russian)
- White DB (1988) The planeforms and onset of convection with a temperature-dependent viscosity. JFM 191:247–286

Features of the Spread Oil Spill in Arctic Conditions



V. P. Pakhnenko

Abstract The article describes the features of the distribution of oil spill in the Arctic. The physical characteristics of the movement of an oil slick in cold water are described, and the processes of interaction between oil and ice are considered. Also, the article discusses various methods of liquidating the consequences of oil spills in arctic conditions and the problems that arise with this issue.

Keywords Oil spill · Ice · Oil · Arctic zone · Cold water

Due to the constant growth of oil production volumes, as well as the improvement of technologies for their production, in recent years there has been observed a noticeable increase in interest in oil exploration on the Arctic shelf and in other poorly studied and hard-to-reach regions. Although oil exploration in such places seems new, actually, oil production in the Arctic has been going on for a long time. In the 1970s and 1980s, about 100 wells were drilled in the Canadian Arctic and in the Canadian territorial waters of the Beaufort Sea. Five wells were drilled in US territorial waters in the Chukchi Sea around the same period. In Cook Bay in Alaska, oil production has been going on for 50 years, and more than 30 years ago oil production began on the northern coast of Alaska. Recently, oil and gas production has begun on the Russian shelves. Naturally, further offshore oil exploration is planned in other regions of the Arctic, in Western Greenland, in the Chukchi Sea, in the Kara and Barents seas.

Leakage of oil products, fuel or various other hydrocarbons is always a very serious environmental problem, the consequences of which are difficult to eliminate. Oil spill response is costly and requires lots of efforts under any circumstances, while in arctic conditions these efforts are multiplied. Additional difficulties are related to environmental protection, preserving of natural conditions, logistics and many other. At the same time, the unique features of the Arctic environment in some cases contribute to the oil spill response.

V. P. Pakhnenko (✉)

Ishlinsky Institute for Problems in Mechanics RAS, Vernadskogo ave., 101-1, 119526 Moscow, Russia

e-mail: terkin95@mail.ru

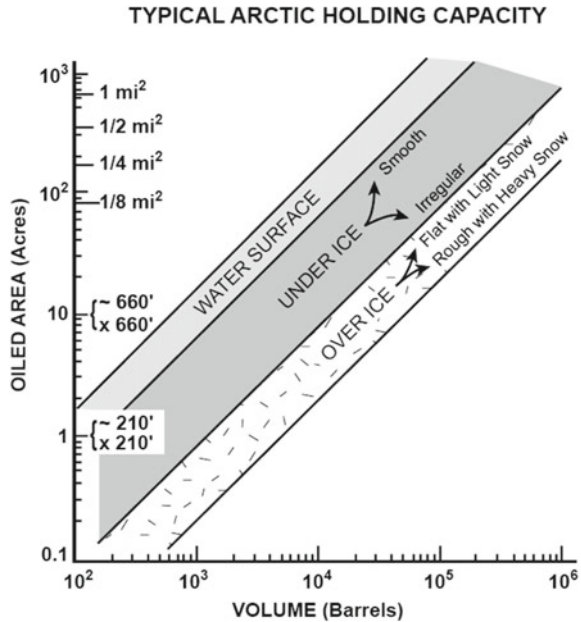
Of course, the first and most obvious issue is the presence of ice. Ice in its various forms can significantly complicate oil detection, monitoring, and, most importantly, the localization and collection of oil slicks, using booms and other similar floating equipment. Nonetheless, the natural localization, provided by ice, can simplify the collection task. In open water as rivers, lakes, the sea, and the ocean, spills can spread and drift fast enough that the coastline is contaminated even before any spill response measures are started. At the same time, ice can localize an oil spill. Due to this localization time can be gained for preparing respond to the spill. Moreover, low temperatures and small wave amplitudes in the ice field can play a positive role, which slow down the process of oil slick spreading along the surface; this gives additional opportunities for more effective application of various measures to eliminate the consequences of hydrocarbon pollution.

In this work various physical and mathematical models, used in the study of oil slick spreading, were considered. A very common approach for estimating the size of oil slicks on the water surface is to simplify the mathematical formulation of the spreading problem. In this formulation, it is assumed that the balance of the force of resistance to the movement of oil and the prevailing force of the forces causing the movement (Fay 1969, 1971; Hoult 1972). However, in some works (Reed et al. 1999; Fingas and Hollebone 2003) it is noted that the selection of «two main» factors from all the factors that are responsible for spreading is a rather rough approximation. At the same time, Fay's ratios, which were proposed about 50 years ago for assessing the size of an oil pollution area, turned out to be one of the simplest methods for calculating the parameters of an oil spill and, therefore, are still in demand in practical problems.

Despite the fact that these relationships were obtained so long ago, the choice of a friction model for oil spreading over the sea surface remains a question that does not have a rigorous solution today. According to Fay, the gravitational-viscous flow regime for spreading an oil slick over a calm water surface is made up of the balance of gravitational forces and viscous friction at the oil-water interface. Considering that oil spreads over the turbulized upper layer of the sea, and the size of the oil slick is often hundreds or even thousands of meters, the model of friction at the oil-water interface in the form of a stationary boundary layer with a logarithmic profile of the velocities difference seems more realistic. When spreading under natural conditions and with significant sizes of spills, the friction force of oil on water can be represented as proportional to the difference between the local velocities of oil and water; this was shown in Nihoul (1984). In another approach, more classical (Fay 1969; Hoult 1972), the friction between oil and water was taken on the basis of the theory of a laminar boundary layer.

It should be said that analytical solutions can be found not for all practically important scenarios of oil and other hydrocarbon spills. At the same time, even successful attempts to find analytical solutions for one-dimensional or axisymmetric spreading variants are associated with a number of assumptions. For instance, assumptions about the model of friction at the oil-water interface or about the relative importance of certain factors, affecting the flow of oil. Thus in some cases the value of analytical solutions, applied to real oil spills at sea, can be questioned.

Fig. 1 Oil-holding capacity of various surfaces in arctic conditions



In the Arctic zone, it is very difficult to competently plan priority measures to protect the marine environment and coasts; it is almost impossible to plan response without analyzing the likely scenarios for the spreads of oil spills. Assessment of the possible scale of hydrocarbon spills under various hydrometeorological conditions, including oil spills on moving or stationary ice sheets, is an essential part of analyzing the risk of spill spreading.

The article (СТИВЕНН et al. 2013) describes decently the key processes, affecting the behavior and dynamics of an oil slick in the Arctic. The distribution of oil products on solid ice is similar to its distribution on the ground. Thus, various physical dependencies remain, for example: the speed of oil spreading depends mainly on the viscosity of oil products, therefore, at low temperatures, a slowdown in the propagation speed is noted; the total area of the oil spill depends on the degree of roughness of the ice surface. As a rule, the ice is a rather irregular surface, even with smooth first-year sea ice, the surface is quite uneven. Also, discrete ice deformations, for example, bedding, the formation of ice boulders, can lead to a local increase in irregularities, which in turn can rise up to tens of meters above sea level. Therefore, oil products spilled onto an inhomogeneous ice surface, can be completely confined in a closed space, limited by a complex ice shape. This usually results in thicker oil patches on the ice and a much slower oil spreading speed than in situation with an open water spill.

Also, if the ice is covered with a layer of snow, then the snow absorbs the spilled oil products, further reducing the speed of their spread. (Fig. 1) shows an estimate

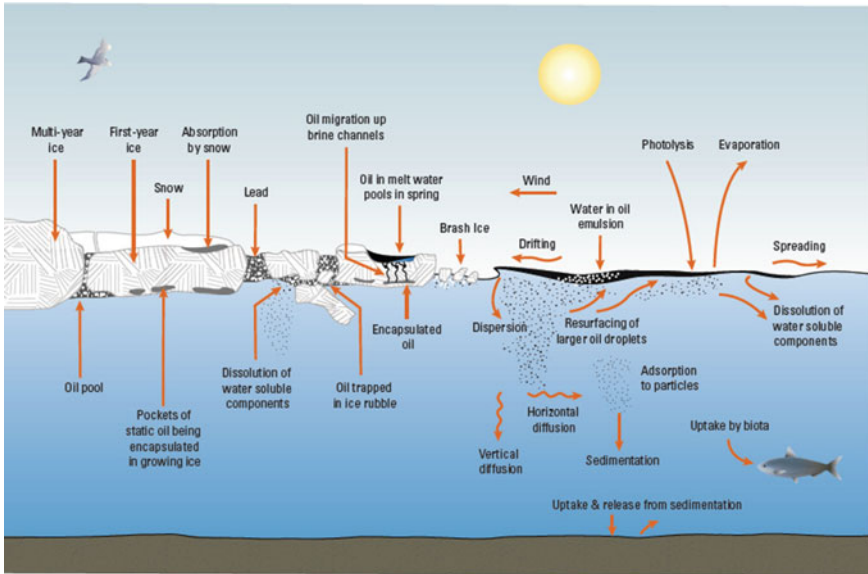


Fig. 2 Scheme of the processes of interaction of oil and ice

of the oil-holding capacity. When oil spills onto the snow cover, it flows down to the ice layer, and then slowly spills over its surface under the snow.

The next important case is an oil spill in cold water. Quite a lot of such research has been done, examining both cold water and pack ice conditions. According to several conclusions of such studies, the equations of oil propagation in warm water do not give a sufficiently accurate prediction in the case of cold viscous oil. Other studies show that in models of oil propagation, one can introduce a correction factor for viscosity or replace the viscosity of oil with the viscosity of water (Buist et al. 2009). It is also noted, that the temperature of the surrounding water may approach the point of the liquidity loss of oil, where the spreading of oil stops (The point of oil's liquidity loss is the temperature at which the oil stops spreading). Due to the higher viscosity the oil slick in cold water is usually thicker and therefore takes up less surface area.

Another unique case is the spread of oil under continuous ice. On this process, both field and laboratory tests were carried out (Chen et al. 1976). Key propagation parameters of oil were identified under laboratory testing. Detailed information, providing a clearer picture of likely propagation dynamics, was obtained through field testing. Even large spills of crude oil under continuous ice cover are usually located at a relatively short distance from the source of the spill, comparing to an open water spill of oil. However, the size of spill is influenced by under-ice currents and the characteristics of the roughness of the ice itself. Nevertheless, in this case, large natural reservoirs can be created in the ice, that the oil slick under the ice is effectively localized over a relatively small area (Fig. 2 <https://www.nap.edu/read/18625/chapter/5>).

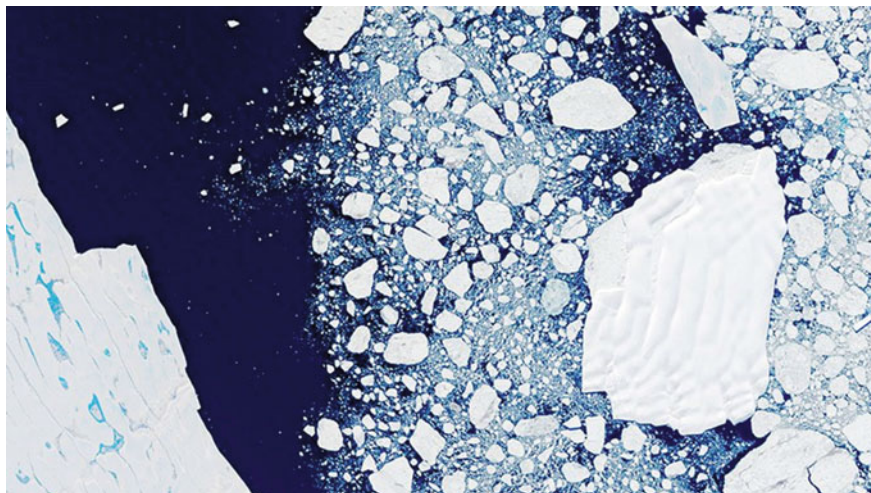


Fig. 3 Dense pack ice provides natural containment of spilled oil

The spread of oil in pack ice is also a crucial process. The studies show a tendency towards less spreading of the oil slick with its higher thickness, in comparison to the oil spreading in the open water. In a situation where the ice concentration exceeds 60–70%, and the ice floes touch each other, the degree of natural localization of the spill increases (Fig. 3). The first documentary confirmation of this phenomenon was made during the study of a series of experimental spills off the coast of Cape Breton Island in 1986 (S.L. Ross Environmental Research Limited and D.F. Dickins Associates Limited 1987). According to the study, the lower the ice concentration, the higher the rate of contamination propagation; when reaching the level of 30% of the ice concentration, the oil slick propagation rate will be practically the same as in open water.

Two full-scale experiments were carried out off the coast in 1989 and 1993. Basing on the results of these tests, it was concluded that with a high concentration of pack ice (which initially reached 90%, but by the end of the experiment had decreased to 70%) the spread of the oil slick was significantly reduced. An important result of the experiment was that the oil spot remained motionless for several days. This was ensured by the combination of factors, low temperatures and damping of waves by the ice, which significantly reduced the oil weathering processes. Additionally, in 2009, during a series of experimental spills in the Norwegian territorial waters of the Barents Sea, it was documented in detail (Singsaas et al. 1994), that under conditions of low temperature and the presence of pack ice, a slower spreading rate of the oil spill, greater slick thickness, and a decrease in oil weathering process are observed.

There are many works devoted to the study of the movement of an oil slick. Oil, spilled on the surface of the ice or/and under it, usually cannot move independently without the ice. In this case oil remains close to the zone of initial contact with ice, and if the ice drifts, the spilled oil will drift along with it too. As various experiments

have shown, for oil movement under the ice surface the flow velocity must be about 5 cm/s for smooth freshwater ice and about 15–30 cm/s for ordinary sea ice (Sørstrøm et al. 2010). Simultaneously, the evidence shows that the speed of currents under winter ice in the Arctic latitudes is usually insufficiently low to move the spilled oil. However, there are exceptions to this observation, such as areas of fjords with strong tidal currents, as well as areas near the deltas of large river systems. Still even in such areas, the irregularities on the lower surface of the ice are sufficient to prevent large-scale spreading or movement of oil.

The study (Sørstrøm et al. 2010) by Buist illustrated that an oil slick, that enters pack ice, usually moves with the ice mass. Considering the conditions of thin pack ice, the oil slick and ice mass can move both at different speeds and in different directions. It is not only low water temperature and the presence of pack ice that reduce the spread and drift rate of the oil slick. The oil slick spreading is also influenced by the processes of evaporation and emulsification, which are slowed down in icy waters too. In addition to these processes, the coastal fast ice should be mentioned: it prevents the oil slick in the sea from reaching the coastline. In some areas, fast ice protects the coast for up to 9 months. Thus, taking into account all the processes, mentioned above, the time for taking effective measures to eliminate hydrocarbon spills increases. All in all, time for response in arctic conditions may be longer than in warmer regions.

At the same time, the properties of the ice itself also affect the degree of spreading of hydrocarbon spills. And an oil slick under one-year-old sea ice and perennial sea ice will behave differently. When oil gets under the one-year growing sea ice, the new ice mass, as the ice grows, will completely cover the oil layer in a short period of time (from several hours to several days, depending on the season). Freezing of oil into ice occurs when the air temperature drops low enough for ice to begin to form. However, if the intensity of the growth of new ice is insufficient, then the oil trapped under the ice may not be covered with ice.

If an oil slick spreading under the ice is frozen into it, then it remains in a closed state until it melts in the spring. It should be noted that during the period when the ice cover is rapidly cooling and growing (for example, in the middle of winter), oil penetration into it is unlikely. As the temperature of the ice rises, the brine that is between the crystals of the sea ice begins to flow downward, leaving vertical channels. Through these channels, oil subsequently rises to the surface (Fig. 2). This effect was also observed in field experiments (Dickins and Buist 1981). The rate of such migration can be very rapid and is temperature dependent. In some experiments, about 50% of the oil initially in the ice fell on its surface (Dickins and Buist 1981). In such a situation, having reached the ice surface, oil begins to float in thawed patches or remains on melting ice floes.

Another process in which frozen oil comes out is ablation. Ablation is the natural melting of ice from the surface downward, driven by evaporation, increased temperatures and wind erosion. Correspondingly, at the moment when ablation reaches the level where ice accumulation took place during the spill, then oil flows to the surface. The ablation process is more likely to yield viscous oils, such as fuel oil and emulsions, because lighter oils tend to weather after freezing. This process of oil migration has also been described in a more recent publication (Dickins et al. 2006).

The oil spilled beneath perennial ice acts a bit different. It lingers because of roughness of ice lower surface, as in the case of the first-year ice. But beneath perennial ice the oil stays more comparing to smooth first-year ice. But in turn, this could lead to formation of separate large accumulations of oil. In some field experiments the thickness up to 19 cm was noticed (Comfort and Purves 1982). Such type of oil will not be heavily eroded. One more difference is that the salt content in old ice is far less, therefore it contains less thawed channels. At the same time channels have smaller diameter. That's why oil migration inside ice surface is slower. So, although the oil spilled beneath perennial ice can appear in thawed patches on the surface of ice, it happens much later at spring season comparing to first-year ice melting.

Cold conditions also affect evaporation, which often plays a prominent role in the natural weathering of a spilled oil after a spill. Oil spilled at subzero temperatures evaporates more slowly than it would at higher temperatures. Moreover, if the spill is covered with snow, the evaporation rate of the oil will decrease even more. Moreover, oil, which is liquid at higher temperatures, can thicken if the ambient temperature falls below its fluidity loss point. The thickened oil, in turn, evaporates very slowly. It is worth noting that oil frozen into the ice cover practically does not evaporate during the winter months, accordingly, when it comes to the ice surface during the spring thaw, the oil will be almost fresh. Cold conditions also affect the emulsification process.

Emulsification is a process of mixing spilled oil and water droplets. As a result, a viscous mixture is formed, which is much more difficult to liquidate, it is less susceptible to weathering, it is much more difficult to burn and collect it mechanically. At the same time, waves and wind contribute to the mixing of water and oil, which leads to the formation of water-oil emulsions. Emulsification has also been observed in laboratory conditions when oil is spilled onto snow and small pieces of ice. Despite the waves influence, natural dispersion of oil slicks is unlikely.

Natural dispersion is a process in which oil droplets under the influence of waves are drawn into the water column, as a result of which the slick practically dissipates on the surface. Such dispersion is possible only in cases of larger debris or under the action of swaying ice floes at their edges, then a temporary dispersion of a certain amount of oil in water can be noted. But more often than not, the bulk of the resulting oil droplets is too large for long-term dispersion. It is also worth noting that the share of the natural dissolution process among all processes is very insignificant. The dissolution rate in cold water is lower than in warmer conditions (Faksness et al. 2011).

Hydrocarbons in the marine environment are also biodegradable. This is the process by which naturally occurring bacteria break down hydrocarbons as a result of their life-course. Oil can be decomposed by atmospheric oxygen (aerobic way), or without oxygen (anaerobic way). At the same time, the biodegradation process reduces the harmful effects of oil on the environment. This is because the relatively water-soluble components, which are the most toxic, decompose first. Biodegradation of hydrocarbons under the influence of microbial populations in natural conditions depends on physical, chemical and biological factors (Margesin and Schinner 2001). It should be noted that bacteria are present in large quantities in a clean

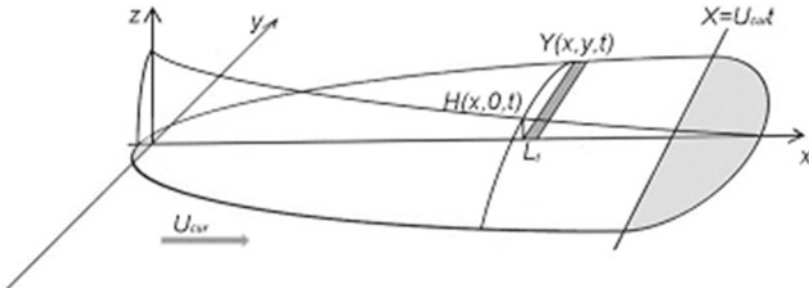


Fig. 4 Scheme of the oil spill on the flow

environment, and the presence of oil compounds only increases their total number, which in turn contributes to a faster elimination of the oil slick. In Arctic waters, local microorganisms exist that survive in both cold waters and high salt conditions. Experiments with such microorganisms have shown that when interacting with them, oil is subject to rather rapid biodegradation (McFarlin et al. 2011a, 2011b; Hazen et al. 2010).

According to the report of the Arctic Council “Assessment of the oil and gas potential of the Arctic”, approximately 80–90% of petroleum hydrocarbons that enter the Arctic environment comes there from their natural outlet to the surface (AMAP Arctic Oil and Gas 2007). Natural outcrops of oil are the largest sources of oil entering the oceans (Kenvolden and Cooper 2003). At the same time, the annual volume of emissions is from 4 to 14 million barrels. It is worth noting that oil undergoes significant biodegradation even before it reaches bottom sediments.

The presence of ice and low temperatures reduce the rate of spread and weathering of spilled oil. Some processes are described and calculated using numerical simulations. The article considers several practically important cases of oil spreading over the ocean surface. To date, there are no ready-made mathematical solutions for them. The proposed approach for estimating the parameters of an oil spill is applied to the problem of oil spreading over a porous surface of ice or snow. Initially, it is assumed that the change in the mass of the spreading substance due to evaporation and the change in the physical parameters of the spreading substance (density and viscosity) can be neglected.

The first case: spreading in a constant flow with a constant intensity. The spread of an oil slick, when it hits the sea surface, is determined by the processes of transfer by surface currents and spreading due to buoyancy forces. In turn, the flow is the reason for the formation of an elongated extended shape of the oil slick. Further, it is assumed that in the main part of the pollution area, excluding the “head” and “tail” of the extended spill, which are indicated in gray in (Fig. 4), the spreading will take place only in the direction perpendicular to the oil transport by the current.

It is assumed that oil is supplied with constant intensity Q to the surface of water moving relative to a stationary source of oil discharge at a speed U_{cur} . The coordinate system is chosen so that the source is at the origin, the O_y axis is directed along the

surface current velocity, and the Oy axis in the perpendicular direction V_1 is the volume of oil that is poured onto the sea surface in the amount of Qt_1 during time t_1 . Accordingly, in the direction of the main flow, such an elementary volume of oil will have the size $L_1 = U_{cur}t_1$. The equations of motion of oil spreading over the water surface are written in the form:

balance of buoyancy force and friction force in the Oy direction

$$\rho_{oil}gH \frac{\partial H}{\partial y} = -\beta u^p \tag{1a}$$

balance of oil mass in each element of the highlighted band

$$\frac{\partial H}{\partial y} + div(Hu) = 0 \tag{1b}$$

integral oil balance in the strip

$$L_1 \int_0^y H(x, y, t)dy = \frac{1}{2}V_1 \tag{1c}$$

Then, by transformations, a formula is derived for calculating the growth of the spot size in the direction perpendicular to the velocity of the main flow. Growth will vary according to a power law, and the spot area $A(t)$ will be determined as:

$$A(t) \approx 2 \int_0^X Y(x)dx = 2 \frac{2p+3}{p+3} \left(\frac{1}{4}\right)^{\frac{1}{p+3}} \left[\frac{\rho_{oil}gQ^2}{\beta}\right]^{\frac{1}{p+3}} U^{\frac{p+1}{p+3}} t^{\frac{2p+3}{p+3}} \tag{2}$$

In this way, with “linear” friction of oil on water, at $p = 1$, the dependence of the spill area on time and flow rate will be expressed as:

$$A(t) \begin{cases} U^{\frac{1}{2}} t^{\frac{5}{4}} n p u & p = 1 \\ U^{\frac{3}{5}} t^{\frac{7}{5}} n p u & p = 2 \end{cases} \tag{3}$$

With a linear dependence of friction on the difference in oil-water velocities, the growth of the slick area $A(t)$ is determined by the dependence $A \sim t^{\frac{5}{4}}$, and with a quadratic dependence, it is slightly faster, according to the law $A \sim t^{\frac{7}{5}}$. This is explained by the fact that at small oil-water velocity differences, in the case of square friction, spreading will be faster.

The next case is spreading with constant intensity in the absence of currents. In this case, the source of the discharge ensures the flow of oil to the surface with a constant intensity Q_0 . In the absence of flows, it can be assumed that the spreading will be axisymmetric. Then the balance of the forces of gravity and friction will be

written as

$$\rho_{oil} g H \frac{\partial H}{\partial r} = -\beta u^p \quad (4)$$

By means of transformations, formulas for the radius $R(t)$ and area $A(t)$ of the spot are written, depending on time for a constantly operating source

$$A(t) = \pi R^2 \approx \pi \left[\frac{\rho_{oil} g Q^2}{\beta} \right]^{\frac{2}{p+5}} t^{2(\frac{2+p}{5+p})} \quad (5)$$

$$R(t) = \left(\frac{p+5}{p+2} \right)^{\frac{p}{p+5}} \left[\frac{1}{\pi^2} \frac{(p+2)^2}{p+1} \right]^{\frac{1}{p+5}} \left[\frac{\rho_{oil} g Q^2}{\beta} \right]^{\frac{1}{p+5}} t^{\frac{p+2}{p+5}} \quad (6)$$

The has also been considered a case of spreading onto a stationary snow-ice cover. It was the radially symmetric spreading of a fixed volume of oil V_0 over the horizontal surface of a porous snow-ice massif for low Reynolds number. In a quasi-stationary regime, when the spreading is due to the balance of the forces of viscous friction and gravity. On a solid substrate, the boundary condition at the interface is that the horizontal velocity is zero, that is, the adhesion condition. Taking into account the assumptions made, the momentum balance equation integrated over the vertical coordinate is written in the form

$$g \frac{\partial H}{\partial y} \approx -v \frac{u}{H^2} \quad (7)$$

Next, the maximum spill radius is calculated

$$R_m = K_R \left(\frac{g}{\nu u_f} \right)^{\frac{1}{10}} V(0)^{\frac{2}{5}} \quad (8)$$

This estimate was obtained on the assumption that there is no heat transfer between the spreading substance and the underlying substrate, and also without taking into account the decrease in oil volume due to evaporation.

In the case of spreading onto a moving snow-ice cover, the results above are used to estimate the parameters of the oil spill flowing onto the moving ice. Such a situation can be imagined, for example, when an emergency well is flowing from the deck of a production platform, past which an ice field is drifting. By analogy with an oil spill on the sea surface during a current, the volume of oil flowing out of a source over time t_1 defined as $V_1(t) = H(t)Y L_1$, where $L_1 = Ut_1$. Oil flow is considered in areas located at some distance from the “head” and “tail” of the spill, it is considered that spreading occurs only in the direction which is perpendicular to the movement of the ice field (transverse direction). Further, taking into account the fact that spreading over a solid porous substrate is described similarly to (7)

$$g \frac{\partial H}{\partial y} \approx -v \frac{u}{H^2} \quad (9)$$

As a result, the time of cessation of spreading in the transverse direction is displayed.

$$t_m = \left[\left(\frac{6}{a} \right) \left(\frac{Q}{U} \right)^{\frac{2}{3}} \right]^{\frac{5}{6}} = \left(\frac{6}{a} \right)^{\frac{5}{6}} \left(\frac{Q}{U} \right)^{\frac{5}{6}} \quad (10)$$

and the limiting size in the transverse direction is determined as

$$Y_m \approx 6^{\frac{1}{6}} \left(\frac{g}{v u_f} \right)^{\frac{1}{6}} \left(\frac{Q}{U} \right)^{\frac{3}{6}} \quad (11)$$

The formulas for the time of cessation of spreading on a porous surface and the maximum size of the contaminated underlying substrate were obtained in many ways similar to Fay's formulas (Fay 1969, 1971; Hoult 1972) using the results of Nihoul (1984). Simplification of the equations of motion, that is, the reduction of the system of equations of hydrodynamics to the balance of only two "main" forces, makes it possible, as a result, to obtain estimates of the spill parameters with sufficient accuracy for solving practical problems. In obtaining these estimates, the weathering processes were not considered. When analyzing oil spills in the sea of long duration (in the case when the current velocity cannot be considered constant throughout the entire period of the pollution process), these assessments are useful from the point of view of the possibility of considering a long-term oil spill as a superposition of its separate parts, formed sequentially in the accident area, taking into account the current velocity at the time of oil hitting the sea surface.

It should be noted that in the Arctic conditions there are both disadvantages in terms of effective response to various accidents associated with the leakage of hydrocarbons, and obvious advantages, such as: biodegradation, decomposition of hydrocarbons under the influence of bacteria in any marine environment, which is a natural process that reduces the level the harmful effects of oil emissions on the environment, and of course the low temperature, which slows down the process of oil slick stretching, as well as pack ice, which localizes and restrains the oil slick. It is also noteworthy that oil frozen into the ice during the period of its freezing tends to return to the surface during spring thawing, under the influence of migration or ablation processes. At the same time, the dynamics of frozen oil that got into the water as a result of the spring melting of ice differs only slightly from the dynamics of oil spilled in open water.

Acknowledgements The work was carried out with the financial support of the project of the Russian Federation represented by the Ministry of Education and Science of Russia № 075-15-2020-802.

References

<https://www.nap.edu/read/18625/chapter/5>

- AMAP Arctic Oil and Gas 2007 (2007) Report to the Arctic monitoring and assessment programme (AMAP), P.O. Box 8100, Dep., N-0032 Oslo, Norway (www.amap.no). Bobra AM, Fingas MF (1986) The behavior and fate of arctic oil spills. *Water Sci Technol* 18(2):13-23
- Buist I, Belore R, Dickins D, Guarino A, Hackenberg D, Wang Z (2009) Empirical weathering properties of oil in ice and snow. In: Proceedings Arctic and marine oilspill program (AMOP) technical seminar no 32, vol 1. Environment Canada, Ottawa, Canada, pp 67–107
- Chen EC, Keevil BE, Ramseier RO (1976) Behaviour of crude oil under fresh-water ice. *J Can Pet Technol*
- Comfort G, Purves W (1982) The behaviour of crude oil spilled under multi- year ice. Environmental Protection Service Report EPS 4-EC-82-4. Environment Canada, Ottawa, Canada
- Dickins DF, Buist IA (1981) Oil and gas under sea ice study, vol 1&2. Prepared by Dome Petroleum Ltd. for COOSRA, Report CV-1, Calgary, AB, Canada (also published In: Proceedings 1981 international oil spill conference, Atlanta GA, USA)
- Dickins DF, Brandvik PJ, Bradford J, Faksness L-G, Liberty L, Daniloff R (2008) Svalbard 2006 experimental oil spill under ice: remote sensing, oil weathering under Arctic conditions and assessment of oil removal by in-situ burning. In: Proceedings 2008 international oil spill conference. American Petroleum Institute, Washington, DC, USA
- Fay JA (1969) The spread of oil slicks on a calm sea. In: Hoult DP (ed) *Oil on the sea*. Plenum Press, New York, pp 53–63
- Fay JA (1971) Physical processes in the spread of oil on a water surface. In: Proceedings of international conference on prevention and control of oil spills, Washington DC, USA, vol 1971(1), pp 463–467
- Faksness L-G, Brandvik PJ, Daae RL, Leirvik F, Borseth JF (2011) Large-scale Oil-in-ice Experiment in the Barents Sea: Monitoring of oil in water and MetOcean interactions. *Mar Pollut Bull* 62(2011):976–984
- Fingas MF, Hollebone BP (2003) Review of behaviour of oil in freezing environments. *Mar Pollut Bull* 47:333–340
- Hazen TC, Dubinsky EA, DeSantis TZ, Andersen GL, Piceno YM, Singh N, Jansson JK, Probst A, Borglin SE, Fortney JL, Stringfellow WT, Bill M, Conrad ME, Tom LM, Chavarria KL, Alusi R, Lamendella R, Joyner DC, Spier C, Baelum J, Auer M, Zemla ML, Chakraborty R, Sonnenthal EL, D'haeseleer P, Ying H, Holman N, Osman S, Lu Z, Nostrand JDV, Deng Y, Zhou J, Mason OU (2010) Deep-sea oil plume enriches indigenous oil-degrading bacteria. *Science* 330:204–208
- Hoult DP (1972) Oil spreading on the sea. *Ann Rev Fluid Mech* 4:341–368
- Kenvolden KA, Cooper CK (2003) Natural seepage of crude oil into the marine environment. *GeoMarine Lett* 23:140–146
- Margesin R, Schinner F (2001) Biodegradation and bioremediation of hydrocarbons in extreme environments. *Appl Microbiol Biotechnol* 56:650–663
- McFarlin KM, Leigh MB, Perkins R (2011a) Indigenous microorganisms degrade oil in Arctic seawater (poster). In: Proceedings of the 2011 international oil spill conference, Portland, OR, USA, 1 p
- McFarlin KM, Perkins RA, Gardiner WW, Word JD (2011b) Evaluating the biodegradability and effects of dispersed oil using arctic test species and conditions: phase 2 activities. In: Proceedings of the 34th Arctic and marine oilspill program (AMOP) technical seminar on environmental contamination and response, Calgary, AB. Environment Canada, Ottawa, Ontario, Canada
- Nihoul CJJ (1984) A non-linear mathematical model for the transport and spreading of oil slicks. *Ecol Model* 22(1-4):325–339
- Reed M, Johansen O, Brandvik PJ, Daling P, Lewis A, Fiocco R, Mackay D, Prentki R (1999) Oil spill modeling towards the close of the 20th century: overview of the state-of-the-art. *Spill Sci Technol Bull* 5:3–16

- Singsaas I, Brandvik PJ, Daling PS, Reed M Lewis A (1994) Fate and behaviour of oils spilled in the presence of ice - a comparison of the results from recent laboratory, meso-scale flume and field tests. In: Proceedings Arctic and marine oilspill program (AMOP) technical seminar, no 17, vol 1. Environment Canada, Ottawa, Canada, pp 355–370
- SL Ross Environmental Research Limited and DF Dickins Associates Limited (1987) Field research spills to investigate the physical and chemical fate of oil in pack ice. Environmental Studies Research Funds. Report no. 062. ESRF, Calgary
- Sørstrøm SE, Brandvik PJ, Buist I, Daling P, Dickins D, Faksness L-G, Potter S, Fritt Rasmussen J, Singaas I (2010) Joint industry program on oil spill contingency for Arctic and ice-covered waters: summary report. SINTEF report A14181. SINTEF, Trondheim, Norway. www.sintef.no/Projectweb/JIP-Oil-In-Ice/Publications
- Стивенн П, Иан Б, Кен Т, Дэвид Д, Эд О (2013) Ликвидация разливов нефти на арктическом шельфе. Exxonmobil

Study of Undercurrents in the Black Sea Northeastern Part by Using Numerical Simulation and Observation Data



S. G. Demyshev, N. V. Markova, and O. A. Dymova

Abstract Based on the numerical MHI model of 1.6 km horizontal resolution, a prognostic experiment was carried out to reconstruct the circulation of the Black Sea in 2011. The temperature and salinity profiling data of ARGO floats obtained for this year are used to validate the calculations results. As well, the simulation results are agreed with the data of deep-water measurements of the current velocity in June 2011 in the region of the North Caucasian coast (northeastern part of the Black Sea). The qualitative and quantitative characteristics of the deep-water currents in the northeastern part of the Black Sea are obtained.

Keywords The Black Sea · Modeling · Undercurrents · Observation data

1 Introduction

In recent decades, the structure of the Black Sea hydrophysical fields has been actively studied using contact measurements, remote sensing, numerical modeling, analytical as-assessments, etc. However, the most observations and other studies were carried out within the upper 300 m layer of the sea. The existence of intensive currents and eddies in the 0–200 m layer was confirmed. At the same time, concepts of the deep-water currents structure are rather general. There is no complete clarity even in the issue of the integral direction of deep-water circulation. A number of works indicates the existence of currents in the deep layers of the Black Sea, directed oppositely to the surface circulation. Thus, in research (Poulain et al. 2016) with using ARGO data, the anticyclonic circulation in the eastern part of the Black Sea is found out at depths of more than 400 m. Long-term (about a year) measurements of the current velocity by moored ADCP at the continental slope zone at a depth of 1700 m in the central part of the Black Sea showed a change of the current direction on time scales of the order of several weeks and velocities up to 13 cm/s (Klyuvitkin et al. 2019). Anticyclonic currents were obtained by simulation the climatic fields of the Black Sea (Demyshev et al. 2009) on a 5 km grid with assimilation of averaged

S. G. Demyshev · N. V. Markova (✉) · O. A. Dymova
Marine Hydrophysical Institute of RAS, Sevastopol, Russian Federation

hydrological temperature and salinity in the model, as well as, in Markova (2018) where the processing of a long-term reanalysis data (Dorofeev and Sukhikh 2016) obtained with assimilation of the altimetric sea level is carried out.

The aim of this study is to investigate the deep-water currents in the Black Sea northeastern part. For this purpose, the three-dimensional structure of currents in the Black Sea is reconstructed using a numerical MHI model (model of the Marine Hydrophysical Institute of RAS) with a high resolution of 1.6 km horizontally, without assimilation of observations in the model (prognostic experiment). The obtained results are compared with velocity measurements available for summer 2011 in the northeastern part of the sea. The results of the numerical experiment are validated using autonomous profiling floats ARGO observation data of temperature and salinity, which significantly exceed the data of single experiments on current velocity observations.

2 Numerical Model

A three-dimensional eddy-resolving MHI model is used (Demyshev and Korotaev 1992; Demyshev 2012) for the numerical analysis of the Black Sea circulation. The model is based on a complete system of equations of ocean thermohydrodynamics in the Boussinesq and hydrostatic approximations. The finite-difference system of equations is approximated on a C-grid and has the second order of accuracy in spatial variables (up to a non-uniform step). The model implements a «leap-frog» scheme for approximation in time, a semi-implicit representation for pressure, and a TVD-scheme (Harten 1983) for approximating advective terms in the heat transfer and salt transfer equations. A biharmonic operator with a coefficient of 10^{-16} cm⁴/s is used to describe horizontal turbulent diffusion and viscosity in the equations for the transfer of momentum, heat and salt. Vertical turbulent processes are parameterized on the basis of the Mellor-Yamada 2.5 theory (Mellor and Yamada 1982), river runoff and water exchanges through the straits are taken into account. The spatial resolution of the model is 1.6 km horizontally; 27 z-horizons are preset vertically.

Data on atmospheric forcing in 2011 were obtained using the SKIRON/Eta model (NonHydrostatic SKIRON/Eta Modelling System) with resolution of 0.1° in latitude and longitude. Fields of wind velocity at a height of 10 m, fluxes of long-wave radiation, sensible and latent heat, solar short-wave radiation, precipitation and evaporation fluxes, and sea surface temperature are considered. Processing of these arrays is carried out in order to bring the SKIRON units in accordance with the dimension of the model parameters. Components of the wind velocity vector are recalculated into the components of the wind stress vector according to the aerodynamic formula (Large and Pond 1981). The basin bathymetry is based on a 1/8-min horizontal resolution depth array provided by the European Marine Observation and Data Network (EMODnet). Climatic fields of the Black Sea circulation on January 1, calculated with the assimilation of the data of long-term averaged observations of temperature and salinity on a 5 km grid (Demyshev et al. 2009), are used as initial fields. All boundary

and initial fields are linearly interpolated into the model grid nodes. The procedure of adjusting of the hydrophysical and atmospheric fields with a fixed atmospheric forcing is performed before the calculation. When the spatial-integral divergence of the horizontal velocity, which characterizes the proximity of the velocity to the geostrophic one, decreases by an order of magnitude, it is considered that hydrophysical fields are adapted to atmospheric forcing. Modeling of the Black Sea circulation is carried out for one year (2011). Fields of sea level, salinity, temperature and current velocity are obtained for each day.

3 Validation

Since in 2011 the data on current velocity measured at horizons deeper than 500 m are available only at one point, the modeling results are confirmed by using data of ARGO floats, which make profiles from horizons of at least 500 m to the surface. We reviewed 377 deep-water profiles of temperature and salinity provided by the ARGO project (<http://www.argodatamgt.org>; floats no. 7900465, 7900466, 1901200, 6900803, 6900804, 6900805) which were mainly performed in the abyssal part of the Black Sea during the year. To compare the modeled and measured temperature and salinity, for each float the root-mean-square deviation (RMSD) is calculated in the typical layers of the Black Sea with average interval corresponding to the operating time of the float in 2011. Table 1 shows the temperature and salinity RMSDs obtained as arithmetic mean for all mentioned floats in appropriate layers. The highest RMSD-temperature value of 0.386 °C is found in the upper mixed layer at a depth of 5–30 m, the maximum salinity RMSD of 0.326 ‰—in the layer of permanent halocline (depth 30–100 m). The minimum RMSDs of both temperature and salinity are observed at horizons deeper than 300 m with satisfactory accuracy.

Table 1 RMSDs of model temperature and salinity from ARGO floats data

Depth, m	RMSD temperature, °C	RMSD salinity, ‰
0–5	0.182	0.177
5–30	0.386	0.172
30–100	0.242	0.326
100–300	0.112	0.231
300–800	0.013	0.091
800–1500	0.027	0.007

4 Results

To assess the spatial variability of the velocity field in the northeastern part of the Black Sea, the current maps at different horizons are analyzed. The dynamics in the upper 300-m layer is determined by the Rim Current propagating along the continental slope and directed in this area to the northwest. The current velocity on the sea surface reaches 40 cm/s in winter; the current intensity decreases and the mainly anticyclonic mesoscale eddies are formed between it and the coast in the warm season. At depths of more than 1000 m, approximately between 34.5 and 41° E, there is a deep current (undercurrent) directed to the southeast oppositely to the surface currents. The undercurrent is generated in April south of Cape Meganom, where a significant narrowing of the continental slope leads to increase of current velocities. Formed as a continuous narrow stream, the undercurrent is detected from late May to August. The maximum velocities of the undercurrent up to 10 cm/s are found toward south of the coast of Abkhazia. As an example, Fig. 1 shows the velocity field in the northeastern part of the sea at the horizons of 300 m (Fig. 1a) and 1100 m (Fig. 1b). It is seen that the direction of the undercurrent is opposite to the direction of the currents in the upper layer.

A field experiment was performed to measure current velocity profiles and other parameters of seawater using the «Aqualog» probe complex (Ostrovskii et al. 2013) on June 17–19, 2011 at the Gelendzhik Black Sea test site of the Institute of Oceanology of RAS. The measurements were carried out in the deep-water part of the continental slope at the point (44°28'17" N, 37°56'14" E), the maximum depth of measurements was 1020 m. There was a significant decrease in velocity at horizons of 100–150 m, and the currents were almost absent at depths of 200–400 m. In the course of the measurements, “a deep southeastern countercurrent was recorded, the core of which (velocity up to 0.03 m/s) lies in a layer of 700–850 m” [13, p. 9, fig. 5]. Our calculations of the current velocity obtained in the numerical experiment are generally in agreement with these observations. In Fig. 2 the profiles of the model current velocity are shown at the model grid node (44°23'24" N, 37°51'36" E) closest

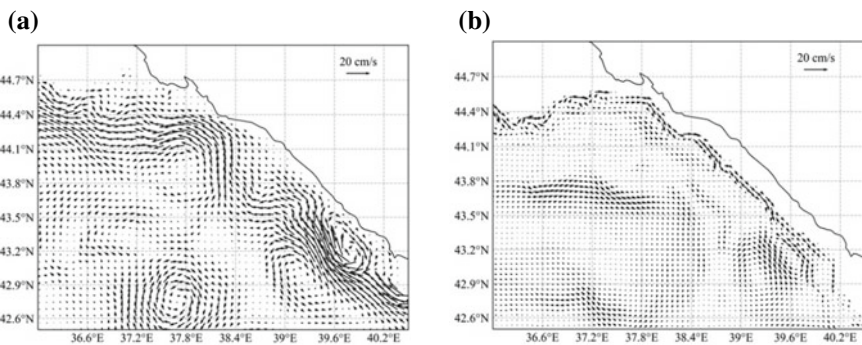


Fig. 1 Current velocity field on June 16, 2011: **a**—depth of 300 m; **b**—depth of 1100 m

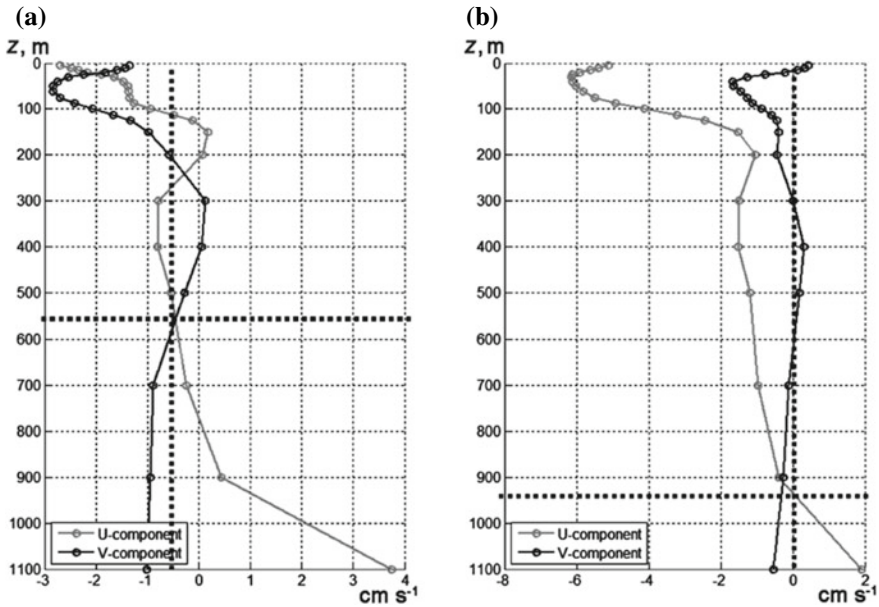


Fig. 2 Model profiles of the current velocity components at point (44°23'24'' N, 37°51'36'' E): **a**—June 16, 2011; **b**—June 20, 2011

to the probe point. It is seen that in period of the field experiment, the change in the direction of the model velocity occurred some deeper than observed by «Aqualog» data (Fig. 2a), and only after a few days the profile of the model currents became close to the observed one (Fig. 2b). Thus, the phase shift between the model and observed data is determined, amounting to several days. The horizontal dash-line in this figure denotes the depth of the appearance of the southeastern deep-water undercurrent ($U > 0, V < 0$) with velocities from 2 to 4 cm/s.

Analysis of the direction of the current velocity vectors in the area of the Gelendzhik test site during 2011 shows that the undercurrents directed to the southeast are observed at depth of 1100 m near the continental slope in all seasons. In Fig. 3 the timing charts of the current velocity vectors at the point (44°23'24'' N, 37°51'36'' E) on horizons of 300 m and 1100 m are shown. The average velocities of the deep undercurrents in this region are reached 5–7 cm/s, lifetime—from several days to 4–5 weeks, width—5–8 km. It should be noted that undercurrents reach their maximum intensity during the Rim Current weakening, when the average velocity near the surface are less 25–30 cm/s.

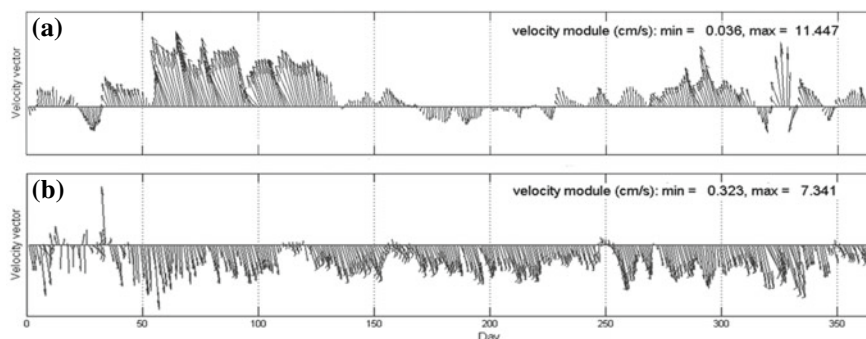


Fig. 3 Model current vectors at point ($44^{\circ}23'24''$ N, $37^{\circ}51'36''$ E) during 2011: **a**—depth of 300 m; **b**—depth of 1100 m

5 Conclusion

In this work the three-dimensional fields of the Black Sea currents in 2011 are simulated by using of the MHI model prognostic version on 1.6 km grid. The calculation results are validated by temperature and salinity data of ARGO profiling floats. Analysis of current velocity fields in the northeastern part of the sea and their comparison with the velocity data obtained during the field experiment with the «Aqualog» probe complex shows the existence of deep undercurrents along the continental slope in the region. The direction of undercurrents is opposite to the direction of surface circulation. Similar undercurrents were obtained on a 5 km grid when the Black Sea climate was calculated (Demyshev et al. 2009), as well as in study (Markova 2018) based on the processing of long-term reanalysis data for 1992–2012 (Dorofeev and Sukhikh 2016) with assimilation of altimetric sea level. In mentioned works, the Black Sea undercurrents were of a quasiperiodic character and observed at depths of more than 300 m, mainly in the spring and summer periods, but they were some wider and slower in comparison with the present results. The use of high-resolution model makes it possible to detail the scales of deep currents and compare them with the available velocity observations.

Thus, the presence of the undercurrents in the region of the North Caucasian coast in the summer of 2011 is proved. Its characteristics calculated in the present work for the period of 2011 and confirmed by the «Aqualog» data must be compared with subsequent field observations, which are desirable for long-term intervals, but at least in the spring and summer.

There are a number of assumptions explaining the possibility of the forming of such currents in the literature. Thus, a number of authors point to the possibility of generating undercurrents propagating along the depth slope in the anticyclonic direction, as a result of low-frequency wave processes under the main pycnocline in the Black Sea. The generation of such currents at horizons of more than 300 m is indicated, for example, in Morozov et al. (2017).

The formation of deep undercurrents can also be associated with the passage of mesoscale eddies near the continental slope (Zatsepin et al. 2016), which act both directly as generators of narrow currents between the eddy periphery and the continental slope, and change the slope of isopycnic surfaces. As a result, internal waves and gradient currents can also be generated. Similar undercurrents could be associated with the passage of mesoscale anticyclonic eddies near the shelf zone boundary were previously noted for other regions of the World Ocean, for example, for the western coast of the Bay of Bengal (Francis et al. 2020). Features of stratification and bottom topography also play an important role in deep-sea processes. Due to insufficiency of the field data, it is difficult to specify the only reason of irregular currents in deep layers of the Black Sea. To elucidate the causes and mechanisms of deep-water anticyclonic currents in the Black Sea and to determine the dominant forcing factor, a much larger number of observational data and further studies are required.

Acknowledgements Present work was carried out within the framework of the State assignment (theme № 0555-2021-0003).

References

- Demyshev SG (2012) A numerical model of online forecasting Black Sea currents. *Izv. Atmos Ocean Phys* 48(1):120–132. <https://doi.org/10.1134/S0001433812010021>
- Demyshev SG, Ivanov VA, Markova NV (2009) Analysis of the Black Sea climatic fields below the main Pycnocline obtained on the basis of assimilation of the Archival data on temperature and salinity in the numerical Hydrodynamic model. *Phys Oceanogr* 19(1):1–12. <https://doi.org/10.1007/s11110-009-9034-x>
- Demyshev SG, Korotaev GK (1992) Numerical energy-balanced model of the baroclinic ocean currents on a C-grid. In: Numerical models and results of calibration calculations of currents in the Atlantic Ocean. INM RAS, Moscow. pp 163–231 (in Russian)
- Dorofeev VL, Sukhikh LI (2016) Analysis of variability of the Black Sea hydrophysical fields in 1993–2012 based on the reanalysis results. *Phys Oceanogr* 1:33–47. <https://doi.org/10.22449/1573-160X-2016-1-33-47>
- EMODnet. <http://portal.emodnet-bathymetry.eu>
- Francis PA, Jithin AK, Chatterjee A et al (2020) Structure and dynamics of undercurrents in the Western boundary current of the Bay of Bengal. *Ocean Dyn* 70:387–404. <https://doi.org/10.1007/s10236-019-01340-9>
- Harten A (1983) High resolution schemes for hyperbolic conservation laws. *J Comput Phys* 49(3):357–393
- Klyuvitkin AA, Ostrovskii AG, Lisitzin AP, Konovalov SK (2019) The energy spectrum of the current velocity in deep layers of the Black Sea. *Dokl Earth Sc* 488(2):1222–1226. <https://doi.org/10.1134/S1028334X1910012X>
- Large WG, Pond S (1981) Open ocean momentum Flux measurements in moderate to strong winds. *J Phys Oceanogr* 11(3):324–336. [https://doi.org/10.1175/1520-0485\(1981\)011%3c0324:OOMFMI%3e2.0.CO;2](https://doi.org/10.1175/1520-0485(1981)011%3c0324:OOMFMI%3e2.0.CO;2)
- Markova NV (2018) Variability of the Black Sea deep-water hydrophysical reanalysis results. *IOP Conf Series J* 1128:012145. <https://doi.org/10.1088/1742-6596/1128/1/012145>

- Mellor GL, Yamada T (1982) Development of a turbulence closure model for geophysical fluid problems. *Rev Geophys* 20(4):851–875. <https://doi.org/10.1029/RG020i004p00851>
- Morozov AN, Lemeshko EM, Shutov SA et al (2017) Structure of the Black Sea currents based on the results of the LADCP observations in 2004–2014. *Phys Oceanogr* 1:25–40. <https://doi.org/10.22449/1573-160X-2017-1-25-40>
- NonHydrostatic SKIRON/Eta Modelling System. <http://forecast.uoa.gr/forecastnewinfo.php>
- Ostrovskii AG, Zatspein AG, Soloviev VA et al (2013) Autonomous system for vertical profiling of the marine environment at a moored station. *Oceanology* 53(2):233–242. <https://doi.org/10.1134/S0001437013020124>
- Poulain PM, Menna M, Zu Z (2016) Geostrophic currents in the Mediterranean and Black Seas derived from Argo float profiles. Argo-Italy Project. <https://www.researchgate.net/publication/308983483>
- Zatspein AG, Elkin DN, Korzh AO et al (2016) On influence of current variability in the deep part of the Black Sea upon water dynamics of the North-Caucasian narrow shelf. *Phys Oceanogr* 3:14–22. <https://doi.org/10.22449/1573-160X-2016-3-14-22>

Modeling Group Structure of the Sea Surface Waves



P. Shumeiko  and A. Yu. Abramovich 

Abstract The group structure of sea waves is one of the main properties of sea surface waves, which must be taken into account when solving both fundamental and applied problems. The nonlinearity of sea waves is weak, but it has a significant effect on wave dynamics. When modeling the group structure, it is necessary to simultaneously take into account the asymmetry of the wave profile. In this work, on the basis of numerical modeling, methodological features of calculating the characteristics of the group structure of sea surface waves using the SIWEH (Smoothed Instantaneous Wave Energy History) function are analyzed. The difference between the groupiness factors calculated by the a priori given nonlinear model of the wave profile and by the SIWEH function constructed for this profile is shown. The influence of the group structure of sea waves on the skewness coefficient is also shown.

Keywords Sea surface · Wave groups · Groupiness factor · Skewness · SIWEH function · Nonlinear random wave

1 Introduction

Currently, there is great interest in the work related to the study of the group structure of surface waves, which is primarily related to the solution of practical problems. Regular and grouped waves have different effects on ships, breakwaters, sediment accumulation, coastal erosion, and beach formation (Johnson et al. 1978; Medina et al. 1994; Baldock et al. 2011; Haller and Dalrymple 1995). Despite the fact that the effects created by the group structure have been known for a long time, they are still poorly taken into account in engineering calculations. One of the problems associated with the inclusion of these models in engineering calculations, as noted in the review (Medina and Hudspeth 1990), is associated with the variety of theories and parameters characterizing the group structure, as well as the complexity of their determination. The group structure is also associated with the appearance of abnormally high waves, the height of which is more than twice the significant height (Fedele 2007).

P. Shumeiko (✉) · A. Yu. Abramovich
Sevastopol State University, Sevastopol, Russian Federation

Sea waves are a random nonlinear process. There are several approaches to calculating the characteristics of the envelope sea waves group. The most widely used methods are based on the Hilbert transform (Kosyan et al. 2003; Presnukhin 2009), as well as on the basis of the SIWEH (Smoothed Instantaneous Wave Energy History) function introduced in Funke and Mansard (1979). This paper analyzes the second approach.

The displacement of the weakly nonlinear wave train envelope can be described by the nonlinear Schrödinger equation, which's solution is describing using the second-order Jacobi elliptic function in the case of a steady-state regime (Yuen and Lake 1982; Pokazeev et al. 2015). The complexity of the expression's analysis, including special functions, an opaque connection with integral parameters describing the group structure, stimulated the construction and analysis of simpler analytical models (Shumeyko et al. 2018).

The main parameter that characterizes the group structure of surface waves is the groupiness factor (GF), which determines the depth of wave height modulation in the group (Mase 1989; Ma et al. 2011). In this paper, analytical models describing the group structure of sea waves using elementary functions are used to analyze its variability.

2 Characteristics the Group Structure of Waves

Let the function $\xi(t)$ describe the wave changing in the sea surface level at a fixed point. The average value of $\xi(t)$ is zero. The SIWEH function, $E(t)$, is expressed as follows (Funke and Mansard 1979).

$$E(t) = \frac{1}{T_p} \int_{-\infty}^{\infty} \xi^2(t + \tau) Q(\tau) d\tau, \quad (1)$$

where t is time; $Q(\tau)$ is the low-frequency filter; $T_p = 1/f_0$ is the period of dominant waves; f_0 is the frequency [Hz] of the maximum of the wave spectrum. As a rule, the filter has the form.

$$Q(\tau) = \begin{cases} 1 - |\tau|/T_0 & \text{if } |\tau| \leq T_0 \\ 0 & \text{if } |\tau| > T_0 \end{cases}, \quad (2)$$

Thus, SIWEH function is a quadratic waveform smoothed by the Bartlett filter (2). It can be considered as a measure of the instantaneous wave is energy in a time signal.

The wave spectrum of the sea waves is a narrow-band function of frequency. Therefore, the use of low-frequency filter other than the Bartlett filter has little effect on SIWEH function (Shumeyko et al. 2018).

With the help of SIWEH function, the GF is defined as (Mase 1989).

$$GF_{SIWEH} = \frac{1}{\overline{E}} \sqrt{\frac{1}{T_w} \int_0^{T_w} [E(t) - \overline{E}]^2 dt}, \quad (3)$$

where T_w is duration of the excitement recording,

$$\overline{E} = \frac{1}{T_w} \int_0^{T_w} E(t) dt. \quad (4)$$

In a situation where the shape of the envelope a priori is known, the GF can be defined as (List 1991).

$$GF_L = \sqrt{2}S / H, \quad (5)$$

where H is the average value of the envelope; S is the standard deviation of the envelope from its mean. The higher GF value, more clearly expressed the group structure, if $GF = 0$, then the group structure is absent.

3 Modeling the Group Structure of Waves

Sea waves are a random weakly nonlinear process. As a consequence, the distributions of elevations and slopes of the sea surface deviate from the Gauss distribution (Zapevalov and Ratner 2003; Longuet-Higgins 1963; Phillips 1961). Deviations from the Gaussian distribution are small, as indicated by the measurement data of the higher cumulants (Babanin and Polnikov 1995; Zapevalov et al. 2011; Zapevalov 2011), but they have a significant effect on the wave dynamics. The crest of the wave is more pointed than its trough. Note that the asymmetry of the wave profile, as well as the group structure, must be taken into account when analyzing the impact of sea waves on ships and coastal structures (Song et al. 2000; Agarwal and Manuel 2009). This means that when modeling the group structure, it is necessary to simultaneously take into account the deviations of the skewness coefficient from the zero value.

Traditionally, the group structure of sea waves is described in the carrier wave $\eta(x, t)$ product form of the and its envelope $G(x, t)$. We define the wave profile by a simple analytical function (Shumeyko et al. 2018).

$$\xi(x, t) = A G(x, t) (\eta(x, t) - \overline{\eta(x, t)}), \quad (6)$$

where A is the parameter that determines the wave heights; x is spatial coordinate; the bar above means averaging. The envelope $G(x, t)$ and carrier wave $\eta(x, t)$ are given as.

$$G(x, t) = \exp\left[-\rho_1 \cos^2\left(\frac{k_0 x - (\omega_0/2)t}{2\rho_2}\right)\right], \quad (7)$$

$$\eta(x, t) = \exp\left[-\rho_0 \cos^2\left(\frac{k_0 x - \omega_0 t}{2}\right)\right], \quad (8)$$

where k_0 and $\omega_0 = 2\pi f_0$ is the wave number and cyclic frequency of the carrier (dominant) wave; parameters ρ_1 and ρ_2 determine the shape of the envelope and the number of waves in the group; parameter ρ_0 determines the carrier wave asymmetry.

Dominant waves (i.e. waves with frequencies close to the peak frequency in the surface elevation spectrum) belong to the class of gravitational ones. Accordingly, the parameters k_0 and ω_0 are related to each other by the dispersion relation, for gravitational waves. In deep water, where the bottom's influence on surface waves can be neglected, the dispersion relation has the form.

$$\omega^2 = gk, \quad (9)$$

where g is the gravitational acceleration.

Wave profiles and SIWEH function constructed on the basis of model (6)–(8) are shown in Fig. 1. When constructing the figure (normalizations were used), according to which the amplitude of the highest wave in the group is equal to unity, and the time is measured in periods of the wave's groups T_G .

4 Groupiness Factor and Skewness

The GF determined according to (3) and (5) are somewhat different. This is, in particular, due to the nonlinear transformation of the modulated wave $\xi(x, t)$ in Eq. (1) (Haller and Dalrymple 1995; List 1991). Using the analytical model, which is described by Eqs. (6)–(8), compare GF_{SIWEN} and GF_L . In the framework of the model $\xi(x, t)$ considered here, the shape of the envelope $G(x, t)$ does not depend on the number of waves in the group and on the asymmetry of the carrier wave. Accordingly, the value GF_L does not depend on these factors, but GF_{SIWEN} one can do it.

Graphs describing the relationship of the GF_{SIWEN} and GF_L obtained in two ways are shown in Fig. 2. It can be seen that as the number of waves in the group N are growing, the values GF_{SIWEN} are also doing it.

Let us define the skewness coefficients of the carrier $\eta(t)$ and modulated $\xi(t)$ waves as.

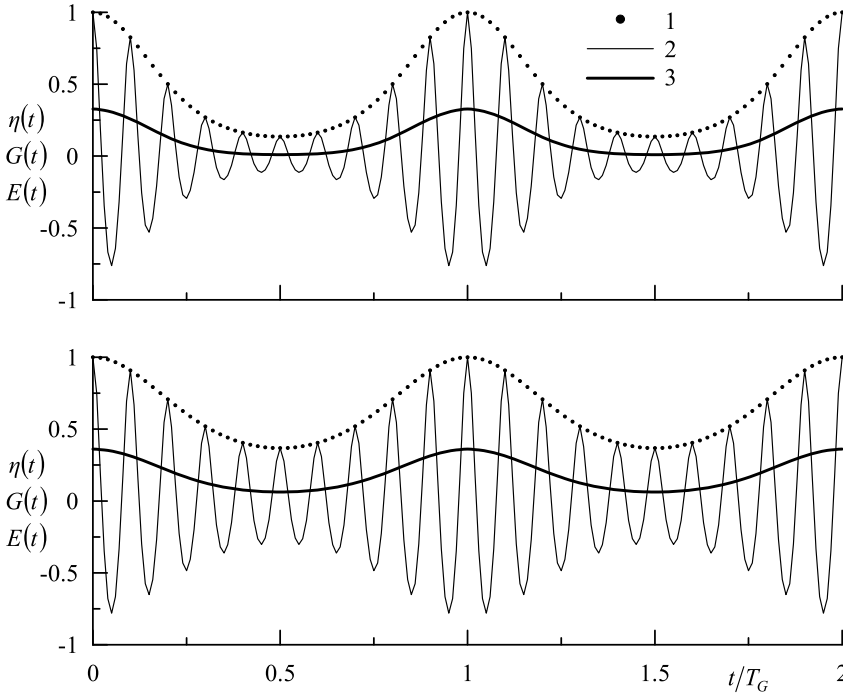


Fig. 1 Group structure of surface waves. Curve 1 is $G(t)$, curve 2 is $\xi(t)$, curve 3 is $E(t)$. Top fragment $GF_{SIWEN} = 0.78$, bottom fragment $GF_{SIWEN} = 0.56$

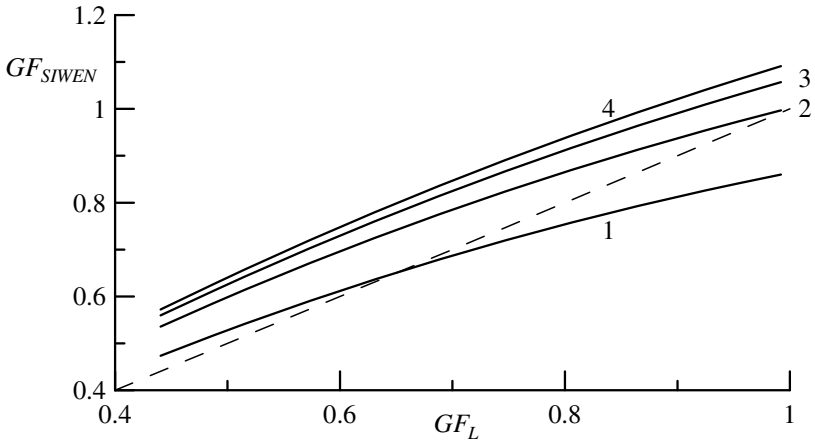
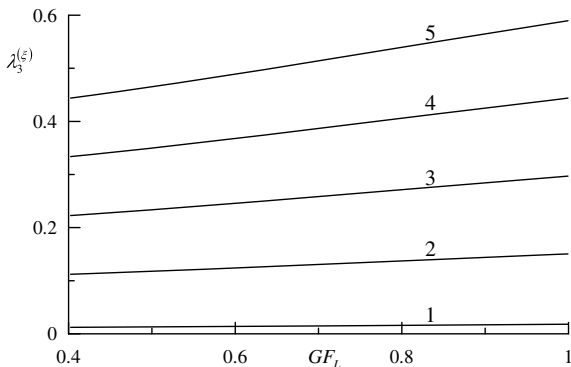


Fig. 2 The ratio between the groupiness factors GF_{SIWEN} and GF_L . Solid curves 1–4 correspond to changes in the parameter N from 4 to 10 with a step of 2. The dashed line corresponds to $GF_{SIWEN} = GF_L$

Fig. 3 Dependences of the skewness coefficient $\lambda_3^{(\xi)}$ of the amplitude-modulated wave on the groupiness factor GF_L . Curves 1–5 are obtained for situations when the skewness coefficient of the nonmodulated wave is respectively $\lambda_3^{(\eta)} = 0.01, 0.1, 0.2, 0.3$ and 0.5



$$\lambda_3^{(\eta)} = \left(\lambda_2^{(\eta)}\right)^{-3/2} \frac{1}{T_W} \int_0^{T_W} (\eta(t) - \overline{\eta(t)})^3 dt, \quad (10)$$

$$\lambda_3^{(\xi)} = \left(\lambda_2^{(\xi)}\right)^{-3/2} \frac{1}{T_W} \int_0^{T_W} (\xi(t) - \overline{\xi(t)})^3 dt, \quad (11)$$

where $\lambda_2^{(\eta)}$ and $\lambda_2^{(\xi)}$ are the variances of the wave elevations $\eta(t)$ and $\xi(t)$, respectively.

The analysis of the carrier wave's asymmetry influence on GF_{SIWEN} showed the following. When the skewness coefficient changing between 0 and 4, the GF_{SIWEN} changes are less than 1%. The indicated range corresponds to the range of variation of the skewness coefficient obtained in sea waves (Jha and Winterstein 2000). Thus, the influence of the carrier wave asymmetry on the GF_{SIWEN} can be neglected.

There is another non-linear effect. When the GF_L changes, the skewness coefficient $\lambda_3^{(\xi)}$ also changes (Fig. 3). With an increase in GF_L , the skewness coefficient also increases. When GF_L change from 0.4 to 1.0, the values $\lambda_3^{(\xi)}$ increase by 35–50%.

5 Conclusion

On the basis of numerical modeling, the analysis of the methodological features of the calculation of the characteristics of the group structure of sea surface waves using the SIWEH function is carried out. For the analysis, an analytical model was used that allows one to take into account two manifestations of the nonlinearity of sea surface waves. The model takes into account both the group structure and the asymmetry of the wave profile.

The difference between the groupiness factors GF_L and GF_{SIWEN} , calculated from the a priori given nonlinear model of the wave profile and from the SIWEH

function constructed for this profile, is shown. The groupiness factor GF_{SIWEN} depend on the number of waves in the group N , with an increase in N , an increase in GF_{SIWEN} occurs. The grouping factor GF_L does not depend on N .

Changes in the carrier wave skewness coefficient $\lambda_3^{(\eta)}$ do not affect on the value of GF_{SIWEN} . However, with the growth of the groupiness factor, the skewness coefficient $\lambda_3^{(\xi)}$ of the amplitude-modulated wave increases.

Acknowledgements The authors thank A. S. Zapevalov for useful discussions of the problems considered in this paper. The work was carried out within the framework of the research conducted at the Sevastopol State University

References

- Agarwal P, Manuel L (2009) On the modeling of nonlinear waves for prediction of long-term offshore wind turbine loads. *J Offshore Mech Arct Eng* 131(4). <https://doi.org/10.1115/1.3160647>
- Babanin AV, Polnikov VG (1995) On the non-Gaussian nature of wind waves. *Phys Oceanogr* 6(3):241–245
- Baldock TE, Alsina J, Caceres I, Vicinanza D, Contestabile P, Power H, Sanchez A (2011) Large-scale experiments on beach profile evolution and surf and swash zone sediment transport induced by long waves, wave groups and random waves. *Coast Eng* 58:214–227
- Fedele F (2007) Explaining extreme waves by a theory of stochastic wave groups. *Comput Struct* 85(5–6):291–303
- Funke ER, Mansard EPD (1979) On the synthesis of realistic sea states in a laboratory flume. Report LTR-HY-66 of the Division of Mechanical Engineering, National Research Council Canada
- Haller MC, Dalrymple RA (1995) Looking for wave groups in the surf zone. In: *Proceedings of the 1995 International Conference on Coastal Research in Terms of Large Scale Experiments*. pp 81–92
- Jha AK, Winterstein SR (2000) Nonlinear random ocean waves: prediction and comparison with data. In: *Proceedings of the 19th International Offshore Mechanical Arctic Engineering Symposium ASME*. Paper No. ETCE/OMAE 2000–6125
- Johnson RR, Mansard EPD, Plog J (1978) Effects of wave grouping on breakwater stability. In: *Proceedings of the 16th Coastal Engineering Conference*. pp 2228–2243
- Kosyan RD, Podymov IS, Pykhov NV (2003) *Dynamic processes of the coastal zone of the sea*. Nauchnyy mir, Moscow [in Russian]
- List JH (1991) Wave groupiness variations in the nearshore. *Coast Eng* 15:475–496
- Longuet MS (1963) The effect of non-linearities on statistical distribution in the theory of sea waves. *J Fluid Mech* 17(3):459–480. <https://doi.org/10.1017/S0022112063001452>
- Ma X, Sun Z, Zhang Z, Yang G, Zhou F (2011) The effect of wave groupiness on a moored ship studied by numerical simulations. *J Hydrodyn Ser B* 23(2):145–153
- Mase H (1989) Groupiness factor and wave height distribution. *J Waterw Port Coast Ocean Eng* 115(1):105–121
- Medina JR, Hudspeth RT (1990) A review of the analyses of wave groups. *Coast Eng* 14:515–542
- Medina JR, Hudspeth RT, Fassardi C (1994) Breakwater armor damage due to wave groups. *J Waterw Port Coast Ocean Eng ASCE* 120:179–197
- Phillips OM (1961) On the dynamics of unsteady gravity waves of finite amplitude. Part 2. *J Fluid Mech* 11:143–155
- Pokazeev KV, Zapevalov AS, Pustovoytenko VV (2015) A nonlinear model of sea surface waves. *Mosc Univ Phys Bull* 70(3):213–215

- Presnukhin AV (2009) Group structure of wind waves in the Caspian Sea. *Lithodinamika bottom. contact zone of the ocean. Mater. int. conf., dedicated. 100th anniversary of the birth of the professor V.V. Longinov (September 14–17, 2009, Moscow)* 31–33 [in Russian]
- Shumeyko IP, Ozhiganova MI, Voronina NN, Kril MV, Narivonchik SV (2018) To calculation of the groupiness factor of marine surface waves. *Protsessy v geosredakh* 3(16) 1077–1081 [in Russian]
- Song J-B, Wu Y-H, Wiwatanapataphee B (2000) Probability distribution of random wave forces in weakly nonlinear random waves. *Ocean Eng* 27(12):1391–1405. [https://doi.org/10.1016/s0029-8018\(99\)00067-0](https://doi.org/10.1016/s0029-8018(99)00067-0)
- Yuen HC, Lake BM (1982) Nonlinear dynamics of deep-water gravity waves. *Adv Appl Mech* 22:67–229
- Zapevalov AS (2011) High-order cumulants of sea surface elevations. *Russ Meteorol Hydrol* 36(9):624–629
- Zapevalov AS, Ratner YuB (2003) Analytic model of the probability density of slopes of the sea surface. *Phys Oceanogr* 13(1):1–13
- Zapevalov AS, Bol'shakov AN, Smolov VE (2011) Simulating of the probability density of sea surface elevations using the Gram-Charlier series. *Oceanology* 51(3) 406–413

Identification of the Time-Variable Power of a Point Pollution Source in the Azov Sea Based on the Variational Assimilation Algorithm



Kochergin Vladimir Sergeevich  and Kochergin Sergey Vladimirovich 

Abstract In this paper, calculations are made using the passive admixture transport model for the water area of the Azov Sea. A variational procedure for identifying the time-variable power of the pollution source is implemented on the basis of minimizing the quadratic cost function of the forecast quality and solving adjoint problems. The simulation results were obtained with the north-east wind stress influence prevailing in this water area.

Keywords Transport model · Adjoint equations · Identification of pollution sources · Azov Sea

1 Introduction

When solving environmental problems based on the use of numerical dynamic models and models describing the processes of propagation of certain pollutants (Ivanov and Fomin 2008; Fomin 2002), the natural task is to improve the predicted model fields by identifying the input parameters of the models. One of the methods of such identification is the variational method (Marchuk and Penenko 1978; Penenko 1981; Agoshkov et al. 2013) based on minimizing the forecast residuals and solving adjoint problems of a special type. The development of such algorithms is an important and urgent task due to the increasing anthropogenic load on the water area of the Azov-Black Sea basin and the need to create systems for monitoring the state of the environment. In (Kochergin and Kochergin 2010), a variational algorithm for identifying the time-variable source power is considered, based on this approach for a two-dimensional problem. In this paper, the method of adjoint equations (Marchuk 1982; Kochergin and Kochergin 2015) is used to identify the time-variable power of the pollution source for the model of passive admixture transport in the Azov Sea. The model (Ivanov and Fomin 2008; Fomin 2002) is implemented as a dynamic model. The obtained model fields of velocities and coefficients of turbulent diffusion

K. V. Sergeevich (✉) · K. S. Vladimirovich
Marine Hydrophysical Institute RAS, Sevastopol 299029, Russian Federation

are used as input information when integrating the adjoint problem and the passive admixture transfer model itself.

2 Transport Model

Consider the transport model of a passive admixture in σ -coordinates:

$$\frac{\partial DC}{\partial t} + \frac{\partial DUC}{\partial x} + \frac{\partial DVC}{\partial y} + \frac{\partial WC}{\partial \sigma} = \frac{\partial}{\partial x} A_H \frac{\partial DC}{\partial x} + \frac{\partial}{\partial y} A_H \frac{\partial DC}{\partial y} + \frac{\partial}{\partial \sigma} \frac{K}{D} \frac{\partial C}{\partial \sigma} \quad (1)$$

with the conditions on the lateral boundaries:

$$\Gamma : \frac{\partial C}{\partial n} = 0, \quad (2)$$

boundary conditions on the surface and at the bottom

$$\begin{aligned} \sigma = 0 : \frac{\partial C}{\partial \sigma} &= Q(t), \quad Q(t) = Q_S(t) \cdot \delta(x - x_0) \cdot \delta(y - y_0) \\ \sigma = -1 : \frac{\partial C}{\partial \sigma} &= 0 \end{aligned} \quad (3)$$

and initial data

$$C(x, y, \sigma, 0) = 0, \quad (4)$$

where x_0, y_0 —coordinates of the point source; t —time; C —admixture concentration; D —dynamic depth; $Q(t)$ —point source of time-variable power; U, V, W —components of the velocity field; A_H and K —coefficients of horizontal and vertical turbulent diffusion, respectively; n —normal to the lateral boundary. Without limiting generality, we assume that the point source is located on the surface of the sea. The problem is solved similarly when setting the source at the bottom and at the side boundary, but this requires corresponding changes in the boundary conditions (2), (3).

3 Variational Identification Algorithm

The task of assimilating the final time measurement data consist of following cost function minimization

$$I_0 = \frac{1}{2}[P(RC - C_m), P(RC - C_m)]_M, \tag{5}$$

where P —operator of filling in the field of forecast residuals with zeros in the absence of measurement data, M —area of integration of the model on the time interval $[0, T]$, R —operator of projecting to the observation points, and the scalar product is determined in the standard way. Minimizing (5) with model limitations (1)–(3) is equivalent to finding the minimum of the following cost function

$$I = I_0 + \left[\frac{\partial DC}{\partial t} + \frac{\partial DUC}{\partial x} + \frac{\partial DVC}{\partial y} + \frac{\partial WC}{\partial \sigma} - \frac{\partial}{\partial x} A_H \frac{\partial DC}{\partial x} - \frac{\partial}{\partial y} A_H \frac{\partial DC}{\partial y} - \frac{\partial}{\partial \sigma} \frac{K_H}{D} \frac{\partial C}{\partial \sigma}, C^* \right]_{M_t} + \left(\frac{\partial C}{\partial n}, C^* \right)_{\Gamma_t} + (C - C_0, C^*)_M + \left(\frac{\partial C}{\partial \sigma} - Q(t), C^* \right)_{\sigma_t^0}, \tag{6}$$

where $M_t = M \times [0, T]$, $\sigma_t^0 = \sigma^0 \times [0, T]$. Let the variation of the functional (6) with it integrating in parts and the boundary conditions account continuity equation in σ –coordinates, we obtain

$$\delta I = (\delta Q_s(t) \cdot \delta(x - x_0) \cdot \delta(y - y_0), C^*)_{\sigma_t^0}, \tag{7}$$

where C^* —solution of the following adjoint problem

$$-\frac{\partial DC^*}{\partial t} - \frac{\partial DUC^*}{\partial x} - \frac{\partial DVC^*}{\partial y} - \frac{\partial WC^*}{\partial \sigma} - \frac{\partial}{\partial x} A_H \frac{\partial DC^*}{\partial x} - \frac{\partial}{\partial y} A_H \frac{\partial DC^*}{\partial y} - \frac{\partial}{\partial \sigma} \frac{K_H}{D} \frac{\partial C^*}{\partial \sigma} = 0, \tag{8}$$

$$\Gamma : \frac{\partial C^*}{\partial n} = 0, \sigma = 0 : \frac{\partial C^*}{\partial \sigma} = 0, \sigma = -1 : \frac{\partial C^*}{\partial \sigma} = 0, \tag{9}$$

$$t = T : C^* = -P(RC - C_m). \tag{10}$$

Follow equation we have from the stationarity of the functional and the definition of its gradient

$$\nabla_{Q_s(t)} I = C^*(x_0, y_0, 0, t) \tag{11}$$

The value Q_s is found iteratively

$$Q_S^{n+1}(t) = Q_S^n(t) + \tau \cdot \nabla_{Q_S(t)} I \quad (12)$$

where τ —iterative parameter that can be selected in one of the known ways, for example

$$\tau = \frac{(P(RC - C_m), PR\delta C)_M}{(PR\delta C, PR\delta C)_M} \quad (13)$$

where δC —solution of the solution of the corresponding (1)–(4) problem in variations

$$\begin{aligned} \frac{\partial D\delta C}{\partial t} + \frac{\partial DU\delta C}{\partial x} + \frac{\partial DV\delta C}{\partial y} + \frac{\partial W\delta C}{\partial \sigma} &= \frac{\partial}{\partial x} A_H \frac{\partial D\delta C}{\partial x} + \frac{\partial}{\partial y} A_H \frac{\partial D\delta C}{\partial y} \\ &+ \frac{\partial}{\partial \sigma} \frac{K}{D} \frac{\partial \delta C}{\partial \sigma} \end{aligned} \quad (14)$$

with conditions on the lateral boundaries

$$\Gamma : \frac{\partial \delta C}{\partial n} = 0, \quad (15)$$

at the surface and bottom we use boundary conditions

$$\sigma = 0 : \frac{\partial \delta C}{\partial \sigma} = C^*(x_0, y_0, 0, t), \quad \sigma = -1 : \frac{\partial \delta C}{\partial \sigma} = 0 \quad (16)$$

and initial data

$$\delta C(x, y, \sigma, 0) = 0, \quad (17)$$

In general, the identification procedure is as follows:

- the direct problem (1) (4) with some initial value is solved;
- the forecast residuals are found and the functional (5) is determined);
- the adjoint problem (8) (10) is solved);
- the gradient (11) of the functional (6) is determined);
- the problem is integrated in variations (14) (17);
- the iterative parameter is calculated using the formula (13);
- iteratively, the power of the source is found by the formula (12).

4 Results of Numerical Experiments

Numerical experiments were carried out using the model from [11] for the water area of the Sea of Azov. To implement the procedure for identifying the time-variable power of pollution, a calculation was made to establish a model field of currents under the influence of a constant wind of the north-east direction at a speed of 10 m/s. As a result of the simulation, the spatial distribution of the coefficients A_H and K was also obtained. The velocity fields and turbulent diffusion coefficients were used as input information when integrating the passive admixture transport model for a period of 5 days. Figure 1 shows the model field of concentration on the sea surface and the location of the point source of pollution is indicated by a circle. The initial profile $Q(t)$ is shown in picture 2 as a bold line, defined as a sine with a maximum in the middle of the integration period. The total integration time of the model is 1800 steps (m is the step number). The resulting model field was used as measurement data on the sea surface both completely and partially, i.e., the data were not absorbed in all nodes of the calculated grid. The results shown in the pictures are obtained by assimilating every fifth point on the x and y axes. In addition, random noise of 2.5%, 5%, and 10% was superimposed on the data. Figure 2, in addition to the initial power profile of the pollution source, shows the values $Q(t)$ when using 2.5% random noise for the first (thin solid line), fifth (thin dotted line), and tenth (thick dotted line) iteration. Calculations have shown that with the measurement data used, 5 iterations are sufficient to achieve the minimum functional. Further iterations do not improve the result and are probably due to the uncertainty of the model in relation to the data. A similar result was obtained for data assimilation with 5.0% random noise. The result of assimilation of such information is shown in Fig. 3. The line designations are the same as in Fig. 2. Figure 4 describes a similar calculation when setting 10%

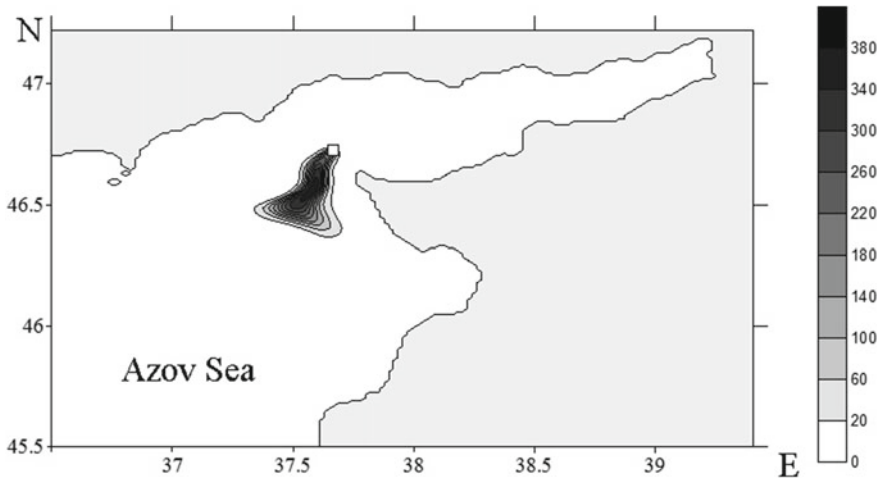


Fig. 1 Location of the pollution source and the model concentration field at the final time

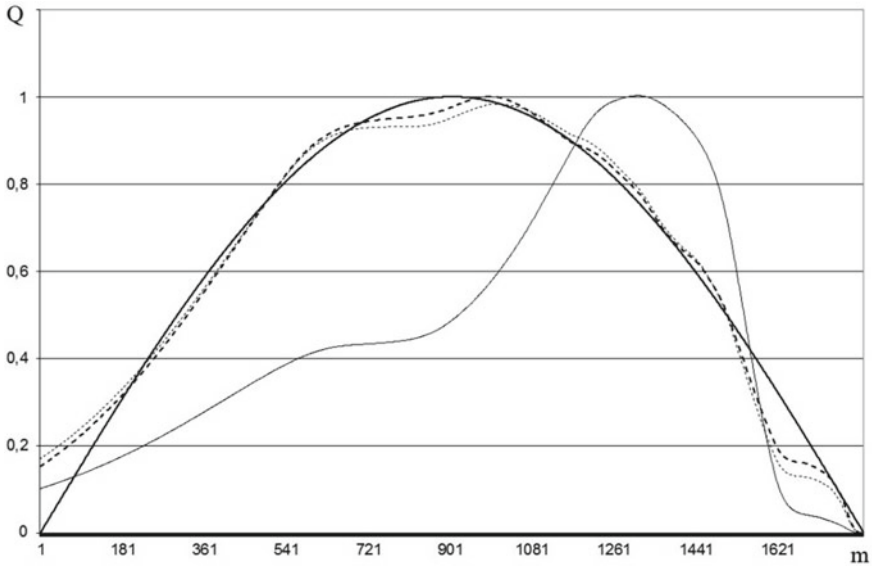


Fig. 2 Identification $Q(t)$ during iterations (2.5% noise)

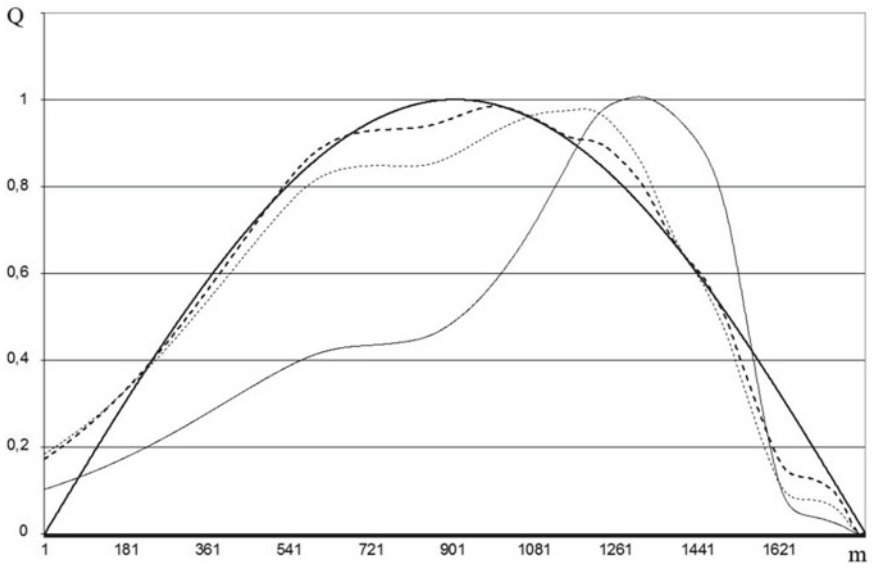


Fig. 3 Identification $Q(t)$ during iterations (5.0% noise)

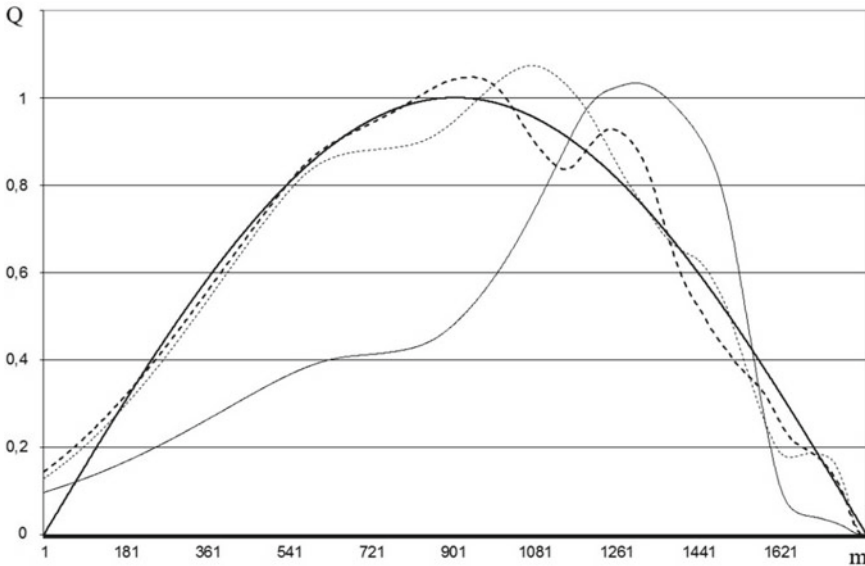


Fig. 4 Identification $Q(t)$ during iterations (10.0% noise)

of the noise in the measurement data. Numerical experiments have shown that an increase in the number of measurement data, especially in the area of significant concentration values, leads to improved results in identifying the desired parameter. In addition, the decrease in measurement errors set using the random number counter leads to an increase in the reliability of the results obtained.

5 Conclusions

Numerical experiments have shown that it is possible to identify a time-varying point source of contamination in a three-dimensional model of passive admixture transport. It is shown that with variational identification, it is possible to obtain reliable results when setting measurement data not in all nodes of the calculated grid. This is an important interpolation feature of the algorithm. And the assimilation of measurement data with random noise demonstrated the filtering properties of the assimilation procedure. The results can be used to solve various environmental problems when studying the impact of anthropogenic pollution sources in the waters of the Azov and Black Seas.

The work was carried out within the framework of the state task on the topic 0555–2021-0005 " Complex interdisciplinary studies of oceanological processes that determine the functioning and evolution of ecosystems in the coastal zones of the Black and Azov Seas.

References

- Agoshkov VI, Parmuzin EI, SHutyayev VP (2013) Observational data assimilation in the problem of Black Sea circulation and sensitivity analysis of its solution. In: *Izv. RAN, Fizika atmosfery i okeana*, vol 49. no. 6, pp 643–654
- Fomin VV (2002) Numerical model of the water circulation of the Sea of Azov. In: *Nauchnye trudy UkrNIGMI*, 249, pp 246–255
- Ivanov VA, Fomin VV (2008) Mathematical modeling of dynamic processes in the sea-land zone. *ECOSI-Gidrophisika*, Sevastopol, p 363
- Kochergin VS, Kochergin SV (2010) The use of variational principles and the solution of the adjoint problem, identification of input parameters for models of transport of passive tracer. *Ecological Safety of Coastal and Shelf Zones and Comprehensive Use of Shelf Resources*, MGI, Sevastopol, 22:240–244
- Kochergin VS, Kochergin SV (2015) Identification of a pollution source power in the Kazantip Bay applying the variation algorithm. *Phys Oceanogr* 2:69–76
- Marchuk GI, Penenko VV (1978) Application of optimization methods to the problem of mathematical simulation of atmospheric processes and environment. In: *Modelling and optimization of complex systems*, IFIP-TC7 Working conference. New York: Springer, pp 240–252
- Marchuk GI (1982) *Mathematical modeling in the environmental problem*. M. Nauka, p 320
- Penenko VV (1981) *Methods for numerical modeling of atmospheric processes*. L.: Gidrometeoizdat, p 350

Increase in Illumination of 253.7 nm in a Cylindrical PTFE Cavity



Mikhail A. Kotov, Andrey N. Shemyakin, Nikolay G. Solovyov,
and Mikhail Yu. Yakimov

Abstract The study is devoted to the possibility of increasing illumination in the UV range using materials with a high diffuse scattering coefficient, such as PTFE. When using a cylindrical cavity made of such a material, the illumination inside the volume of the cavity tends to the illumination of the radiation source located longitudinally and coaxially with the cavity. Experiments with a low-pressure ozone-free mercury lamp have been carried out, demonstrating scattering of UV radiation in a cylindrical PTFE cavity. Due to effective diffuse UV scattering inside the cavity, the illumination increased by more than 4 times compared to its absence. Numerical calculations performed by ray tracing give similar data. The results obtained are of interest for UV germicidal application.

Keywords Diffuse scattering · UV mercury lamp · PTFE · Illumination increase · Cylindrical cavity

1 Introduction

The bactericidal effect of ultraviolet irradiation on biological objects (cells, bacteria, viruses, etc.) is well known. It is usually associated with radiation in the wavelength range of 200–300 nm. Such irradiation is capable of leading to irreversible damage in the cell due to photochemical reactions. As a rule, this is primarily understood as a violation of the structures of DNA and RNA, as well as proteins and other components of the cell (Chatterley and Linden 2010 Sep; Kostyuchenko et al. 2009). UV irradiation on microorganisms leads to the loss of their ability to conduct normal life and reproduce, which ultimately leads to their death. The bactericidal effect of light makes it possible to effectively use UV emitters of the appropriate range for sterilizing water (Chatterley and Linden 2010 Sep) and air (Kostyuchenko et al. 2009). Low pressure mercury lamps are most commonly used as such sources. The ozone-free version of these lamps is due to the radiation of the resonant transition

M. A. Kotov (✉) · A. N. Shemyakin · N. G. Solovyov · M. Yu. Yakimov
Ishlinsky Institute for Problems in Mechanics of the Russian Academy of Sciences, Prospekt
Vernadskogo, 101-1, Moscow 119526, Russia
e-mail: kotov@ipmnet.ru

of the $6^3P_1-6^1S_0$ mercury atom with a wavelength of ~ 253.7 nm. Bactericidal light sources are installed in a “closed” bactericidal irradiator, when the exit of bactericidal irradiation from the cavity of the irradiator is blocked in one way or another (Clark 2012; Lizotte 2012; Rudoy et al. 2018, 2020). Such an irradiator also includes a lamp power source and a fan for pumping the sterilized flow (including multiple pumping). Hence the common name for this kind of apparatus—“recirculator”.

One of the main problems of such devices is that only a negligible fraction of light energy is actually spent on suppressing the vital activity and reproduction of microorganisms, and the bulk of the radiation is absorbed by the surface of the irradiator body. For increase the efficiency of the recirculator, it is advisable to maximize the illumination of the lamp radiation. It is possible to advance in this direction if the recirculator is manufactured in such a way that most of the inner surface of its cavity is reflective for UV radiation.

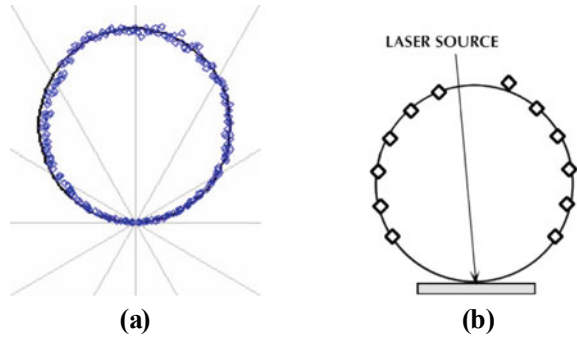
2 Possibilities of Using a Diffuse Reflective Material

A sharp increase in the efficiency of using bactericidal radiation can be realized when using a diffusely reflecting inner surface of the irradiator housing, for which it is possible to provide an effective reflection coefficient of $>90\%$ (Rudoy et al. 2020). Inner surface of the cavity of the UV irradiator is made of a material that diffusely reflects radiation with an effective reflectance of at least 90% . This makes it possible to multiply the radiation intensity in the cavity, including in comparison with recirculators with an inner surface made of specularly reflecting materials (stainless steel, aluminum)—Fig. 1. Also, in the cavity, in comparison with specular reflection, a significantly higher uniformity of radiation is provided (Judd 1942).



Fig. 1 General views of «Aerolit» air bactericidal recirculators (<https://www.bakt.ru/>)

Fig. 2 Radiance of PTFE diffuse reflectance material (point) and an ideal Lambertian reflector (line) under unit irradiance at a different incident angle—**a** 15 degrees (Waldwick et al. 2007); **b** 5 degrees (Reflectance Materials and Coatings xxxx)



2.1 PTFE Peculiarities

PTFE (teflon) can be considered as such a material. It has a high coefficient of diffuse reflection in the bactericidal region of the spectrum—above 90–93% with a thickness of ~2–4 mm (Janecek June 2012; Quill et al. 2016). Pure PTFE almost does not absorb UV radiation of the bactericidal range. Specialized materials such as Spectralon by Labsphere, Inc with a reflectance of more than 93–95% for a wavelength of ~250 nm may also be of interest (Reflectance Materials and Coatings xxxx). It should be pointed out that the reflection becomes essentially diffuse also in the case of a metal surface with sufficiently small-scale irregularities. But the effective coefficient of diffuse reflection from a rough aluminum surface will not be greater than the coefficient of reflection from a smooth mirror surface of aluminum. Figure 2 shows the results of comparing the diffuse reflection of the PTFE material (experiment) with an ideal Lambertian reflector.

2.2 Longitudinal Radiation Source in the Cylindrical Cavity

Consider a case with a source of bactericidal radiation located along the cylindrical cavity of the recirculator. Imagine a longitudinal cylindrical mercury lamp as a source. As is known from the theory of integrating spheres (Judd 1942; Jacquez and Kuppenheim 1955), with ideal diffuse reflection from the walls of a cylindrical cavity, the radiation flux inside this cavity in the absence of various limiting factors (imperfect radiation/reflection processes, nonlinearity of the medium, taking into account the size of dust/bacteria particles, etc.) will be uniform and as much as possible. If we assume the presence of small particles in such a cavity, the dimensions of which are much smaller than the dimensions of the cavity (dust, bacteria), then we can say that the average illumination of their surfaces under considered conditions will tend to illumination from source in the entire volume of the cavity.

3 Attenuation of the Radiation Flux of 253.7 nm by PTFE Layers

If we talk about the use of a cylindrical cavity made of fluoroplastic as an effective diffuse scatterer of short-wave UV radiation, it is necessary to have data to determine the value of its scattering coefficient. It makes sense to evaluate such characteristics with a specific material and in a specific experiment. We will not consider possible chemical reactions caused by structural inhomogeneities of the material and exposure to UV radiation, as well as the possible accumulation of biological and organic substances in the air on the fluoroplastic surface. Then, according to the law of energy conservation, the remaining fraction of radiation must pass through the material or be absorbed by it. The values of such parameters can be estimated if we consider the transmission of radiation through different thicknesses of fluoroplastic and determine the degree of attenuation of radiation depending on the thickness.

A Heraeus NNI 125/84 ozone-free low pressure mercury UV lamp was used in experiments to measure the degree of attenuation of the radiation flux at a wavelength of $\lambda = 253.7$ nm by PTFE layers. The outer diameter of the lamp was 15 mm, the distance between the electrodes was 780 mm. The receiving hole of the Ocean Optics HR4000CG-UV-NIR spectrometer was located in the middle of the lamp at a distance of 23 mm from its wall. The rest of the space surrounding the lamp was covered with sheets of acrylic, transparent to the visible spectrum and absorbing short-wave UV radiation. A photograph of the experiment is shown in Fig. 3. The lamp consumed 156 W from the mains power supply.

After turning on the power, before measuring the radiation, a time delay of 3–4 min was made to ensure that the lamp warmed up and reached an effective stationary radiation mode. This feature is due to the physicochemical processes occurring in the lamp (Vasilyev et al. 2009; Vasilyak et al. 2011). We compared the flux of spectral radiation at a distance of 23 mm from the lamp with the same flux weakened by a layer of fluoroplastic with a thickness of 1 mm (Figs. 4 and 5), 2 mm, and 3 mm



Fig. 3 Placement of a mercury lamp for experiments to measure the attenuation of radiation passing through the PTFE layers

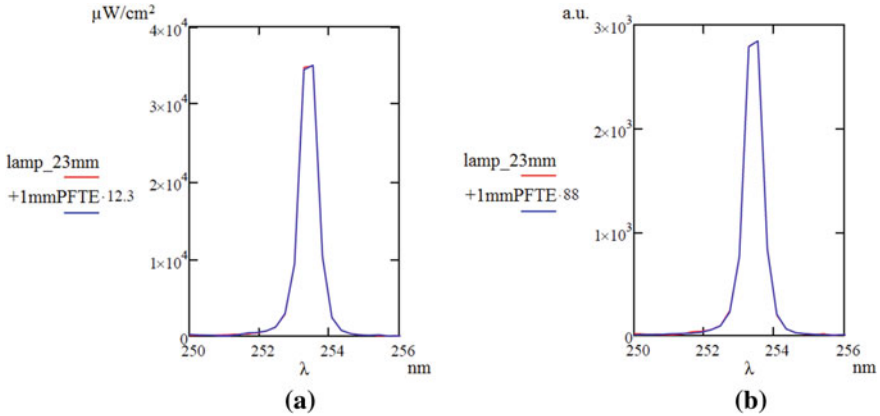


Fig. 4 Comparison of radiation attenuation at a distance of 23 mm from the lamp before and after 1 mm PTFE with a cosine corrector (a) and without it (b). The radiation attenuation coefficient is 12.3 and 88, respectively

(Fig. 6). The relative values of the radiation flux were measured by the open aperture of the optical fiber of the spectrograph (Fig. 4b). The scan angle was $\sim 25.4^\circ$ ($=2 \cdot \arcsin(0.22)$). The receiving aperture of the sensor was 3.9 mm. The absolute values in [$\mu\text{W}/(\text{cm}^2 \text{ nm})$] were measured using a cosine corrector (Figs. 4a and 5). Thicknesses of 2 mm and 3 mm PTFE (Fig. 6) were collected from 1 mm thick layers—2 and 3 layers, respectively. The multipliers of the function in Figs. 4–6 show the attenuation coefficient. These coefficients are selected before aligning the spectral curves.

According to the cosine law, the cosine corrector diffusely absorbs radiation arriving at it from all sides of the receiving hemisphere. It shows the value of this radiation. The values of the attenuation coefficients in Fig. 4a, b indicate that, despite the fact that the receiving elements were close to the PTFE sheet, their values differ by more than 7 times ($88/12.3$). This is due both to the difference in the aperture angles of the receivers and to the arrival of additional radiation from the lamp. Not only radiation that has passed directly through the PTFE sheet hits the receiver, but also additional radiation due to the arrival at the receiver at different angles due to the processes of passage, reabsorption, re-reflection and refraction occurring along the entire sheet. It is very difficult to accurately assess such a value and, probably, unreasonable and beside the purpose.

To estimate the radiation power in the remaining parts of the spectrum of the mercury lamp, using a cosine corrector, similar measurements were carried out about $\lambda = 313;404;577;579 \text{ nm}$ (Fig. 5).

We can say that closer to the middle of the visible range, radiation is better transmitted by PTFE than in short-wave UV (the values of the attenuation coefficients are much lower than the values in Fig. 18). The total radiation flux of a mercury lamp is up to about 40% of the consumed power (Voronov et al. 2003; Waymouth 1971), i.e. up to $\sim 62 \text{ W}$ in our case. From the values shown in Fig. 5, we can say that in

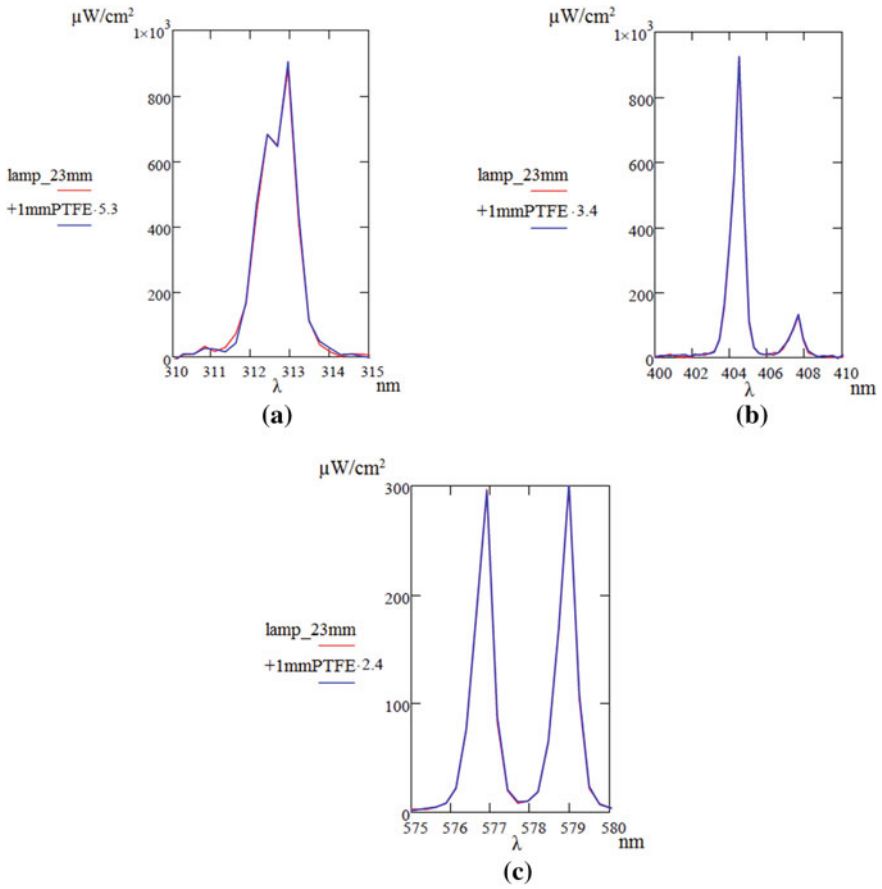
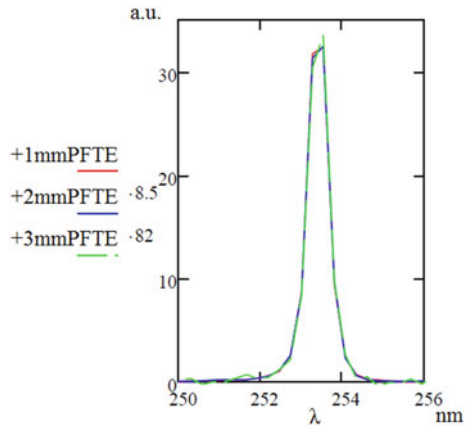


Fig. 5 Comparison of radiation attenuation at a distance of 23 mm from the lamp before and after 1 mm PTFE with a cosine corrector. Radiation attenuation coefficients 5.3, 3.4 and 2.4

Fig. 6 Comparison of radiation attenuation after 1 mm, 2 mm and 3 mm PTFE with an open hole in the optical fiber of the spectrograph. The radiation attenuation coefficients are 8.5 and 82, respectively.



addition to the 253.7 nm region, somewhere about a third of the lamp radiation power goes to other spectral ranges. At 253.7 nm, the total radiation from the lamp can be estimated at about ~40 W. It should be noted here that in this case, the Keitz formula (Keitz 1971) cannot be used to estimate the total output radiation power, since the distance from the sensor to the lamp is much less than the length of the lamp. Even a concise derivation of its equation (Sasges and Daynouri 2012) is advisable to use at long distances.

Figure 6 shows the attenuation of the radiation flux by the PTFE sheets used in a particular experiment. It should be noted that in addition to the reasons that introduce an error in the attenuation measurement and described under Fig. 4, this adds a thin airspace created between the layers of material when it is aligned. Due to the peculiarities of PTFE it will not be possible to realize a sufficiently tight fit of the layers to each other. Due to the highly diffuse nature of scattering, re-reflection, refraction, absorption, the data obtained are of an estimate nature. It is very difficult to perform a pure experiment to measure the dependence of the reflection coefficient on the thickness of such a material. But we can say that the reflectance at 253.7 nm will be higher with a thickness of 2 mm (2 layers of 1 mm) than with a thickness of 1 mm (1 layer). The same is with the 3 mm thickness.

4 PTFE Cylindrical Cavity

4.1 Experiment

A PTFE sheet was used with a size of 1020 × 785 mm, which was rolled into a pipe with a diameter of 122/126 mm inside/outside. Wall thickness was 2 mm (exactly two layers). On the sides were 3 mm thick PTFE end caps with lamp holes in the center. The lamp caps inside the cavity were wrapped with a PTFE strip 90 mm wide and 0.1 mm thick. The radiation sensor was tightly inserted into the hole in the center of the tube (Fig. 7). The receiving aperture of the sensor was at a distance of 54 mm from the lamp wall (Fig. 8).

In the absence of a scattering cavity, the radiation flux in the 253.7 nm line created by a Heraeus NNI 125/84 mercury lamp at a power of 156 W consumed by the power supply from the mains, measured at a distance of 54 mm from the lamp wall in the middle of its length, is 12.4 mW/cm². In the presence of a scattering PTFE cavity, the radiation flux to the sensor increases to 52.4 mW/cm² with all other things being equal, i.e. more than 4 times. The measurements were carried out with a cosine corrector.

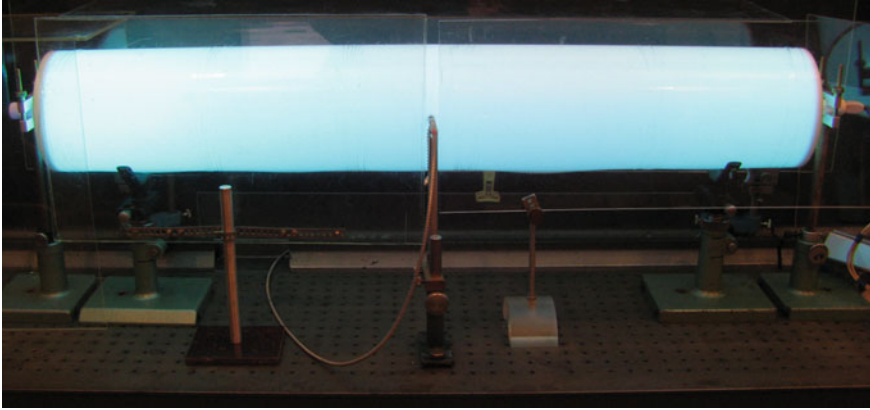


Fig. 7 Photo of the experiment with the cavity

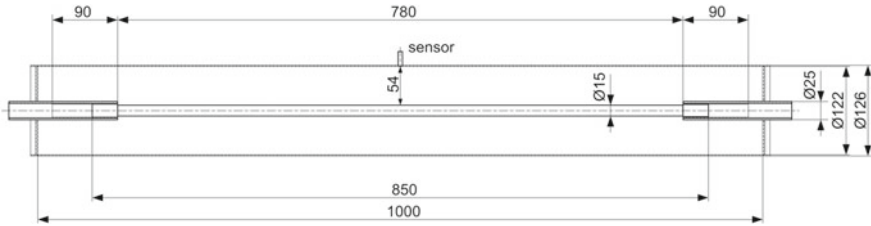


Fig. 8 Experiment layout (dimensions in mm)

4.2 Numerical Simulation

4.2.1 Absence of a Cavity

For numerical calculations, the ray tracing method was used in the Comsol software (<https://doc.comsol.com/5.4/doc/com.comsol.help.roptics/RayOpticsModuleUsersGuide.pdf>). First, the simulation was carried out in the absence of a cavity. As the lamp a cylinder with dimensions similar to Fig. 8 was set. The radiation from the lamp was approximated by the radiation of a set of diffuse sources located on the surface of the cylinder, with the outward propagation of the rays. $N_s = 3000$ normal-emitting diffuse sources with probability distribution based on Lambert's cosine law - $N_r = 300$ rays are released at each point, sampled from a hemisphere in wave vector space with probability density based on the cosine law. The total radiation power of the set of sources was equal to $E = 40$ W. The ray travel time was 3 ns (the beam path was slightly less than 1 m).

The radiation flux from the lamp came to a cylindrical area $w = 40$ mm wide, located in the middle of the lamp at a distance of 54 mm from its walls and absorbing all radiation arriving at it (Fig. 9).

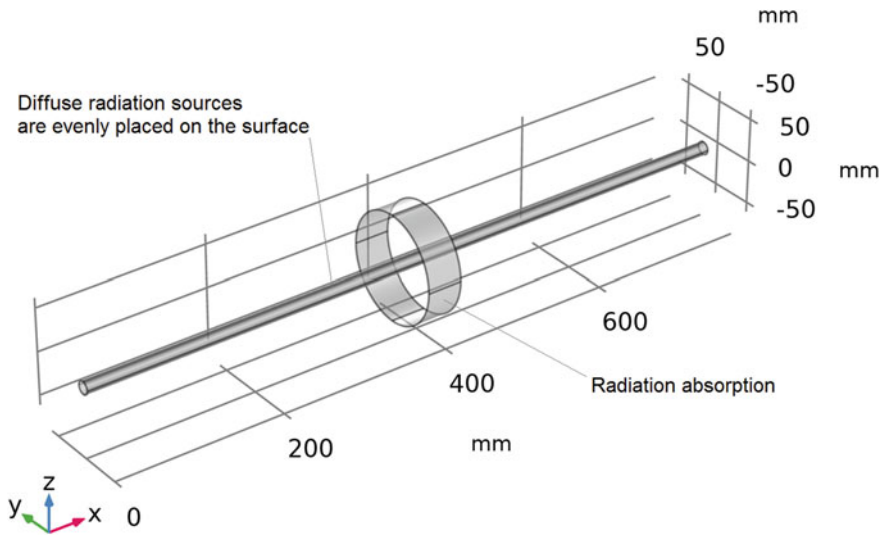


Fig. 9 Computational domain geometry for modeling in the absence of a cavity

The average value of the radiation density on the surface of the cylindrical area was found to be equal to $E_{ave} = 12.06 \text{ mW/cm}^2$. A series of calculations was carried out to determine the dependence of the values from each other, the results are presented in Table 1.

As can be seen from Table 1, the changes in the calculation results are small. Their nature, rather random, can be associated with the probability distribution according to the cosine law. That is, the probability of a ray propagating in a given direction within a solid angle $d\omega$ is given by $\cos\theta d\omega$ where θ is the angle between the direction of the ray and the wall normal. The direction of the rays from the sources and their arrival at the receiving site area depend on this. Nevertheless, to reduce the influence of this effect, it is more expedient to carry out calculations with a large number of beams. And these initial conditions are more like the real picture. As for the comparison with the result of the experiment, the agreement is quite good. This testifies in favor

Table 1 Comparison of results obtained at different initial values

$N_s \times N_r = 1000 \times 100$		$N_s \times N_r = 2000 \times 200$		$N_s \times N_r = 3000 \times 300$	
w, mm	E_{ave} , mW/cm ²	w, mm	E_{ave} , mW/cm ²	w, mm	E_{ave} , mW/cm ²
50	12.96	50	12.99	50	12.12
40	13.03	40	12.92	40	12.06
30	13.33	30	12.91	30	12.07
20	13.47	20	12.81	20	12.03
10	13.59	10	12.9	10	11.99

of the suitability of such a description of the radiation from a mercury lamp used in experiments for further calculations.

4.2.2 Presence of a Scattering Cylindrical Cavity

The geometry of the computational domain is shown in Fig. 10. The radiation from the lamp was set in the same way as in Sect. 4.2.1. The dimensions of the cavity and the elements fixing the lamp are similar to Fig. 8. The receiving cylindrical surface was also located in the middle of the lamp length and had a width $w = 40$ mm (Fig. 10).

On the entire inner surface of the cavity (except for the receiving surface), the condition of diffuse reflection was set—reflection at a surface in a random direction, following a probability distribution based on Lambert’s cosine law. The coefficient of such scattering is $q = 0.875$. In other cases, the incoming radiation was absorbed.

The number of radiation sources and the number of rays of each source is $N_s = 3000$ and $N_r = 300$. For the rays reflected from the diffuse scattering surface and passing through the volume of the inner cylinder, we set the absorption coefficient $k_{lamp} = 0.5$. The refractive index of the cylinder $n_{ri} = 1.5$ was approximately equal to the refractive index for 253.7 nm for the quartz walls of the lamp used in the experiment. This is how the absorption of reflected radiation in a mercury lamp and the passage of radiation through its volume were described. The travel time of the beams was 10 ns (the maximum possible distance of one beam is slightly less than 3 m).

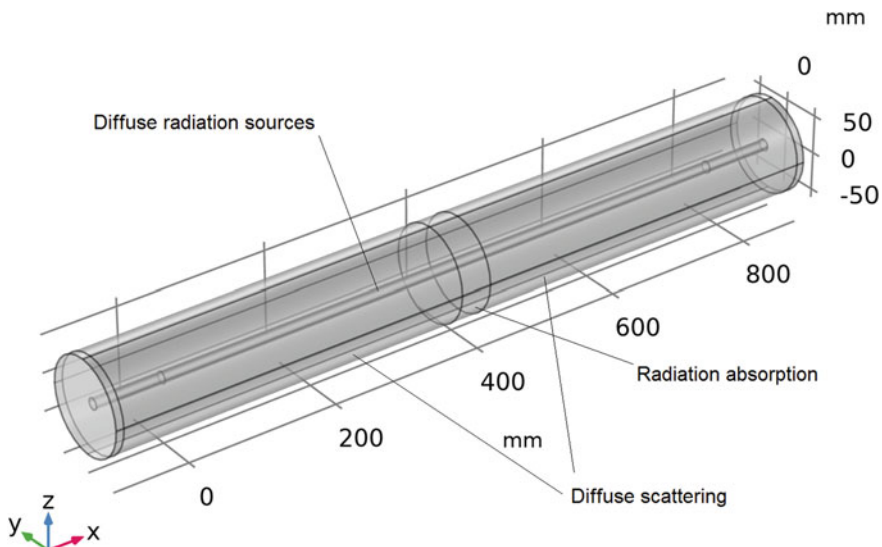


Fig. 10 Computational domain geometry for modeling in the presence of a scattering cavity

The average value of the radiation density on the surface of the cylindrical area turned out to be equal to $E_{ave_c} = 50.25 \text{ mW/cm}^2$. It turns out that in the presence of a scattering cavity, the radiation flux to the receiving area, as in the experiment, increased more than 4 times (from 12.06 to 50.25 mW/cm^2), all other things being equal. We can say that due to the good agreement between the experimental and calculated data, such a formulation of the problem of computational modeling is suitable for describing the phenomena observed in an experiment and interpreting its results.

5 Illumination Increase

The statement of the study in Sect. 4 cannot be suitable for describing a recirculator, since there is no pumping of the medium through the cavity. At the same time, the obtained data clearly demonstrate the prospects of using such diffusely scattering materials as PTFE for internal placement in the recirculator cavity. A series of calculations were performed to determine the dependence of the E_{ave_c} value on the absorption of radiation in the lamp and on the surface scattering properties. The width of the receiving area was constant ($w = 40 \text{ mm}$). The values of k_{lamp} (0.4;0.5;0.6) were chosen on the assumption that, in one way or another, the lamp absorbs about half of the radiation passing through it. A deviation of 0.1 was set as the interval for subsequent data analysis. $q = 0.85;0.875;0.9;0.925$. The calculation results are shown in Fig. 11.

There is a strong correlation between the increases in the values of E_{ave_c} and k . However, the nature of the growth of E_{ave_c} changes insignificantly when k changes in the range 0.4–0.6. It can be assumed that with a decrease in the level of diffuse scattering to $q \sim 0.7$ (or 70%), the difference E_{ave_c} due to different absorption in the lamp may cease to be taken into account—more and more light will be absorbed by the surface of the cavity and less and less light will be reflected and pass through the lamp.

The average increase in illumination M can be considered as the ratio of the values of the radiation density of the receiving areas with and without a cavity. In the case of numerical calculations, $M = E_{ave_c}/E_{ave}$. In Fig. 12 there is good agreement between the M value of experiment and calculations. The values obtained at $q = 0.875$ agree best.

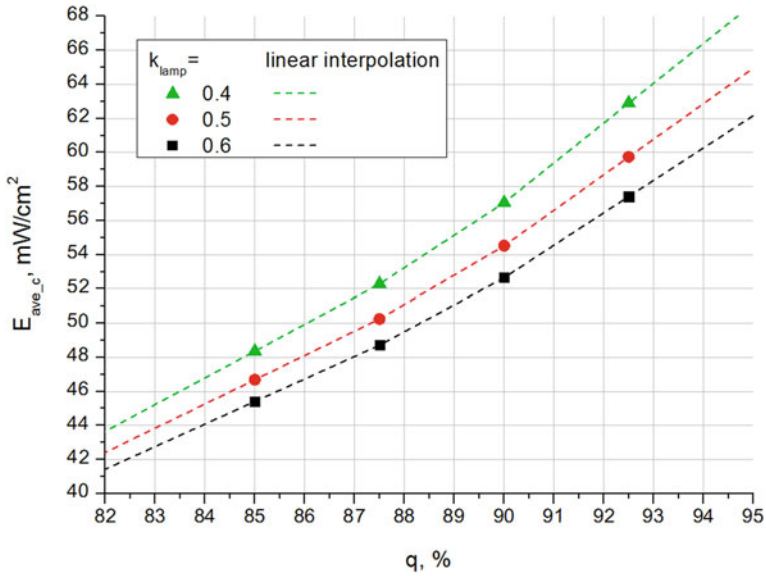


Fig. 11 Comparison of the results obtained at different values of q and k for the case with a cavity. Shapes—calculation data, dashed lines—linear interpolation

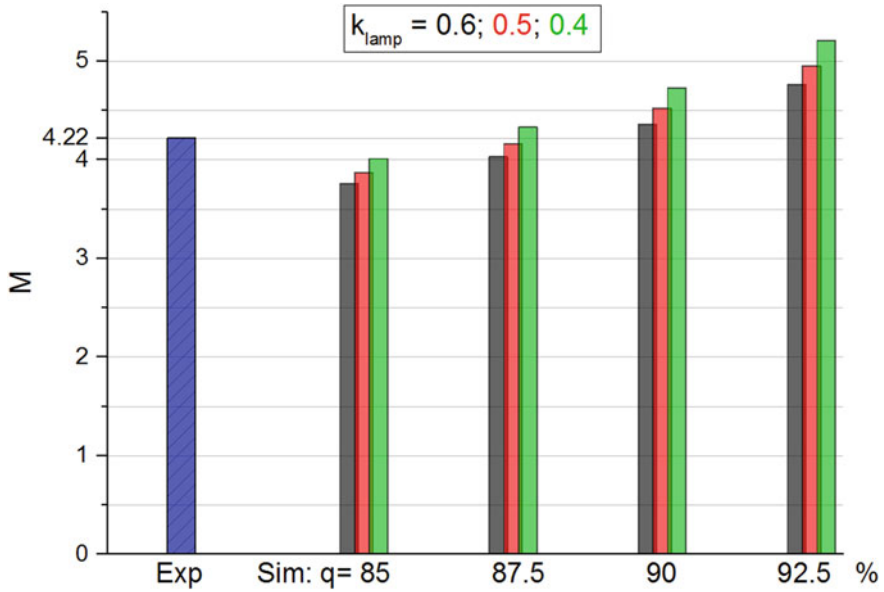


Fig. 12 Comparison of the coefficient of increasing illumination in the experiment and calculations

6 Conclusion

To increase the energy efficiency of recirculators and UV cleaning, it is necessary to increase the efficiency of using bactericidal radiation. This is especially important if it is necessary to provide a high degree of sterilization or to sterilize air containing microorganisms more resistant to UV radiation. This increase can be achieved by using a material that diffusely scatters UV radiation. The use of a cylindrical cavity made of a scattering material with a longitudinal cylindrical radiation source is excellent for this.

The use of PTFE is considered as a material that diffusely scatters UV radiation. A UV ozone-free mercury lamp with the main radiation at a wavelength of 253.7 nm is considered as a radiation source. Experiments have been carried out to demonstrate the transmission and scattering of UV radiation in a cylindrical PTFE cavity. Numerical calculations of the study of experimental geometry, carried out by the ray tracing method, give similar results. The use of a cylindrical PTFE cavity with a mercury lamp inside made it possible to increase the illumination value by 253.7 nm due to effective diffuse UV scattering by more than 4 times inside the cavity compared to its absence. When using materials with a higher UV scattering coefficient, such as expanded fluoroplastic (ePTFE) or spectralon, the increase in illumination inside the cavity will be higher. The results obtained are of interest for UV germicidal application.

Acknowledgements The support received by the Government program (#AAAA-A20-120011690135-5) is highly acknowledged.

References

- Chatterley C, Linden K (2010 Sep) Demonstration and evaluation of germicidal UV-LEDs for point-of-use water disinfection. *J Water Health* 8(3):479–486
- Clark RW (2012) Methods and apparatus for diffuse reflective UV cavity air treatment, Patent US 2012/0315184 A1
<https://doc.comsol.com/5.4/doc/com.comsol.help.roptics/RayOpticsModuleUsersGuide.pdf>
(reference date 06/05/2021)
- <https://www.bakt.ru/> (reference date 06/05/2021)
- Jacquez JA, Kuppenheim HF (1955) Theory of the integrating sphere. *J Opt Soc Am* 45:460–470
- Janecek M (June 2012) Reflectivity spectra for commonly used reflectors. *IEEE Trans Nucl Sci* 59(3):490–497
- Judd DB (1942) Fresnel reflection of diffusely incident light. *J Res Natl Bur Stand* 29
- Keitz HAE (1971) Light calculations and measurements. Macmillan and Co., Ltd., London, UK
- Kostyuchenko S, Khan A, Volkov S, Giller H (2009) UV disinfection in Moscow metro public transport systems. *IUVA News*, Moscow
- Lizotte TE (2012) UV PTFE diffuser technology, Patent US 2012/0168641 A1
- Quill T, Weiss S, Hirschler C, Pankadzh V, DiBattista G, Arthur M, Chen J (2016) Ultraviolet reflectance of microporous PTFE. UV+EB 2016 Technology Conference [Equipment session]. RadTech North America, Chicago, IL, USA

- Reflectance Materials and Coatings. Technical Guide. Labsphere, Inc. p 21
- Rudoy IG, Solovyev NG, Shemyakin AN, Yakimov MY (2018) Bactericidal irradiator, Patent RU 188 297 U1
- Rudoy IG, Yakimov MY (2020) Optical shutter for a bactericidal irradiation, Patent RU 2 738 770 C1
- Sasges M, Robinson J, Daynouri F (2012) Ultraviolet lamp output measurement: a concise derivation of the Keitz Equation, *Ozone Sci Eng* 34(4):306–309
- Vasilyak LM, Vasiliev AI, Kostyuchenko SV et al (2011) Determination of the cathode and anode voltage drops in high power low-pressure amalgam lamps. *Plasma Phys Rep* 37:1173–1177
- Vasilyev A, Vasilyak L, Kostyuchenko S, Kudryavtsev N, Sokolov D, Startsev AY (2009) Influence of starting mode on service life of low pressure powerful amalgam lamp electrodes. *Light Eng* 17:66–74
- Voronov A, Arnold E, Roth E (2003) Long life technology of high power Amalgam lamps. In: Second International Conference on Ultraviolet Technologies. Vienna, Austria, International Ultraviolet Association, Ayr, ON, Canada. PS2
- Waldwick B, Chase C, Chang BY (2007) Increased efficiency and performance in laser pump chambers through use of diffuse highly reflective materials, *Proc. SPIE* 6663, Laser beam shaping VIII, 66630N
- Waymouth JF (1971) *Electric discharge lamps*. The MIT Press, p 384

Determination of the Matter Fluxes on the Sea Bottom Using a Variational Assimilation Algorithm and Remote Sensing Data



Kochergin Vladimir Sergeevich  and Kochergin Sergey Vladimirovich 

Abstract The paper considers a variational algorithm for the assimilation of satellite measurements of the suspended matter concentration in the upper sea layer by identifying the admixture fluxes at the bottom of the sea. The algorithm is implemented for the model of passive admixture transfer in the time interval of two days. The calculations made it possible to estimate the values of the flows at the bottom of the sea and analyze them. The identification procedure is implemented on the basis of minimizing the quadratic functional of the forecast quality and solving adjoint problems.

Keywords Transport model · Adjoint equations · Identification of matter flows · Sea of Azov

1 Introduction

For a more accurate description of admixture transport in the Sea of Azov, not only modern adequate numerical models (Ivanov and Fomin 2008; Fomin 2002) of hydrodynamics and substance transport are needed, but also algorithms for assimilation of measurements (Marchuk and Penenko 1978; Penenko 1981; Agoshkov et al. 2013), which allow identifying the parameters of these models and correcting them for adequate modeling of processes. Such algorithms are usually based on the minimization of some cost functions under constraints in the form of the used numerical model. In this paper, we consider an example of variational data assimilation on the concentration of suspended matter in the upper layer of the Azov Sea obtained from satellite information. Modern methods of processing satellite images (Kochergin and Kochergin 2010) allow us to obtain operational information about the admixture concentration from images of the sea surface in the optical range. The combined use of surface admixture concentration values and transport models is of interest not only to fill in the gaps in the measurement data, but also to determine the sources of

K. V. Sergeevich (✉) · K. S. Vladimirovich
Marine Hydrophysical Institute RAS, Sevastopol 299029, Russian Federation

suspended matter intake. Therefore, the development of algorithms that allow identifying various input parameters of numerical modeling based on measurement data is important and relevant. In this paper, the flow of matter at the bottom of the sea was chosen as a parameter to be identified. Such joint use of satellite data, models of passive admixture transport, and variational methods of measurement data assimilation is of interest for determining the spatial structure of suspended matter and its fluxes over a given time interval. When implementing the variational identification algorithm, gradient methods are used to find optimal estimates, which are sought by minimizing the quality functional. The solution of the adjoint problem is necessary to construct the gradient of the functional in the direction of which the iterative descent is carried out. When implementing the variation procedure, the integration of the main, adjoint tasks and the task in variations is performed. As input parameters of the transport model, the calculations obtained from the model (Kochergin and Kochergin 2010) for the water area of the Azov Sea under the east wind influence are used.

2 Transport Model

Let's consider the transport model of a passive admixture in σ -coordinates

$$\frac{\partial DC}{\partial t} + \frac{\partial DUC}{\partial x} + \frac{\partial DVC}{\partial y} + \frac{\partial WC}{\partial \sigma} = \frac{\partial}{\partial x} A_H \frac{\partial DC}{\partial x} + \frac{\partial}{\partial y} A_H \frac{\partial DC}{\partial y} + \frac{\partial}{\partial \sigma} \frac{K}{D} \frac{\partial C}{\partial \sigma} \quad (1)$$

on the lateral boundaries we use following condition

$$\Gamma : \frac{\partial C}{\partial n} = 0, \quad (2)$$

at the surface and bottom we use similar boundary conditions

$$\begin{aligned} \sigma = 0 : \frac{\partial C}{\partial \sigma} &= 0 \\ \sigma = -1 : \frac{\partial C}{\partial \sigma} &= 0 \end{aligned} \quad (3)$$

and initial data set as follows

$$C(x, y, \sigma, 0) = 0 \quad (4)$$

where t —time; x_0, y_0 —coordinates of the point source; D —dynamic depth; C —admixture concentration; U, V, W —components of the velocity field; A_H and K —coefficients of horizontal and vertical turbulent diffusion, respectively; n —normal to the lateral boundary.

3 Variational Identification Algorithm

Let the measurement data be available at a finite time, then the task of assimilating the measurement data is to minimize the quadratic functional

$$I_0 = \frac{1}{2} [P(RC - C_m), P(RC - C_m)]_M \tag{5}$$

where M —area of integration of the model on the time interval $[0, T]$, P —operator of filling in the field of forecast residuals with zeros in the absence of measurement data, R —operator of projecting to the observation points, and the scalar product is determined in the standard way. Minimizing (5) with model constraints (1)–(3) is equivalent to finding the extremum of the following functional

$$I = I_0 + \left[\frac{\partial DC}{\partial t} + \frac{\partial DUC}{\partial x} + \frac{\partial DVC}{\partial y} + \frac{\partial WC}{\partial \sigma} - \frac{\partial}{\partial x} A_H \frac{\partial DC}{\partial x} - \frac{\partial}{\partial y} A_H \frac{\partial DC}{\partial y} - \frac{\partial}{\partial \sigma} \frac{K_H}{D} \frac{\partial C}{\partial \sigma}, C^* \right]_{M_t} + \left(\frac{\partial C}{\partial n}, C^* \right)_{\Gamma_t} + (C - C_0, C^*)_M + \left(\frac{\partial C}{\partial \sigma} - Q(x, y), C^* \right)_{\sigma_t^{-1}} \tag{6}$$

where $M_t = M \times [0, T]$, $\sigma_t^{-1} = \sigma^{-1} \times [0, T]$

Writing down the variation of the functional (6) and integrating it in parts, taking into account the boundary conditions and the analogue of the continuity equation in σ -coordinates, we obtain

$$\delta I = (\delta Q(x, y), C^*)_{\sigma_t^{-1}} \tag{7}$$

where C^* —Lagrange multipliers that are chosen from the solution of the following adjoint problem

$$-\frac{\partial DC^*}{\partial t} - \frac{\partial DUC^*}{\partial x} - \frac{\partial DVC^*}{\partial y} - \frac{\partial WC^*}{\partial \sigma} - \frac{\partial}{\partial x} A_H \frac{\partial DC^*}{\partial x} - \frac{\partial}{\partial y} A_H \frac{\partial DC^*}{\partial y} - \frac{\partial}{\partial \sigma} \frac{K_H}{D} \frac{\partial C^*}{\partial \sigma} = 0 \tag{8}$$

$$\Gamma : \frac{\partial C^*}{\partial n} = 0, \sigma = 0 : \frac{\partial C^*}{\partial \sigma} = 0, \sigma = -1 : \frac{\partial C^*}{\partial \sigma} = 0 \tag{9}$$

$$t = T : C^* = -P(RC - C_m) \quad (10)$$

From the stationarity of the functional and the definition of its gradient, we have

$$\nabla_{Q(x,y)} I = \int_0^T C^*(x, y, -1, t) dt \quad (11)$$

The power value of the source is searched iteratively

$$Q^{n+1}(x, y) = Q^n(x, y) + \tau \bullet \nabla_{Q(x,y)} I \quad (12)$$

where τ —iterative parameter is found as

$$\tau = \frac{(P(RC - C_m), PR\delta C)_M}{(PR\delta C, PR\delta C)_M} \quad (13)$$

where δC —solution of the problem in variations

$$\frac{\partial D\delta C}{\partial t} + \frac{\partial DU\delta C}{\partial x} + \frac{\partial DV\delta C}{\partial y} + \frac{\partial W\delta C}{\partial \sigma} = \frac{\partial}{\partial x} A_H \frac{\partial D\delta C}{\partial x} + \frac{\partial}{\partial y} A_H \frac{\partial D\delta C}{\partial y} + \frac{\partial}{\partial \sigma} \frac{K}{D} \frac{\partial \delta C}{\partial \sigma} \quad (14)$$

with conditions on the side borders

$$\Gamma : \frac{\partial \delta C}{\partial n} = 0 \quad (15)$$

boundary conditions on the surface and at the bottom

$$\begin{aligned} \sigma = 0 : \frac{\partial \delta C}{\partial \sigma} &= 0 \\ \sigma = -1 : \frac{\partial \delta C}{\partial \sigma} &= \nabla_{Q(x,y)} I \end{aligned} \quad (16)$$

and initial data set as follows

$$\delta C(x, y, \sigma, 0) = 0 \quad (17)$$

At first the direct problem (1) (4) with some initial value is solved. After then the functional (5) is determined) and the adjoint problem (8) (10) is solved. The gradient (11) of cost function (5) is determined by (6) and the variations problem (14) (17)

is integrated. The iterative parameter is calculated using the formula (13) and the power of the source is found by the formula (12) iteratively.

4 Results of Numerical Experiments

Numerical experiments were carried out using the model from [11] for the water area of the Azov Sea. To implement the procedure for identifying the pollution power, a calculation was made to establish a model field of currents under the influence of a constant wind of the east direction at a speed of 10 m/s. As a result of the simulation, the spatial distribution of the coefficients A_H and K was also obtained. The velocity fields and turbulent diffusion coefficients were used as input information when integrating the passive admixture transport model for a period of 2 days.

As measurement data for October 16, 2015, the concentration values obtained in accordance with the work (Kremenchuckij et al. 2014) on the MODIS AQUA pseudo-color composite were taken. These numerical values of the suspended matter concentration were used for their variational assimilation by initializing the initial data for the previous number. As a result, on October 16, a three-dimensional field was obtained, which is consistent on the surface with the data due to the minimization of the functional and with the model used. The surface concentration values are shown in Fig. 1.

According to (<http://dvs.net.ru/mp/data/201507vw.shtml>) by October 18, there was a decrease in wind impact, which means that the intensity of bottom sediment churning decreased, especially in the dynamically active zones of the Sea of Azov. The model concentration field for October 18, consistent with the measurement data, is shown in Fig. 2. The largest changes in the concentration of suspended matter

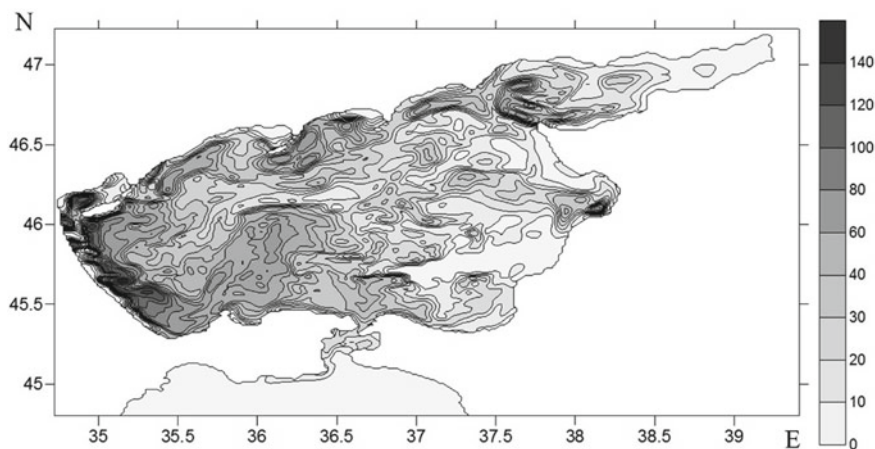


Fig. 1 Sea surface concentration field (mg/m^3), October 16, 2015

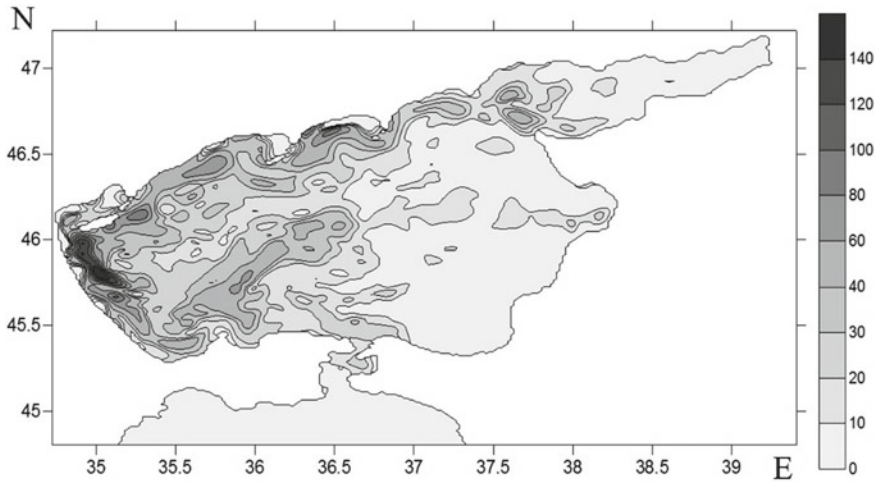


Fig. 2 Sea surface concentration field (mg/m^3), October 18, 2015

occurred in the waters of the Long Spit, the Elenin Bank, the Akhtar Bank, the Zhelezinskaya Bank and the Sandy Islands Bank. Such changes in the concentration of suspended matter in the upper layer of the sea are most likely determined by the composition of the bottom sediments, i.e., the presence of sand, which has a more larger size.

As a result of the assimilation of the numerical data for October 18, due to the identification of the fluxes of matter at the bottom, the values of the forecast quality functional fall. The procedure is implemented iteratively. Figure 3 describes the change in the normalized value of the forecast quality functional to its original value. During iterations, the values of the normalized functional drop by 75% of its original value. In the future, the convergence of the iterative process slows down. It should be noted that the value that the value of the functional reaches in the iteration process remains significant. This means that the model does not fully describe the processes occurring in the sea. Apparently, it is necessary to take into account not only the processes of agitation, but also deposition, taking into account the size of the suspension, namely its component. As a result of the variational assimilation procedure, we obtain the admixture flow field at the bottom, shown in Fig. 4.

The picture below shows the main dynamic formations and characteristic features of the bottom relief, which affect the processes of admixture intake and its dynamics.

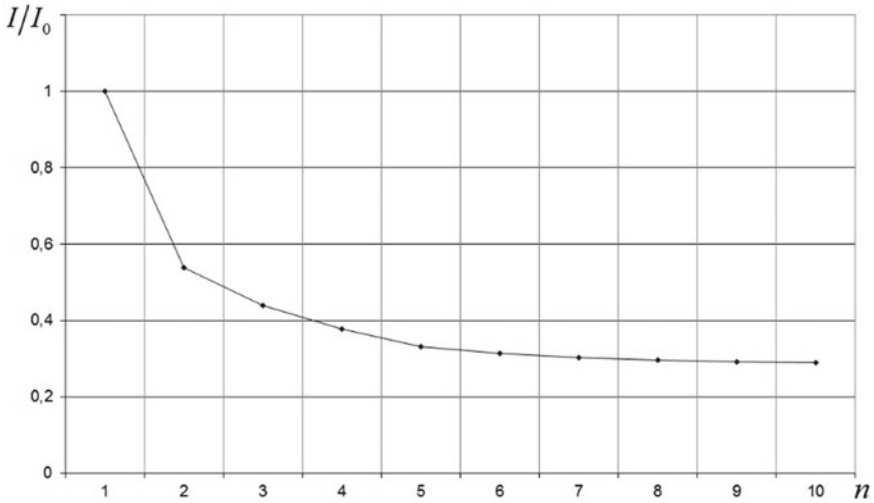


Fig. 3 Dependence of the relative value of the forecast quality functional on the number of iterations

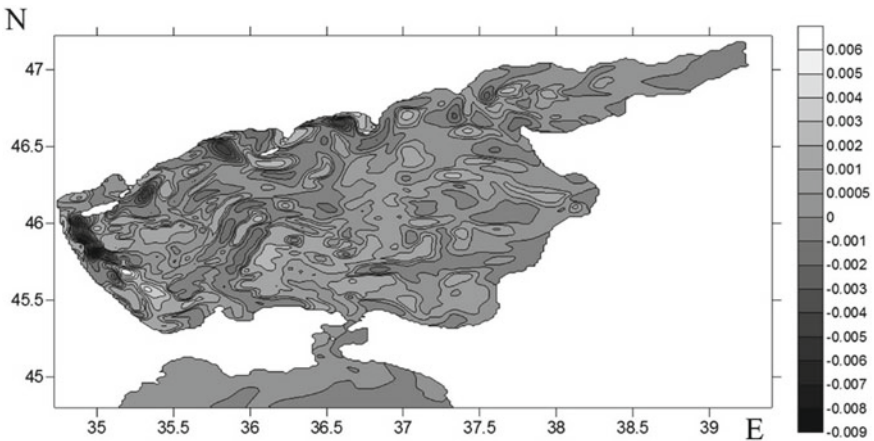


Fig. 4 Admixture flow field at the bottom $mg/(m^3 \cdot sec)$

5 Conclusions

Numerical experiments have shown that it is possible to identify the space-variable admixture flow field at the bottom in the process of implementing a variational algorithm for assimilation of measurement data in a three-dimensional model of passive admixture transport. It is shown that when identifying the values of the admixture flux at the bottom of the sea, the value of the forecast quality functional decreases during iterations. The inability to further minimize the functionality leads

to the need to take into account additional processes in the transport model used for a more adequate description of the processes occurring in the sea.

The work was carried out within the framework of the state task on the topic 0555–2021–0005 “ Complex interdisciplinary studies of oceanological processes that determine the functioning and evolution of ecosystems in the coastal zones of the Black and Azov Seas.

References

- Agoshkov VI, Parmuzin EI, SHutyayev VP (2013) Observational data assimilation in the problem of Black Sea circulation and sensitivity analysis of its solution. In: *Izv. RAN, Fizika atmosfery i okeana*, vol 49, no 6, pp 643–654
- Fomin VV (2002) Numerical model of the water circulation of the Sea of Azov. In: *Nauchnye trudy UkrNIGMI*, 249, pp 246–255 (2002)
- Ivanov VA, Fomin VV (2008) Mathematical modeling of dynamic processes in the sea-land zone. *ECOSI-Gidrophisika*, Sevastopol, p 363
- Kochergin VS, Kochergin SV (2010) The use of variational principles and the solution of the adjoint problem, identification of input parameters for models of transport of passive tracer. *Ecological Safety of Coastal and Shelf Zones and Comprehensive Use of Shelf Resources*, vol 22, MGI, Sevastopol, pp 240–244
- Kochergin VS, Kochergin SV (2015) Identification of a Pollution Source Power in the Kazantip Bay Applying the Variation Algorithm. *Phys Oceanogr* 2:69–76
- Kremenchuckij DA, Kubryakov AA, Zav'yalov PO, Konovalov BV, Stanichnyj SV, Aleskerova AA (2014) Determination of the concentration of suspended matter in the Black Sea according to the data of the MODIS satellite. *Ecological Safety of Coastal and Shelf Zones and Comprehensive Use of Shelf Resources*, vol 29, MGI, Sevastopol, pp 1–9
- Marchuk GI, Penenko VV (1978) Application of optimization methods to the problem of mathematical simulation of atmospheric processes and environment. In: *Modelling and Optimization of Complex Systems*, IFIP-TC7 Working Conference New York: Springer, pp 240–252
- Marchuk GI (1981) *Mathematical modeling in the environmental problem*. M. Nauka, p 320
- Penenko VV (1981) *Methods for numerical modeling of atmospheric processes*. L.: Gidrometeoizdat, p 350

Determination of the Vertical Velocity in Hydrodynamic Model Using Nested Grids



Kochergin Vladimir Sergeevich  and Kochergin Sergey Vladimirovich 

Abstract In this paper, we consider an algorithm for correcting the vertical velocity component in dynamic models, which reduces the influence scheme viscosity. The procedure is based on solving the problem on two grids on a vertical coordinate and calculating the vertical velocity by “excluding” the scheme viscosity. The use of such a procedure allowed us to obtain a solution in its spatial structure consistent with both calculations, but with values even higher than when calculating on a fine grid.

Keywords Dynamic model · Vertical velocity calculation · Exclusion of scheme viscosity · Azov Sea

1 Introduction

In the numerical implementation of hydrodynamic models, a special place is occupied by the procedures for calculating the vertical component of the velocity, which is of great importance in the formation of dynamic fields during integrating the model. Usually, the continuity equation of an incompressible fluid is used to calculate it. It should be noted that the determination of the vertical velocity contains significant errors (Marchuk and Sarkisyan 1988). Error reduction is possible due to the use of special algorithms (Eremeev et al. 2008; Kochergin and Dunets 2001), based on the vertical differentiation of the continuity equation and the organization of the run procedure taking into account both homogeneous boundary conditions on the sea surface and on the bottom. In this approach, the second order of approximation is used and there is no scheme viscosity. In (Kochergin et al. 2021), this approach is compared with the exact analytical solution of the simplified test problem of wind circulation. In addition, an approach to calculating the vertical velocity component based on the method of “exclusion” of the circuit viscosity on nested grids is proposed in Kochergin et al. (2021).

K. V. Sergeevich (✉) · K. S. Vladimirovich
Marine Hydrophysical Institute RAS, Sevastopol 299029, Russian Federation, Russia

2 Method

The idea of the method is to solve the problem on two grids with different depth steps, i.e. in one calculation of the levels twice as much as in the other. The obtained values of the vertical velocity are denoted by W_h and W_{2h} . Then following (Kochergin 1978), you can write the corrector:

$$W = 2W_h - W_{2h} \quad (1)$$

Note that the values satisfy the corresponding continuity equation due to the linearity of the corrector.

3 Results of Numerical Experiments

Numerical experiments were carried out using the model (Ivanov and Fomin 2008; Fomin 2002) for the water area of the Sea of Azov. To implement the procedure for identifying the power of pollution, a calculation was made to establish a model field of currents under the influence of a constant east wind at a speed of 10 m/s. As a result of the simulation, the spatial distribution of velocity fields and turbulent diffusion coefficients was obtained, which were used as input information when integrating the passive admixture transport model for a period of 5 days.

In the first calculation, $k = 15$ vertical horizons were used, and in the second calculation, 30 horizons were selected. The correction was made according to the formula (1) after the solution was released to the stationary state (Fig. 1) in each calculation.

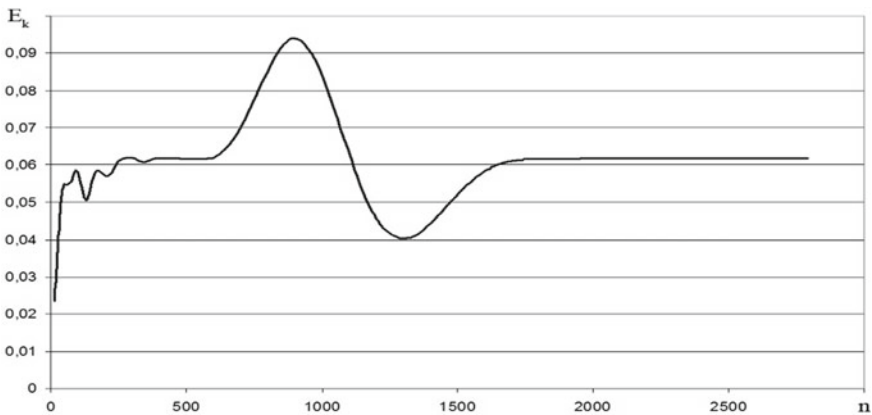


Fig. 1 The behavior of the kinetic energy during the integration of the model (n – the number of steps of the model time)

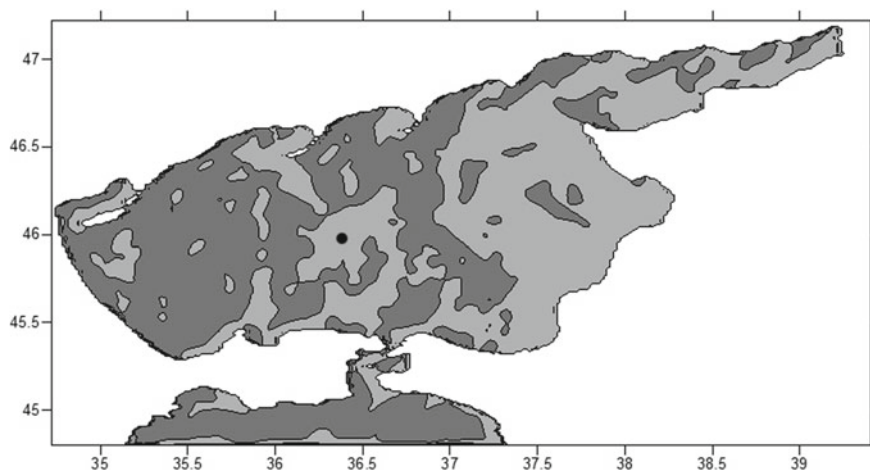


Fig. 2 Vertical velocity in the near-surface layer (the areas of water rise are indicated by a dark tone)

Figure 1 shows that after integrating for 1800 steps of the model time (5 days), the kinetic energy practically does not change, i.e. we have obtained a steady-state solution.

The spatial structure of the vertical velocity, for example, in the near-surface layer, is similar in both calculations. Only the values differ. When using a smaller grid, the values are slightly higher. Figure 2 shows the spatial distribution of the vertical velocity in the near-surface layer when using 15 vertical horizons.

From Fig. 2, it can be seen that in the structure of the vertical velocity field under this wind influence, not only the banks of Elenin and the Long Spit are visible, but also the Zhelezinskaya bank. With the wind influence of the eastern directions, the bench near the western shore of the Long spit is fully manifested. The configuration of the speed at the east wind influence at the Long spit is interesting. The results of numerical simulations of passive admixture transport in the Sea of Azov (Kochergin et al. 2020) showed that such a configuration in the concentration field is obtained under intense wind action of the eastern direction. It should be noted the sinking of the waters in the area of the Obitochnaya spit, Berdyansk and other spit of the northern coast of the Sea of Azov (light gray). This lowering is noticeable in Fig. 3 (dark color), which characterizes the increased concentration of suspended matter (light tones) in the upper layer of the sea (<https://earthdata.nasa.gov/labs/worldview/?p=geographic&l=MODIS>) in case of wind impact of the eastern direction (<http://dvs.net.ru/mp/data/201507vw.shtml>).

Figure 4 describes the values of the vertical velocity in depth for a separately selected point indicated in Fig. 2 by the black dot.

Figure 4 shows that when calculating using 30 horizons, the vertical velocity values are slightly higher than when choosing a larger vertical grid. This is due to the presence of a circuit viscosity when approximating the advective terms in the



Fig. 3 MODIS AQUA pseudo-color composite, October 16, 2015

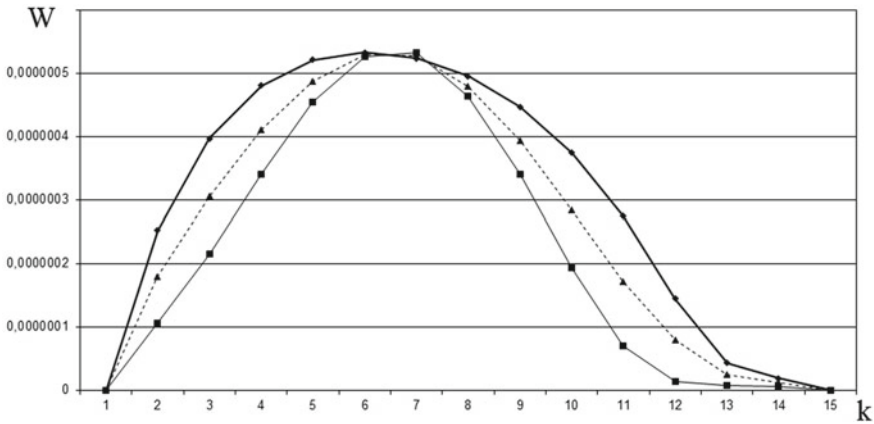


Fig. 4 Vertical velocity values (m/s) at 15 horizons: – thin solid line; – dashed line – bold solid line

calculations of the vertical velocity from the continuity equation. This additional viscosity is proportional to the mesh pitch, so it decreases when using a finer pitch. And when using the corrector, the circuit viscosity is "excluded" (Kochergin 1978) and there is no additional smoothing of the solution, and the speed values are still increased. Figure 4 shows that the modulus of the corrected vertical velocity W at individual horizons exceeds the corresponding values W_{2h} by 1.5–2 times.

4 Conclusions

The numerical experiments made it possible to estimate the values of the vertical velocity due to a special type of corrector, which allows you to exclude the circuit viscosity on nested grids. The results of numerical experiments showed that the corrected velocity exceeds the values obtained with a small vertical step, and therefore with a lower level of additional circuit viscosity. The approach used can be applied to modeling the processes of pollution transport in the sea for a more adequate description of them.

The work was carried out within the framework of the state task on the topic 0555–2021-0005 "Complex interdisciplinary studies of oceanological processes that determine the functioning and evolution of ecosystems of the coastal zones of the Black and Azov Seas" (code "Coastal Research").

References

- Eremeev V N, Kochergin VP, Kochergin SV, Sklyar SN (2008) Mathematical modeling of hydrodynamics of deep-water basins. ECOSI-Gidrophisika, Sevastopol, 363p
- Fomin VV (2002) Numerical model of water circulation in the Azov Sea. Nauchnye Trudy UkrNIGMI, Iss. 249:246–255
- Ivanov VA, Fomin VV (2008) Mathematical modeling of dynamic processes in the sea-land zone. ECOSI-Gidrophisika, Sevastopol, 363p
- Kochergin V.P., Dunets T.V (2001) Computational algorithm of the evaluations of inclinations of the level in the problems of the dynamics of basins. Physical oceanography, №3, Volume 11, pp. 221–232
- Kochergin VS, Kochergin SV, Sklyar SN (2021) Analytical solution of the test three-dimensional problem of wind flows. In: Chaplina T (ed) Processes in GeoMedia – Volume II Springer Geology. Springer, pp 65–71
- Kochergin VS, Kochergin SV, Stanichnyj SV (2020) Variational assimilation of satellite data on the surface concentration of suspended matter in the Azov Sea. In: Sovremennye problemy distancionnogo zondirovaniya Zemli iz kosmosa, T.17, №2, pp 40–48
- Kochergin VP (1978) Theory and methods of ocean currents. M: Nauka, 127p
- Marchuk G.I., Sarkisyan A.S (1988) Mathematical modeling of ocean circulation. M.: Nauka, 302p

Analysis of the Meteorological and Hydrophysical Factors of Massive Wash-Outs of Marine Litter to the Shore of Sambian Peninsula (The Baltic Sea)



S. V. Fetisov, I. P. Chubarenko, and E. E. Esiukova

Abstract Investigations of natural factors leading to large wash-outs of marine debris to the shores of seas and oceans have become urgently needed due to the presence in its composition in the last decades of a significant amount of anthropogenic litter, potentially dangerous to living organisms and humans. This paper provides an analysis of meteorological and hydrophysical factors responsible for the wash-outs of marine debris to the shore of the Baltic Sea. A detailed review of 25 cases of emissions observed on the beach of the northern shore of the Sambian Peninsula. For each of the cases, the variations in time of the wind speed and direction (according to field measurements), the height and the direction of the significant waves (according to reanalysis data) during 10 days preceding the wash-out event are considered. The results of the analysis of the development of hydrophysical situations show that the largest influence on the wash-out of marine debris is exerted by surface waves (the height and direction of the significant waves) during the phase of the storm subsiding. The results obtained are important for the elaboration of a system for predicting massive marine debris wash-outs on the Baltic Sea shores for taking prompt measures to eliminate potentially dangerous contamination.

Keywords Marine debris · Anthropogenic litter · Microplastics · Reanalysis · Significant wave height · Storms · Sambian Peninsula · The Baltic Sea

1 Introduction

The problem of beach contamination with marine debris is becoming more pressing every year and is being actively studied by scientists around the world. Along with natural debris, tons of marine litter of anthropogenic origin are washed ashore each year (UNEP 2016). This poses threats to the health of living organisms and

S. V. Fetisov (✉) · I. P. Chubarenko
Immanuel Kant Baltic Federal University, Kaliningrad, Russia

S. V. Fetisov · E. E. Esiukova
Shirshov Institute of Oceanology RAS, Moscow, Russia

humans, and also negatively affects the touristic and recreational activity in the region.

The drivers for especially large, massive wash-outs of marine debris to the shore is not fully understood (Chubarenko et al. 2021). Typically, sandy beaches of the Baltic Sea are clean (Fig. 1a), but under certain conditions, the sea washes ashore unusually large amount of marine debris (Fig. 1b); this characteristic phenomenon even has a specific local name “brosy” (Chubarenko and Stepanova 2017). General marine litter is a mixture of natural debris or biota and anthropogenic litter: plastic, fishing nets, glass, and other types of litters brought into the environment by humans. Special attention is currently paid to the contamination by synthetic polymers (plastics), since they practically do not degrade under natural conditions, but pose a threat to both marine organisms and the equilibrium of entire ecosystems (Marine Anthropogenic Litter 2015; GESAMP 2016; Wibowo et al. 2019). Only after realizing this danger, programs began to appear to protect the environment from marine litter, which are discussed at the highest levels, both in Russia and around the world. Conducted research, for example, for the Mediterranean Sea, evaluated primarily anthropogenic factors influencing the wash-out and the accumulation of litter, but the drivers influencing the wash-outs of litter on the beach, were not analyzed (Franceschinia et al. 2019). At the same time, the factors influencing the wash-outs are individual for each region (Bakhmet and Naumov 1970; Blinova and Saburin 2005; Kireeva 1960; Suursaar et al. 2014) and are not yet entirely clear, both for the Sambian Peninsula and for other regions of the world (Chubarenko et al. 2021; Weinberger et al. 2020).

There is currently no effective tool for predicting the wash-outs. Attempts have been made to predict the wash-outs of marine debris in the area of the Gulf of Finland, but only seasonal distribution has been achieved (Ryabchenko et al. 2019; Martyanov et al. 2019).

The goal of this study is to analyze the hydrophysical and meteorological situations when (both natural and anthropogenic) litter is washed out onto the shore of the Sambian Peninsula (Fig. 2). Using observational facts, we first try to find the relationship (dependence) between the wash-out events and the preceding meteorological / hydrophysical situation.

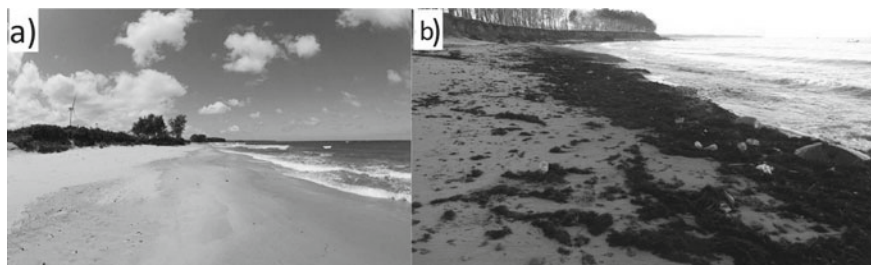


Fig. 1 Photo of the beach in the village Kulikovo: **a** June 2015 (photo by Alexey Milovanov, “New Kalirnigrad.ru”); **b** January 2018 (photo by Elena Esiukova)

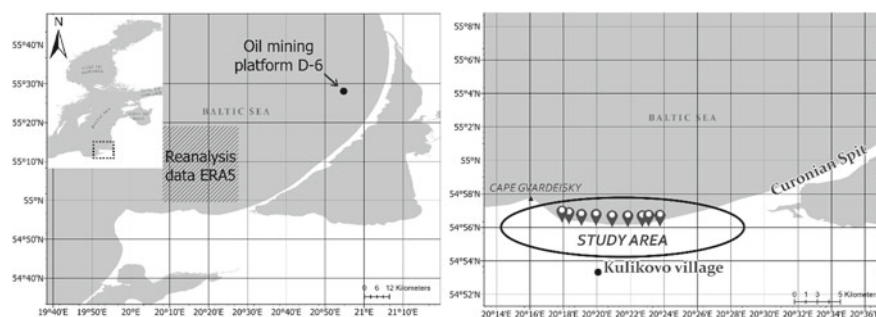


Fig. 2 Research site

2 Data and Methods

2.1 Study Area

Monitoring of wash-out spots on the beaches of the Sambian Peninsula is carried out by scientists from the Shirshov Institute of Oceanology since 2011. During this time, more than 250 cases of the wash-outs of general marine debris with spots of anthropogenic litter were recorded, which inevitably include plastic and microplastic particles. Microplastic particles have their properties (size, density) similar to those of amber particles, which are known to beach the Sambian Peninsula for centuries (Chubarenko et al. 2021, 2018). It has been shown that when amber is washed-out onto the seashore, a rush of anthropogenic litter is also observed (Chubarenko et al. 2018b). In this paper, we have also used the data from open sources about these observations of the massive wash-outs of amber onto the beaches of the Sambian Peninsula.

When choosing a specific site for the analysis, two criteria were applied:

- (i) presence of large enough set of observations of wash-outs;
- (ii) presence of regular sandy underwater slope in the zone of deformation and breaking of waves, required for formation of a more or less uniform wave field.

On the basis of these criteria, the beach of Kulikovo village of the Kaliningrad region (the length of about 5 km) was chosen among, all the beaches of the Sambian Peninsula as the study area. This part of the shore is located between the Cape Gvardeisky and the root of the Curonian Spit. During the observation period (2011–2019) on the shore of the Kulikovo village more than 58 cases of wash-outs spots of marine debris were recorded. This is the maximum quantity among the other beaches of the Sambian Peninsula. Next, we selected 25 most typical cases observed at different times of the year from 2013 to 2019, which are analyzed in detail in this work (Table 1). All the locations of the wash-outs are shown on the map (Fig. 2). Selecting only one beach at the stage of analysis of natural drivers allows to exclude possible influence of anthropogenic factors, such as proximity of settlements, inflowing rivers, fishing activity, etc. on the formation of massive wash-out.

Table 1 Parameters of meteorological and hydrophysical conditions at 12–00 local time (GMT + 2) for each observation.

No	Date of the observed cast	Wind speed at height of 10 m, m/s	Wind direction, degrees	Significant waves height, m	Mean wave direction, degrees
1	13.04.2013	3.5	230	0.52	270
2	12.06.2013	4.3	230	0.28	296
3	14.09.2013	6.9	90	0.65	50
4	24.11.2013	6.9	260	0.93	293
5	15.01.2014	7.8	80	0.70	54
6	30.03.2014	2.6	50	0.11	7
7	27.09.2014	6.1	290	0.75	292
8	6.01.2015	2.6	110	0.50	5
9	24.01.2015	6.1	180	0.47	320
10	31.10.2015	5.2	160	0.27	166
11	21.11.2015	2.6	100	0.50	354
12	5.12.2015	14.7	240	2.13	262
13	10.01.2016	4.3	130	0.76	132
14	12.01.2016	5.2	20	0.58	2
15	16.01.2016	3.5	360	0.61	350
16	18.06.2016	11.2	250	1.66	276
17	9.10.2016	7.8	100	1.00	64
18	4.06.2017	0	0	0.23	96
19	9.01.2018	5.2	230	0.57	298
20	16.06.2018	1.7	280	0.24	293
21	27.10.2018	12.1	260	2.32	263
22	4.11.2018	6.1	160	0.45	120
23	4.01.2019	5.2	280	1.50	297
24	13.04.2019	3.5	50	0.67	45
25	4.08.2019	5.2	340	0.59	357

In this paper anthropogenic factors will not be taken into account, however, in the future, their influence on the amount of anthropogenic litter in the mass of general marine debris should also be taken into account.

2.2 Meteorological and Hydrophysical Data

The development of the meteorological and hydrophysical situation was analyzed for each of the 25 selected cases of massive wash-outs within 10 days before the wash-out event.

For the analysis of the meteorological situation, data on wind speed and direction were considered, obtained on the offshore ice-resistant oil mining platform D-6 (20.67°E, 55.28 °N, Fig. 2). It is located in the open sea at a depth of 30–35 m, in 42 km off the northern shore, selected for our analysis. Wind measurements were performed with steps of 1 h at a height of 32 m, so, before the analysis, the procedure of adjusting the speed values to the standard height of 10 m is applied according to the formula:

$$\frac{w_z}{w_{10}} = \left(\frac{z}{z_{10}} \right)^p$$

where w_z – wind speed at the height z ; w_{10} – wind speed at the height of 10 m; exponent $p = 0.125$. This method of reduction is common, and is widely used by climatologists, forecasters, engineers (Nesterova 2013).

The hydrophysical situation was characterized by the development of surface waves according to the Copernicus reanalysis data (Hersbach et al. 2018). The sea surface wave field is characterized by a combination of waves of different heights, lengths and directions, known as a two-dimensional wave spectrum. The spectrum of waves can be decomposed into wind waves, which are directly driven by local winds, and swell, i.e., the waves that were created by the wind earlier or in another region. In this paper, the significant height of combined wind waves and swells is used for the analysis. The values of these significant waves' height and direction with the time step of 1 h were analyzed within the 0.5° square (around the point 20°E, 55°N) and during 10 days before each of the observed wash-outs of marine debris to the shore.

2.3 Data Analysis

From the reports on visual observations from open sources it is not possible to determine the exact time of the beginning and end of the wash-out. Therefore, in the following analysis, the unified approximate time was used when the observers usually come to the shore—12–00 local time (GMT + 2). During the visits of observers of the IO RAS near the Kulikovo village, for each observation, a detailed description of the place, time and size of the wash-out spot was compiled. Additionally, the type of sediment (sand, small/coarse pebbles, boulders), the location of the wash-outs relative to the characteristic morphodynamic areas, the width of the beach, the predominant

species composition of macroalgae (for example, *Furcellaria lumbricalis*, *Polysiphonia fucoides* or *Cladofora glomerata*) were recorded, with detailed photography. Based on these data, it is possible to draw some additional conclusions about the wash-out event, based on the presence of algae on the beach, on the shoreface, in the water, and by their appearance. For example, if the algae are located in the water and at the water edge, the algae are shiny, elastic, have an integral structure (i.e., they are “fresh”), then the wash-out is currently taking place. If the spot of algae is located on the beach and sprinkled with sand or pebbles (algae are pressed, dried, have a dull look), then the wash-out is more than 3 days old.

3 Results and Discussion

In total, an analysis of the development of hydro-meteorological situation before 25 cases of massive marine debris wash-outs to the shore of the Sambian Peninsula was carried out (Table 1). For the analysis of all the cases, an observation period of 10 days before the wash-out event was used.

3.1 *Typical Example of the Development of the Situation*

Most of the observed cases of wash-outs (84%) developed following a similar scenario. As a typical case, No. 8 of 06.01.2015 was chosen (Table 1): observers' records confirm that the wash-out continued during the observation, i.e., large amounts of algae were found at the shoreface and in water. Also on this day, a wash-out of amber was observed. By the example of observation No. 8, we shall consider the typical development of the hydrophysical and meteorological situation 10 days before the wash-out.

As can be seen from Fig. 3, the wind speed began increasing from 02–00 a.m. (local, GMT + 2) of 30.12.2014: during 12 h it increased from 1 m/s to 15 m/s. Over this time, the wind direction changed from E-NE to the opposite W-SW, and remained the same further until 21–00 of 05.01.2015. During 6 days, wind subsidence down to 5 m/s and sharp increases up to 23 m/s were observed. A similar pattern was observed also in the development of surface waves (Fig. 4). From 06–00 of 30.12.2014, the height of the significant waves, approaching the shore from western directions, began increasing. At the peak moments on 02.01.2015, the heights of the significant waves reached 4.7 m.

At 18–00 of 04.01.2015, the wind speed and the height of the significant waves began to decrease. Wind and wave directions smoothly changed from western to northern directions; they became perpendicular of the considered shore towards the time of the wash-out event (Fig. 3, Fig. 4).

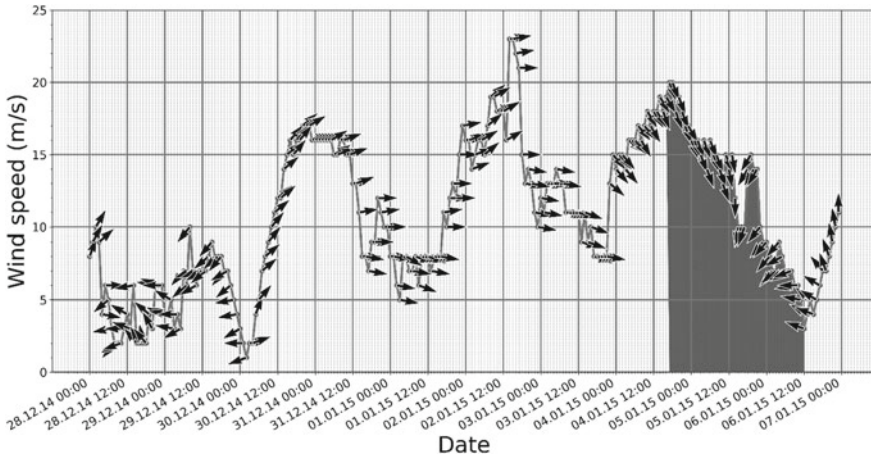


Fig. 3 Change in wind speed (line) and wind direction (arrows) from 28.12.2014 to 06.01.2015

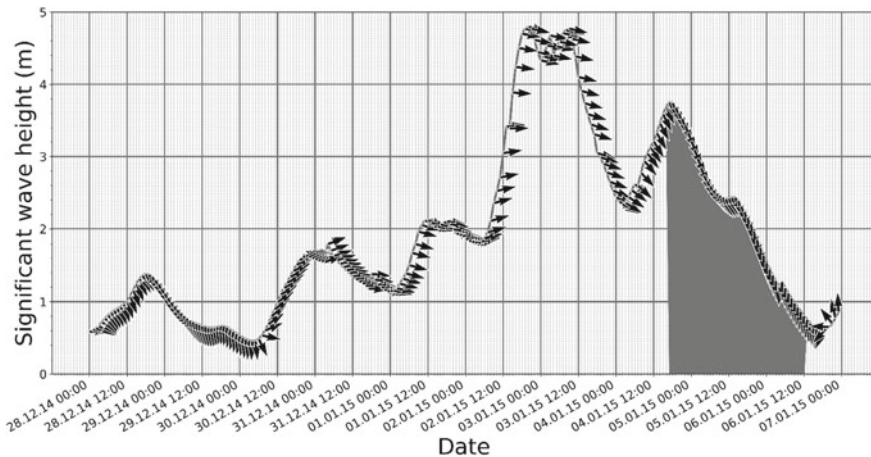


Fig. 4 Change in the height (line) and direction (arrows) of the significant waves from 28.12.2014 to 06.01.2015

3.2 Generalization: A Characteristic Picture and Duration of the Formation of Conditions for a Wash-Out

Based on observations, it was assumed that it is the phase of wind subsidence, supported by a change in the direction of wind and waves approaching the shore, that is the main cause of the massive wash-outs of marine debris (Chubarenko and Stepanova 2017). To confirm this, and also to determine whether there is a similarity in the development of different wash-out situations, the correlation matrices were

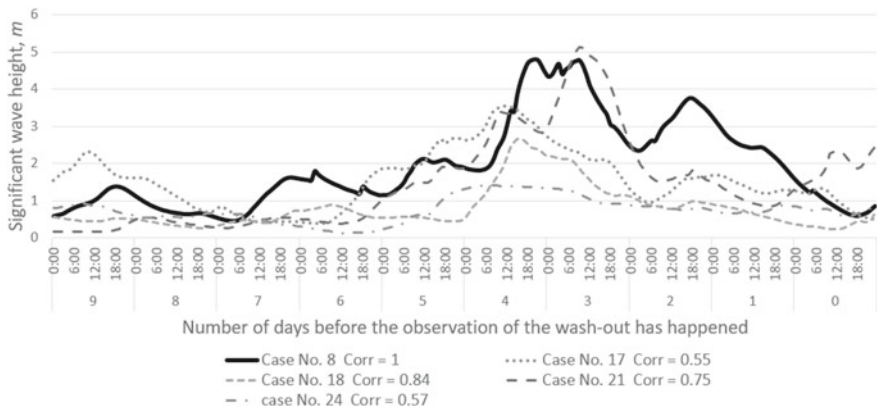


Fig. 5 Graph of changes in altitude over time significant wave height for cases No. 8, 17, 18, 21, 24. Coefficients of correlation with the development of wave situation are shown relatively occasions case No. 8

calculated for each of the parameters considered in this work. Pairwise correlations were calculated using the Pearson criterion between the development in time of the parameters (wind, waves) observed during the formation of the wash-outs listed in Table 1. Each case of observation was represented as the set of values for 10 days with step of 1 h (240 values, Fig. 5).

The maximum correlation coefficients in the development of the wash-out situations were found for parameter a “significant waves height”. For example, for cases № 8 and № 18, the correlation coefficient was 0.84, and № 8 and № 21 - 0.77 (Fig. 5). Based on this, it can be concluded that the development of wave field during wash-outs in different periods of observation is to some extent similar. Moreover, if the time interval is reduced to 5 days, then the correlation coefficient can reach 0.94 (e.g., for cases No. 17 and 20).

Of course, there are pairs of cases with almost zero correlation, i.e., with the absence, at a first glance, of a similarity in the development of the wave field. Or with a negative correlation, i.e., the opposite development trends. The reason for these might be:

- (i) Inaccuracy of binding observations to time: the wash-out ended before it was recorded. Observers can only state the fact of the presence of marine debris on the shore, while the wash-out could have happened earlier.
- (ii) Too long time span was selected for correlation analysis. Indeed, with a decrease in the sampling period, a slight increase in the correlation coefficient is found.

Use of a correlation matrix for the analysis of the direction of wind or wave is formally not possible, since close values of the direction, for example, 1 and 359 degrees, give a significant error, although the direction is practically the same.

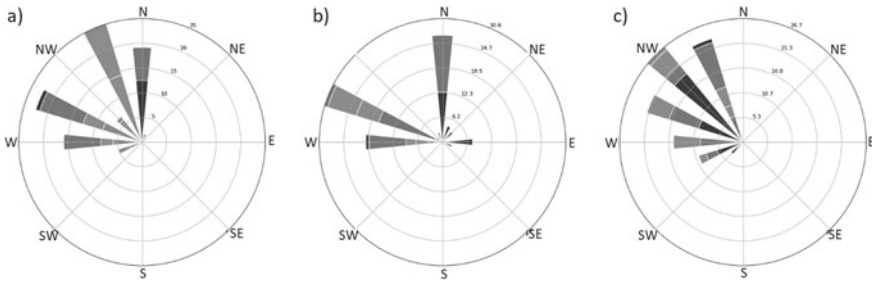


Fig. 6 Roses of the distribution of the direction of the significant wave for 5 days before the moment of observation: a) for case No. 8; b) for case No. 18; c) for case No. 21

Therefore, visual analysis of directions was used with help of the “wind rose” for the wind direction and the “wave rose” for the wave direction according to RD (2018).

As seen at Fig. 6, during the observation period of cases No. 8, 18, 21, the N-NW directions prevailed. If we take a closer look at Fig. 4, it can be seen that for case No. 8 the subsiding phase was slightly less than 2 days, or 42 h (the period is highlighted on the graph). Throughout this period, the direction of the wave and wind was N-NW. For case No. 18, the subsiding phase was also 42 h, and for case No. 21 - 52 h, all with the same wave direction.

For the wind speed, we can also distinguish the subsiding phase. The duration of this phase approximately corresponds to the duration of the wave subsiding phase. However, the wind direction is not so definite. So, for example, for cases No. 8 and No. 21, the N-NW direction prevails, while for case No. 17, the eastern direction is pronounced, and for case No. 9, the direction is from SE-SE.

3.3 Wave Situation During the Very Wash-Outs

From the obtained characteristic picture of the formation of conditions for wash-out, it can be seen that the hydrodynamics exerts obvious influence, related to the height and direction of the significant waves. Based on this, the following conclusions can be drawn:

- (i) Wash-out is observed during the phase of the storm subsiding (decrease the significant wave height and wind speed). The duration of the subsiding phase is on average about 2 days (48 h).
- (ii) The mean direction of the significant wave during the entire subsiding phase is predominantly perpendicular to the shore (from N-NW for the considered beach).
- (iii) The minimum of the significant wave height value in subsided phase at which in fact the wash-out took place was on average about 0.58 ± 0.28 m.

3.4 *The Discussion of the Results*

Events of massive wash-outs of marine debris to the shore of the Sambian Peninsula is traditionally associated with the wind direction. Therefore, prior to the analysis of specific cases of wash-outs, including those used in this paper, it was assumed that the key factor influencing the wash-outs of marine debris from the sea to the shore is the direction of the wind. Historical sources describing the wash-outs of amber to the shore of the Sambian Peninsula claimed that this phenomenon is observed in the presence of a wind directed perpendicular to the shore (Savkevich and Nedra 1970). However, this appeared to be not always the case. The direction of significant waves happened to be much more characteristic.

The influence of waves on the wash-outs of marine debris is quite evident during the subsiding phase. However, before this phase, in almost all the cases, there was a long period in which the direction of the significant wave was westerly. Apparently, this is due to the exposure of the selected study site and suggests similar studies on the western shore of the Sambian Peninsula.

Further development of this work aims at the creation of a forecasting system of the wash-outs of marine debris, where the main tool will be a neural network. The data collected as a part of this work will be used as input parameters. By changing the weighting coefficients between the input data in the learning process, the network itself will be able to outstrip the significance of each parameter and produce the desired result with acceptable accuracy.

4 Conclusion

Based on the results of this research, a relationship was found between the parameters characterizing the development of hydrophysical situations leading to large wash-outs of marine debris to the Baltic Sea shore. The results show that the wave subsiding phase after storms is most important. For the observed cases of wash-outs, there was a similar development of the hydrophysical situation, i.e. the variations in heights and directions of the significant waves. These parameters can be considered the most valuable for the formation of marine debris wash-outs.

Acknowledgements Investigations are supported by the IKBFU competitiveness improvement program for 2016-2020 (project 5-100). Meteorological data collected in the framework of the state assignment of Shirshov Institute of Oceanology RAS No. 0128-2021-0012. Observations of the wash-outs of marine debris on the shore are supported by the Russian Science Foundation, grant No. 19-17-00041 and Russian Foundation for Basic Research, grant No. 18-55-00071. The authors are grateful to "LUKOIL-Kaliningradmorneft" and Zh. Stont for the meteorological information provided.

References

- Bakhmet IN, Naumov AD (2014) Storm emissions of macrophytes in Chupinskaya Bay and in the area of Sonostrov Island (White Sea, Kandalaksha Bay). Modern problems of science and education. No. 2. <http://www.scienceeducation.ru/ru/article/view?id=12990>. Accessed: 21.12.2018
- Blinova EI, Saburin MY (2005) Storm emissions of macrophytes. Formation conditions and influence on the ecological state of the sea (on the example of Anapa Bay, Black Sea). Coastal Hydrobio Res: Proceedings VNIRO. 286–293. <http://hdl.handle.net/123456789/1146>
- Chubarenko B, Woelfel J, Hofmann J, Aldag S, Beldowski J, Burlakovs J, Garrels T, Gorbunova J, Guizani S, Kupczyk A, Kotwicki L (2021) Converting beach wrack into a resource as a challenge for the Baltic Sea (an overview). *Ocean Coastal Manage* 200:105413. <https://doi.org/10.1016/j.ocecoaman.2018.11.015>
- Chubarenko I, Stepanova, N (2017) Microplastics in sea coastal zone: lessons learned from the Baltic amber. *Environ Pollution* 224:243–254. <https://doi.org/10.1016/j.envpol.2017.01.085>
- Chubarenko IP, Esiukova EE, Bagaev AV, Bagaeva MA, Grave AN (2018a). Three-dimensional distribution of anthropogenic microparticles in the body of sandy beaches. *Sci Total Environ* Volumes 628–629:1340–1351. <https://doi.org/10.1016/j.scitotenv.2018.02.167>
- Chubarenko I, Esiukova E, Bagaev A, Isachenko I, Demchenko N, Zobkov M, Efimova I, Bagaeva M, Khatmullina L (2018b) Behavior of microplastics in coastal zones. In: *Microplastic Contamination in Aquatic Environments*. Elsevier, 175– 223, ISBN 9780128137475. <https://doi.org/10.1016/B978-0-12-813747-5.00006-0>
- Franceschinia S, Mattei F, D’Andrea L, Di Nardi A, Fiorentino F, Garofalo G, Scardi M, Cataudella S, Russo T (2019) Rummaging through the bin: modeling marine litter distribution using artificial neural networks. *Marine Pollution Bulletin* 149:110580. <https://doi.org/10.1016/j.marpolbul.2019.110580>
- GESAMP 2016. Sources, fate and effects of microplastics in the marine environment: part two of a global assessment (Kershaw, PJ, and Rochman, CM, eds). (IMO / FAO / UNESCO-IOC / UNIDO / WMO / IAEA / UN / UNEP / UNDP Joint Group of Experts on the Scientific Aspects of Marine Environmental Protection). Rep. Stud. GESAMP No. 93, 220 p.
- Hersbach H, Bell B, Berrisford P, Biavati G, Horányi A, Muñoz Sabater J, Nicolas J, Peubey C, Radu R, Rozum I, Schepers D, Simmons A, Soci C, Dee D, Thépaut JN (2018) ERA5 hourly data on single levels from 1979 to present. Copernicus Climate Change Service (C3S) Climate Data Store (CDS). 147:5–6. <https://doi.org/10.24381/cds.adbb2d477>
- Kireeva M (eds) (1960) Quantitative accounting of algae emissions in the Baltic Sea In: Proceedings of VNIRO, 206–209
- Martyanov SD, Ryabchenko VA, Ershova AA, Eremina TR, Martin G (2019) On the assessment of microplastic distribution in the eastern part of the Gulf of Finland. *Fundamentalnaya i Prikladnaya Gidrofizika*. 12(4) 32–41. <https://doi.org/10.7868/S207366731904004X>
- Nesterova ES (2013) Mode, diagnosis and forecast of wind waves in the Seas and Oceans: scientific and methodological manual. Resp. ed.; MCC of Roshydromet, Research Group Social Sciences, Moscow, Russia, p. 337
- Bergmann M, Gutow L, Klages M (eds) *Marine anthropogenic litter* (2015) Springer p 447. <https://doi.org/10.1007/978-3-319-16510-3>
- Ryabchenko VA, Martyanov SD, Ershova AA, Eremina TR, Martin G (2019) On the distribution of microplastics in the Neva Bay and the eastern part of the Gulf of Finland. The Gulf of Finland Science Days “Facing our Common Future” Helsinki, November 13th–14th 2019
- RD 52.10.865–2017 Guidelines for calculating the operating characteristics of sea wind waves. Moscow: Roshydromet, 2018
- Suursaar Ü, Torn K, Martin G, Herkül K, Kullas T (2014) Formation and species composition of stormcast beach wrack in the Gulf of Riga. *Baltic Sea Oceanologia* 56(4):673–695. <https://doi.org/10.5697/oc.56-4.673>
- Savkevich SS (1970) Amber; Nedra: Leningrad, USSR, p192

- UNEP (2016) Marine plastic debris and microplastics-global lessons and research to in-spire action and guide policy change. United Nations Environment Program: Nairobi, Kenya. Available online: <http://www.unep.org>, <https://www.grida.no>. Accessed: 10.05.2020
- Wibowo YG, Maryani AT, Dewi Rosanti D, Rosarina D (2019) Microplastic in Marine environment and its impact. *Sainmatika* 16:81–87. <https://doi.org/10.31851/sainmatika.v16i1.2884>
- Weinberger F, Paalme T, Wikström S (2020) Seaweed resources of the Baltic Sea, Kattegat and German and Danish North Sea coasts. *Bot Mar* 63(1):61–72. <https://doi.org/10.1515/bot-2019-0019>

The Shores of the Northern Pacific Contact Zones



E. I. Ignatov , V. V. Afanas'ev , and V. Uba 

Abstract On the basis of a map of morphogenetic coastal types, the features of the distribution of coastal types on the sea and ocean sides of the island arc systems were digitized and considered, which became the starting point for the actualization of the problem of the developmental features of the coastlines of linear contact zones dividing sea basins, as well as seas and oceans. The geomorphologic and morphodynamic differences between the sea and ocean coasts of the island arc systems and Sakhalin Island, the eastern shores of which have a subarctic appearance, and the western shores are washed by the temperate sea, are shown. The specificity of the coastal morpholithogenesis of the ocean and seas of the subarctic and temperate zones made it possible to formulate the coastal concept of the contact zones of the North Pacific.

Keywords Contact areas of the seas · Kuril Islands · Aleutian Islands · Sakhalin Island · Coastal morphodynamics

1 Introduction

The boundaries of geosystems are relatively mobile zones of mutual influences and interactions of neighboring geosystems and form so-called contact geographical structures (Likhacheva et al. 2010; Baklanov 2014; Skryl'nik 2017). At the same time, most of the geomorphological boundaries can be considered as a kind of contact zones distinguished in physical geography, and the vast majority of terrestrial processes and phenomena are confined to them (Likhacheva and Timofeyev 2007, 2008).

Earlier, we noted that the morphoclimatic position (geospatial parameters and related differences in morpholithodynamic parameters) of Sakhalin Island and the

E. I. Ignatov
Lomonosov Moscow State University, Moscow, Russia

V. V. Afanas'ev (✉) · V. Uba
FEB RAS, Institute of Marine Geology and Geophysics, Yuzhno-Sakhalinsk, Russia
e-mail: vvasand@mail.ru

island arc systems of the North Pacific allow us to consider them as contact zones of different types of seas, as well as seas and oceans (Afanasev et al. 2020).

The Sakhalin coasts of the temperately cold northern part of the Sea of Japan and the subarctic Sea of Okhotsk are located 30–140 km from each other, and the ocean and sea coasts of large islands in island-arc systems are separated by only a few kilometers. Thus, wind-wave fields and their interaction with swell waves in the contact zones are very complex. The temperature regime of the coasts also largely depends on the geospatial parameters of the contact zones.

The variability of natural conditions also determined the features of the morpholithogenesis of the sea coasts of the contact zones and the specifics of their development and use of natural resources in relation to the zonal and territorial-spatial affiliation.

2 Overview of the Problem

The coasts of the Far Eastern seas of Russia, whose water circulation is part of the general cyclonic circulation of the Northern Pacific, are located in a steadily active transition-contact zone of two of the greatest structures of the Earth, which in the course of interaction exert powerful system-forming influences within the temperate, subarctic and Arctic climatic zones (Skryl'nik 2018).

The geographical location of the Far East on the eastern edge of Eurasia on the border with the Pacific Ocean determines the presence of monsoon circulation here, which can be traced to about 70° n. l. (Dzerdzeevskii 1975; Tunegolovets et al. 2008). At the same time, the features of the monsoon circulation are determined by the interaction of the three main monsoon regions (Lisogurskii and Petrichev 1980). The polar monsoon is developed in a narrow strip along the 70° n. l. From 45° to 65° n. l. the area of the monsoon of temperate latitudes is located. The area of stable subtropical monsoons is located south of the 45th parallel. The interaction of land and ocean is carried out by the interaction of three climatic centers of atmospheric action (the Siberian and North Pacific anticyclones, the Aleutian depression), as well as seasonal centers, namely, the Okhotsk Sea anticyclone and the Amur depression. The influence of the continent is mainly manifested in the form of north-west and north continental air flows (winter monsoon), which greatly reduce the warming effect of the Pacific Ocean on the coast, and the influence of the ocean is manifested by south-east and south marine air flows (summer monsoon).

Other important morphoclimatic factors on the coast are the latitude and weather differentiation of the radiation inflow of solar energy, the influence of climatic fronts (arctic and temperate latitudes) that determine intense cyclonic activity, tropical cyclones, and the barrier role of the terrain.

Modern zonal and provincial features of the relief of the Far East determine the complex and contradictory interacting relief-forming influences, namely, continental and oceanic. There are three groups of countries with a different course of terrain development when combined with different air masses. At the same time, it is noted

that morphostructural features are mainly manifested in the relative youth of the relief, and morphosculptural features in the morphogenetic richness of the appearance of geosystems (Nikol'skaya et al. 1976; Skryl'nik 2008).

It is known that the longitude physical-geographical sectorality and latitudinal zoning of the landscape structure of Europe are formed largely as a result of the interference of heat and moisture flows from the Atlantic and Arctic Oceans (Aleksseev and Golubev 2004; Diakonov et al. 2017). In the case of the Northern Pacific, it was the morphotectonic structure of the continental margins and the history of their development in the Neogene-Quaternary period that determined the features of modern climomorphogenesis, the longitude sectorality and latitudinal zonality of morpholithogenesis on the coast. It should be noted the north-eastern orientation of the main morphostructural elements that determine the main features of the interaction of land and sea, and the relative isolation of the Far Eastern seas from the Pacific Ocean as a result of the development of the Kuril and Aleutian island-arc systems. This has led to the fact that the boundaries of the climatic zones on the coast are significantly shifted counterclockwise (Archikov 1979). Accordingly, the coldest of the Far Eastern seas, the Sea of Okhotsk, belongs to the category of subarctic seas (Matul 2009). Accordingly, the coast of the Sea of Okhotsk has the features of Arctic and subarctic coasts. Summer geomorphological processes occur under the influence of the conditions of the previous winter. The North American coasts of the temperate zone, on the contrary, experience the relief-forming influence of the subtropical zone, since throughout the year coastal morpholithogenesis is influenced by warm ocean currents.

The specificity of the development and modern dynamics of the coasts of the subarctic and temperate zones of the North Pacific was established by analyzing maps of morphogenetic types of coasts (Afanasev et al. 2020; Natsional 2007).

It was noted that the seas of the North Pacific are characterized by a bimodal distribution of the length of the shores of various types (Fig. 1).

The first maximum refers to the abrasive-denudation rocky shores, with a significant contribution to the destruction processes of physical weathering. The second peak is formed by abrasive-accumulative banks. The highest percentage of the total length of this type of coast is on the Sea of Japan and much smaller, even taking into account the actual accumulative shores (types 7 and 8), on the Sea of Okhotsk. It is interesting that the length of the shores with a dead abrasive ledge is higher in percentage terms in the Sea of Okhotsk than in the Sea of Japan. Such a distribution of coast types, along with the structural and geological features of the structure of the coasts, may be associated with the intensive destruction of the coast of the Sea of Okhotsk, during the warm periods of the Holocene, characterized by a longer period of "open sea" at negative air temperatures.

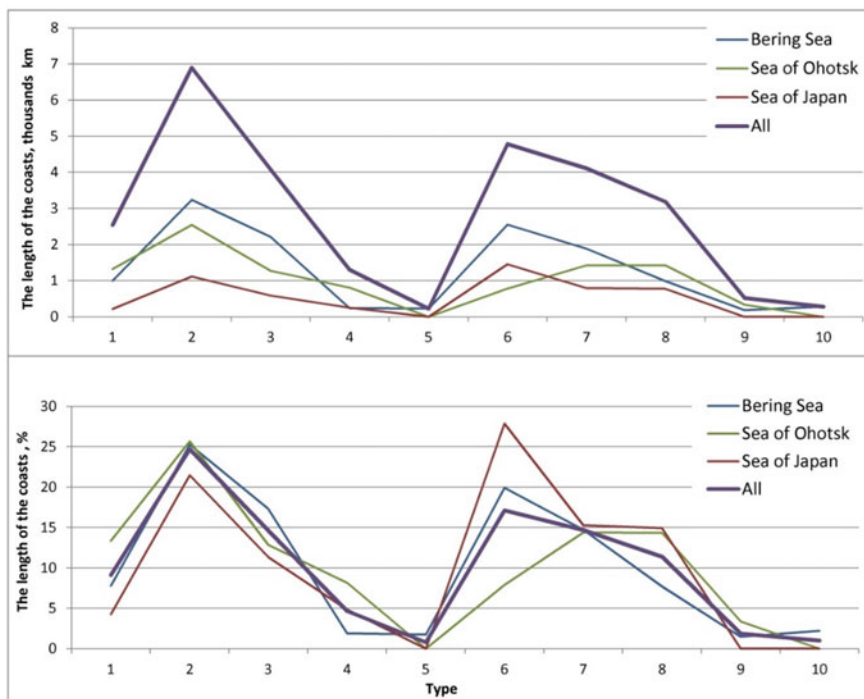


Fig. 1 The length of the types of coasts of the seas of the North Pacific. **a**—the length of the types of coasts in kilometers; **b**—the length of the types of coasts in percent. Types of coasts: 1—with glacial-tectonic dissection (fjord), tectonically determined, 2—abrasion-denudation; 3—abrasion (aligned and coiled); 4—abrasive dead; 5—thermoabrasion and ice; 6—abrasion-accumulative (aligned and coiled); 7—created by wave processes, beach; 8—created by wave processes, lagoon; 9—created by tidal and surging processes; 10—created by wellhead processes (delta) (Afanasev et al. 2020)

3 Research Methodology

The analysis of maps of morphogenetic types of the Northern Pacific coast, which were compiled by one of the authors, was carried out in the geographic information system Quantum GIS, the contours correspond to the accuracy of the original maps (Natsional 2007). To get the length of each type of coastline, use the « Add Geometry Attributes» tool with the « Ellipse Calculation» option. The calculations are made on the ellipse WGS84 EPSG: 7030.

Cartometric studies were carried out on the marine accumulative isthmus of the Wind Island of Iturup (Kuril Islands) and the pyroclastic isthmus of Chuginadak Island (Aleutians). The terrain of the Wind Isthmus is represented by visualization of Aster Global Digital Elevation Model (GDENV2) data, which is a product of the Ministry of Economy, Trade and Industry (METI) and NASA. The information is contained in the Earth Explorer system of the United States Geological Survey. WGS84 coordinate data system, pixel size ~ 20'30 m, mean square error (RMSE) in

height is less than 10 m. To visualize the levels, elevation maps are constructed in a three-dimensional projection with color highlighting of the height ranges from 0 to 120 m in increments of 10 m and shadow washing for higher levels. The analysis of the elevation field allowed us to identify several abrasive and abrasive-accumulative terrace levels in pyroclastic sediments of the Late Pleistocene overlain by coastal-marine and slope sediments. Cartometric studies of the isthmus of Chuginadak Island in the Aster Global Digital Elevation Model (GDEM V2) environment were supplemented with data processing of ALOS World 3D—30 m (AW3D30) Version 2.2; Shuttle Radar Topography Mission (SRTM) 1 Arc-Second Global.

The ground-penetrating radar observations were carried out by the OKO-2 M series ground-penetrating radar (Logis LLC) with the AB-400 antenna unit (the central frequency of the antenna is 400 MHz), which provides a depth of up to 5 m, and with the AB-150 antenna unit (the central frequency is 150 MHz), which provides a depth of up to 12 m. The endpoints of the observation profiles were linked using a satellite receiver indicator. To correctly display the terrain along the profiles, a total station survey was carried out with compensation for inaccuracies in determining the distance of the wheel with control marks every 50 m. According to drilling and drilling data, the selected reflecting surfaces are correlated with layers installed in wells, pits or ditches, for conversion along the entire profile of the temporary section to the deep one. In the analysis and interpretation of the data, the concepts and terms of GPR stratigraphy, such as radar facies (Rf) and radar reflection surfaces associated with the primary deposition structure, are used (Earth-science reviews 2004; Mallinson et al. 2010). The interpretation of GPR data on profiles with a total length of about 20 km fully included geomorphological content based on morphodynamic observations and paleogeographic analysis using C14 dating data (Afanas 2019; Afanasiev et al. 2020).

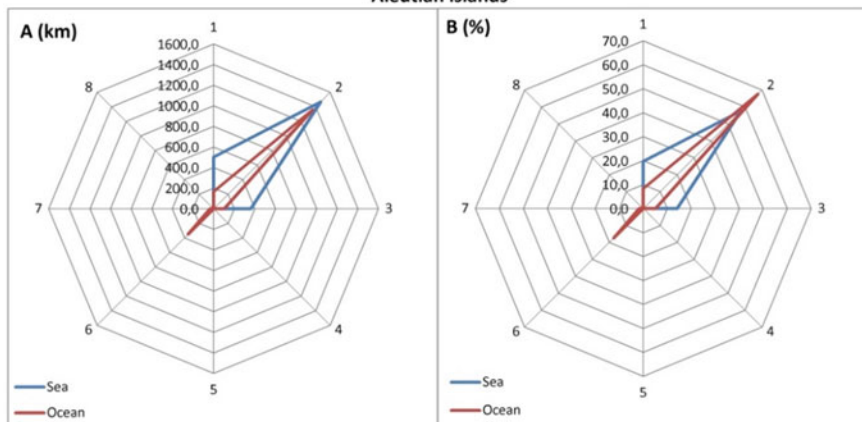
4 Results and Discussion

The main features of the specificity of morpholithogenesis from the sea and ocean sides of the contact zones were established by analyzing the maps of morphogenetic types of the North Pacific coastlines (Fig. 2).

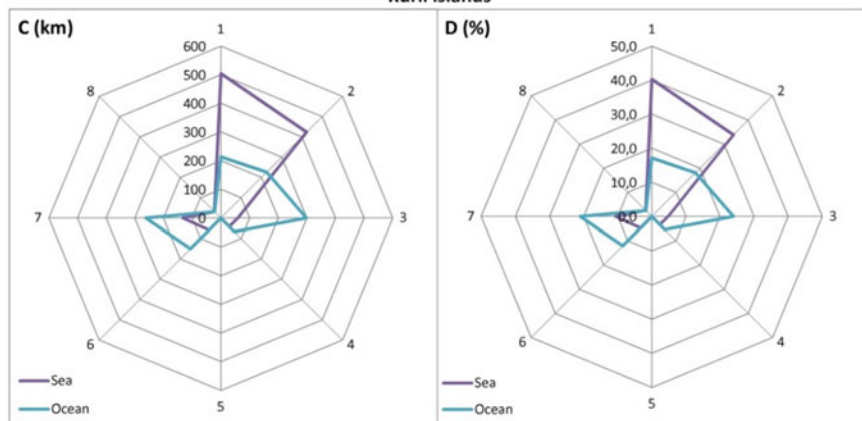
As expected, according to earlier field studies, in percentage terms, type 1 and type 2 sea coasts prevail over the ocean shores of these types, both of the Aleutian Islands and the Kuril Islands.

Abrasive shores in the Aleuts predominate on the sea side, and on the Kuril Islands, on the contrary, on the ocean side. The length of the abrasive-accumulative coasts is higher on the ocean side of the island-arc systems. The length of accumulative shores is also greater on the ocean side in both the Kuril and the Aleuts Islands. The revealed features of the morphogenetic types of sea and ocean coasts indicate the predominant contribution to this distribution of hydrodynamic and thermal regimes of the separated water areas. The morphoclimatic parameters of the actual contact zone (island arc), unlike those on Sakhalin Island, do not affect this distribution. The

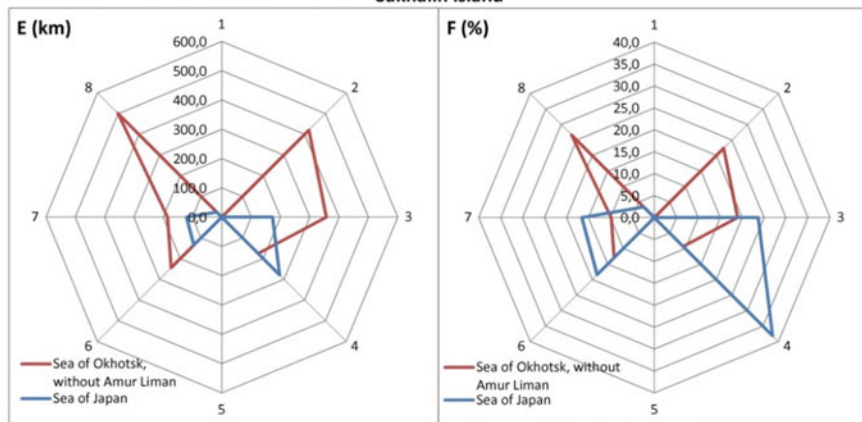
Aleutian islands



Kuril islands



Sakhalin island



◀**Fig. 2** Distribution of morphogenetic types of coasts of the island-arc systems of the North Pacific: 1—with glacial-tectonic dissection (fjord), tectonically determined, 2—abrasion-denudation; 3—abrasive (aligned and coiled); 4—abrasive dead; 5—thermoabrasion and ice; 6—abrasion-battery. (leveled and coiled); 7—created by wave processes, beach; 8—created by wave processes, lagoon, **a**—Aleutian island arc (km), **b**—Aleutian island arc (% of the total length of the coast), **c**—Kuril island arc (km), **d**—Kuril island arc ((% of the total length of the coast), **e**—Sakhalin Island (km), **e**—Sakhalin arc (% of the total length of the coast)

morphotectonic and structural-formational conditionality of the development of the shores of the island arcs is undoubtedly significant and requires further research.

The obtained distributions of shore types from the sea and ocean sides of island-arc systems served as a starting point for updating the problem of the peculiarities of the development of the shores of linear contact zones separating sea basins, as well as seas and oceans.

It turned out that in the opposite parts of the Vetrovoy isthmus, the size of ocean megafestons is more than twice the size of the Okhotsk Sea megafestons](Afanasev et al. 2020).

When analyzing the Aeolian morpholithogenesis associated with the wave processing of mainly pumice-pyroclastic material during explosive eruptions in the Holocene, Neo-Pleistocene, it was found that the dunes on the sea side of the Vetrovoy isthmus of Iturup Island were formed as a result of the destruction of high coastal ledges composed of pumice-pyroclastic material of the Neo-Pleistocene, during the period of increased erosion with sea level rise about 1.5 thousand years ago. The formation of the younger dunes of the ocean coast is largely due to the processing of pyroclastic material that entered the coastal zone about 1000 years ago directly during the eruption (Afanas'yev 2019). A significant proportion of ash material in pyroclastics also caused the very rapid formation of pelitic sediments in the lagoon-type basin on the ocean side of the Vetrovoy isthmus of Iturup Island.

The coasts of the island arcs are known to be affected by tsunamis with enviable regularity, both from the ocean side and from the sea side. Considering the coast of the low-lying land areas of the islands, we, of course, drew attention to this phenomenon. Detailed studies of the structure of the relief and sediments of the Vetrovoy isthmus of Iturup Island were carried out (Afanas 2019; Afanasiev et al. 2020; Afanas'yev 2019).

At present, it is not possible to confidently differentiate the tsunamigenic sediments and sediments of the strait. However, in this regard, it is necessary to pay attention to the asymmetry of the relief of the Vetrovoy isthmus of Iturup Island: the ocean side is more flat and low than the sea side.

The isthmus of Chuginadak Island (Aleutians) has a slightly different type of asymmetry (Afanasev et al. 2020). Unlike the Vetrovoy isthmus of Iturup Island, the ocean side of the isthmus of Chuginadak Island is steeper and shorter. It should be noted that the tsunami caused by the 1957 earthquake (Mw 8.6) reached 6.7–9.0 m on the Bering Sea side of Chuginadak Island, 14.9 – 17.6 m on the Pacific side, and 32 ± 2 m on Unalaska Island 180 km to the northeast (Afanasev et al. 2020). The

heights of historical tsunamis on the South Kuril Islands are significantly lower, but their values are also lower on the sea side (Griswold et al. 1957).

Thus, the obtained distributions of coast types from the sea and ocean sides of island-arc systems served as a starting point for updating the problem of the peculiarities of the development of the shores of linear contact zones separating sea basins, as well as seas and oceans.

The key area of detailed studies of the features of morpholithogenesis of the shores of linear contact zones separating marine basins, as well as seas and oceans was Sakhalin Island, whose unique geographical location allows us to consider it as a kind of contact zone of the border strip of the subarctic and temperate zones, characterized by a consistent change in natural conditions and temperature regime from north to south.

The northern and eastern shores of Sakhalin Island are affected by the physical and geographical conditions of the subarctic zone. The formation and development of the coast is determined by the cold Sea of Okhotsk, which belongs to the category of freezing seas of the subarctic type. The shores of eastern Sakhalin are characterized by the presence of permafrost on the coast, including at the base of lagoon embankments, the development of thermoabrasion and the existence, up to mid-July, of coastal ice.

The western and southern shores of Sakhalin Island are more affected by the physical and geographical conditions of the temperate zone. The moderately cold conditions of the northern sector of the Sea of Japan provide a relatively frequent transition of temperatures through zero, the absence or short-term formation of ice and soldered ice.

Detailed zoning of morpholithodynamic settings of the Sakhalin coast generally confirms the results of the analysis of the map of morphogenetic types of the Northern Pacific coast 2007 (Fig. 3).

Abrasive shores from the Sea of Okhotsk are more than from the Japanese Sea by about 2 times. There are 2.5 times more dead abrasive ledges on the shores of the Sea of Japan, and there are significantly more abrasive-accumulative and terraced shores. It should be noted that the Sakhalin coasts of the Sea of Japan and the Sea of Okhotsk practically do not differ in their resistance to destruction (Fig. 4).

Conclusions

As a result of digitization and subsequent analysis of maps of morphogenetic types of coasts of the Japan, Okhotsk and Bering seas, the originality of the current state of the coasts of these seas was clearly demonstrated. Abrasion-denudation rocky shores have the greatest extent in all seas of the North Pacific. Abrasion-accumulative shores form the second peak in the distribution curves of coastal types in the North Pacific. At the same time, the highest percentage of the total length, the shores of this type are on the Sea of Japan and much smaller, even taking into account the accumulative shores themselves (7th and 8th types), on the Sea of Okhotsk.

Interestingly, the extent of the shores with an inactive abrasion scarp in percentage terms in the Sea of Okhotsk is higher than in the Sea of Japan. In our opinion, this is due to the intense destruction of the shores of the Sea of Okhotsk during the

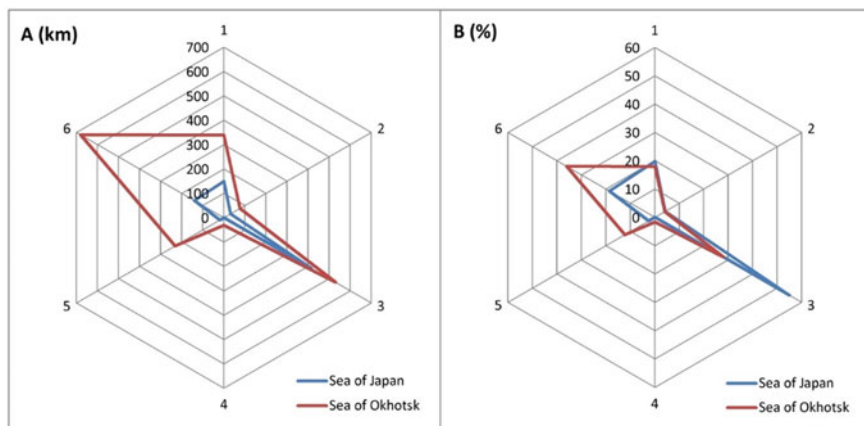


Fig. 3 Distribution of morpholithodynamic conditions along the shores of Sakhalin Island. A—length of coasts with different development trends in km, B—length of coasts with different development trends in%; 1—active cliff in bedrock, 2—active coastal ledge in weakly consolidated and loose formations, 3—dead cliff in bedrock, 4—dead cliff with a low terrace, 5—dead coastal ledge in weakly consolidated and loose formations, 6—accumulative Holocene coastal forms

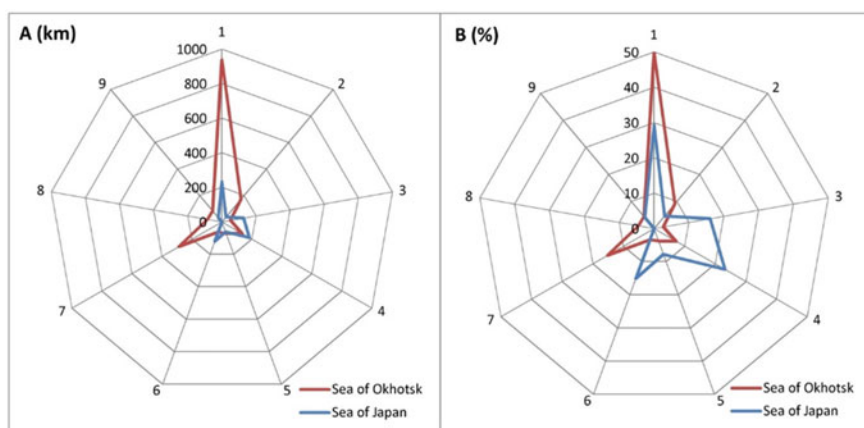


Fig. 4 Distribution of lithological complexes of the coast of O. Sakhalin (using Rock groups; 1—loose; 2—weakly lithified (Maruyam formation); 3—weakly lithified (Okobykai formation); 4—strongly lithified (Kholm Formation); 5—strongly lithified (Pila Formation); 6—strongly lithified (Arakai formation) 7—strongly lithified (Ostrin formation); 8—strongly lithified (Langer formation); 9—strongly lithified intrusive rocks form promontories protruding into the sea

warm periods of the Holocene, characterized by a longer period of the “open sea” at negative air temperatures.

An equally important result of the quantitative analysis of the maps of coastal types in the North Pacific is the actualization of the problem of the developmental

features of the coastlines of linear contact zones separating sea basins, as well as seas and oceans. Comprehensive geological and geomorphological studies confirm the morpholithodynamic and geomorphological specificity of the coasts of the contact zones.

References

- Afanasev V.V., Ignatov E. I., Uba A. V (2020) Mrfogeneticheskaia differentsiatsiia beregov kontaktnykh zon Severnoi Patsifiki // *Gidrosfera. Opasnye protsessy i iavleniia*. № 2. pp. 158–172 (In Russian; abstract in English)
- Alekseev B.A. Golubev G.N. Global'naya model' sovremennykh landshaftov mira [The global model of modern landscapes of the world]. In D'yakov K.N., Romanova E.P. (eds.) *Geografiya, obshchestvo, okruzhayushchaya sreda*. Tom 2. Funktsionirovanie i sovremennoe sostoyanie landshaftov [Geography, society and environment. Vol. 2. Functioning and current state of landscapes]. Moscow, Publ. Dom «Gorodets», 2004, pp. 319–326. (In Russian)
- Archikov E.I. Osobennosti formirovaniya rel'efa beregov Tikhogo okeana v subarkticheskom i umerennom klimaticheskikh poiyasakh [Features of the formation of the relief of the Pacific coast in the subarctic and temperate climatic zones]. *Issledovaniya global'nykh faktorov klimorfo-geneza Dal'nego Vostoka: sbornik trudov* [Research of global factors of climorphogenesis of the Far East: a collection of works]. Vladivostok: Publ. of Far Eastern Scientific Center of the USSR Academy of Sciences, 1979, pp. 70–78. (In Russian)
- Afanasev V.V., Ignatov E.I., Uba A.V., Dunaev N.N., Leontiev I.O. Gorbunov A.O (2019) Vetrovoy isthmus of Iturup island – holocene strait , IOP Conference Series: Earth and Environmental Science. 2019. Vol. 324. III National scientific conference with foreign participants “Geodynamical Processes and Natural Hazards” 27–31, (May 2019) Yuzhno-Sakhalinsk. Russian Federation. <https://doi.org/10.1088/1755-1315/324/1/012029>
- Afanasev V.V., A. O. Gorbunov, A. V. Uba, N. N. Dunaev. The manifestation of caldera-forming volcanism in the formation of the coast (on example of Iturup island of the Great Kuril Ridge) // *Springer Geology*. 2020. Vol. 1. P. 51–61
- Afanasyev V.V. O novom tipe eolovogo morfogeneza na vulkanogennykh beregakh (o. Iturup, Bol'shaya Kuril'skaya gryada) [A new type of aeolian morphogenesis on volcanic shores (Iturup island, Great Kuril ridge)] *Geosistemy perekhodnykh zon* [Geosystems of Transition Zones], 2019, vol. 3, no. 4, pp. 423–427. (In Russian; abstract in English).
- Baklanov P.Y. Geograficheskie i geopoliticheskie faktory v regional'nom razvitii [Geographic and Geopolitical Factors in Regional Development]. *Regional'nye issledovaniya* [Regional Studies], 2014, no. 2, pp. 4–10. (In Russian; abstract in English)
- Dzardzeevskii B.L. Obschaya tsirkulyatsiya atmosfery i klimat [General atmospheric circulation and climate]. Moscow, Publ. Nauka, 1975. 288 p. (In Russian)
- Diakonov K.N., Varlygin D.A., Retejum A.Yu. [Impact of the oceans on geographical zones studied by the remote sensing data on photosynthesis]. *Vestnik Moskovskogo universiteta. Seriya 5: Geografiya*. [Moscow University Bulletin. Series 5. Geography], 2017, no. 2, pp. 11–15. (In Russian; abstract in English)
- Griswold F.R., MacInnes B.T., Higman B. Tsunami-based evidence for large eastern Aleutian slip during the 1957 earthquake. *Quaternary Research*, 2019, vol. 91, iss. 3, pp. 1045–1058. <https://doi.org/10.1017/qua.2018.39>
- Likhacheva E.A., Makkaveyev A.N., Lokshin G.P. (2010) Fizicheskaya sushchnost' geomorfologicheskikh granits [Physical nature of geomorphologic boundaries] *Geomorfologiya* [Geomorphology], 2010, no. 2, pp. 3–10. DOI: <https://doi.org/10.15356/0435-4281-2010-2-3-10>. (In Russian; abstract in English)

- Likhacheva EA, Timofeyev DA (2007) K ierarkhii geomorfologicheskikh sistem s pozitsii ikh organizovannosti [To the hierarchy of geomorphologic systems from the angle of their organization]. *Geomorfologiya [geomorphology]* 4:3–8. <https://doi.org/10.15356/0435-4281-2007-4-3-8>. (In Russian; abstract in English)
- Likhacheva EA, Timofeyev DA (2008) Analiz geomorfologicheskikh sistem: osnovnye ponyatiya [Analysis of geomorphic systems: the fundamental notions]. *Geomorfologiya [geomorphology]* 2:4–21. <https://doi.org/10.15356/0435-4281-2008-2-14-21>. (In Russian; abstract in English)
- Lisogurskii NI, Petrichev AZ (1980) Rasprostranenie mussona nad Vostochnoi Aziei i stepen' ego ustoichivosti [Distribution of the monsoon over East Asia and the degree of its stability]. *Meteorologiya i Gidrologiya [Russian Meteorology and Hydrology]* 5:54–59 (In Russian)
- Matul, A. G. Chetvertichnaia biostratigrafiia i paleookeanologiya Okhotskogo moria i drugikh subarkticheskikh raionov // M.: GEOS, 2009. 182 p. (In Russian)
- Mallinson DJ, Smith CW, Culver S, Riggs SR, Ames D, Geological characteristics and spatial distribution of paleo-inlet channels beneath the outer banks barrier islands, North Carolina, USA. *Estuarine, Coastal and Shelf Science*. (2010) Vol. 88. Iss 2:175–189. <https://doi.org/10.1016/j.ecss.2010.03.024>
- Natsional'nyi atlas Rossii: v 4-kh tomah. Tom 2: Priroda i ekologiya [National Atlas of Russia: in 4 ch. Chapter 2 Environment (Nature). Ecology]. A.V. Borodko, V.N. Aleksandrov, V.M. Kotlyakov, N.G. Rybal'skii et al. (eds.). Moscow, Publ. Kartografiya, 2007. 496 p. (In Russian)
- Neal A, Ground-penetrating radar and its use in sedimentology: principles, problems and progress. *Earth-science reviews*. (2004) Vol. 66. Iss 3–4:261–330. <https://doi.org/10.1016/j.earscirev.2004.01.004>
- Nikol'skaya VV, Skryl'nik GP (1976) Tendentsii razvitiya rel'efa prirodnykh zon i provintsiy Dal'nego Vostoka [Trends in the development of the relief of natural zones and provinces of the Far East]. In: Skryl'nik GP (ed) *Klimaticheskaya geomorfologiya Dal'nego Vostoka [Climatic geomorphology of the Far East]*. Publ of Pacific Institute of Geography Far Eastern Scientific Center of the USSR Academy of Sciences, Vladivostok, pp 5–19 (In Russian)
- Polunin, G. V. Karta litologicheskikh kompleksov i ekzogennykh protsessov sushi i shelfa Sakhalina masshtaba 1:500000 // Khabarovsk, Iuzhno-Sakhalinsk, 1992. (In Russian)
- Skryl'nik G.P. Osnovnye urovni ustoichivosti v obshchei organizatsii geosistem Zemli [The basic levels of stability in the general organization of the geosystems of the Earth] *Uspekhi sovremennoogo estestvoznaniya [Advances in current natural sciences]*, 2017, no. 11, pp. 101–106. (In Russian; abstract in English)
- Skryl'nik G.P. Anomal'nye prirodnye protsessy i yavleniya Rossiiskogo Dal'nego Vostoka [Dangerous natural processes and phenomena the Russian Far East] *Uspekhi sovremennoogo estestvoznaniya [Advances in current natural sciences]*, 2018, no. 10, pp. 114–124. (In Russian; abstract in English).
- Shevchenko G. V., Loskutov A. V., Kaistrenko V. M. Novaia karta tsunamiopasnosti poberezhia iuzhnykh kurilskikh ostrovov // *Problemy kompleksnogo geofizicheskogo monitoringa Dal'nego Vostoka Rossii*. –2017. pp. 250–253. (In Russian)
- Skryl'nik G.P. Vedushchie klimaticheskie faktory razvitiya ekzogennogo rel'efa [Leading climatic factors of the development of exogenous relief]. *Geosistemy Dal'nego Vostoka Rossii na rubezhe XX–XXI vekov. Tom. 1. Prirodnye geosistemy i ikh komponenty [Geosystems of Far East of Russia on boundary of XX–XXI centuries. Chapter 1. Natural geosystems and their components]*. Vladivostok: Publ. Dal'nauka, 2008, pp. 77–81. (In Russian).
- Tunegolovets V.P., Gartsman B.I., Krokhin V.V. *Klimat i gidrografiya [Climate and hydrography]. Geosistemy Dal'nego Vostoka Rossii na rubezhe XX–XXI vekov. Tom. 1. Prirodnye geosistemy i ikh komponenty [Geosystems of Far East of Russia on boundary of XX–XXI centuries. Chapter 1. Natural geosystems and their components]*. Vladivostok: Publ. Dal'nauka, 2008, pp. 119–143. (In Russian).

https://pdaac.usgs.gov/dataset_discovery/aster/aster_products_table/aster_gdem_version_2_validation

<https://www.eorc.jaxa.jp/ALOS/en/aw3d30/index.htm> (date of request: 02.02.2020)

<https://doi.org/10.5066/F7PR7TFT> (date of request: 03.02.2020)

Formation of Temperature Anomalies in the Laptev Sea (2000–2020 Years)



M. V. Kraineva and E. N. Golubeva

Abstract This paper analyzes the increase in water temperature in the Laptev Sea in the present century. It is shown that such a phenomenon as “marine heat waves” can be isolated in the region. Marine heat waves are obtained both from observations and from numerical simulations based on the SibCIOM regional numerical model. Observational data show an increase in the frequency and intensity of these phenomena in the last few years in this region. Based on numerical experiments, in this paper we demonstrate intensive warming in the bottom layer, because of the increase in the surface temperature of the Laptev Sea in recent years.

Keywords Marine heat waves · Numerical simulation · Laptev Sea

1 Introduction

According to the World Meteorological Organization, 2019 ended the hottest decade in the history of observations (Pörtner et al. 2019). 2019 was the second warmest year among the warmest years for the period of observations since 1936, the anomaly of the average annual air temperature averaged for the Northern Polar Region reached 2.8 °C (Review of hydrometeorological processes in the Northern Polar region 2019). At the same time, the Laptev Sea region was at the center of one of the largest temperature anomalies, reaching 3.6 °C, which was the highest value since 1936. The year 2020 turned out to be even hotter for the Arctic seas. According to the Copernicus Climate Change Service (C3S, <https://climate.copernicus.eu/>) the anomaly of the surface air temperature for 12 months (from October 2019 to September 2020) for the Laptev Sea region was 5–7 °C. A prolonged period of elevated atmospheric temperature contributed to additional heat input and warming of sea waters, which shifted the

M. V. Kraineva (✉) · E. N. Golubeva
Institute of Computational Mathematics and Mathematical Geophysics SB RAS, 6, Ac.
Lavrentieva ave, Novosibirsk 630090, Russia
e-mail: krayneva.marina@sscc.ru

E. N. Golubeva
e-mail: elen@ommfao.sccc.ru

period of ice cover formation to November. During October, the Laptev Sea remained ice-free (Maslanik and Stroeve 1999).

Questions related to changes in the temperature of the waters of the Arctic shelf seas arise in connection with the study of the possible consequences of such changes. The data of drilling profiles (Rachold et al. 2007) and the results of numerical modeling (Nicolosky et al. 2012; Malakhova 2018; Gavrilov et al. 2020) indicate that the existence of permafrost subaqueous soils is possible on the shelf of the Arctic seas. At present, the existence of subaqueous permafrost provides conditions for the stability of gas hydrates at shallow water depths (Malakhova 2020). An increase in the temperature of the bottom layer of the sea can contribute to the destabilization of gas hydrates due to the degradation of permafrost (Golubeva et al. 2017) and the release of methane into the atmosphere (Thornton et al. 2020). Observational data (Golubeva et al. 2020; Kraineva et al. 2019; Dmitrenko et al. 2011; Hölemann et al. 2011; Janout et al. 2013, 2016) indicate the warming of the bottom waters of the Laptev Sea, which began in mid-1980.

The use of three-dimensional numerical modeling is a modern approach for conducting research aimed at studying the climatic variability of natural objects. Our previous studies concerning the Laptev Sea region (Golubeva et al. 2017, 2020; Kraineva et al. 2019) present the results of numerical modeling of the variability of the sea ice and thermohaline fields, and show the features of the formation of water circulation caused by the dynamic state of the region's atmosphere. Based on the analysis of the results of numerical modeling, it is shown that in the Laptev Sea there is a gradual increase in the temperature of the bottom layer, caused by a reduction in the ice cover and an increase in the time of the ice-free period. The areas of increasing the temperature of the bottom layers are highlighted. The analysis of the numerical results ended in 2014. In this paper, we continued our research until 2020 and showed that the process of increasing the temperature of the bottom layers has spread to the region bordering the continental slope. In addition, based on the analysis of observational data and the results of numerical simulations, we have shown that the processes occurring in the Laptev Sea in recent years can be interpreted as "marine heat waves" (MHW) related to extreme events.

2 Marine Heat Waves in the Laptev Sea. Observation Data Analysis

A MHW is a discrete long-term event with abnormally high water temperature values at a certain point in the World Ocean (Hobdey et al. 2016). It belongs to one of the dangerous natural phenomena. Over the past decades, there has been a steady warming of the global climate, which leads to an increase in the frequency and duration of the occurrence of marine heat waves (Hu et al. 2020). The analysis of NOAA surface temperature data (Reynolds et al. 2007) makes it possible to identify marine heat waves based on the method presented in Hobdey et al. (2016). The

method is based on the identification of positive temperature anomalies in a certain water area that exist for 5 days or longer, above the climatic daily distribution and the threshold value. The climate daily distribution is calculated based on the selected base period (in this study, selected from 1982 to 2010). The threshold value is presented as a daily distribution of ocean temperature, defined as the 90th percentile based on the base period. The calculation of MHW was carried out for the period from 2000 to 2020. Based on the annual time series, the average annual characteristics were calculated: the average and maximum intensity of events and the total number of days in which marine heat waves occurred at a given point in space. Linear trends with a 95% confidence interval were calculated for each characteristic.

The analysis of the received marine heat waves shows long-term positive anomalies over the last three years on the territory of the Laptev Sea (Fig. 1). The main part of the Laptev Sea is isolated from the path of the Atlantic and Pacific waters, which are considered the main sources of heat for the Arctic Ocean. The only sources of heat for the shelf waters of the Laptev Sea are the sun and river's water. Nevertheless, heat waves exist even in winter. Geographically, heat waves are also tracked throughout the entire water area, not only in the offshore zone, but also in the deep sea. In the last five years, the area where heat waves are recorded in total for almost 300 days has significantly increased.

The analysis of linear trends shows a stable increase in the intensity and duration of marine heat waves over the past 20 years in the Laptev Sea (Fig. 2). In the area of the Lena River Delta, the intensity of warm events increases by 1.5 °C for every 10 years. In most of the offshore zone of the sea, the total annual duration of heat waves increases by 12 days per year, which means 120 days in 10 years.

3 Research Method

The three-dimensional numerical model of the ocean and sea ice SibCIOM (Siberian coupled ice-ocean model), developed at the IMIMG SB RAS (Golubeva and Platov 2007; Golubeva 2008), is used to study the physical mechanisms of spatial-temporal variability of the hydrological and ice characteristics of the Arctic Ocean and its shelf seas. The numerical model of the ocean is based on the nonlinear equations of hydrothermodynamics of the ocean, taking into account the traditional approximations of hydrostatics and Boussinesq. The ice model is an adaptation of the CICE numerical model (<https://www.cesm.ucar.edu/models/ccsm4.0/cice/>; Hunke and Dukowicz 1997). The modeling area includes the Atlantic Ocean above 20 °S and the Arctic Ocean, bounded at the latitude of the Bering Strait. These borders, as well as river mouths, are considered “liquid”, where information about the climatic values of temperature, salinity, and flow rate is set. To solve the problems of this project, a numerical experiment using atmospheric reanalysis data was conducted for the period from January 1948 to December 2020. Using a three-polar numerical grid, the spatial resolution of the model is 50 km outside the polar zone, 25 km in the

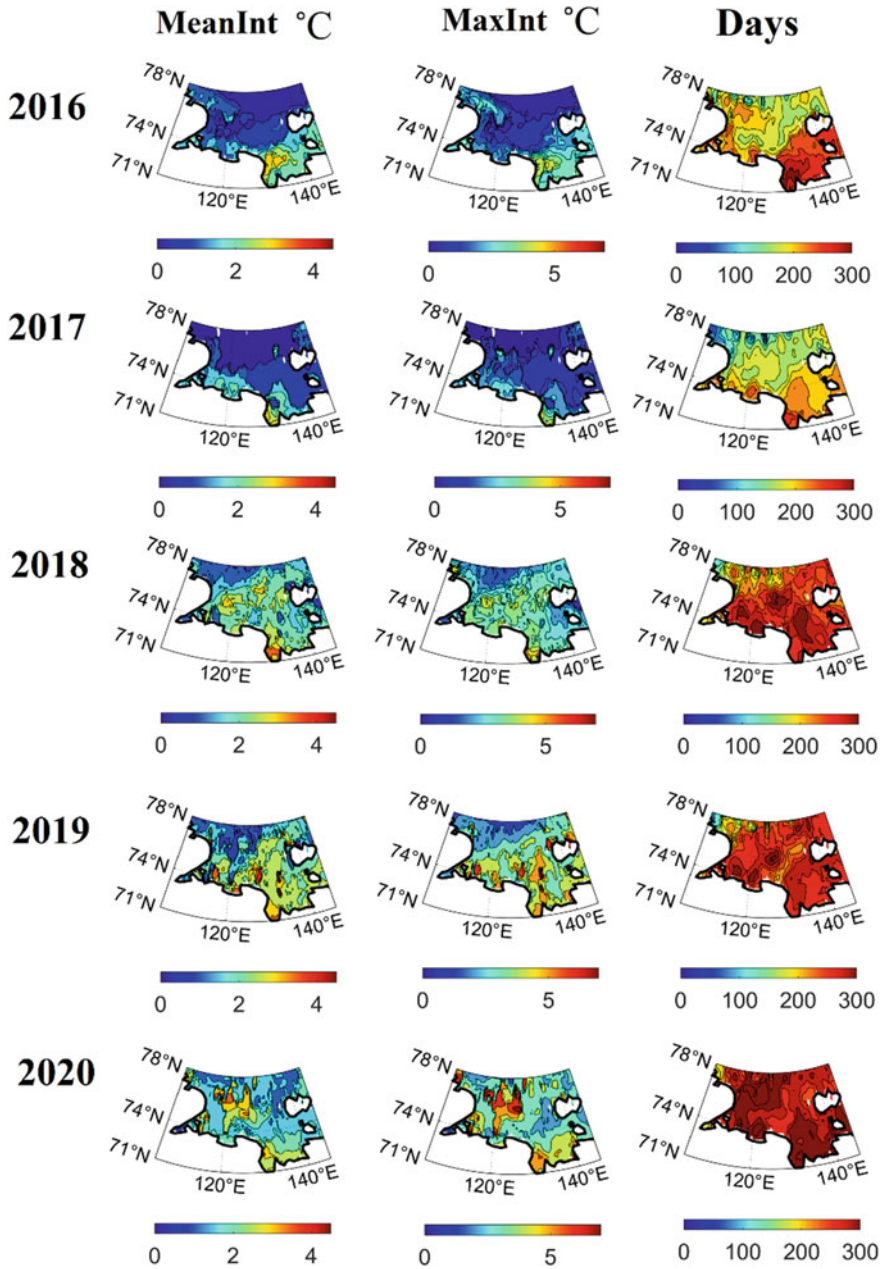


Fig. 1 The mean intensity of MHW (°C), the maximum intensity of sea heat waves (°C), and the total number of days in which heat waves were recorded for five years

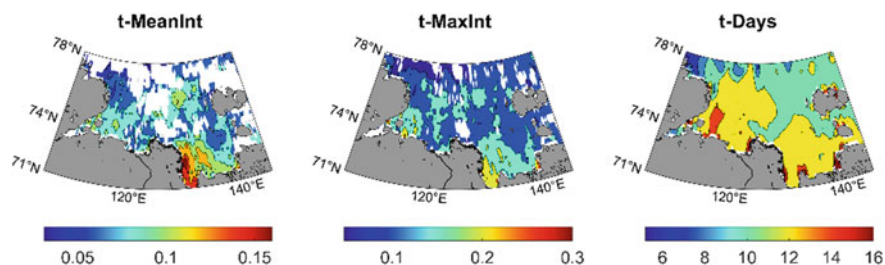


Fig. 2 Linear trends by three characteristics. Points with a confidence interval of less than 95% are colored white

deep-water part of the Arctic Ocean, and 15 km in the shelf area. The NCEP/NCAR reanalysis are used as atmospheric forcing (Kalnay et al. 1996).

The results of three-dimensional numerical modeling obtained for the time period from the middle of the last century to the present allow us to trace the changes in the average monthly characteristics of the ice cover, the temperature and salinity of sea water, and the speed of currents.

4 Numerical Simulation Results

Analysis of the input atmospheric data for numerical simulations shows an increase in surface air temperature during the summer months. Since the beginning of the 2000s, the average monthly temperature of the atmosphere for August increases from zero temperatures to positive, for September – from negative to zero and positive. This trend is also reflected in the increase in the surface temperature of the sea (Fig. 3).

The calculation of the MHW was also made on the basis of the average monthly data obtained from the results of numerical modeling. The model temperature fields reflect the existence of heat waves during the entire summer period in 2019 and 2020. In 2019, the maximum excess of the threshold values in July and August is 4–5 °C each (Fig. 4). In September 2020, the threshold values are exceeded by 6 °C (Fig. 4). Territorial MHW are observed up to the 76th parallel in 2019 and beyond the 80th parallel in 2020.

Assessing the changes that have occurred in the thermal state of the waters over a ten-year period, we compare the averaged temperature fields for the period 2001–2010 and 2011–2020. Figure 5c shows the deviation of the average annual temperature averaged for the period 2011–2020 from the corresponding values for the period 2001–2010 in the surface (temperature anomaly, (a) and bottom layer (temperature anomaly, (c). According to our estimates, the process of increasing the temperature of both the surface and bottom layers of the Laptev Sea, noted earlier in Golubeva et al. (2017, 2020; Kraineva et al. 2019), continues. Moreover, the most significant positive anomalies of the water temperature of the surface and bottom layer were obtained in the last three years (Fig. 5b, d).

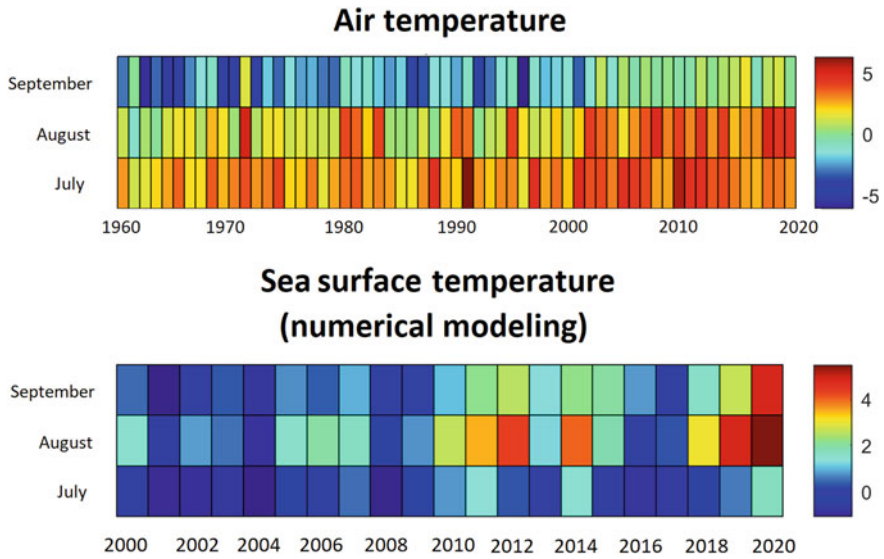


Fig. 3 The monthly mean air temperature (°C) averaged over the Laptev Sea basin according to reanalysis data and the water surface temperature (°C) according to numerical simulation results

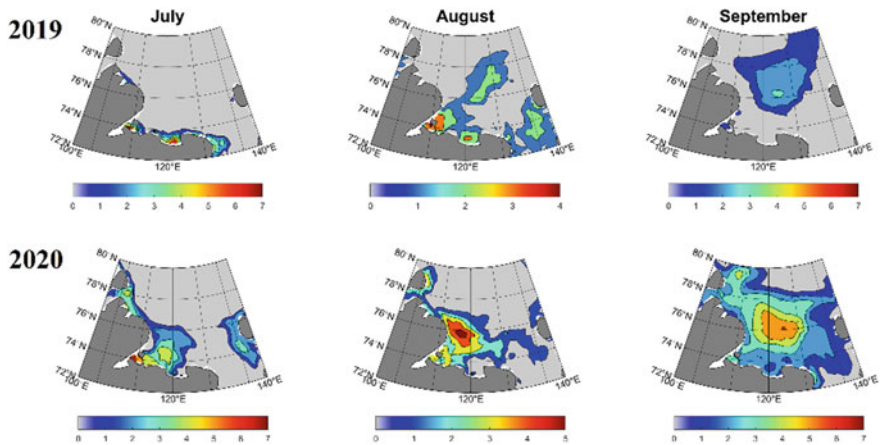


Fig. 4 Marine heat waves (°C) in the Laptev Sea, calculated from the results of numerical modeling for 2019–2020

In the previous study, it was found that the anomalies of the bottom temperature relative to the base period of 1960–1975, calculated up to 2014, are mainly concentrated in the coastal region (Golubeva et al. 2020). The latest numerical experiments conducted before December 2020 show that the warming of the bottom layers can spread to the area of the continental slope. The numerical model shows the highest positive values of temperature anomalies in this region.

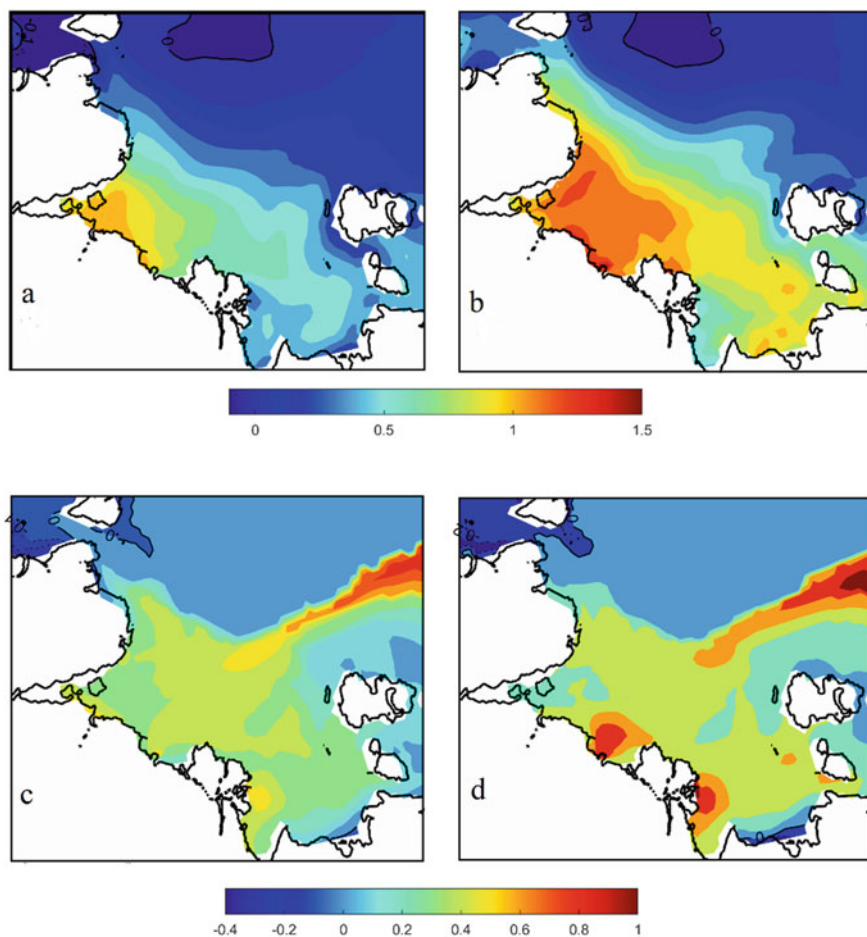


Fig. 5 Deviation of the average annual water temperature ($^{\circ}\text{C}$) values averaged over the corresponding period from the average annual temperature values for the period 2001–2010: Left column (a, c)— $T(2011\text{--}2020) - T(2001\text{--}2010)$, right column (b, d)— $T(2018\text{--}2020) - T(2001\text{--}2010)$. The upper figures (a, b) show deviations in the surface layer, the lower ones (c, d)—in the bottom layer of the shelf to a depth of 125 m

In the field of surface temperature averaged over the corresponding period, the largest positive anomalies are concentrated in the western part of the sea, but the sea heat waves calculated for September 2019 and 2020 are noted in Fig. 4 in the central part of the sea, facing the outer shelf. Analysis of the velocity field (Fig. 6) showed that the dynamic state of the atmosphere of the region contributed to the formation of a current directed from the coast, transferring heat from the coastal areas of the sea to the outer shelf area.

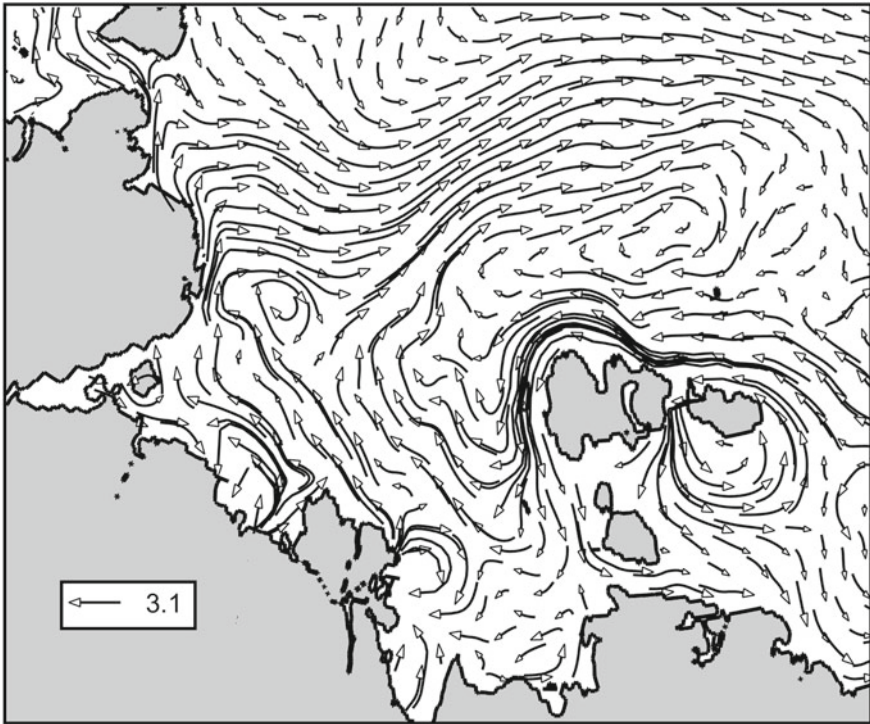


Fig. 6 Monthly mean velocity field in August 2020 (cm/s). Model simulation

5 Conclusions

In this paper, based on the analysis of observational data and the results of numerical modeling, we demonstrate the increase in the temperature of the Laptev Sea in the present century. Extreme values of the temperature of the surface layer of water allow us to characterize this process as the existence of marine heat waves. The analysis of the observed data shows an increase in the frequency and intensity of this phenomenon in the Laptev Sea region in recent years. The results of three-dimensional numerical modeling reflect the process of heat transfer by currents in the direction of the continental slope and the subsequent warming of the bottom layer of the sea. Positive anomalies of the bottom temperature relative to the period from 2001 to 2010 reach 0.8 °C. According to the results of numerical modeling, the most intense warming of the bottom layer occurred in the last three years.

Acknowledgements The work was supported by the Russian Science Foundation (Grant No.20-11-20112). Numerical calculations were carried out based on the SSCC SB RAS.

References

- IPCC. 2019. Special Report on the Ocean and Cryosphere in a Changing Climate/ Edited by H.-O. Pörtner, D. C. Roberts, V. Masson-Delmotte, and P. Zhai. Cambridge, UK: Cambridge University Press URL:<https://www.ipcc.ch/srocc/>.
- Review of hydrometeorological processes in the Northern Polar region 2019 // St. Petersburg: AANI, - 2020. – 94 p. (In Russian)
- Maslanik, J. and J. Stroeve. *Near-Real-Time DMSP SSMIS Daily Polar Gridded Sea Ice Concentrations, Version 1*, // Boulder, Colorado USA. NASA National Snow and Ice Data Center Distributed Active Archive Center – 1999. <https://nsidc.org/data/NSIDC-0081/versions/1> (date of request: 27.04.2021).
- Rachold V., Bolshiyannov D. Yu., Grigoriev M.N., Hubberten H-W., Junker R., Kunitsky V.V., Merker F., Overduin P., Schneider W. Near-shore Arctic subsea permafrost in transition // EOS Trans Am Geophys Union. 2007. V. 88. № 13. P. 149–156. <https://doi.org/10.1029/2007EO130001>.
- Nicolosky D.J., Romanovsky V.E., Romanovskii N.N., Kholodov A.L., Shakhova N.E., Semiletov I.P. Modeling sub-sea permafrost in the East Siberian Arctic Shelf: The Laptev Sea region // J. Geophys. Res.: Earth Surface. 2012. V.117. № F3. F03028.
- Malakhova, V.V. Estimation of the subsea permafrost thickness in the Arctic Shelf // Proceedings of SPIE 10833, 24th International Symposium on Atmospheric and Ocean Optics: Atmospheric Physics, 2018, 108337T (13 December 2018); doi:<https://doi.org/10.1117/12.2504197>
- Gavrilov A, Malakhova V, Pizhankova E, Popova A (2020) Permafrost and Gas Hydrate Stability Zone of the Glacial Part of the East-Siberian Shelf // Geosciences 10(12):484. <https://doi.org/10.3390/geosciences10120484>
- Malakhova, V.V., “The response of the Arctic Ocean gas hydrate associated with subsea permafrost to natural and anthropogenic climate changes,” IOP Conference Series: Earth and Environmental Science 606, 012035 (2020).
- Golubeva E., Platov G., Malakhova V., Kraineva M., Iakshina D. Modelling the Long-Term and Inter-Annual Variability in the Laptev Sea Hydrography and Subsea Permafrost State // Polarforschung, Bremerhaven, Alfred Wegener Institute for Polar and Marine Research – 2017. – Vol. 87, №2. – P. 195- 210.
- Thornton B. F., Prytherch J., Andersson K., Brooks I. M., Salisbury D., Tjernström M., Crill P. M. Shipborne eddy covariance observations of methane fluxes constrain Arctic sea emissions // Sci. Adv. 2020. V.6. № 5. P. eaay7934. <https://doi.org/10.1126/sciadv.aay7934>.
- Dmitrenko, I., Kirillov, S., Tremblay, L., Kassens, H., Anisimov, O., Lavrov, S., Razumov, S. & Grigoriev, M. (2011): Recent changes in shelf hydrography in the Siberian Arctic: Potential for subsea permafrost instability.- J. Geophys. Res. 116: C10027
- Hölemann, J.A, Kirillov, S., Klagge, T., Novikhin, A., Kassens, H. & Timokhov, L. (2011): Near-bottom water warming in the Laptev Sea in response to atmospheric and sea-ice conditions in 2007.- Polar Research 30: 6425.
- Janout MA, Hölemann J, Krumpen T (2013) Cross-shelf transport of warm and saline water in response to sea ice drift on the Laptev Sea shelf.- J. Geophys. Res. Oceans. 118:563–576
- Janout, M., Hölemann, J., Juhls, B., Krumpen, T., Rabe, B., Bauch, D., Wegner, C., Kassens, H. & Timokhov, L. (2016): Episodic warming of 210 near-bottom waters under the Arctic sea ice on the central Laptev Sea shelf.- Geophys. Res. Lett. 43(1): 264–272
- Golubeva, E., Kraineva, M., & Platov, G. (2020) Simulation of near-bottom water warming in the Laptev Sea.- IOP Conf. Ser.: Earth Environ. Sci. 611 012010
- Kraineva M, Golubeva E, Platov G (2019) Simulation of the near-bottom water warming in the Laptev Sea in 2007–2008 Bull. Nov. Comp. Center. Num. Model. in Atmosph. Etc. 17:21–30
- Hu, S., Zhang, L., & Qian, S. Marine heatwaves in the Arctic region: Variation in different ice covers // Geophysical Research Letters – 2020. – 47 – e2020GL089329.
- Reynolds, Richard W., Thomas M. Smith, Chunying Liu, Dudley B. Chelton, Kenneth S. Casey, Michael G. Schlax. Daily High-Resolution-Blended Analyses for Sea Surface Temperature // J. Climate – 2007. – 20. – p.5473–5496.

- A.J. Hobday et al. A hierarchical approach to defining marine heatwaves // *Progress in Oceanography* – 2016. – 141. – pp.227–238.
- Golubeva E. N., Platov G. A. On improving the simulation of Atlantic Water circulation in the Arctic Ocean // *J. Geophys. Res.* – 2007. – V.112. – C04S05. doi:<https://doi.org/10.1029/2006JC003734>
- Golubeva E. N. Numerical modeling of Atlantic water dynamics in the Arctic basin using the QUICKEST scheme // *Vych. tekhnol.* - 2008. - No. 5. - pp. 11–24 (In Russian)
- Hunke E. C., Dukowicz J. K. An elastic-viscous-plastic model for ice dynamics // *J. Phys. Oceanography.* – 1997. – V. 27. – P. 1849–1867. doi:<https://doi.org/10.1016/j.ocemod.2009.01.004>.
- Kalnay, et al. The NCEP/NCAR 40-year reanalysis project // *Bull. Amer. Meteor. Soc.* – 1996. – V. 77. – P. 437–470. <https://psl.noaa.gov/data/gridded/data.ncep.reanalysis.html> (дата обращения: 17.06.2020).

On Possibility of Applying Aircraft Scanning Laser Locator for Solving Problems of Operational Oceanology



V. N. Nosov , S. B. Kaledin , S. G. Ivanov , E. A. Zevakin ,
L. V. Serebrinikov , A. S. Savin , and V. I. Timonin 

Abstract The use of laser-glare method of sea surface sounding for aircraft recording various characteristics of surface waving (surface curvature, spatial scale and slopes of the waves) is under discussion. The model of aircraft scanning laser locator (ASLL) implementing this method is presented. The estimates of basic locator parameters and necessary technical requirements are given. Preliminary ASLL field tests have been performed confirming the possibility of recording requested surface waving parameters. The performed analysis of ASLL-recorded histograms of spatial waving periods revealed the presence of two main groups of waves. The results of analysis are confirmed by comparison with photo recording data. Finally, the conclusion on prospects of ASLL using for solving problems of operational oceanology is drawn.

Keywords Surface waving · Remote sensing · Scanning laser locator · Aircraft

V. N. Nosov (✉) · S. G. Ivanov · E. A. Zevakin
Vernadsky Institute of Geochemistry and Analytical Chemistry of the RAS, Moscow, Russia
e-mail: viktor_nosov@mail.ru

S. G. Ivanov
e-mail: ivanovsg5167@yandex.ru

E. A. Zevakin
e-mail: ezevakin.zev@yandex.ru

S. B. Kaledin · A. S. Savin · V. I. Timonin
Bauman Moscow State Technical University, Moscow, Russia
e-mail: sbkaledin@mail.ru

A. S. Savin
e-mail: assavin@list.ru

V. I. Timonin
e-mail: timoninmgtu52@mail.ru

L. V. Serebrinikov
INENERGI Ltd., Moscow, Russia
e-mail: l.serebrinikov@inenergy.ru

1 Introduction

Many processes occurring in the deep layers of oceanic water cause significant disturbances in aquatic environment. For example, gas emissions as well as volcanic and tectonic processes lead to significant hydrodynamic effects on the oceanic environment. Anthropogenic activity also noticeably effects on the marine environment state. Moving ships and underwater constructions flowed around by water streams disturb the marine environment generating waves and vortices. All these processes are manifested at sea surface as changes in the waving pattern and form anomalous zones as «slicks» or «rifts» and «smoothed» areas (Bakhanov et al. 2007; Yu et al. 2011; Gargett and Hughes 1972; Phillips 1973; Curtin and Mooers 2005; Ya and Talanov 1977; Ya 1977; Ermakov and Salashin 1994; Gorshkov et al. 2020). Thus, the sea surface reflects the deep-water phenomena inaccessible for direct observation. Therefore, the methods of remote sea surface sensing have been developed by now and continue to be improved. In particular, the optical methods are of great importance because of high sensitivity and spatial resolution as well as the absence of resonance phenomena when recording reflected radiation (in contrast to radiolocation).

Different scales of phenomena under study fix requirements for methods and recording equipment placed on different carriers. The widest observation area may be provided using artificial earth satellites (Bondur and Murynin 2020; Bondur et al. 2010; Yurovskaya et al. 2014; Nosov et al. 2015; Apel et al. 1975). The sea surface image recording by spacecraft significantly expands the observation area, but, in some cases, it does not provide the necessary spatial resolution and efficient monitoring for given water area due to the spacecraft orbit precession. The use of low speed (with speed of 8–14 knots) scientific research vessels as recording equipment carriers allows us to study in details the local sea surface areas but does not provide wide coverage of sea surface which limits significantly the large-scale phenomena study. Airplanes and helicopters as well as unmanned aircrafts occupy intermediate position between space and shipboard recording equipment carriers. Using such carriers will allow us to solve problems of operational oceanology, i.e. to carry out research work for given water area at specified estimated time. In this case, it become possible to study hydrophysical phenomena manifested on the sea surface at the areas with scale of tens and even hundreds of kilometers. The possibility to use aircrafts for carrying out full-scale hydrophysical studies is shown in Yurovskaya et al. (2018), Goldin et al. (1979), Buften et al. (1983), Bunkin et al. (1985).

2 Surface Waving Research Method

This paper describes the use of laser-glare method based on scanning the sea surface with laser beam (Goldin et al. 1979; Buften et al. 1983; Bunkin et al. 1985; Nosov et al. 2020a, 2019, 2017, 2016). There was aircraft used as sounding equipment carrier. Hydrodynamic disturbances in aquatic area with scale of several tens of kilometers have been recorded.

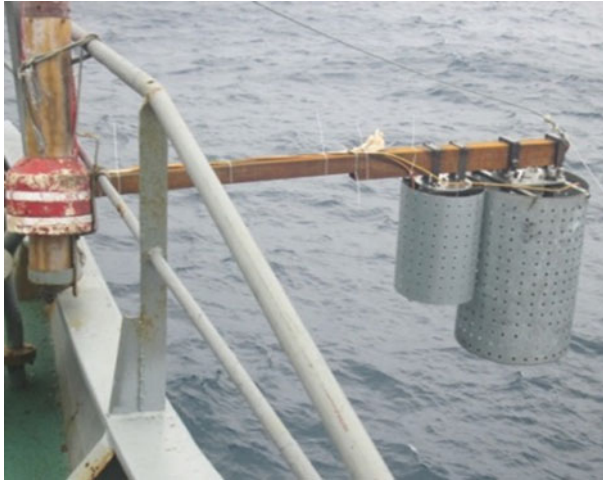


Fig. 1 The scanning laser locator models aboard the ship

The method we use is based on scanning sea surface by narrow laser beam and recording the specular laser-glare reflections. Specular laser glares appear when aligned axes of laser beam and receiving optical system coincide with the normal to the sea surface at reflection point. Since the sea surface has a random profile due to wind ripples, the laser-glare reflections also appear randomly but in compliance with waving profile. Previously, in Vernadsky Geochemistry Institute several models of shipboard scanning laser locators making possible to measure sea surface parameters have been developed and later used for the field studies (Nosov et al. 2020a, 2019, 2017, 2016). These models were aboard scientific research ship (Fig. 1) and recorded laser-glare pattern changes during the ship movement.

Let us consider analytical relationship between intensity of laser beam reflection from sea surface within glare area and basic waving parameters. Generally, received signal depends on such parameters: energy density of radiation on sea surface, curvature of sea surface profile, sensitivity of receiving equipment and receiving lens aperture. The random sea surface profile may be considered as equivalent spherical surface. So, we can use equivalent curvature radius as parameter for analyzing. In addition, the value of angle of receiving laser-glare signal from the vertical is also important informative parameter. This angle depends on the wave slope in the moment of glare reflecting. Due to the random sea surface profile the method is based on accumulating and processing statistical data on reflected laser-glare signals.

The equivalent sea surface radius may be calculated by formula:

$$R = 2H / D \sqrt{((4\mu\Phi_{\Pi}A_0) / (\Pi\tau\tau_A^2 P))} \quad (1)$$

where Φ is the signal-to-noise ratio, Φ_{Π} is the threshold flow for PhD (photodetector), A_0 is the surface area illuminated by the laser beam, H is the flight altitude, ρ is the specular reflection coefficient of the sea surface, τ and τ_A is the transmittance of optical device and atmosphere, respectively, P is the laser radiation power, D is the diameter of receiving lens entrance pupil.

The signal-to-noise ratio for the PhD dark current may be calculated by the formula:

$$\mu = \frac{D^2 R \rho \tau \tau_A^2 P}{(2H)^2 \Phi_{\Pi} d^2} \quad (2)$$

Statistical processing of accumulated data on wave radii and slopes allows us to analyze the sea surface state. Undisturbed sea surface has some initial «background» statistical characteristics, which change under influence of hydrodynamic disturbances or surfactant films. The gravitational-capillary region of sea waving spectrum characterized by smaller values of equivalent curvature radius is the most informative.

3 Technical Implementation of ASLL Model Aboard Aircraft

Based on experience of creating shipboard scanning laser locators the aircraft scanning laser locator (ASLL) has been developed (Nosov et al. 2020b). The structural and functional scheme of ASLL is shown in Fig. 2.

Two channels can be outlined in the ASLL structural scheme, namely: laser illumination channel consisting of laser (3) and forming optical system (4), and receiving channel including objective lens (9) and photodetector (5). To combine

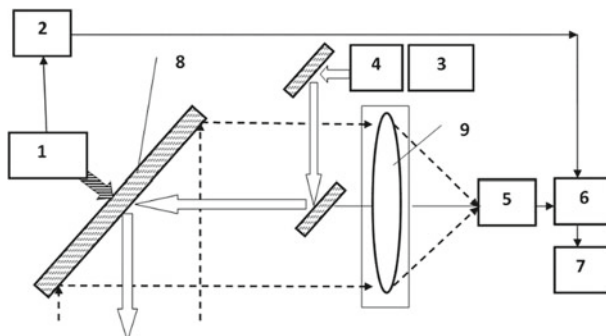


Fig. 2 Structural and functional scheme of ASLL. (1) electric motor, (2) synchronization system, (3) laser, (4) forming optical system (FOS), (5) photodetector, (6) analog-to-digital converter, (7) personal computer, (8) scanning mirror, (9) lens

laser-illuminated sea surface area with instantaneous angular field of receiving channel the optical scheme of locator with aligned optical axis of the named channels was chosen as technical solution.

To scan the sea surface with laser beam the drive equipped with swinging mirror (8) and powered by electric motor (1) through crank mechanism is used. The angular position of scanning mirror is monitored by synchronization device (2) based on optocoupler and strobe disk. Such a device allows us, during information processing, to determine the angular position of laser glare relative to vertical in the moment of photodetector recording, and, therefore, to obtain data on the slopes of the waves appearing on the sea surface.

ASLL has been developed taking into account operational conditions, namely: the carrier speed of about 400 km/h, the flight altitude of 300–350 m, the atmosphere state, etc. In addition, it was necessary to provide storage and accumulation of measured data for subsequent statistical processing. The aircraft motion parameters define requirements for energy sensitivity and spatial resolution of device.

The illumination channel uses continuous DPSS laser with radiation power of 2500 mW at wavelength of 532 nm. Laser beam divergence is 1.5 mrad, and diameter is 4 mm. The forming optical system (FOS) represents Galilean telescopic system with visible magnification 3 times. The laser beam divergence decreases to 0.5 mrad after FOS while the diameter rises up to 12 mm.

SAMYANG mirror lens with focal length of 800 mm and entrance pupil diameter of 100 mm is used in ASLL receiving channel. The central shielding allows laser beam to enter coaxially with optical axis of objective lens without additional losses of received radiation. Field point aperture with diameter of 0.7 mm is installed in the image plane. In this case, the instantaneous angular field of receiving channel is of 0.9 mrad, which exceeds the angular laser beam divergence. This ratio allows us to ensure field overlapping on sea surface and to simplify adjustment of the model.

For spectral filtering the received radiation interference filter with bandwidth of 5 nm installed in front of entrance window of PhD photomultiplier tube is used. Filtering allows us to select narrow spectral band near the operating wavelength of laser radiation and suppress significantly the interference background solar radiation spreading from the sea.

Photo of ASLL with removed cover and without power supplies is shown in Fig. 3.

The scanning mode should provide the most possible frequent (without gaps) sea surface scanning. This is nontrivial task because of large dimensions and weight of scanning element included into optical-mechanical scanning system. ASLL model includes scanner with swinging mirror across the carrier flight direction providing the scanning frequency of 28 Hz and angular deviation to the vertical of $\pm 10^\circ$. The scanning speed of laser beam over sea surface at flight altitude of 300 m is 6000 m/s average. In this case, the minimum duration of glare signal is estimated at 15 μ s. Zigzag-form strip about 100 m wide is scanned by laser beam on the sea surface.

The selected parameters of scanning device are matched with photodetector electronic path bandwidth equal to 30 kHz.

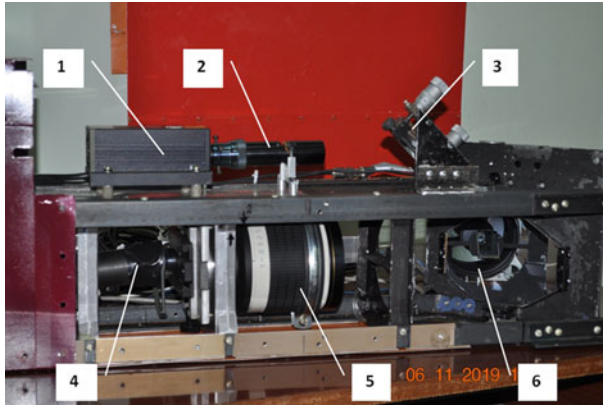


Fig. 3 Photo of ASLL with removed cover: (1) laser, (2) FOS, (3) rotary adjusting mirror, (4) photodetector, (5) lens, (6) scanner mirror

Signals are recorded and processed in digital form after digitization by 14-bit analog-to-digital converter (ADC) (6) using special algorithm included into PC software unit (7). Note that operational scheme provides adjustment of photodetector amplification mode by operator. Adjustment is performed by changing photomultiplier supply voltage. Depending on external light conditions (background solar radiation intensity) operator can adjust the optimal PhD photomultiplier voltage by control software through digital-to-analog converter unit. Such an algorithm excludes saturation of useful signal and provides its necessary excess over the noise. Thus, dynamic range of ASLL model is possible to be controlled.

General ASLL view with accompanying power supply units is shown in photo (Fig. 4).

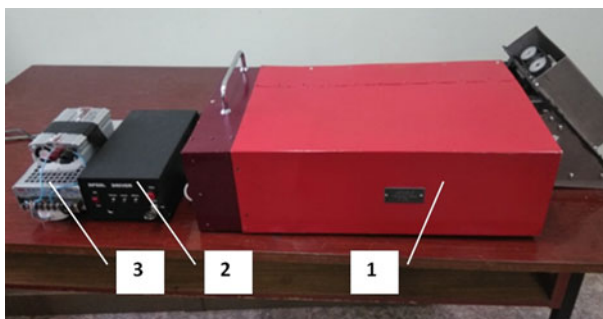


Fig. 4 General view of ASLL set (without PC): (1) main unit, (2) laser control unit, (3) power supply units

4 Results of Field Experimental Studies

The model has been tested aboard aircraft at flight altitudes of 300–350 m above the water surface at flight speed of about 400 km/h. The developed programs for processing ASLL signals allow us to construct histograms for various signal parameters, namely: average values of signal amplitudes (depending on wave curvature radii), time intervals between single pulses (depending on spatial waving periods), pulse durations, dependences of pulse amplitudes on the mirror rotation angle (depending on wave slopes), and pulse rate. Figure 5 shows histogram of intervals between pulses measured during one of the aircraft tacks with duration of about 7 min.

Signal processing under constructing histograms was performed at following parameters: noise cutoff level is of 10 mV, signal averaging is of 3 s, number of histogram partitions along X-axis is of 100. Values along X-axis are presented in μ s. Y-scale histogram is given in percent. The presented results of measurements have been obtained at voltage on photomultiplier tube of 1.8 kV. According to position of peaks in histogram we can estimate the spatial waving period.

The speed of laser beam scanning over sea surface may be calculated by formula: $V_{sc} = 4\alpha f_M * H$, where laser-beam scanning angle $\alpha = \pm 10^\circ$. At scanning frequency $f_M = 28$ Hz and flight altitude $H = 330$ m we obtain the value for speed of laser beam scanning over sea surface: $V_{sk} = 6450$ m/s. The spatial period of waving can be found from the relation: $L = V_{sk} * \Delta t$, where Δt is time interval between peaks in pulse interval histogram for ASLL model. Taking into account calculated speed value for laser beam scanning over sea surface we obtain estimates of spatial waving period.

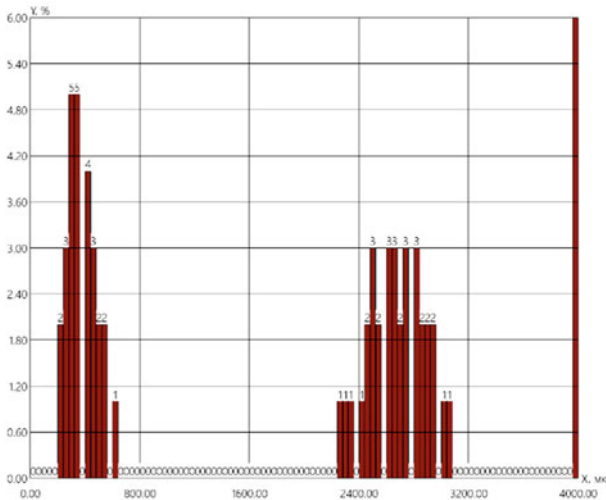


Fig. 5 Histogram of intervals between pulses

Average pulse interval in histogram maximum, μs	Spatial period, m
312.5	2
265	17

The obtained data indicate that two systems of waves with spatial period of about 2 and 17 m on the water surface were observed. Note that wave structure of water surface with minimum period of 3 m is also observed in sea surface images made from the aircraft during the measuring.

The presence of two systems of surface waves with significantly different wavelengths can be explained by the fact that system of shorter waves is in initial stage of formation under the influence of the wind, and system of long waves is in relaxation stage after the end of the earlier wind influence. This situation is typical for large lakes and seas (Shuleikin 1968; Davidan et al. 1985). Surface waves produced by the wind pass through different stages of development: from capillary waves with millimeter characteristic length to developed waves with length up to tens of meters. When the wind influence ends disturbed water surface gradually comes to equilibrium state, and the longer waves, or «swell waves», are observed. The formation of new system of wind-generated waves started against «not-calmed swell» background under the influence of changeable wind typical for field experiment region, which was recorded in process of measurements.

Using model calibration against topographic reflector performed before the flight tests and considering the average laser-glare pulse amplitude of 60 mV (derived from amplitude histogram) the effective wave curvature radius (the most probable in the day of measurements) was estimated as 10 cm. The estimates show that ASLL model allows us to measure sea surface curvature radii and spatial waving scales in the range of 5–80 cm and 20–30 m, respectively. The spatial resolution of ASLL is 10 cm at flight altitude of 300 m. The observed surface area during 1 h of flight, at flight speed of 400 km/h, is of 40 km². In this case, the length of sea surface area under study may achieve up to tens—hundreds of kilometers.

5 Conclusions

The full-scale tests of developed ASLL aboard aircraft have shown the efficiency of such a system for water surface sensing. ASLL allowed us to obtain information about waves on the sea surface, while measured values of spatial waving periods turned out to be comparable to those estimated using photographs of aquatic area under study. Thus, possibility of placing ASLL model aboard the aircraft for carrying out operational oceanological research work with scale of several tens, or hundreds kilometers, has been proved. At the same time, note that studies using manned aircrafts are of great expense and require much organization efforts. Using the newer components and decreasing flight altitude and speed we can greatly diminish weight, size and energy parameters of ASLL. Such devices will significantly expand abilities for

solving problems of operational oceanology, since the use of simpler and cost efficient unmanned aircrafts launched both from the shore and shipboard will become possible.

References

- Bakhanov VV, Goryachkin YuN, Korchagin NN, Repina IA (2007) Local manifestations of deep processes on the sea surface and in the near-water layer of the atmosphere. *Dokl RAS* 414(1):111–115 (in Russian)
- Yu VI, Korchagin NN, Savin AS (2011) Surface effects in the flowing around obstacles in inhomogeneously stratified medium. *Dokl RAS* 440(6):826–829 (in Russian)
- Gargett AE, Hughes BA (1972) On the interaction of surface and internal waves. *J Fluid Mech* 52(1):179–191
- Phillips OM (1973) On interaction of internal and surface waves. *Izv Acad Sci USSR FAO* 9(9):954–961 (in Russian)
- Curtin TB, Mooers CNK (2005) Observation and interpretation of a high frequency internal wave packet and surface slick pattern. *J Geophys Res* 80(6):882–894
- Ya BA, Talanov VI (1977) On transformation of short surface waves by inhomogeneous flows. *Izv Acad Sci USSR FAO* 13(7):766–773 (in Russian)
- Ya BA (1977) Transformation of surface waving spectrum under internal wave action. *Izv Acad Sci USSR FAO* 15(6):655–661 (in Russian)
- Ermakov SA, Salashin SG (1994) On effect of strong modulation of capillary-gravitational ripples by internal waves. *Dokl Acad Sci USSR* 337(1):108–111 (in Russian)
- Gorshkov KA, Dolina IS, Soustova IA, Troitskaya YuI. Modulation of short wind waves in the presence of intense internal waves. The effect of increment modulation. *Izv RAS FAO* 39(5):661–672 (in Russian)
- Bondur VG, Murynin AB. Methods of reconstructing sea waving spectra by spectra of aerospace images. In: *Investigation of the Earth from Space*, vol 6, no (3), pp 1–4 (in Russian)
- Bondur VG, Dulov VA, Murynin AB, Yu YY (2010) Investigation of sea waving spectra in a wide wavelength range using satellite and contact data. In: *Investigation of the Earth from Space*, vol 1–2, pp 7–24 (in Russian)
- Yurovskaya MV, Kudryavtsev VN, Shapron B, Dulov VA (2014) Interpretation of optical satellite images of the Black Sea in solar glare zone. *Marine Hydrophys J* 4:68–82 (in Russian)
- Nosov VN, Ivanov SG, Timonin VI, Podgrebenkov AL, Plishkin AN, Kaledin SB, Glebova TV, Yadrentsev AN, Zakharov VK (2015) Joint space and marine experiment on integrated recording ship trace using subsatellite measurements. *Fund Appl Hydrophys* 8(4):34–35 (in Russian)
- Apel JR, Byrne HM, Proni JR, Charnell RL (1975) Observation of oceanic internal and surface waves from the Earth Resources Technology Satellite. *J Geophys Res* 80:865–881
- Yurovskaya MV, Kudryavtsev VN, Shirokov AS, Nadolya I (2018) Field measurements of surface wave spectrum using photographs made from unmanned multicopter. In: *Modern problems of remote sensing of the Earth from space*, vol 15, no 1, pp 245–257 (in Russian)
- Goldin YuA, Kagain VE, Kelbelikhanov BF, Locke JF, Pelevin VN (1979) Location of waving sea surface using laser from helicopter. In: Galaziy GI (ed) *Optical methods for studying oceans and inland water bodies*. Nauka, Novosibirsk, pp 135–140 (in Russian)
- Buften JL, Hoge FE, Swift RN (1983) Airborn measurements of laser backscatter from the ocean surface. *Appl Opt* 22:2603–2618
- Bunkin FV, Yak KN, Malyarovskii AI et al (1985) Aircraft measurements of sea waves by specular reflection of laser beam. *Dokl Acad Sci USSR* 281(6):1441–1445 (in Russian)

- Nosov VN, Ivanov G, Timonin VI, Kaledin SB (2020) Anisotropy study of statistical characteristics of wind waves under the influence of hydrodynamic perturbations in laser-reflective method. In: Olegovna C (eds) *Processes in GeoMedia I*. Springer Geology. Springer, Cham, pp 93–100.
- Nosov VN, Kaledin SB, Ivanov SG, Timonin VI (2019) Remote tracking to monitor ship tracks at or near the water surface. *Opt Spectrosc* 127:669–674
- Nosov VN, Ivanov SG, Kaledin SB, Savin AS (2017) Recording manifestations of deep processes in the near-surface layers of marine environment and atmosphere. *Processy v Geosredah* 2(11):522–528 (in Russian)
- Nosov VN, Kaledin SB, Ivanov SG, Glebova TV, Timonin VI (2016) On increasing the efficiency of detecting anomalies excited by marine underwater source with integrated use of laser-optical recording methods. *Processy v Geosredah* 1(5):85–94 (in Russian)
- Shuleikin VV (1968) *Physics of the sea*. Nauka, Moscow (in Russian)
- Davidan IN, Lopatukhin LI, Rozhkov VA (1985) *Wind waving in the World Ocean*. Hydrometeoizdat, Leningrad (in Russian)
- Nosov VN, Kaledin SB, Ivanov SG, Zevakin EA, Serebrinikov LV (2020) Aircraft scanning laser locator for recording sea waving characteristics. In: *Physical and mathematical modeling of processes in Geomedia*. 6th International School-Conference of Young Scientists. IPMech RAS, Moscow, pp 169–171 (in Russian)

The Methodology for Enhancement in Determining the Area of Total Underwork of the Rock Mass



S. B. Kulibaba and E. N. Esina 

Abstract The experience of applying in Russian Federation of the operating methodology for calculating displacements and deformations of the Earth's surface have revealed the ambiguity of determining the position of the fully underworked horizon over the developed space, which is a source of prognosis inaccuracy for the degree of destructive influence upon the underworked facilities. The method of eliminating this ambiguity by correcting the angles of complete displacements is justified.

Keywords Underground deposits development · Rock mass movement · Calculation method · Fully underwork · Prognosis ambiguity · Method for inaccuracy eradication

Changes in the conditions of underground mining of stratified mineral deposits require constant improvement of the methods used to predict the movement of rocks and the Earth's surface. The increase of these methods enhances accuracy reduces the degree of negative impact of mining on the underworked objects development (Trubetskoy et al. 2012; Okolnishnikov et al. 2019; Li and Yang 2020; Galvin 2016; Kulibaba and Esina 2018).

One of the most important parameters used in the rock movement calculations is the Earth's surface underwork degree, determined by the ratio of the size of the worked space in the developed reservoir and the average depth of development. Depending on this ratio, the Earth's surface can be completely or incompletely underworked. The signs of full underworking are the stabilization of the maximum subsidence of the Earth's surface with a further increase in the worked-out space, as well as the presence of a flat bottom in the displacement mould. While underworking is incomplete, there is no flat bottom of the mould, and an increase in worked-out space size leads to an increase in the maximum subsidence. Thus, the entire underworked mountain range above the excavation can generally be divided into two areas

S. B. Kulibaba · E. N. Esina (✉)

Institute of Comprehensive Exploitation of Mineral Resources, Russian Academy of Sciences, 4 Kryukovsky tupik, 111020 Moscow, Russia
e-mail: esina555@list.ru

located one above the other. A completely underwork of layers is presented in the lower part, and in the upper—there is not. The boundary separating these two areas is the fully underwork horizon, the position of which on each of the main sections of the displacement mould is determined by the critical depth H_0 , at which incomplete underwork shifts into complete under other equal conditions.

In the scientific and normative-methodological sources, there are two methods for determining the H_0 depth, one uses the coefficient of underworking—the ratio of the actual size of the developed space to the minimum size at which the complete underwork of the Earth's surface occurs (Trubetskoy and Kaplunova 2016) (method I); the second is based on the angles of complete displacement (Akimov et al. 1970) (method II). Let the values H_0 calculated by the first and second methods be denoted respectively $H_{0(I)}$ and $H_{0(II)}$.

The parameter of the surface underwork degree determines the value of the maximum subsidence and the configuration of the typical mould displacement curves in calculations, which are the basis for predicting without exception of all movements and deformations of the underworking rock mass. In the current Rules (Pravila 1998), the surface underwork degree is characterized by a coefficient N , which depends on the ratio of the size of the worked-out space D in each of the two main sections of the displacement mould to the average mine depth H :

$$N = f\left(\frac{D}{H}\right) \quad (1)$$

When the depth H is reduced to the critical value H_0 for a given size of the excavation D , the coefficient N takes the value of one, which is the requirement for the complete Earth's surface underwork. The value of the $K_0 = D/H_0$ ratio in the document (Viktorov et al. 2019) is determined for each coal-mining region of Russia. Thereby, for Kuzbass, the K_0 value is 1.6, for Donbass 1.2, for the Chelyabinsk basin 1.1, for the Vorkuta field 1.4, etc. Knowing the value of K_0 coefficient, the value $H_{0(I)}$ is first calculated using the formula:

$$H_{0(I)} = \frac{D}{K_0} \quad (2)$$

In the second method, the angles of complete displacements ψ_1 , ψ_2 and ψ_3 are used to determine the total surface underwork, with the help of which the output to the Earth's surface of the complete displacements zone is specified with the flat bottom mould formation in each of its main sections (Akimov et al. 1970; Pravila 1998; Viktorov et al. 2019). The value of $H_{0(II)}$ in this case can be determined by the formula:

$$H_{0(II)} = D \left[\frac{\sin \psi_1 \sin(\psi_2 - \alpha)}{\sin(\psi_1 + \psi_2)} + 0.5 \sin \alpha \right] \quad (3)$$

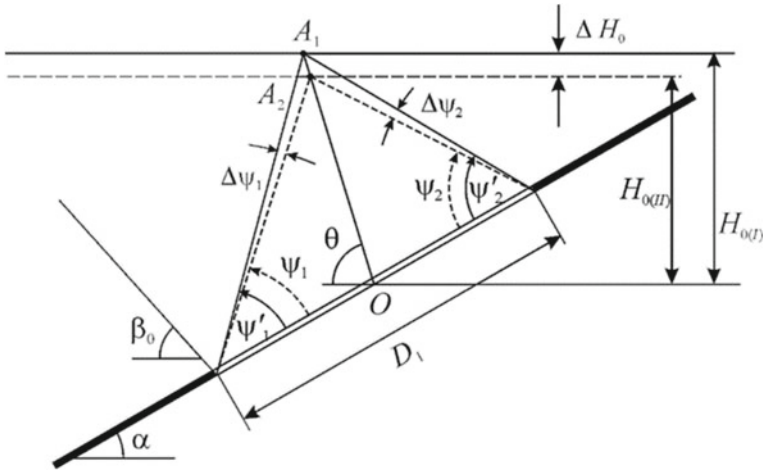


Fig. 1 Scheme for determining the H_0 value in two ways

Here D is the length of the excavation in the considered main section of the displacement mould (m), ψ_1 , ψ_2 and ψ_3 are the angles of total displacement, respectively, from the seam, uprising, and bedding of the stratum (degree), α —the seam inclination of the stratum (degree).

The problem is that in practice, these two methods of determining the same critical depth H_0 , provide results different one from the other. The vertical cross-section of the reservoir bedding (Fig. 1) shows the scheme for determining H_0 by these methods.

In other words, in the massif, instead of one, there are two calculated horizons of complete surface underwork, between which there is a certain conditional layer with a thickness of ΔH_0 with an unambiguously defined underwork degree.

To estimate the thickness of this layer, the depth H_0 , which provides a complete Earth's surface underwork, is calculated by the two methods given above according to the methodic (Pravila 1998) for the conditions of Kuzbass when working out mine with a length of 350 m in a horizontally lying coal seam. The condition $N_1 = 1$ is satisfied at the depth $H_{0(I)} = 218.8$ m (as according Table 7.17 in Pravila (1998) $D/H = 1.6$) in first method, while in the second one, the minimum depth of complete underwork $H_{0(II)}$ will be 208.6 m. Here for the conditions under consideration, the definition of the parameter $\Delta H_0 = H_{0(I)} - H_{0(II)}$ exceeds 10 m. Moreover, this difference is not constant—it changes both within one basin when the size of the excavation D and the seam inclination α of the stratum change, and in different basins (for example, in the Donbass conditions, deviation can reach more than 50 m). This ambiguity has a particularly sensitive effect on the accuracy of calculations of the rock mass displacement containing excavations (Kulibaba 2018, 2019a, b).

The illustration by a specific example for the consequences of the ambiguity of determining the position of the complete underwork horizon when predicting the deformed state of the moonlighting mountain range is depicted. The vertical cross-section of the strata (Fig. 2) the scheme of a hypothetical vertical shaft underwork

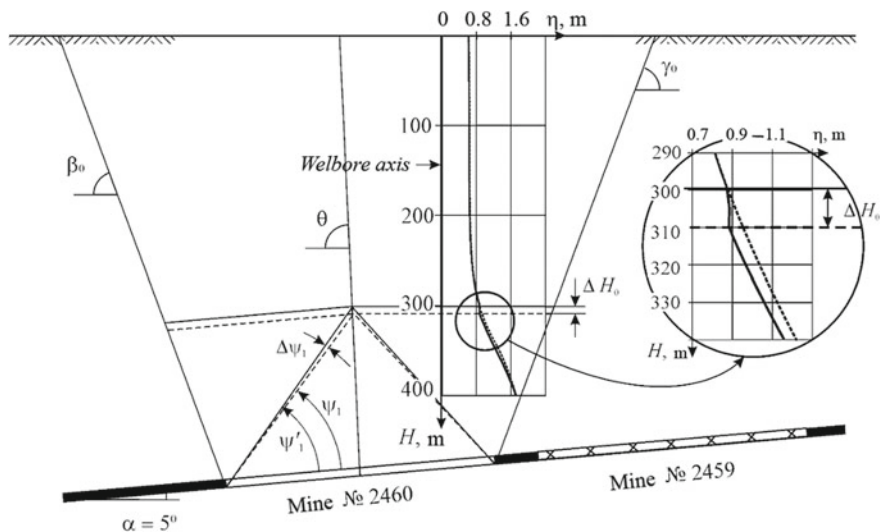


Fig. 2 The scheme of the vertical wellbore underwork

in the conditions of the Kirov mine of JSC “SUEK-Kuzbass” is shown with excavation 2460 of the Boldyrevsky formation. Solid line shows the graph of expected subsidence of the rock mass along the axis of this shaft, calculated according to the method (Kulibaba 2019b) for the following conditions: the average depth of the dredging is 490 m, the seam inclination angle of the formation is 5°, the extracted strength is 2.4 m, the excavation length is 300 m, the size of the excavation area along the bedding is 1340 m.

On the plot of the forecast subsidence in the depth range of 300–310 m, there is an obvious leap in the pattern change, caused by the described ambiguity in determining the complete underwork horizon position. The graphs of other expected deformations of the massif in this section, both vertical and horizontal (relative deformations, slopes, curvature, etc.), will also have an abrupt leap appearance, which will inevitably lead to erroneous decision at choice of geomechanical impact protection measures for the excavations.

One of the possible ways to solve this issue is to reduce the calculated parameters involved in determining the position of the complete underwork horizon to a state in which the described ambiguity disappears, i.e., the equality $H_{0(I)} = H_{0(II)}$ will take place. This reduction can be carried out in two ways—either by changing the value of the coefficient K_0 in formula (1), or by changing the values of total displacement angles ψ_1, ψ_2, ψ_3 in formula (3), by introducing the relevant corrections $\Delta\psi$ (see Figs. 1 and 2). Since the calculated values of these parameters are determined in different ways, the accuracy of each method can be evaluated on the results of studies conducted in 1959–1961, which then formed the basis of the methodology (Pravila 1998).

The article by M.A. Iofis (Iofis 1961) presents the analysis of the dependence of vector of the maximum total Earth’s surface displacement on the D / H ratio during the development of one isolated mine under complete underwork mining conditions based on the actual data for 14 mines. Using these data as the origin, it is found that the root-mean-square deviation in determining the $H_{0(I)}$ depth in the region of the greatest subsidence of the Earth’s surface during its underwork equals 7.7 m.

To assess the accuracy of determining the angles of total displacement, the results obtained in 1959 in the Ukrainian branch of VNIMI of studies of angles changes depending on the D/H ratio are analyzed. It is found that the standard deviation when measuring the angles ψ_1, ψ_2, ψ_3 , which determine the flat bottom of the mould of the Earth’s surface displacement in the zone of total displacement, is 4.0–4.5°. Such a dispersion in the angles of total displacement values, in addition to measurement errors, is particularly explained by the fact that in the rock mass, the boundaries of the zone of total displacement over the underworked space are not straight, but curved, and therefore, at different distances from the stratum plane, the values of the angles ψ_1, ψ_2, ψ_3 are not the same, as shown earlier (Kulibaba 2018). The calculations carried out according (3) show that the specified dispersion in the values of complete displacement angles entails an error in determining the depth $H_{0(II)}$, which reaches 16% of the length of the breakage heading, which, when length changes within 200–300 m, is yet 32–48 m.

It is obvious that the error in determining the $H_{0(II)}$ depth is several times greater than this in determining $H_{0(I)}$. Based on this fact, it can be concluded that the ambiguity in determining the position of the complete underwork horizon occurs mainly due to the inaccuracy of its calculation by the second method, i.e. using the total displacement angles according to the formula (3). Therefore, the most effective method, from author’s point of view, of eliminating this ambiguity is the adjustment of the standard values of the angles ψ_1, ψ_2, ψ_3 so that the top of the zone of total displacement moved from point A_2 , determined by method II, to the point A_1 on the complete underwork horizon calculated by method I (see Fig. 1). The new modified values of these angles $\psi'_1, \psi'_2, \psi'_3$ will be determined by the formulas:

$$\begin{aligned} \psi'_1 &= \operatorname{arctg} \left[\frac{2K_0^{-1} + \sin \alpha}{\cos \alpha - 2K_0^{-1} \operatorname{ctg} \theta} \right] - \alpha \\ \psi'_2 &= \operatorname{arctg} \left[\frac{2K_0^{-1} - \sin \alpha}{\cos \alpha + 2K_0^{-1} \operatorname{ctg} \theta} \right] + \alpha \\ \psi'_3 &= \operatorname{arctg}(2K_0^{-1}), \end{aligned} \tag{4}$$

Mapping changed angles $\psi'_1, \psi'_2, \psi'_3$ with tabular data (Pravila 1998), made for the conditions of the Donbass and Kuzbass, shows that deviation $\Delta\psi$ is 1°–3° on average which does not exceed the value of the standard deviation when measuring the angles of total displacement in full-scale conditions.

Dotted line in Fig. 2 shows the expected subsidence of the rock mass along the axis of the wellbore, calculated with implementation of the proposed changes, which confirms their effectiveness in eliminating ambiguity in determining of complete underwork horizon.

Thus, the analysis of the practice of the methodology for calculating displacements and deformations of the Earth's surface, governed by the current regulatory and methodological document (Pravila 1998), revealed ambiguity in determining the position of the complete underwork horizon over the excavation between two methods, the first of which uses the coefficient of underworking, and the second—the total displacement angles. It is shown, that the lack of an unambiguous determination of the complete underwork horizon is the origin of errors in the rock mass movements and deformations prognosis, which can lead to negative consequences for the underworked objects due to the incorrect choice of security measures. Based on the accuracy evaluation for each of two methods to calculate the position of the complete underwork horizon, the method to eradicate the identified ambiguity by adjusting the total displacement angles is substantiated.

References

- Akimov AG et al (1970) Sdvizhenie gornyh porod pri podzemnoj razrabotke ugol'nyh i slancevnyh mestorozhdenij. Nedra, Moscow (in Russian)
- Galvin JM (2016) Ground engineering: principles and practices for underground coal mining. Springer. <https://doi.org/10.1007/978-3-319-25005-2>
- Iofis MA (1961) Predraschet naibol'shikh osedaniy zemnoj poverhnosti. In: Sbornik trudov po voprosam issledovaniya gornogo davleniya i sdvizeniya gornyh porod. VNIMI, Leningrad (in Russian)
- Kulibaba SB (2018) Polozhenie granic zony polnyh sdvizenij v massive nad vyrabo-tannym prostranstvom. Markshejderija i Nedropol'zovanie 4(96):31–33 (in Russian)
- Kulibaba SB (2019a) Otnositel'noe maksimal'noe osedanie podrabatyvaemogo gornogo massiva. Markshejderija i Nedropol'zovanie 4(102):32–34 (in Russian)
- Kulibaba SB (2019b) Osnovnye polozhenija metodiki rascheta vertikal'nyh sdvizenij i deformacij podrabatyvaemogo gornogo massiva. Markshejderija i Nedropol'zo-Vanie 5(103):42–45 (in Russian)
- Kulibaba S, Esina EA (2018) New approach to the problem of protection of undermined objects on the earth's surface. E3S Web Conf 41(01043):1–5. <https://doi.org/10.1051/e3sconf/20184101043>
- Li G, Yang Q (2020) Prediction of mining subsidence in shallow coal seam. Math Probl Eng 2:1–9. <https://doi.org/10.1155/2020/7956947>
- Okolnishnikov VV, Ordin AA, Rudometov S (2019) Modeling of underground coal mining processes. Optoelectron Instrum Data Proc 55(4):383–387. <https://doi.org/10.3103/S8756699019040095>
- Pravila (1998) Pravila ohrany sooruzhenij i prirodnyh ob#ektov ot vrednogo vlijaniya podzemnyh gornyh razrabotok na ugol'nyh mestorozhdenijah. VNIMI, S.-Peterburg (in Russian)
- Trubetskoy KN, Kaplunov DR, Ryl'nikova MV (2012) Problems and prospects in the resource-saving and resource-reproducing geotechnology development for comprehensive mineral wealth development. J Mining Sci

- Trubetskoy KN, Kaplunov DR (eds) (2016) Mining: terminology dictionary. Gornaya kniga, Moscow (in Russian)
- Viktorov SD, Goncharov SA, Iofis MA, Zakalinskij VM (2019) Mehanika sdvizenija i razrushenija gornyh porod. RAS, Moscow (in Russian)

Kinematic Model of the Development of the Bottom of the Powell Basin (Weddell Sea)



A. A. Schreider, A. E. Sazhneva, M. S. Kluyev, A. L. Brekhovskikh, F. Bohoyo, J. Galindo-Zaldivar, C. Morales, and E. I. Evsenko

Abstract Based on the results of previously unpublished research in recent years by the Spanish research vessel *Hesperidas*, new and, if necessary, reinterpreted previously known sequences of linear magnetic anomalies in the Powell basin. Magnetic field anomalies were modeled from the perspective of lithospheric plate tectonics and a modern version of the electronic map-scheme of the basin bottom geochronology was compiled. The determination of Euler poles and rotation angles, carried out using original programs developed at IO RAS, allowed for the first time to conduct a detailed kinematic analysis of the features of the bottom expansion process based on the original technologies for calculating instantaneous spreading rates, and the asymmetry of the bottom expansion process, including the determination of the corresponding errors. The expansion of the bottom began during the C17n.3n chron (38.159–38.333 million years) and stopped during chron C11n. 2n (29.527–29.970 million years). Spreading took place at an average speed of 1 cm/year. Based on the calculations, detailed paleogeodynamics of the Orkney microcontinent splitting off from the Antarctic Peninsula during the spreading process has been restored.

Keywords Weddell sea · Powell basin · Eulerian poles · Paleogeodynamics

A. A. Schreider (✉) · A. E. Sazhneva · M. S. Kluyev · A. L. Brekhovskikh · E. I. Evsenko
Shirshov Institute of Oceanology RAS, 36 Nakhimov Ave, Moscow 117997, Russia
e-mail: aschr@ocean.ru

F. Bohoyo
Spanish Institute of Geology and Mineralogy, 23 Rios Rosas, 28003 Madrid, Spain

J. Galindo-Zaldivar
University of Granada, s/n C. P., St. del Ospicio, 18010 Granada, Spain

C. Morales
Andalusian Institute of Earth Sciences, St. De Las Palmeras, 4, 18071 Armilla Union, Granada, Spain

1 Introduction

The geological development of the northwest of the Weddell Sea in the context of the destruction of the continental bridge between South America and Antarctica and the evolution of the bottom of the transition zone from the Pacific to the Atlantic remain a subject of discussion (Dubinin et al. 2016; Teterin and Gol 2007; Udintsev and Schenke 2004; Khain 2001; Shemenda and Groholsky 1986; Schreider et al. 2016, 2006; Schreider Al 2005; Schreider Al et al. 2014; Aldaya and Maldonado 1996; Barker 1972; Barker and Burell 1977; Barker and Griffith 1972; Barker et al. 2013; Bohoyo et al. 2002; Catalan et al. 2013; Civile et al. 2012; Cuningham et al. 1995; Dziak et al. 2010; Eagles 2010; Eagles and Livermore 2002; Eagles et al. 2005, 2006; Ghidella et al. 2002; Herve et al. 2008; King et al. 1997; Konig and Jokat 2006; Larter and Barker 1989; Lodolo et al. 2010). The solution of these questions is of fundamental importance for studying the interaction of the Scotia lithospheric (Maldonado et al. 2014; Perez et al. 2014; Tanahashi et al. 1997; Verard et al. 2012; Weaver et al. 1979; topex.ucsd 2020) plate and the Antarctic lithospheric plate (Thomas et al. 2003), as well as for determining the primary spatial position of the elements of the American-Antarctic continental bridge and restoring on a quantitative basis the initial stages of the expansion of the bottom of the northwest Weddell Sea in connection with the initialization of the American-Antarctic sector of the southern circumpolar ocean current—the most important element of the evolution of the climate of the southern hemisphere of the Earth and the planet as a whole. The most important role in the study of the paleogeodynamics of the north of the Weddell Sea is played by the reconstruction of the evolution of the bottom of the Powell Basin (Fig. 1).

2 The Analysis of the Current State of Geological and Geophysical Studies of the Powell Basin

In numerous (including those listed above) published studies, there is no single approach to the use of geographical nomenclature for the structures of the studied area. Thus, in Udintsev and Schenke (2004) the terms Sea of Scosh and South Orkney microcontinent are used, while in Ivanov et al. (2008), Sadovnichy et al. (2003) and Khain (2001) the terms Sea of Scotia and South Orkney microcontinent are used. The South Orkney microcontinent itself is presented in the literature either schematically without dismemberment (for example, Civile et al. 2012), or with the allocation of a number of additional internal tectonic block structures and troughs-throgs, among which the most significant (Maestro et al. 2013) are the depressions of Airy (or Air Udintsev and Schenke 2004), Bourguer, Eotvos and Newton.

The basin west of the South Orkney microcontinent—Powell Basin (Lodolo et al. 2010) in the text of the work (Udintsev and Schenke 2004) is transcribed differently in different places of the article. The basin is bounded on the south by an elongated

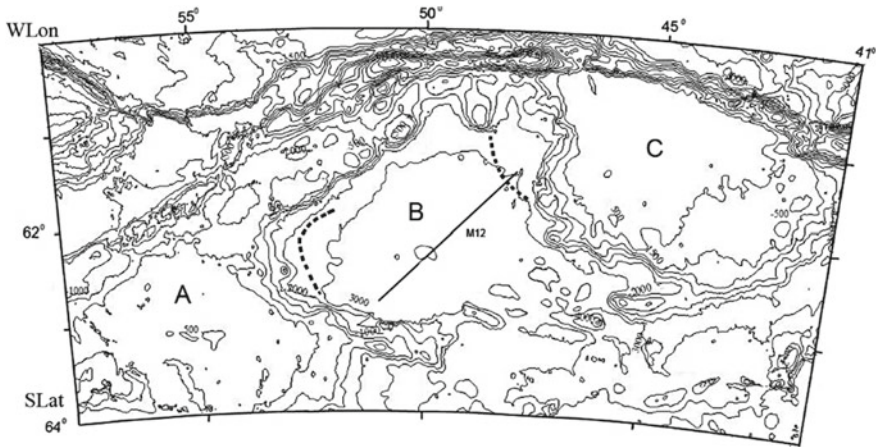


Fig. 1 Bathymetry of the Antarctic Peninsula (a), the Powell Basin (b), and the South Orkney microcontinent (c) according to Wernike (1985) and topex.ucsd (2020). The position of the borders of the spreading area (dotted line) is given according to the data (Eagles and Livermore 2002), as well as Figs. 3 and 4 of the present work. Isobates in meters

ridge-like hill, which either has no name (for example, Eagles et al. 2005 and Lodolo et al. 2010) or is designated as the South Powell ridge (Udintsev and Schenke 2004; Maldonado et al. 1998).

In the literature, there are also no unified ideas about the mutual arrangement of the various tectonic elements of the continental bridge. For the research region, published studies do not have a single approach not only to determining the relative position, but also to determining the configuration of individual bridge elements at the initial stage of its development. In (Barker 1972), these elements are not marked in any way, are difficult to recognize, and (by the nature of the hatching) are often referred to as intermediate blocks (Barker 1972). At the same time, in Verard et al. (2012), the contours of the bridge elements are presented so schematically that there is no confidence in restoring even their geographical names. In other works, this kind of uncertainty is overcome by the introduction of symbols (for example, Barker and Burell 1977; Konig and Jokat 2006).

An important role in the study of the paleogeodynamics of the north-west of the Weddell Sea and adjacent areas could be played by information about the tectonic features of the bottom. But the underlying in these models linear magnetic anomalies and transform faults in these areas are still not precisely defined and, being based on a limited amount of geological and geophysical data, differ in their drawing in various publications (Coren et al. 2000, 1997; Eagles and Livermore 2002; Eagles et al. 2005; Galindo-Zaldivar et al. 2002; Maldonado et al. 1998, 2014; Rodriguez-Fernandez et al. 1994). The most important tectonic events of the split of the American-Antarctic continental bridge in the north-west of the Weddell Sea are associated with the breakaway of the South Orkney microcontinent from the Antarctic Peninsula, which occurred along the spreading axis system in the Powell Basin.

The paper (Coren et al. 2000) presents the results of geomagnetic studies in the Powell Basin of the Italian research vessel "Explora" and data from the BAS (British Antarctic Surveys) geological and geophysical research data bank. The modeling of linear magnetic anomalies in the framework of the bottom spreading concept was carried out by visual comparison of the model and the observed curves of the anomalous magnetic field, which made it possible to identify the C5E—C8 crones. In this case, the spreading axis is connected either to the local maximum of the magnetic field or to the gradient zone (and this zone has different vergencies on the model and on the different observed curves of the anomalous magnetic field).

In the paper (Eagles and Livermore 2002), as a result of modeling the data of aeromagnetic studies, C6AA-C11 crones were identified on the observation profiles. The spreading axis on the model curve for the Powell Basin corresponds to the C6AA crone and coincides with the minimum of the theoretical magnetic anomaly. At the same time, on the observed curves of the anomalous magnetic field, the spreading axis is drawn along the minima, or along gradient zones, or maxima of the observed curves.

In the study Eagles et al. (2005), another variant of modeling the data of aeromagnetic observations in the Powell Basin was presented, which allowed the above-mentioned authors to isolate the C6-C9 crones. A number of discrepancies can be noted in the geochronological dating of the works Eagles and Livermore (2002) and Eagles et al. (2005). The C6B chron in the first cited work corresponds to the C8 chron in the second, and the C8 chron corresponds to the C11 chron. The paleoaxis of spreading in the second cited work corresponds to an unnamed reverse-polarity chron enclosed between the C6 conjugate chrons (apparently, this is the C5Er chron). At the same time, the death of the paleoaxis of the bottom extension in Eagles and Livermore (2002) occurred during the C6AA chron (and, thus, earlier than the C5Er chron).

In paper Coren et al. (2000), along with the calculations of theoretical magnetic anomalies in the bottom expansion model, a scheme of the planned position of the chrons in the Powell basin is presented, which demonstrates their direction at an angle of about 35 degrees. In contrast, the joint analysis of the gridded aeromagnetic and hydromagnetic data collected in the BAS geological and geophysical information bank led Eagles and Livermore (2002) to create a scheme for the planned position of the regions of forward and reverse polarity P0 (chron C6AA)—P6 (chron C11) with the direction of the presented chrons at an angle close to 45 degrees. Comparison of the schemes of the distribution of chrons in the plan from the works Coren et al. (2000) and Eagles and Livermore (2002) showed their discrepancy between each other. So the chron C6 from the second work is close to the position in terms of the chron C5E from the first work. The position of the C9 chron from the second work is between the C6B and C6C chrons from the first work, and the position of the C11 chron from the second work occupies the space between the C7 and C8 chrons from the first work.

In Civile et al. (2012) and Nerlich et al. (2013), a single spreading axis extending at an angle of about 50 degrees is distinguished in the Powell Basin. In the works Galindo-Zaldivar et al. (2002, 2006, 2014), Maldonado et al. (1998, 2014) and Perez

et al. (2014) there are two parallel axes, the southernmost of which has a shorter spatial length.

In paper Wit (1977), it is assumed that the beginning of the destruction of the American-Antarctic continental bridge (including the expansion of the bottom in the Powell Basin from some time) dates back to 70–80 million years ago.

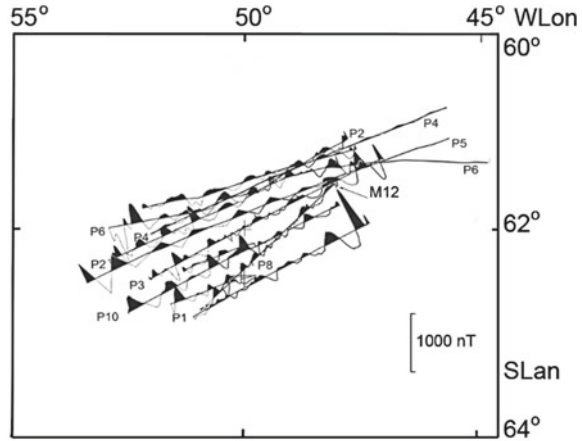
The beginning of spreading in the Powell Basin in Barker (2001) and Verard et al. (2012) is dated to the age of 32 million years (chron C12r), and the end of the process of spreading the bottom in it is dated to the time of 24 million years (chron C7r). In Eagles and Livermore (2002), the beginning of spreading in the basin is dated to the time of 29.7 million years (chron C11n.2n), and the end of the process of spreading of the bottom is attributed to the time of 21.8 million years (chron C6Bn.1n). In Civile et al. (2012), the beginning of the split is dated to a time of about 25 million years (chron C7Ar). At the same time, the end of the spreading in the basin is not precisely defined. In Nerlich et al. (2013), the beginning of spreading is correlated with the time of 21 million years (chron C6Ar), and the end time of the bottom expansion process is not specified.

Summing up the analysis, it is necessary to state that in the literature there are no uniform ideas about the dating of the beginning and end of the process of bottom expansion, but also uniformity in the nomenclature of geographical names of forms of underwater relief for the north-western part of the Weddell Sea. Therefore, in this study, for the presentation of the material (taking into account the works Agapova et al. 1993; Sadovnichy et al. 2003; Khain 2001, etc.), the terms will be used: the Scotia and Weddell Seas, the Powell and Jane Basins, the South Orkney microcontinent, the Antarctic Peninsula.

From the stated positions, the analysis of the materials shows that the Antarctic Peninsula belongs to the most important parts of the American-Antarctic continental bridge and the destruction of the bridge is interrelated with the dispersion of the elements of the peninsula, among the most important of which is the South Orkney microcontinent. Its evolution took place mainly in the process of spreading the bottom in the Powell Basin.

It was mentioned above that the analysis of the numerous literature sources cited above shows that the dating of linear magnetic anomalies and polarity chrons, the configuration of spreading axes, their number, spatial position, as well as the position of shifting transform faults differ in different studies. These differences undoubtedly reflect the scarcity of available geological and geophysical materials, which does not allow us to confidently analyze the evolution of the north-west of the Weddell Sea and adjacent regions, for example, Eagles and Vaughan (2009). In the literature, there is no quantitative basis for reconstructing the stages of the evolution of the bottom of the region, including the confident determination of the coordinates of the Eulerian poles and the angles of rotation. This work is devoted to the detailed reconstruction of the initial spatial position of the tectonic elements of the bridge in the region of the northwest of the Weddell Sea, the first reconstruction on a quantitative basis (including the calculation of the Eulerian poles and rotation angles) of the stages of the collapse of the bridge in relation to the evolution of the bottom of the surrounding regions. At the same time, an important role in the study of the paleogeodynamics

Fig. 2 Profiles of the anomalous magnetic field of the Powell basin, based on the results of geomagnetic observations along the profiles P1-P10 and M12 of the research vessel “Hesperidas”, supplemented with information from the BAS (British Antarctic Surveys) geological and geophysical research data bank



of the northwest of the Weddell Sea is played by previously unpublished geological and geophysical (and primarily geomagnetic) data from Spanish expeditions in recent years, obtained from the Spanish research vessel "Hesperidas" (Fig. 2).

Information about for the first time restoring data based on the result of research vessel “Hesperidas” expedition for geochronology of the bottom, the spatial position of transform disturbances for the region of the north-west of the Weddell Sea, is the basis for the first detailed quantitative paleogeodynamics reconstructions of the stages of the bottom expansion according to the original domestic methodology (Zonenshein et al. 1990; Schreider Al 2005), which develops on the basis of a modern database of geological and geophysical data (topex ucSD 2020) paleogeodynamics representations of works Bullard et al. (1965) and Wernike (1985).

3 Calculation Results

Based on a comprehensive geological and geophysical interpretation of anomalous magnetic field data, taking into account information about seismicity, heat flow, and the results of deep-sea drilling in wells 695, 696, 697, 1100, 1102, 1103 (Barker et al. 2013; Coren et al. 2000; Maldonado et al. 2014; Thomas et al. 2003), in this paper, we analyzed the boundaries of lithospheric plates identified in the literature, linear magnetic anomalies, and their paleogeodynamics interpretation from the standpoint of the concept of lithospheric plate tectonics.

Aeromagnetic and hydromagnetic observations, the main results of which are presented in Fig. 2, allowed us to obtain information about the distribution of magnetic anomalies in the Powell Basin. According to them, the anomalous magnetic field is characterized by the presence of linear magnetic anomalies of small amplitude (less than 200 nT) with a wavelength of up to 35 km. A comparison of the observed and theoretical magnetic anomalies in the model of the bottom expansion

allowed us to identify the paleomagnetic anomalies A11-A17, as well as the corresponding C11n.2n–C17n.3n polarity chrons (Fig. 3), the most modern version of the distribution of which in the Powell Basin is shown in Fig. 4. Here, according to the displacement of the axes of the anomalies, three not long transform faults are outlined, which violate the linearity of the selected anomalies.

A comparison of the spatial position of the C17r crone with the position of the boundary between the continental and oceanic crust from Eagles and Livermore (2002) and taking into account the data in Figs. 3 and 4 of this paper indicates that the boundary is located on the periphery of the A17 anomaly. At the same time, the spreading paleo-axis is associated with the position of the C11n.2n (29.527–29.970 Ma) chron, and the beginning of the bottom expansion process is dated to the C17n.3n (38.159–38.333 Ma) chron, and possibly to the C17r (38.333–38.615 Ma) chron (Gradstein et al. 2012). Thus, the spreading of the bottom in the Powell basin took about 9 million years.

The boundary itself marks the transition from the continental crust to the crust born during the spreading process and in the Powell Basin is spatially located in the isobath

Fig. 3 The observed (a) and theoretical (b) linear magnetic anomalies, as well as the corresponding C11n.2n–C17n.3n polarity chrons in the framework of the concept of spreading the bottom along the M12 profile (see Figs. 1 and 2, topex ucscd 2020). The paleospreading axis corresponds to the C11n.2n chron

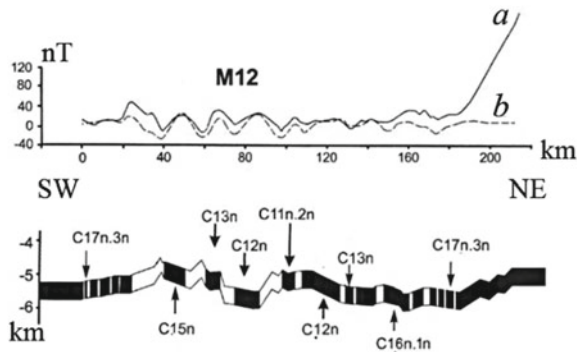
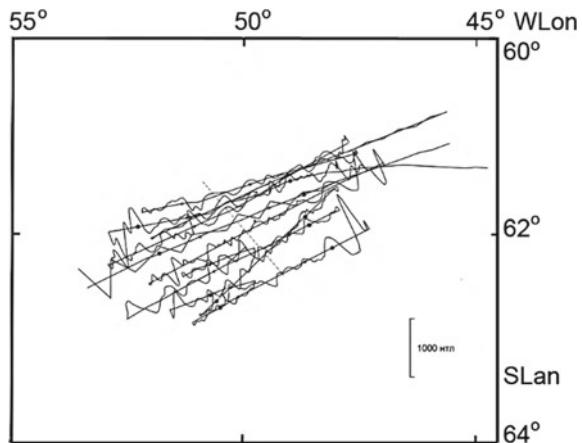


Fig. 4 Examples of identification of linear magnetic anomalies A11 (dotted line), A13 (small dots) and A16 (large dots) on profiles in the Powell Basin, based on the results of modeling the anomalous magnetic field, an example of which along the M12 profile is shown in Fig. 3 (topex ucscd 2020)



interval of 2.5–3.0 km. The spreading of the bottom occurs in the direction of 300, orthogonal to the direction of the paleo-axial magnetic anomaly. Kinematic calculations indicate that in the range of paleoanomalies A11–A17, the bottom spreading was at a rate of 0.7–3.3 cm/year and was generally close to 1.9 cm/year. The build-up of new oceanic crust in the basin to the west of the spreading paleo cline was generally 10% more intense (1 cm/year) than to the east of it (0.9 cm/year). The spreading reached its maximum values in the range of anomalies A15–A16 (up to 1.6 cm/year in the east–1.7 cm/year in the west), and its minimum values were observed in the range of anomalies A12–A13 (up to 0.2 cm/year in the east–0.5 cm/year in the west).

4 Calculation of Breakaway Parameters

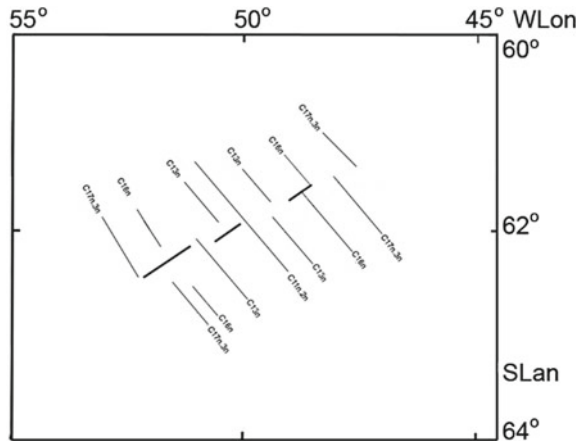
In this paper, the Bullard method (Bullard et al. 1965) is used for the first time for the case of combining the C17n chron.3n for two sequences of paleomagnetic anomalies, displaced along with other anomalies by the first identified disturbance, which may be of a transform nature. Calculations of the Eulerian poles and rotation angles were carried out according to the original programs of the Laboratory of Geophysics and Tectonics of the World Ocean Floor of the IO RAS, incorporated into the Global Mapper software environment (Schreider et al. 2005), the calculation principles for which are set out in Zonenshein et al. (1990) and Schreider et al. (2005). In the analyzed area of the Powell Basin, the bottom depth reaches 3 km (the area between the contours shown by the strokes on Fig. 1).

According to the estimated calculations, at the position of the Eulerian pole of the final rotation at the point with coordinates 51.18° S Lat 62.53° W Lon. it is possible to get a very good combination of the C17n.3n crone south of 61°. The angle of rotation was $17.8^\circ \pm 0.5^\circ$. At the same time, the standard deviation in the calculated points of alignment was ± 22 km (12 points of alignment). Paleogeodynamic calculations of the Euler pole and the angle of rotation allowed for the first time to estimate the paleogeodynamic parameters of the opening of the bottom of the Powell basin using a new geochronology scheme (Fig. 5).

5 Conclusions

Thus, as a result of the conducted studies, new sequences of linear magnetic anomalies in the Powell Basin were identified and, if necessary, reinterpreted. Modeling of paleomagnetic anomalies made it possible to create a modern version of an electronic map—a diagram of the geochronology of its bottom. The expansion of the bottom in the basin began during the chron C17n.3n (38.159–38.333 million years), and perhaps the chron C17r (38.333–38.615 million years). Spreading occurred at an average rate of 1 cm/year. The accumulation of new oceanic crust in the basin to the west of the spreading paleoaxis was generally 10% more intense than to the east of it.

Fig. 5 Diagram of the geochronology of the bottom of the Powell basin based on the results of modeling the anomalous magnetic field along the profiles shown in Fig. 3 (topex ucSD 2020). The thick lines show tectonic disturbances, including those of a possible transform nature



At the same time, the spreading reached its maximum values in the range of anomalies A15-A16 (up to 1.6 cm/year in the east–1.7 cm/year in the west), and its minimum values were observed in the range of anomalies A12-A13 (up to 0.2 cm/year in the east–0.5 cm/year in the west). The determination of the Eulerian poles and the angles of rotation allowed for the first time to conduct a detailed analysis of the features of the process of bottom expansion during the evolution of the breakaway of the Orkney microcontinent from the Antarctic Peninsula during the spreading process.

Acknowledgements This work was carried out within the framework of the RFBR project No. 20-05-00089. At the same time, the methodological issues of calculating the model curves of magnetic anomalies were worked out within the framework of State Task No. 0128-2021-0004.

References

- Agapova GV, Vinogradova IV, Kashnikova IP (1993) Dictionary of geographical names of underwater landforms. Geological Institute RAS, Moscow (In Russian)
- Aldaya F, Maldonado A (1996) Tectonics of the triple junction at the southern end of the Shackleton Fracture Zone (Antarctic Peninsula). *Geo-Mar Lett* 16:279–286
- Barker PA (1972) Spreading center in the east Scotia sea. *Earth Planet Sci Lett* 15:123–132
- Barker P (2001) Scotia sea regional tectonic evolution: implications for mantle flow and paleocirculation. *Earth Sci Rev* 55:1–39
- Barker P, Burrell J (1977) The opening of the Drake Passage. *Mar Geoph Res* 25:15–34
- Barker P, Griffith D (1972) The evolution of the Scotia ridge and Scotia sea. *Phil Trans R Soc Lond* 271:151–183
- Barker P, Lawver L, Larter R (2013) Heat-flow determinations of basement age in small oceanic basins of the southern central Scotia Sea. *Geol Soc London Spec Pub* 381
- Bohoyo F, Galindo-Zaldívar J, Maldonado A, Schreider AA, Suriñach E (2002) Basin development subsequent to ridge-trench collision: the Jane Basin. *Mar Geoph Res* 23:413–421
- Bullard E, Everett J, Smith A (1965) The fit of continents around Atlantic Symposium on continental drift. *Philos Trans R Soc Lond* 258A:41–51

- Catalan M, Galindo-Zaldivar J, Davila J et al (2013) Initial stages of oceanic spreading in the Bransfield Rift from magnetic and gravity data analysis. *Tectonophysics* 585:102–112
- Civile D, Lodolo E, Vuan A, Loreto M, (2012) Tectonics of the Scotia-Antarctica plate boundary constrained from seismic and seismological data. *Tectonophysics* 550–553:17–34
- Coren F, Ceccone G, Lodolo E et al (1997) Morphology, seismic structure and tectonic development of the Powell Basin, Antarctica. *J Geol Soc Lond* 154:849–862
- Coren F, Lodolo E, Ceccone G (2000) Age constraints for the evolution of the northern Powell basin (Antarctica). *Boll Teor Geoph, Appl* 41:193–205
- Cunningham W, Dalziel I, Lee T, Lawver L (1995) Southernmost America-Antarctic peninsula relative plate motion since 84 Ma: implications for the tectonic evolution of the Scotia arc region. *J Geoph Res* 100:8257–8266
- De Wit M (1977) The evolution of the Scotia arc as a key to the reconstruction of southwestern Gondwanaland. *Tectonophysics* 37:53–81
- Dubinin EP, Kohan AV, Teterin DE et al (2016) Tectonic structure and types of rift basins of the Scotia Sea, South Atlantic. *Geotectonics* 1:41–61 (In Russian)
- Dziak R, Park M, Lee W (2010) Tectonomagmatic activity and ice dynamics in the Bransfield Strait back-arc basin, Antarctica. *J G R* 115 (B12)
- Eagles G (2010) South Georgia and Gondwana Pacific margin : lost in translation? *J South Am Earth Sci* 30:65–70
- Eagles G, Livermore R (2002) Opening history of Powell basin, Antarctic peninsula. *Mar Geol* 185:195–205
- Eagles G, Livermore RA, Morris P (2006) Small basins in the Scotia Sea: the Eocene Drake Passage gateway. *Earth Planet Sci Lett* 242:343–353
- Eagles G, Vaughan A (2009) Gondwana breakup and plate kinematics: business as usual. *Geoph Res Lett* 36
- Eagles G, Livermore RA, Fairhead JD, Morris P (2005) Tectonic evolution of the west Scotia Sea. *J G R* 110 (BO 2401): 1–19
- Galindo-Zaldivar J, Balanya J, Bohoyo F et al (2002) Active crustal fragmentation along the Scotia-Antarctic plate boundary east of the South Orkney Microcontinent (Antarctica). *Earth Planet Sci Lett* 204:33–46
- Galindo-Zaldivar J, Bohoyo F, Maldonado A et al (2006) Propagating rift during the opening of a small oceanic basin: the Protector Basin (Scotia Arc, Antarctica). *Earth Planet Sci Lett* 241:398–412
- Galindo-Zaldivar J, Puga E, Bohoyo F et al (2014) Magmatism, structure and age o Dove Basin (Antarctica): a key to understanding South Scotia Arc development. *Glob Planet Change* 122:50–69
- Ghidella M, Yanez G, LaBrecque J (2002) Revised tectonic implications for the magnetic anomalies of the western Weddell Sea. *Tectonophysics* 347:65–86
- Gradstein F, Ogg J, Schmitz M, Ogg G (2012) *The geologic time scale 2012*. Elsevier, Amsterdam
- Herve F, Calderon M, Faundez V (2008) The metamorphic complexes of the Patagonian and Fuegian Andes. *Geol Act* 6:43–53
- https://www.topexucsdedu/html/mar_topo(2020)
- Ivanov VA, Pokazeev KV, Schreider AA (2008) *Fundamentals of Oceanology*. Lan', Moscow (In Russian)
- Khain VE (2001) *Tectonics of continents and oceans*. Nauchny Mir, Moscow (In Russian)
- King E, Leitchenkov G, Galindo-Zaldivar J et al (1997) Crustal structure and sedimentation in Powell basin. *Ant Res Ser* 71:75–93
- Konig M, Jokat W (2006) The Mesozoic breakup of the Weddell Sea. *J G R* 111 (B12102)
- Larter R, Barker P (1989) Seismic stratigraphy of the Antarctic Peninsula Pacific margin: a record of Pliocene-Pleistocene ice volume and paleoclimate. *Geology* 17:731–734
- Lodolo E, Civile D, Vuan F et al (2010) The Scotia-Antarctica plate boundary from 35° W to 45° W. *Earth and Planet Sci Lett* 293:200–215

- Maestro A, Lopez-Martinez J, Bohoyo F (2013) Mesozoic to recent evolution of intraplate stress fields under multiple remote stresses: The case of Signy Island (South Orkney Microcontinent, Antarctica). *Geol Soc London Spec Publ* 381
- Maldonado A, Zitellini N, Leitchenkov G et al (1998) Small ocean basin development along the Scotia-Antarctica plate boundary and in the northern Weddell Sea. *Tectonophysics* 296:371–402
- Maldonado A, Bohoyo F, Galindo-Zaldívar J et al (2014) A model of oceanic development by ridge jumping: opening of the Scotia Sea. *Glob Planet Change* 123:152–173
- Nerlich R, Clark S, Bunge H (2013) The Scotia gateway: no outlet for Pacific mantle. *Tectonophysics* 604:41–50
- Perez L, Maldonado A, Bohoyo F et al (2014) Depositional processes and growth patterns of isolated oceanic basins the Protector and Pirie basins of the southern Scotia sea (Antarctica). *Mar Geol* 357:163–181
- Rodriguez-Fernandez J, Balanya J, Galindo-Zaldívar J, Maldonado A (1994) Margin styles of Powell basin and their tectonic implications (NE Antarctic Peninsula). *Terra Ant* 1:315–316
- Sadovnichy VA, Kozoderov VV, Ushakov SA, et al (2003) Oceans and continents. MSU, Moscow (In Russian)
- Schreider AA, Schreider AI A, Bulychev AA, Galindo-Zaldívar H, Maldonado A, Kashintsev GL (2006) Geochronology of the American-Antarctic Ridge. *Oceanology* 46(1):123–132 (In Russian)
- Schreider AA, Schreider AI A, Klyuev MS, Sazhneva AE (2016) Destruction of the American-Antarctic continental bridge. *Prosessy v Geosredah* 4:378–382 (In Russian)
- Schreider AI A (2005) Uncovering the deep-sea basin of the Black Sea. *Oceanology* 45(4):592–604 (In Russian)
- Schreider AI A, Schreider AA, Evsenko EI (2014) Stages of development of the Bransfield Strait Basin. *Oceanology* 53(3):396–405 (In Russian)
- Shemenda AI, Groholsky AL (1986) Geodynamics of the South-Antillean region. *Geotectonics* 1:84–95 (In Russian)
- Tanahashi M, Nashimura A, Oda H, Murakami F (1997) Preliminary report of the 1997 of the geological and geophysical survey results, north of the Antarctic peninsula. *Polar Geosci* 12:192–214
- Teterin DE, Gol K (2007) Geodynamics of the continental margins of the Bellingshausen and Amundsen seas. In: *Proceedings of XL Tectonic Meeting, Moscow*, pp 290–294 (In Russian)
- Thomas C, Livermore R, Pollitz F (2003) Motion of the Scotia plates. *Geoph J Int* 155:789–804
- Udintsev GB, Schenke GV (2004) Essays on the geodynamics of West Antarctica. *GEOS, Moscow* (In Russian)
- Verard C, Flores K, Stampfli G (2012) Geodynamic reconstructions of the South America-Antarctica plate system. *J Geodynam* 53:43–60
- Weaver S, Saunders A, Pankhurst R et al (1979) A geochemical study of magmatism associated with the initial stages of back-arc spreading. *Contrib Mineral Petrol* 68:151–169
- Wernike B (1985) Uniform sense normal simple shear of the continental lithosphere. *Can J Earth Sci* 22:108–125
- Zonsenshein DD, Lomize MG, Ryabukhin AG (1990) Manual for practical classes in geotectonics Moscow MSU (In Russian)

Investigation of Influence of the Screw Propeller Working Towards the Flow on Parameters of Near Water Aerosol



V. N. Nosov , S. G. Ivanov , V. I. Pogonin , S. B. Kaledin ,
E. A. Zevakin , and N. A. Zavyalov 

Abstract Laboratory studies of hydrodynamic disturbance effects caused by the screw propeller working towards the flow on the disperse composition of the near water aerosol are presented. The marine conditions are simulated by aerated water in the flow-through tank. The elastic scattering of laser beam by aerosol is used for monitoring. The pulses of laser scattering by aerosol particles within the lens focal area of photosensor module (based on photomultiplier FEU-157) are registered for fixed interval 300 s. The distribution of scattering pulse amplitudes proportional to aerosol particle sizes is represented in histogram form. The screw on–off difference histograms are used to study screw-caused hydrodynamic disturbance effect on aerosol disperse composition. The data obtained indicate that the addition of hydrodynamic disturbances formed by the screw propeller working towards the aerated flow leads to increasing the proportion of larger aerosol particles.

Keywords Hydrodynamic disturbance · Aerosol scattering · Laser radiation · Histograms · Aerosol disperse composition

1 Introduction

The study of some processes and phenomena occurring in the World Ocean often relates to the need of recording weak hydrodynamic disturbances (HDD) in the marine environment caused by different sources. Such disturbances may be recorded as parameter changes of sea surface, near-surface water layers, and atmosphere. To study HDD remote laser optical methods can be used (Shifrin 1981). The present work considers the recording the near-water atmosphere manifestations of model hydrodynamic disturbances occurring in the near-surface water layer in laboratory conditions. Such processes occurring in the marine environment may have different

V. N. Nosov · S. G. Ivanov (✉) · V. I. Pogonin · E. A. Zevakin · N. A. Zavyalov
Institute of Geochemistry and Analytical Chemistry, V.I. Vernadsky RAS, Moscow, Russia
e-mail: ivanovsg5167@yandex.ru

S. B. Kaledin
N.E. Bauman Moscow State Technical University, Moscow, Russia

nature: geological, biochemical, or hydrodynamic. The influence of processes occurring in deep-sea water layers on the near-water aerosol may be conducted by vertical up-flow of sea water from depth to surface. As a result, gases dissolved in the water release as many bubbles rising up to the sea surface. Passing through the surface bubbles burst and throw out small drops to the atmosphere. Thus, concentration and disperse composition of near-water aerosol are changed. The sources of deep-sea water disturbances causing the bubble appearance in the sea-surface water layer may be both natural (gas evolution in volcanic zones or gas hydrate dissolution) and artificial (for instance, subsea wells or streamed-around parts of underwater constructions: bridge supports or pipelines). As a whole, the effects of deep-sea processes on the near-water aerosol are still poorly studied.

The aerosol formation by bursting the bubbles passing through the sea surface has already long been in study (Resch et al. 1986; Leifer 2000). Most aerosol particles above the sea have been determined to be 0.1–0.3 microns in size and belong to the «film» particles. Aerosol particles of the same size commonly arise in passing gas bubbles with diameters of 1–2 mm through aquatic medium too (Ghulanov and Petryanov 1980).

The influence of hydrodynamic processes on the near-surface aerosol has been noted in Piskozub (1995), Zielinski et al. (1995). Authors used lidar to measure distribution of aerosol particle concentration in the shelf zone over the height. They have proposed that the bottom relief affects the concentration of near-water aerosol.

Earlier our field experiments have been carried out in the Black Sea, Theodosia Bay. We have revealed the change in parameters of laser radiation scattered by aerosol near sea surface measured at various altitudes under the influence of artificial HDD (formed by underwater jet issuing from submersible pump) (Nosov et al. 2012). Our model laboratory experiments have showed the differences in the distribution of aerosol disperse composition over the water surface under the influence of HDD formed by screw propellers and obstacles streamlined with the flow (Nosov et al. 2017, 2018).

2 The Order of the Experiments

The purpose of the present laboratory studies is to research HDD effect caused by screw propeller working towards the flow on the change of near-water aerosol disperse composition.

The experiments have been carried out in the flow-through tank (Fig. 1), $1000 \times 145 \times 150$ mm in size. The water layer height is 90 mm. To approach field conditions the aquatic medium in the pan is aerated. The pan equipment consisted of screw propeller, aerated flow generator, KLM-650/40 semiconductor laser (wavelength 660 nm, power 58 mW, and oval beam cross section 3×5 mm), screen with aperture and lens, photosensor module based on photomultiplier (PMT) FEU-157, and trap for laser beam passing parallel to the water surface at 50 mm height. The screw propeller 35 mm in diameter is immersed to the depth 60 mm and offset 300 mm

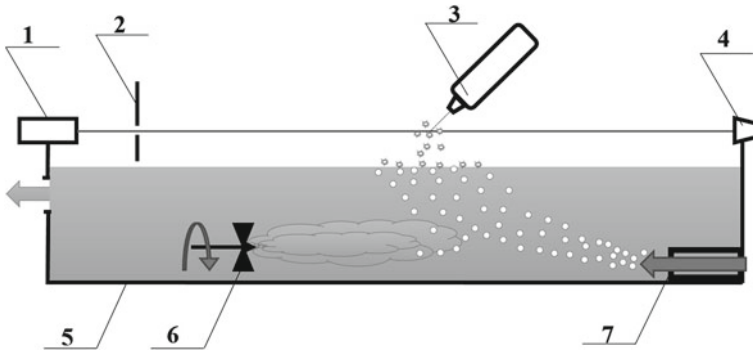


Fig. 1 Scheme of laboratory installation with flow-through tank: 1—semiconductor laser; 2—screen with aperture; 3—photosensor module with a lens; 4—laser beam trap; 5—tank; 6—screw propeller; 7—generator (laminar flow aerator)

from the focal lens area downstream. The screw propeller is rotated by DC motor DPR-62-N1-02 using flexible drive. Motor rotation speed is less than the maximum possible value in order to avoid too large disturbances in the water. The water flow is aerated by supplying the air to the tap water stream using aquarium compressor. To laminarize water flow the aerated water is fed into cylindrical tube located at the pan bottom, provided with the holes in which the short tubes are inserted.

The optical axis of the photosensor module consisting of the lens (focal length 19 mm, and diameter 8 mm) mounted on the adapter tube in front of PMT is inclined at angle of 30° towards the laser beam. To eliminate the effect of external illumination KS-14 colored glass filter cutting radiation with wavelength shorter than 630 nm is placed in front of the PMT window. PMT sensitivity could be controlled by applying voltage from 0.5 to 2.0 V to the high-voltage unit integrated into PMT. All results below have been measured at high voltage on PMT amounted to 1980 V (which is close to maximum). The output PMT signal is fed to L-Card analog-to-digital converter (ADC) E14-440 as pulse sequence of laser radiation scattered by aerosol particles. ADC conversion frequency is 38 kHz. Analog-to-digital converter is operated by attached program «LGraph2». All the measured data are transferred to computer and stored in memory for further processing. At laser radiation power 58 mW and beam cross-sectional area $1.5 \times 10^{-5} \text{ m}^2$ the laser radiation power density in recording area amounted to about $4 \times 10^3 \text{ W/m}^2$. Conditions for experiments with various combinations of HDD and water-flow aeration are presented in Table 1.

Table 1 Experiment conditions

Number of experiment	Screw propeller	Aeration	Flow
Exp. 1	–	–	Yes
Exp. 2	–	Yes	Yes
Exp. 3	Yes	Yes	Yes

To increase the measurement accuracy three sets of measurements are carried out consequentially during each experiment. Duration of each set is 300 s. Then the measured data are averaged. Using LGraph2 program pulse amplitudes of laser radiation scattering by aerosol particles are represented as histograms showing the statistics of amplitude distribution. Then histograms are processed by means of Excel.

We have developed Excel templates including such actions with initial histogram data as formatting, averaging, smoothing, normalization, cutting off the background pulses, and counting integral statistics in each experiment. Excel templates are based on mathematical and logical functions described in Excel spreadsheet documentation. The total number of array points in typical histogram is 1000 pairs. To provide visual control the respective graphs are drawn for each step of processing.

Furthermore, graphs are plotted for histogram differences for HDD on-off experiment conditions (named “Signal” and “Background”, respectively) using Excel templates with built-in tools. The histogram differences are used for detailed study of changing the histogram shape which indicates increasing or decreasing the particle size under HDD influence.

3 Experiment Results

The typical histograms constructed in three experiments and processed by Excel template are shown in Figs. 2, 3 and 4. In all figures, abscissa shows the amplitude of PMT voltage pulses (in volts), and ordinate shows the number of recorded pulses of this amplitude within histogram step.

According to calculation, for a certain range of particle size to laser wavelength ratios when

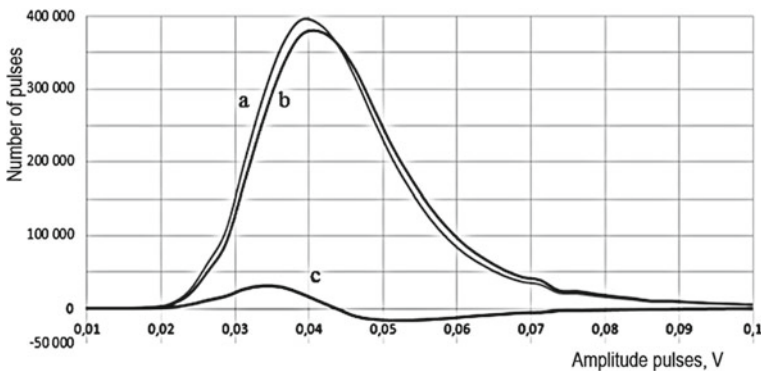


Fig. 2 “Signal” («On», with aeration), histogram of experiment 2—(a); “Background” («Off», without aeration), histogram of experiment 1—(b); histogram difference “Signal-Background” (“On-Off”)—(c)

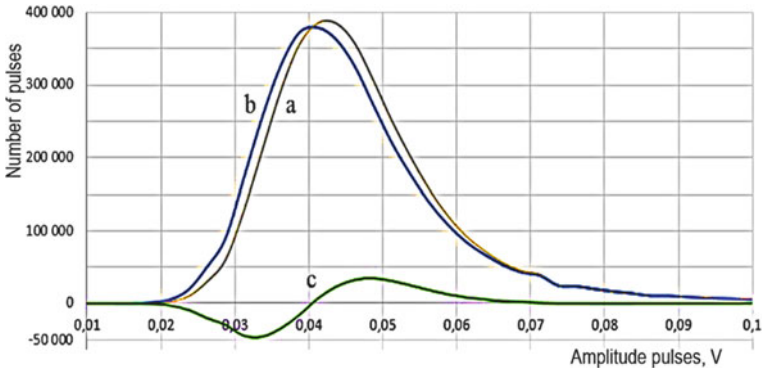


Fig. 3 “Signal”, histogram of experiment 3 (flow, screw propeller and aeration)—(a); “Background”, histogram of experiment 1 (flow only)—(b); histogram difference “Signal-Background”—(c)

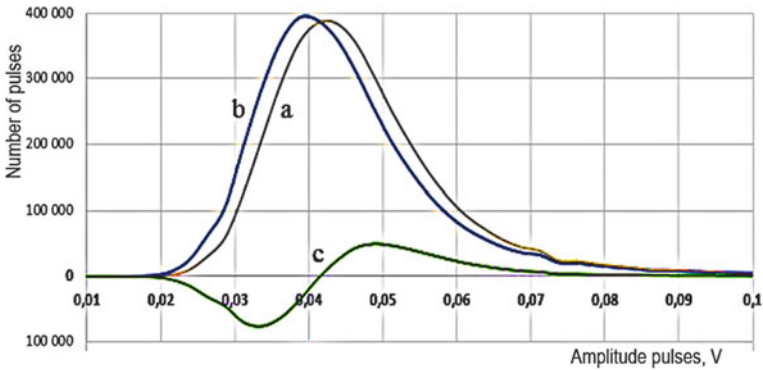


Fig. 4 “Signal”, histogram of experiment 3 (flow, screw propeller and aeration)—(a); “Background”, histogram of experiment 2 (flow and aeration)—(b); histogram difference “Signal-Background”—(c)

$$\rho = 2\pi a/\lambda < 4$$

where a is the particle radius, and λ is the laser wavelength), the scattering amplitude is proportional to the particle size (Krekov 1988; Hinkli 1976). For laser wavelength of 660 nm the maximum particle diameter satisfying above relation is estimated at 0.8 μm . This allows us to use proportionality of laser radiation scattering amplitudes and particle sizes in our experiments since the particle size estimated by bubbling conditions is 0.1–0.3 mm.

Figure 2 shows comparison of experiments 2 and 1. Histograms of signals represent the effect of flow aeration on aerosol particle size distribution without screw-caused HDD.

Note that flow aeration (histogram (a), “Signal”) leads to the slight increase in the number of smaller aerosol particles formed by bursting the bubbles produced by aerator in the air above the water surface. The histogram maxima meet scattering signal amplitudes of about 40 mV which corresponds to small «film» aerosol particles. Large particles corresponding to signal amplitudes up to 2.5 V (not shown in Fig. 2) are observed too. However, the number of such particles is much smaller than that of small particles.

Figure 3 compares data from experiments 3 and 1. The case of combined HDD effect caused by screw propeller and aeration on the particle size distribution in the presence of flow is shown.

In this case, the presence of HDD caused by two sources (screw propeller and flow aeration) leads to increasing the number of larger particles. Figure 4 shows data of experiments 3 and 2, when screw-caused HDD effect on particle distribution in the presence of aeration is studied.

The data shown in Fig. 4 indicate that for the flow with aeration the presence of screw-caused HDD, as in the previous case, leads to increasing the number of «film» particles with larger sizes.

4 Discussion of Results and Conclusions

The histogram difference shows redistribution of aerosol particle sizes in the presence of HDD (Nosov et al. 2017, 2018). The data obtained show that addition of HDD (as the screw propeller working towards the flow) to aerated flow leads to changing aerosol particles distribution towards large sizes. The observed redistribution may be due to the turbulence appearing in laminar flow under the influence of the screw propeller, which possibly affects the process of bubble collapse. Note, this phenomenon has not been studied before in theory.

Presented experimental data indicate that it is possible to study effects from various HDD on aerosol formation above water surface in laboratory conditions using laser radiation scattering on aerosol particles. To estimate absolute values of aerosol particle sizes the numerical calculations based on Mie scattering theory are to be used.

The data obtained may be used in conducting field experimental studies on recording manifestations for various hydrodynamic processes in near-water layer of the atmosphere.

References

- Ghulanov YuV, Petryanov IV (1980) Study of generation of marine aerosol. AC USSR Reports Ser Geophys 4:845–848 (in Russian)
- Hinkli ED (ed) (1976) Laser monitoring of the atmosphere. Springer-Verlag, Berlin-Heidelberg-New-York
- Krekov GM (ed) (1988) Optical properties of coastal mists. Nauka, Novosibirsk (in Russian)
- Leifer I (2000) Secondary bubble production from breaking waves the bubble burst mechanism. Geophys Res Lett 27(24):4077–4080
- Nosov VN, Kaledin SB, Gorelov AM, Leonov SO, Kuznetsov VA, Pogonin VI, Savin AS (2012) Light scattering in the atmospheric near-water layer above areas of long-living hydrodynamic disturbances of the marine environment. Dokl Earth Sci 442(2):247–248
- Nosov VN, Ivanov SG, Pogonin VI, Timonin VI, Zevakin EA, Zavyalov NA, Savin AS (2017) Effect of hydrodynamic disturbances on disperse characteristics of near-water aerosol. Processy v Geosredah 4(13):688–682 (in Russian)
- Nosov VN, Ivanov SG, Pogonin VI, Timonin VI, Zavyalov NA, Zevakin EA, Savin AS (2018) Influence of hydrodynamic perturbations on dispersion characteristics of a near-water aerosol. In: Karev V, Klimov D, Pokazeev K (eds) Physical and mathematical modeling of earth and environment processes—2017, pp 282–288. Springer Geology Springer, Cham. https://doi.org/10.1007/978-3-319-77788-7_29
- Piskozub J (1995) Study of spatial distribution of marine aerosol over sea coast with a multifrequency lidar system. Proc SPIE 2471:387–389
- Resch FJ, Darrozes JS, Afeti GM (1986) Marine liquid production from bursting of air bubbles. J Geophys Res 91(C1):1019–1029
- Shifrin KS (ed) (1981) Atmosphere and ocean optics. Nauka, Moscow (in Russian)
- Zielinski A, Piskozub J, Irczuk M (1995) Lidar studies of marine aerosol in the coastal zone. Proc SPIE 2471:428–438

Gold of Riftogenic Structures of the East Ural Uplift



A. V. Kolomoets  and P. V. Pankratiev

Abstract Studies have been carried out to study the gold occurrences of riftogenic structures of the East Ural uplift. The article reflects the features of the geological and structural-tectonic structure of the Kirov, Anikhov and Staro-Karabutak grabens of deep occurrence. Mineralization of grabens forms a number of extended ore zones and gold-bearing nodes enriched in them, which are of the greatest industrial interest. As a result of a generalization of geological materials and gold analysis results, the nature of the distribution of gold mineralization is revealed. Significant concentrations are recorded in carbon weakly metamorphosed siltstones, shales, and fine-grained sandstones. Packs of ore-bearing rocks reach tens of meters of capacity. They noted high carbon content, reaching 7–11.2%. A specific feature of the graben deposits of the East Ural uplift is noted—the transition of the volcanogenic part of the section to carbon-terrigenous. The tuffogenic-sedimentary sequence is characterized by scattered gold mineralization without the formation of large manifestations, where the noble metal content is only several times higher than their clarks. These strata can be one of the potential sources of gold in the formation of industrial manifestations of this metal in overlying black shale formations.

Keywords Gold · Carbon shales · Kirov graben · Anikhov graben · Old Karabutak graben · East ural uplift · Southern urals

1 Introduction

All over the world, gold deposits are one of the most attractive mineral resources. The Orenburg Urals, on the territory of which there are about 130 deposits and ore occurrences of gold, is one of the old gold-ore regions. Known medium and small deposits and ore occurrences: Kirov (Aydyrlinsky ore region), Blakskoe, Barambaevsk (Blaksko-Buzbiinsky ore regions), Kumak, Commercial, Vasin (Kumaksky ore regions) and a number of ore occurrences Sineshikhansk, Kainda and Kamenetsk

A. V. Kolomoets (✉) · P. V. Pankratiev
Orenburg State University, 13 Pobedy ave, Orenburg 460018, Russia
e-mail: kolomoets56@mail.ru

(Arifulov and Plugin 2006; Arsenteva 2010; Dubenko and Voin 1965; Loshchinin et al. 2003; Pankratiev et al. 2020; Sazonov et al. 1999). Industrial concentrations of gold in the Orenburg region are represented by endogenous and exogenous formations.

2 Research Methods

The research was of a complex nature and included: field work, analysis and scientific generalization of geological materials. The map was built using the ArcGis software product (version 10.0).

Exogenous formations of the Orenburg part of the Southern Urals are represented by deposits of the weathering crust and buried auriferous placers of karst and erosional-structural depressions. Gold-bearing weathering crusts are widely developed at the Kirov, Kamensk, Vasin deposits, as well as at the South -Kirovsk, Belozerskoye, Solenodolskoye and Kvarkenskoye deposits. They are mainly represented by linear-fractured, less often contact-karst types. Abnormal and industrial concentrations in the bedrock are traced in the weathering crusts along them. At the same time, there is an increase in the concentration of gold in 1.5–3 times (Arsenteva 2010; Pankratiev and Loshchinin 2005).

Endogenous deposits and occurrences of gold belong to gold-quartz-sulfide and gold-carbonaceous formations. The most intense gold mineralization is manifested in sections of carbonaceous-terrigenous-carbonate strata composing meridional fractures of the second order, represented from north to south by Kirov, Anikhovsky and Old Karabutak grabens of deep origin (Fig. 1).

The Kirov graben stretches in the northern part of the East Ural uplift and has a length of several tens of kilometers. It fills with numerous fractures of a higher order and the same direction, confined to the suture zone of the deep West Kirov fault. Within it are the Kirovsk, Kamensk, South -Kirovskoye gold deposits. The widespread development of these zones of various types of weathering crusts enriched in gold determines the industrial significance of the Kirovsky ore region. The structure in the form of a linear graben was formed in the zone of a deep fault separating the Magnitogorsk trough and the East Ural uplift.

The lower part of the graben section is composed of carbonaceous terrigenous deposits of the Bredinskaya Formation (C_1bd), the upper part is composed of volcanogenic-sedimentary carbonate rocks of the Kamensk sequence. The eastern part of the graben is composed of carbonate rocks of the Birgildinskaya strata (C_1br) (Arifulov and Plugin 2006; Arsenteva 2010). The internal structure of the graben is complex and is represented by a system of linear submeridional folds from 0.3 to 2 km. Anticlinal folds are usually asymmetric, thrown back to the east, sometimes turning into recumbent folds, which are complicated by longitudinal reverse faults, high-order thrust faults and diagonal reverse- and normal-strike faults of northeastern, less often northwestern strike.

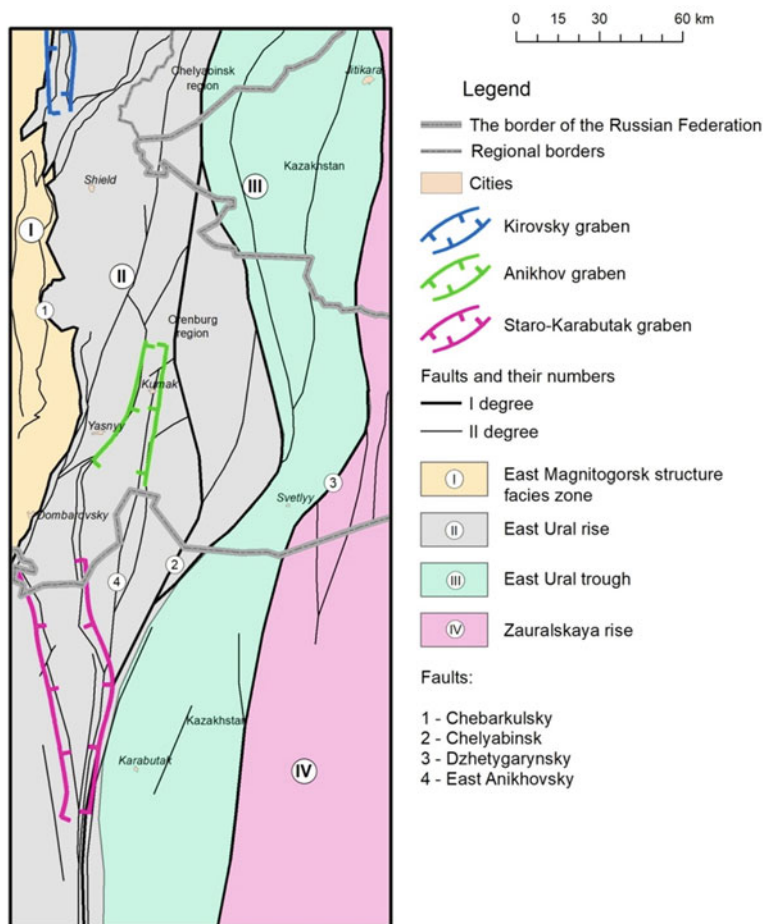


Fig. 1 Structural-tectonic map of the Kirov graben, Anikhovskiy graben and Old Karabutak grabens

The Anikhov graben is filled with carbonaceous-terrigenous deposits of the Bredinsk Formation (C_{1bd}). Its side parts are composed of volcanic-sedimentary formations. Graben is complicated by the Kumak-Kotansun zone of collapse, which is one of the fragments of a large tectonic fault (Chelyabinsk-Taldyk deep fault), which can be traced along the East Ural uplift. In the central part of the crumple zone, at a ten-kilometer interval along its strike, there is a number of gold-ore occurrences of the Kumak ore field (the Kumak, Kommerchesk, Vasin deposits) (Dubenko and Voin 1965; Loshchinin et al. 2003; Pankratev and Loshchinin 2005; Pankratiev et al. 2020; Sazonov et al. 1999).

The Old Karabutak graben looks like a feathering structure branching to the northwest of the East Mugodzhar fault. Boundary faults are represented by the East Mugodzhar and Old-Karabutak faults. The first has a submeridional strike and only its

northern end deviates to the east. The fault is clearly manifested in the magnetic field by linear positive anomalies. Graben is made by Lower Paleozoic, Lower Carboniferous and Lower Permian formations. In its section, the structure is stepped—the eastern block, filled with C_1 black shale deposits, is more lowered.

Graben-filled Lower Paleozoic black shale formations in the northern part of the East Ural uplift (Kirov graben) are represented by the Novoorenburg strata of the Middle Ordovician age (O_2no). Its deposits form two extended submeridional stripes up to 50 km long and correspond to the territories of the Solonchanskiy and Aydyrlinskiy horsts. Within the southern part of the East Ural uplift (Old-Karabutak graben), these are deposits of the Shebekty (O_2sb) and Balataldyk (O_2bt) strata of the Middle Ordovician (Loshchinin et al. 2003; Pankratev and Loshchinin 2005). Lower Paleozoic black shale formations are developed in all three structures.

Mineralization of grabens forms a number of extended ore zones and gold-bearing clusters enriched in them, which are of the greatest industrial interest. Their formation is associated with shallow-water basins, which were formed in zones of local short-term extension in the Middle Ordovician and Lower Carboniferous times (Pankratev and Loshchinin 2005). The studied deposits are broken by numerous granitoid intrusions of the Upper Paleozoic age. In the northern part of the East Ural uplift (Kirov-Kryklinskaya zone), these are porphyry-like biotite granites of the Suunduk complex. The Anikhovsky graben contains microcline granites of the Adamovsky complex and diorite and granodiorite dikes of the Kumaksky complex of small intrusions. Within the Old-Karabutak graben, the Upper Paleozoic granitoids are represented by a group of intrusions forming the East Mugodzhary granitoid belt, composed of leucocratic and biotite-amphibolite granites of the Shotinsky, Aktastinsky and Kokpasaysky massifs.

As a result of generalization of geological materials and the results of spectrochemical, assay and atomic absorption analyzes for gold, the nature of the distribution of gold mineralization in the formations of grabens was revealed (Arifulov and Plugin 2006; Arsenteva 2010; Dubenko and Voin 1965; Loshchinin et al. 2003; Pankratev and Loshchinin 2005; Pankratiev et al. 2020; Sazonov et al. 1999). It is noted that significant concentrations of gold are recorded in weakly metamorphosed carbonaceous siltstones, shales and fine-grained sandstones (the average content of noble metal in them is 0.5–0.9 g/ton, with maximums of 2–3 g/ton). They are confined to the lower strata of the Middle Ordovician and Lower Carboniferous deposits to the contacts of rocks contrasting in lithological properties—interbedded fine-grained sandstones, siltstones, carbonaceous-argillaceous and carbonaceous-siliceous shales. Members of ore-bearing rocks reach tens of meters of thickness. They have a high content of carbonaceous matter, reaching 7–11.2%.

Also, a feature of the sediments of the studied grabens of the East Ural uplift is the transition of the volcanogenic part of the section to the carbonaceous-terrigenous one. Volcanic and volcanic-sedimentary formations, underlying the Ordovician and Lower Carboniferous deposits, are represented by interbedding of tuff sandstones, tuff siltstones, less often tuffs, tuff gravelites, volcanomictic sandstones, carbonaceous sandstones, siltstones, carbonaceous-clayey, carbonaceous. The prevailing

pyroclastic-sedimentary rocks in the section consist of angularly rounded fragments of aphyric and pyroxene-plagiophyric basalts, basaltic andesites, fragments of plagioclase crystals, and amphibolized pyroxene. Sedimentary material is represented by quartz, siliceous rocks, feldspars, siliceous tuffites, less often limestones and carbonaceous-argillaceous-siliceous shales.

The tuffaceous-sedimentary sequence is characterized by diffuse gold mineralization without the formation of large occurrences, where the content of noble metal is only several times higher than their clark. These strata can be one of the potential sources of gold in the formation of industrial manifestations of this metal in the overlying black shale formations.

3 Conclusions

The prospect of the structures of the riftogenic type of the East Ural uplift for gold mineralization is determined by the increased gold content in carbonaceous shales, the presence of sulfide mineralization, stratigraphic confinement to the sections of the lower sub-strata of the Middle Ordian and Lower Carboniferous deposits, as well as complex tectonic dislocation. These factors indicate the possibility of expanding the direction of prospecting for gold deposits in the area of the East Ural uplift.

Acknowledgements This work was supported by the Regional Grant in the field of scientific and scientific and technical activities in 2019 (Agreement No. 23 dated August 14, 2019).

References

- Arifulov CHH, Plugin DV, Chernoyarov VG (2006) Zolotorudnye mestorozhdeniya "chernoslancevogo tipa" na YUzhnom Urale i zakonomernosti ih razmeshcheniya // *Otechestvennaya geologiya* 1:13–22
- Arsenteva IV (2010) *Usloviya lokalizatsii zolotorudnyh mestorozhdenij Kirovsko-Kvarkenskogo rudnogo rajona i ih poiskovye kriterii*. Avtoref. dis. kand. geol.-min. nauk. M.: CNIGRI, 24 p
- Dubenko IG, Voin MI (1965) *Osnovnye cherty geologicheskogo stroeniya i zolotonosnosti severnoj chasti Kumakskogo zolotorudnogo mestorozhdeniya*. – *Izv. vysshih uch. zaved. geologiya i razvedka*, 11
- Loshchinin VP, Pankrat'ev PV, Hasanov VN (2003) *Zolotorudnye mestorozhdeniya v uglerodistoterrigennyh formatsiyah Orenburgskoj oblasti i ih perspektivnaya ocenka*. V sb. «Modelirovanie strategii i processov osvoeniya georesursov. Materialy mezhdunarodnoj konferencii i nauchnoj sessii gornogo instituta UrORAN».—Perm', pp 216–219
- Pankratev PV, Loshchinin VP (2005) *Zolotoe orudnenie riftogennyh bassejnov Orenburzh'ya // Strategiya i processy osvoeniya georesursov*.—Perm, pp 13–15
- Pankratiev PV, Kolomoets AV, Bagmanova SV, Pantelev VS (2020) *Features of the formation of gold manifestations in the black shale deposits of the kumakskoye ore field*. *Processes in GeoMedia*, vol I, pp 11–15. Springer, Cham. https://doi.org/10.1007/978-3-030-38177-6_2
- Sazonov VN, Ogorodnikov VN, Koroteev VA, Polenov YuA (1999) *Mestorozhdeniya zolota Urala*.—Ekaterinburg: izd. UGGGA, 570 p

Aeolian Morpholithogenesis on the Shores of the Northern Pacific



V. V. Afanas'ev  and A. I. Levitsky

Abstract The features of the distribution of aeolian forms on the shores of the seas of the North Pacific have been established. The main reasons for the formation of an excess of sediment in the coastal zone, which explains the aeolian accumulation of short-range transport, are considered. It is shown that the cyclical nature of aeolian relief formation on the coast is associated with changes in the balance of sediments in the coastal zone, which are mainly determined by fluctuations in sea level. The main regularities of aeolodynamics on the shores of the Far Eastern seas in the Holocene are presented as follows. In coastal areas characterized by large volumes of detrital material removal from land, the development of aeolian accumulation processes is associated with a decrease in sea level. On the coast, where the influx of sediments into the coastal zone is provided mainly by marine hydrodynamic processes, aeolian deposits are formed during the period of increased erosion of the shores and the formation of excess sediment in areas of accumulation during sea level rise. Aeolian morpholithogenesis on volcanic shores may also be associated with the influx of a large amount of pyroclastic material into the zone of wave processing during explosive eruptions. The age of such dunes correlates with the age of volcanic pumice-tephra deposits and is in no way related to the established periods of high or low sea level.

Keywords Coastal dunes · North Pacific · Explosive volcanic eruption · Subaerial beach · Sea level

1 Introduction

The boundaries of geosystems are relatively mobile zones of mutual Coastal dunes can form in most of the world's climates (Ruz and Hesp 2014; Forbes and Taylor 1994; Razzhigaeva and Ganzei 2006). The types, sizes and morphology of coastal aeolian forms of dunes depend on the budget and composition of sediments of the coastal

V. V. Afanas'ev (✉) · A. I. Levitsky
Institute of Marine Geology and Geophysics, FEB RAS, Yuzhno-Sakhalinsk, Russia
e-mail: vvasand@mail.ru

zone, the period and intensity of the processes of mobilization and transfer of sediments, as well as the conditions of stabilization and accumulation of aeolian material. In preparing this work, the entire spectrum of aeolian formations was considered, from small ephemeral forms to stable dune fields. The location of the main aeolian formations on the shores of the North Pacific and the adjacent part of the Arctic Ocean is shown in Fig. 1. When compiling the map, the results of earlier studies were fully used (Chilchigsheva 2020; Dikova 1983; Kononova 1986; Short 2007; Korotkiy et al. 1996).

Aeolian accumulation of the so-called short-range transport on the shores of seas and oceans should be attributed to this category of coastal processes proper (Ignatov 2006). This avoids many misunderstandings associated with aeolian morpholithogenesis on the coast. Including, in the issues of origin, morpholithodynamics and cyclicity of aeolian morpholithogenesis, despite the huge number of publications devoted to the problem (Tamura et al. 2016; Provoost et al. 2011; Szkornik et al. 2008).

In Russia, studies of coasts mainly along estuarine areas of large rivers laid the foundation for the regressive theory of the formation of dunes (with a drop in sea level) (Razzhigaeva and Ganzei 2006; Short 2007; Korotkiy et al. 1996). And on the example of coasts with active erosion of the coast, an opinion was formed about the activation of aeolian relief formation during the rise in sea level (Badyukova and Solovieva 1997).

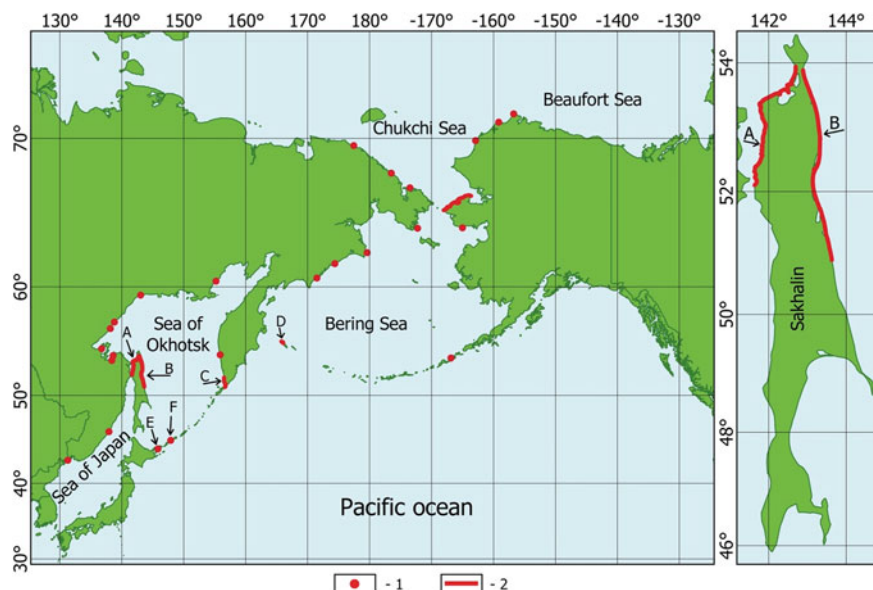


Fig. 1 Location of the main manifestations of aeolian processes on the shores of the North Pacific and the adjacent part of the Arctic Ocean: 1—areas of stable manifestation of aeolian processes; 2—dune massifs

In fairness, it should be noted that recently there has been an understanding that aeolian processes in the coastal zone are associated with the presence of sediments in the subaerial part of the beach and are controlled by sea level fluctuations of different signs (Aagaard et al. 2007; Badyukova and Solovieva 2015). Moreover, recent observations on the shores of the Netherlands have shown that there is no significant correlation between variability in annual wind conditions and annual changes in dune volume. Conversely, a significant temporal correlation was found between the variability of the annual state of the beach and the change in the volume of dunes (Vries de et al. 2012; Vries de et al. 2014). This suggests that the traditional aeolian morpholithodynamic models developed for desert aeolian morpholithogenesis overestimate the importance of wind conditions, especially in a monsoon climate.

In our opinion, the intensity and cyclicity of aeolian relief formation on the coast is associated with changes in the balance of sediments in the coastal zone, which are mainly determined by fluctuations in sea level. The main regularities of aeolo-dynamics on the shores of the Far Eastern seas in the Holocene were previously presented by us as follows (Afanasyev 1992). In coastal areas characterized by large volumes of detrital material removal from land, the development of aeolian accumulation processes is associated with a decrease in sea level. For example, in the area of the Viakhtu Bay, on northern Sakhalin, the formation of an aeolian stratum 2.0–2.5 m thick on the surface of a 20-m alluvial-marine Upper Pleistocene terrace began simultaneously with a young eutrophic peat bog on the estuarine-lagoon stratum of the bay (440 ± 83 cal. BP., DVGU-187; 440 ± 85 cal BP, DVGU-178).

On the coast, where the influx of sediments into the coastal zone is provided mainly by marine hydrodynamic processes, aeolian deposits are formed during the period of increased erosion during sea level rise. Powerful dune deposits on the Sakhalin coast of the Amur estuary began to form on the accumulative segments of the abrasion-accumulative systems precisely at the beginning of the second phase of wave accumulation (4615 ± 579 cal BP, DVGU-109) (Afanasyev 1992).

Some modern forms of aeolian-coastal accumulation owe their origin to changes in hydrodynamic activity in the last few decades, provided that these processes are inherited in the development areas. This applies, in particular, to the dunes on the coast of the Sakhalin Bay, the Tatar Strait, northeastern Sakhalin, the Kuril Islands, and southern Primorye. Modern aeolian deposits are observed here at elevations of up to +25 m, foredunes up to 8–10 m high are actively formed. The high mobility of sandy material also explains, in particular, the presence of aeolian deposits of coastlines of the Early—Middle Holocene on the coast of Japan (Afanasyev 2020).

2 Research Methodology

The analysis of materials for remote sensing of the earth from publicly available sources was carried out in the geographic information system Quantum GIS, the contours correspond to the accuracy of the initial data. To obtain the area of the

plots, the Add Geometry Attributes tool with the Ellipse Calculation option was used. Calculated using WGS84 EPSG: 7030 ellipse.

The data obtained on about. Sakhalin, the Kuril Islands and Primorye are certified by field research, including drilling data and ground-penetrating radar observations by the OKO-2 M series GPR (Logis LLC) with an AB-400 antenna unit (antenna central frequency 400 MHz), providing a depth of investigation up to 5 m and with antenna unit AB-150 (central frequency 150 MHz), providing a depth of investigation up to 12 m. An example of certification of geospatial information with geological sections is shown in Fig. 2.

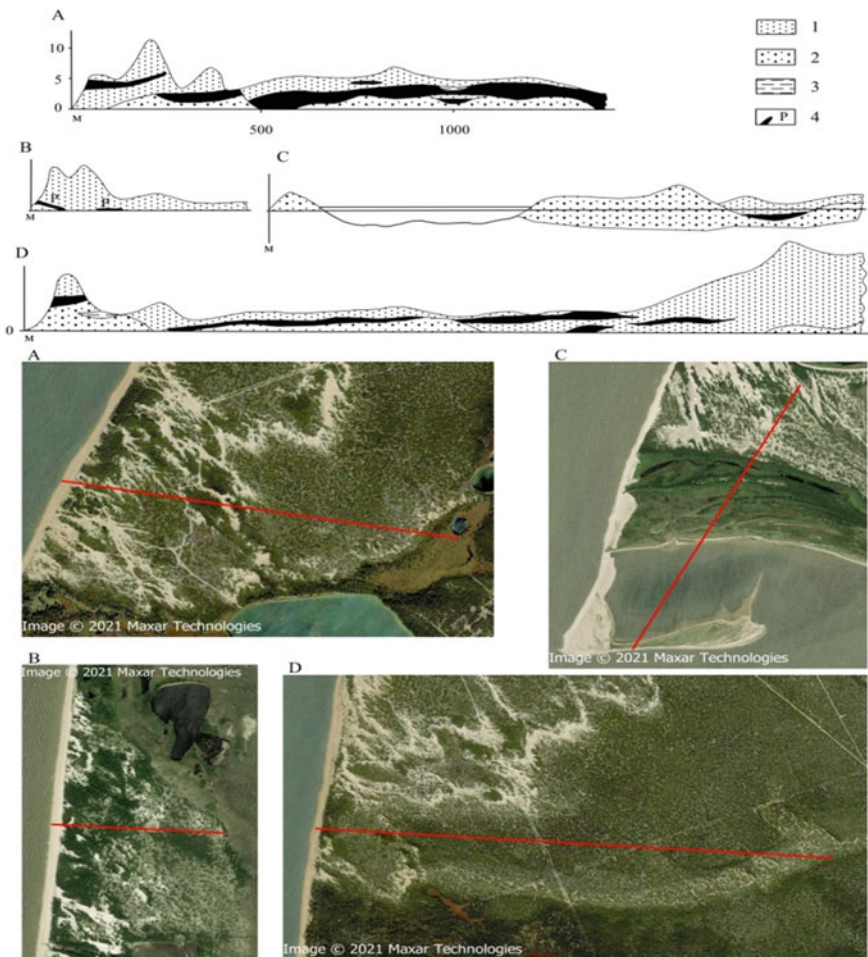


Fig. 2 Geological and geomorphological structure of the coastal plain with landscape reference of sections according to space photographs: 1- fine-medium-grained, predominantly aeolian sands; 2— uneven-grained sands with gravel and pebbles of aeolian-surf origin; 3—clays and loams; 4—peat bogs

The interpretation of remote sensing data fully included geomorphological content based on morphodynamic observations and paleogeographic analysis using dating data C₁₄.

3 Results and Discussion

The main As a result of the studies carried out, it was established that aeolian morpholithogenesis is characteristic of the sandy shores of the temperate, subarctic and arctic belts of the North Pacific. Six main dune fields were identified, for which the main cartometric parameters were calculated (Fig. 1, Table 1).

Aeolian landforms are most widely represented on the Sakhalin shores of the Amur estuary and Sakhalin Bay, as well as on the lagoon coast of northeastern Sakhalin, the shores of southwestern Kamchatka and the southern Kuril Islands. A large dune field is formed on the island. Bering. On the other shores of the Okhotsk, Chukchi and Bering Seas, and on the shores of Primorye, aeolian formations are represented mainly by small ephemeral forms and foredunes in the estuarine parts of rivers and on sandy barrier forms.

It was found that almost any elements of the subaerial part of the beach are the result of aeolian morpholithogenesis (Afanasyev 2020). As an example, Fig. 3 shows the granulometric spectra of the foredune and coastal swell systems. Therefore, aeolian morpholithogenesis takes part in the formation of sandy shores almost everywhere. The types, sizes and morphology of coastal aeolian forms of dunes depend on the budget and composition of sediments of the coastal zone, the period and intensity of the processes of mobilization and transfer of sediments, as well as the conditions of stabilization and accumulation of aeolian material.

Aeolian sheets and dunes on the coasts in volcanic centers associated with the processing of pyroclastic material that entered the coastal zone during explosive eruptions in the Neopleistocene and Holocene were established by us on the Kuril Islands. In particular, the formation of young dunes on the ocean coast of the Vetrovaya Isthmus is associated with the processing of pyroclastic material that entered the coastal zone about 1000 years ago (Afanasyev 2019). Obviously, on volcanic shores,

Table 1 Main cartometric characteristics dune fields of the North Pacific

Location	Area (sq. Km.)	Length (km)	Width
A	169	295,463	0.572
B	85	352,629	0.241
C	23	75,798	0.300
D	7	35,698	0.189
E	17	57,285	0.296
F	12	45,850	0.262
Total	312	863	0.361

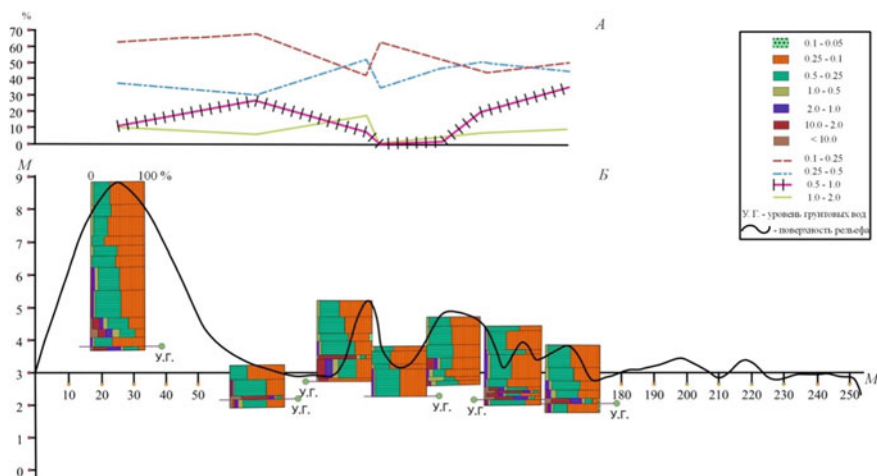


Fig. 3 Section of the system of coastal ramparts and foredunes on the coast of the bay. Aniva (southern Sakhalin); **A**—distribution of grain-size dimensions according to generalized sections of forms, **B**—aeolian grain-size spectra in deposits of coastal swells and foredune

we are dealing with a special type of aeolian morpholithogenesis associated with overcompensated sedimentation in some parts of the coastal zone as a result of wave processing of large volumes of easily destroyed pyroclastics.

Attention should also be paid to the dunes formed during the processing of near-estuarine accumulative formations of the transgressive river network during the formation of alluvial marine plains in the Late Pleistocene (Black 1951; Afanasyev 1998). These formations show almost complete identity with modern dunes in the granulometric pattern of the geological section (Fig. 4).

The high mobility of sandy material is also explained by the presence of aeolian formations on high terraces. We studied dunes on Late Pleistocene terraces with a height of 18–25 m. It turned out that 2 generations of dunes with a thickness of 5–7 m on high terraces adjacent to estuarine zones correspond to the “Little Ice Age” and are about 400 years old, and the dune on a fragment of the complexly constructed barrier form of the Piltun Lagoon, represented by a high terrace, probably somewhat older (Fig. 5). It should be noted that the coastline during the formation of aeolian deposits of this age was several hundred meters farther from the sea (Afanasyev 2018; Vladimirov 1961). The marginal part of the aeolian massif, a 30-cm interlayer of which is exposed in the coastal scarp, began to form about 3000 years ago. At a high sea level, at a distance of 1.5–2.0 km from the coastline of that time (Fig. 6).

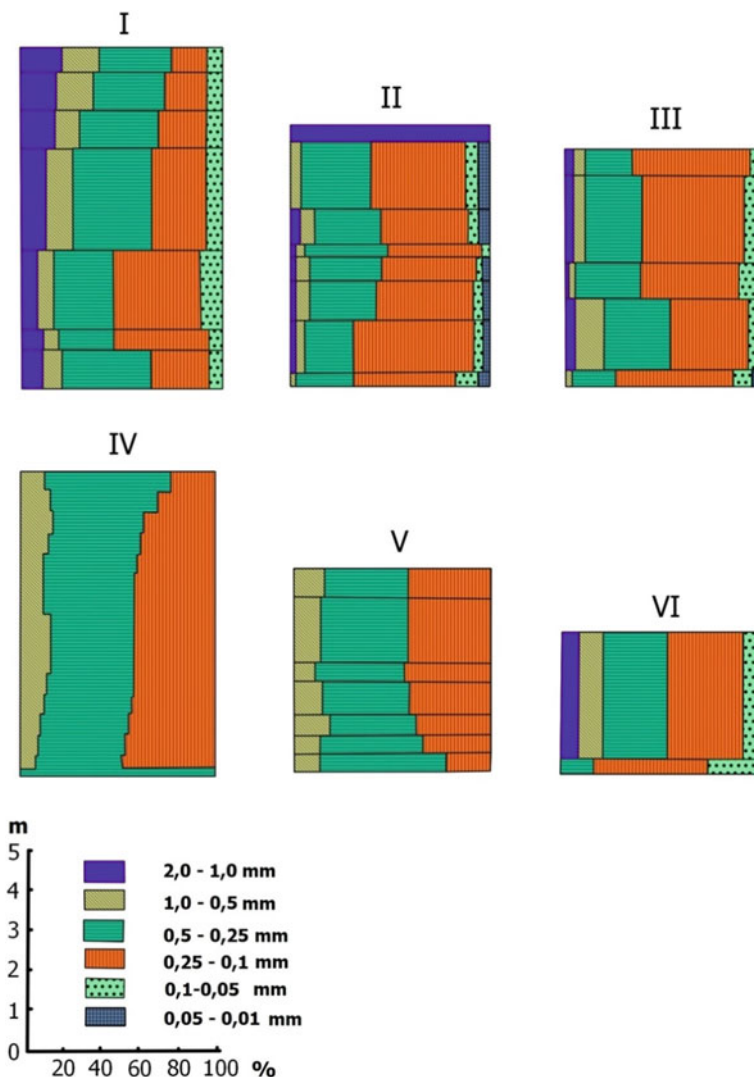


Fig. 4 Granulometric spectra of sediments along channel (ridges) and coastal dunes of the coast of northwestern Sakhalin: I—mane (Uanga river), II—mane (Vagis river), III—mane (Pogibi river), IV—dune (Rybnovsk), V—dune (m. Tamlevo), VI—dune (m. Pogibi)

4 Conclusions

When studying aeolian accumulation, the so-called short-range transport, on the shores of seas and oceans, the features of the coastal morpholithogenesis proper are not sufficiently taken into account. Focusing on the specifics of coastal processes, we reviewed aeolian relief formation on the shores of the North Pacific, located in



Fig. 5 Aeolian deposits up to 4 m thick on a Late Pleistocene terrace 18–20 m high (Northeastern Sakhalin)

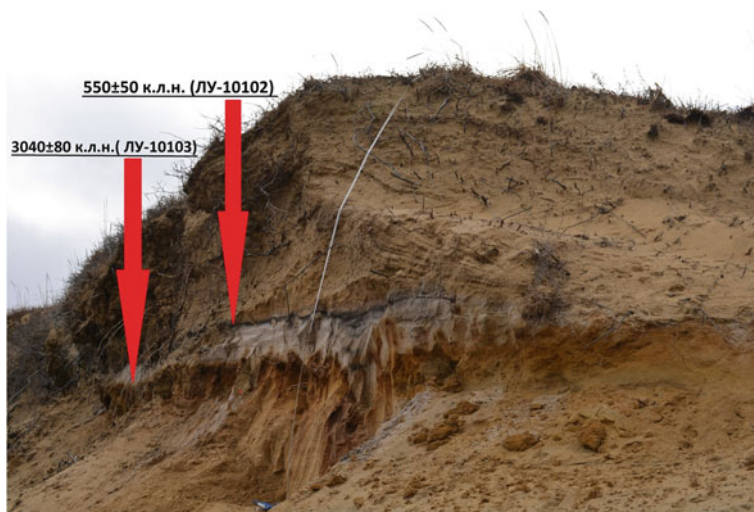


Fig. 6 Aeolian sediments of two generations, 2.2 and 0.4 m thick, in the coastal cliff, on the Late Pleistocene terrace (the values of the calendar age are given on the basis of the calibration program “OxCal 4.4.1” (calibration curve “IntCal 20”))

the stably active transitional contact zone of the two greatest structures of the Earth, which, in the course of interaction, exert powerful system-forming influences within the temperate, subarctic and arctic natural-climatic zones.

References

- Aagaard T, Orford JD, Murray AS (2007) Environmental controls on coastal dune formation; Skallingen Spit, Denmark. *Geomorphology* 83(1–2):29–47. <https://doi.org/10.1016/j.geomorph.2006.06.007>
- Afanasyev VV (1992) Evolution of the coast of the Far Eastern seas in the Holocene. Evolution of the coast in conditions of rising ocean levels. IO RAN, Moscow, pp 166–174
- Afanasyev VV (1998) Geomorphological structure and morphodynamics of the north-western coast of Sakhalin Island: diss.Cand Geogr Sci (Moscow State University M.V. Lomonosov. - M.), 185 p
- Afanasyev VV (2018) Erosion of the sea shores of northeastern Sakhalin (VV Afanasyev, AV Uba). *Geomorphology* 4:25–35
- Afanasyev VV (2019) A new type of aeolian morphogenesis on volcanic shores (Iturup Island, Great Kuril Ridge). *Geosystems Transit Zones (In Russian)* 3(4):423–427. <https://doi.org/10.30730/2541-8912.2019.3.4>
- Afanasyev VV (2020) Morpholithodynamic processes and development of the coasts of the contact zone of the subarctic and temperate seas of the North Pacific. - Yuzhno-Sakhalinsk: IMGIG FEB RAS, 234 p. ISBN 978-5-6040621-8. <https://doi.org/10.30730/978-5-6040621-8-0.2020-120>
- Badyukova EN, Solovieva GD (1997) The relief of coastal dunes as an indicator of sea level fluctuations. *Vestnik Moskov. un-that. Ser. 5, Geography. No. 5.* pp 10–19
- Badyukova EN, Solovieva GD (2015) Coastal eolian landforms and sea level fluctuations. *Oceanology* 55(1):124–130. <https://doi.org/10.1134/s0001437015010014>
- Black RF (1951) Eolian deposits of Alaska. *Arctic* 4(2):89–111
- Chilchigsheva IV (2020) Current state of the landscapes of the Commander Islands. *Science, nature and society*, pp 153–15
- Dikova TM (1983) South Kamchatka archeology in connection with the ainu occupation problem. *M: Nauka*, p 231s
- Forbes DL, Taylor RB (1994) Ice in the shore zone and the geomorphology of cold coasts. *Prog Phys Geogr* 18(1):59–89. <https://doi.org/10.1177/030913339401800104>
- Ignatov EI (2006) Morphosystemic analysis of the banks. M.; Smolensk: Magenta, 328 p
- Kononova NN (1986) Aeolian processes and coastal landscapes. Publishing house of the Far Eastern State University, Vladivostok, p 132
- Korotkiy AM, Razzhigaeva NG, Mokhova LM, Hanzei LA, Grebennikova TA, Bazarova VB (1996) Coastal dunes - an indicator of global cooling (Kunashir Island, Kuril Islands). *Pacific Geology* T 15(1):53–59
- Provoost S, Jones MLM, Edmondson SE (2011) Changes in landscape and vegetation of coastal dunes in northwest Europe: a review. *J Coast Conserv* 15(1):207–226. <https://doi.org/10.1007/s11852-009-0068-5>
- Razzhigaeva NG, Ganzei LA (2006) Sedimentation conditions of island territories in the Pleistocene-Holocene. *Dal'nauka, Vladivostok*, 365 p
- Ruz M-H, Hesp PA (2014) Geomorphology of high-latitude coastal dunes: a review. *Geol Soc Lond Spec Publ* 388(1):199–212. <https://doi.org/10.1144/sp388.17>
- Short AM (2007) Aeolian relief of Primorye and adjacent territories of East Asia (paleogeographic aspect). *Geomorphology* 4:79–95
- Szkornik K, Gehrels WR, Murray AS (2008) Aeolian sand movement and relative sea-level rise in Ho Bugt, western Denmark, during the 'Little Ice Age'. *Holocene* 18(6):951–965. <https://doi.org/10.1177/0959683608091800>
- Tamura T, Kodama Y, Bateman MD, Saitoh Y, Yamaguchi N, Matsumoto D (2016) Late Holocene aeolian sedimentation in the Tottori coastal dune field, Japan Sea, affected by the East Asian winter monsoon. *Quat Int* 397:147–158. <https://doi.org/10.1016/j.quaint.2015.09.062>
- Vladimirov AT (1961) Morphology and evolution of the lagoon coast of Sakhalin Island / AT Vladimirov. Tr. Institute of Oceanology of the Academy of Sciences of the USSR. M.: AN SSSR 48:145–171

- Vries de S, Arens SM, De Schipper MA, Ranasinghe R (2014) Aeolian sediment transport on a beach with a varying sediment supply. *Aeolian Research*. 15:235–244. <https://doi.org/10.1016/j.aeolia.2014.08.001>
- Vries de S, Southgate HN, Kanning W, Ranasinghe R (2012) Dune behavior and aeolian transport on decadal timescales. *Coast Eng* 67:41–53. <https://doi.org/10.1016/j.coastaleng.2012.04.002>

Variants of Visualization of the Marine Forecast on the Examples of the Crimean Basin of the Black Sea



N. Voronina 

Abstract This paper compares the results of the functioning of software modules for the oceanographic environment using modern graphic resources of well-known programming languages R, JS, PHP, HTML, both with the use of tools of the Google Maps service and without the use of satellite maps. Recall that JS, PHP, HTML software is used in Web-development, while R is a programming language for statistical data processing and work with graphics. The results of the work of various software modules shown in the article are generally the same—graphical displays of geophysical parameters using examples of forecasts of the state of the Black Sea. However, the software tools to achieve the equal results are different. The aim is to determine the most optimal means of presentation of oceanographic data for future use in the visualization of marine forecasts. An important result of this work is the compilation of assessment recommendations for the use of various software tools for visualizing oceanographic data.

Keywords Black Sea · Visualization · Geophysical parameters · Sea surface temperature · Salinity of the marine environment · Mapping services google maps

1 Introduction

The World Ocean occupies the most part of the Earth and naturally, a wide range of scientific research aims at studying it. Therefore, the most reliable visual monitoring of the research results is of great importance.

There were have being marked 550 years in May 2020 since the appearance of the first world geographic atlas—the first experience of the visualization of geographic data, and such visualization a few years ago implied the possibility of only static display just in the style of atlases. Until recently a giant breakthrough in increasing of the reliability of the result interpretation of geophysical, geographical, geological data of studies has made in the second half of the XX century, due to the appearing and

N. Voronina (✉)
Marine Hydrophysical Institute RAS, Sevastopol 299011, Russia
e-mail: voronina.nataly@mail.ru

rapid developing of computer technology as well as space exploration with satellites. There appeared new opportunities for the realization of the goals of improving visual monitoring of the World Ocean. Modern tools possess such a software that allows one not only to view the results of the research as a static geographical atlas, but also to work with the data at various scales, as well as obtain values of geographic coordinates of any point of interest in the image.

The problem of visualization has become especially acute with the development of remote sensing devices installed on spacecraft, which make it possible to obtain information about the temperature and salinity of the sea surface, its level, surface wind speed and currents, as well as other parameters throughout the entire water area of the World Ocean (Armand et al. 2010; Glazman and Greysukh 1993; Zapevalov 2012).

In 2009 the project of the European Union MyOcean (2018 (now named Copernicus) focused on the collection and display of data on the state of the World ocean (the results of satellite monitoring, probing, forecast data of the marine environment, etc.) was established and is functioning currently. All project data are available free. Satellite maps at the display the moving trace of drifters and buoys ARGO (2010) have already being use in the project MyOcean. Analysis of the temperature profiles obtained from the data of measurements of the floating buoys Argo (Lishaev et al. 2020), made it possible to improve the values of this geophysical parameter. There are also displays of geophysical parameters of the seas on the satellite maps in project Copernicus, but such images were make up using specialized hardware.

In the period from 01.04.2009 to 09.30.2014, the authors of this paper were the MyOcean project participants in a team of Department of Oceanography Marine Hydrophysical Institute (MHI) RAS. Within the framework of this project site of the “Operational Oceanography Branch” MHI (Black sea marine forecasting centre <http://bsmfc.net>) was established and is functioning now. The site provides a range of geophysical data on the Black Sea on an operational basis. They all have a visual representation with modern software and hardware tools. Nevertheless, just in the course of the work on the MyOcean project the purpose of obtaining such images of geophysical fields, which the user can instantly view with a maximum range of capabilities without the using of specialized hardware have appeared.

The authors have implemented the assigned task within a new project, named the same as this paper and supported by the RFBR, on the example of a local area of the Black Sea basin. The project was used data from the operational work of the Center of Experimental Marine forecast (ETMP) (Eksperimental’nyy tsentr morskikh prognozov 2015) MHI RAS. Achieving the goal, we relied open-source software for drawing construction, as well as working experience. This project has both scientific and practical character, as its results are currently being use in the operational work.

Package TkrPlot (Lawrence and Verzani 2012), as a part of the open-source programming language R (Shipunov et al. 2020; Akinshin 2013; Zaryadov 2010), allows to realize the obtaining of geographic coordinates of any point of interest on a static image. Appearance of the map service Google Maps (Dincer 2013) with its powerful set of tools for using this service in the development of own software products, has opened a completely different, higher level of visualization with computation satellite maps with the obtained results on the pages of Web-sites. This, in turn,

made it possible to bring the resulting images anywhere. This level includes the visualization and the ability to remove the values of the coordinates of any point of interest to an image similar to the package TkrPlot, but there are differences, which we will explain later in the course of the presentation of the results of our research. In addition, scripting language, JavaScript (JS), which has the tool of Google Maps, allows viewing dynamically the images on a Web page that is necessary for a visual assessment of variability of geophysical parameters of the marine environment. However, before you give the image the dynamics, you have to create this image, and that has done in the project, by means of programming languages R (actually a graphical representation of data) and PHP (processing of the constructed static images, as well as archive files of geophysical data on the server side). So our challenge was a practical testing of several ways of constructing of images of geophysical parameters, comparing the obtained results and making recommendations for further use (or disuse) of each of them.

2 Style of “Geographical Atlases”

Numerous examples of images in the style of geographical atlases obtained on a daily basis as result of the automated operational work can see on the Web site of the Center of Experimental Marine Forecast (CEMF). One such example is also shown in Fig. 1 and only for the temperature parameter, so that not to overload the content of this paper. Sample images of other geophysical parameters (salinity, current velocity, the level of the marine environment) present well on the site CEMF.

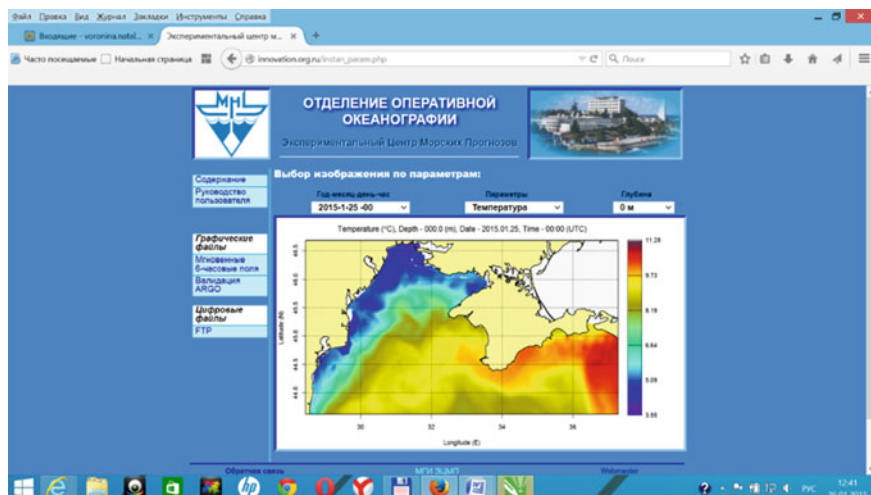


Fig. 1 Image of geophysical parameter of temperature for region of the Black Sea

These **static images**, shown in Fig. 1, are constructed using the programming language R, which has been chosen by the authors because of many reasons, among which of them are of importance i.e. the presence of a powerful set of tools to work with graphics, as well as free software environment of computing (Copernicus Marine service 2018). The results of calculations of marine forecasts format GRD have used as input data. As it should be noted that actually the input format can be of any kind (DAT, NC, GRD, etc.), containing the geophysical data. As the program of the forming of graphics uses the function of pre-reading of geophysical data, such functions can being write in any format. In our case, the function was written for reading data in the format GRD, because the files in the format GRD are the result of operational work of model to calculate marine forecasts and further just these files get a graphical presentation with their subsequent uploads on the page of Website.

But the static images constructed in such a way have serious drawbacks:

- possibility of obtaining the coordinates of any point of the image is absent;
- possibility of the image scaling is absent too.

3 Visualization with Using of TkrPlot

Analysis of the latest achievements in the field of data visualization software showed that the first of the drawbacks can be solved by **the application of the package tkrplot**, built-in programming language R. Using tkrplot became the next higher stage of schedules construction to display geophysical parameters. The authors of the book (Lawrence and Verzani 2012) considered in detail the possibility of constructing a graphical image using the widget tkrplot. We took advantage of this opportunity and developed a program of construction of images in the same software environment R, but with using of this widget TkrPlot. The result of the program work with using of the widget tkrplot as an image of Black Sea temperature field has shown in Fig. 2. As the input data the data of calculated results of marine forecasts were used in format DAT (we have already noted that the format of the input geophysical data can be various, it does not affect the result).

And indeed, as it can be seen in the upper left corner of Fig. 2, now the coordinates (values X, Y) of any point of the image, as well as the Z value of the geophysical parameter (in this case the temperature field) at a given point on the map are displayed. Thus, as our experience has shown, we managed to get rid of one of the drawbacks of static images. However, the image obtained with the widget TkrPlot turned out not only to lack the possibility to be scaled, but it can't be set at a proper size for the displayed image (as the authors Lawrence and Verzani 2012 warned). Thus, one can conclude that the using of the widget TkrPlot allows to get rid of one of the drawbacks of a simple static image by mapping the coordinates at any point of the map, but it makes the other drawback more serious i.e. the lack of scalability. Such a visualization of data can also be applied, but, in our opinion, this applying is limited to only narrow range of research, and it cannot be use in operational work, i.e. to the daily processing of large amounts of data.

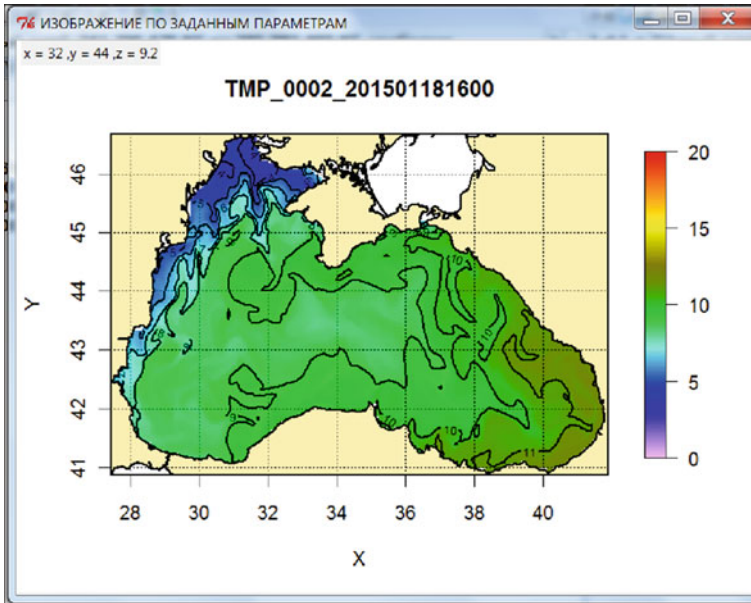


Fig. 2 Image of temperature geophysical parameter of the Black Sea, built with the using of the widget tkplot

4 The Use of Satellite Maps for the Visualisation of Geophysical Parameters

The appearance of the map service Google Maps with its own powerful set of tools allowing to use a full range of services, for example, in the scenario language JS, raised the geophysical data visualization at a totally different, much higher level with the possibility of overlaying of own results on the satellite maps, posted on Websites pages (Dincer 2013; Google Maps JavaScript API 2009). Such overlays allow using all the tools, available in the mapping service, while working with your own results. An example of such a collaborative using of satellite maps with the local images is being show in Fig. 3. It should be note that non-commercial using of services Google Maps, as in the case of software environment R, implies free spread. This level of visualization includes both the possibility of determination of the coordinate values at any point of interest in the image, and a convenient visual scaling, which has being clearly see in Fig. 3.

It makes images on Google Maps different absolutely from the usual graphic images, which we have already mentioned above, and allows to get rid of their inherent drawbacks completely. Besides, the use of language JS allows to develop scripts for viewing images in animation (select “Year-Month-Day-Hour” on the Web-page for Sevastopol region), which is very useful for visual assessment of variability

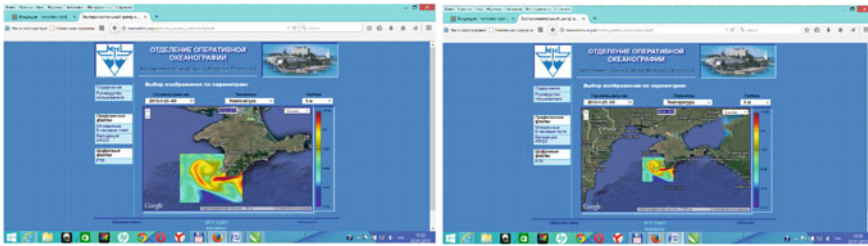


Fig. 3 Image of geophysical parameter of temperature for Sevastopol region Black Sea as an overlay on the satellite map Google Maps using different scaling

of geophysical parameters of the marine environment at a certain point of time. In particular, our website CEMF time point is the point of calculated forecast.

It should be noted the appearance of images on the corresponding page of the satellite map is preceded by preliminary work:

- the developed in the programming environment R program generates a graphic image files with a local geophysical parameters in PNG format, and upload this files to the server HTTP;
- then the files are processed by means of scripting language PHP on the server side.

Testing of using the Google Maps for our own purposes has opened another opportunity—the view of the archives In Situ. To do this, the authors had to develop programs (programming language R) of optimal filtering of such archives satisfying the conditions of loading archive data on a Web page, an example has shown in Fig. 4.

However, this testing showed that for the most versatile viewing of archived data the further work is need to obtain the optimal size and content of the archive contact measurements in order to maximize the full data display on the map Google Maps.

Thus, the proposed approach to the problem of data visualization using the map service Google Maps consists of software implementation of the overlay of static images with geophysical parameters on the satellite map Google Maps that allows using the entire range of tools Google Maps for your own images and, because of this, avoiding the drawbacks of static images. Adding the mechanism of embedding of these developments in the operational work will allow viewing regularly the current geophysical parameters of the Black Sea in the form of images on the satellite map.

5 Conclusion

The using of the Google Maps or widget TkrPlot is not new and, for example, in the European Union project MyOcean here can be find a wide use of maps Google Maps. However, in combination with all of our needs (division into districts, use of local maps in conjunction with maps Google Maps, withdrawal coordinate values of

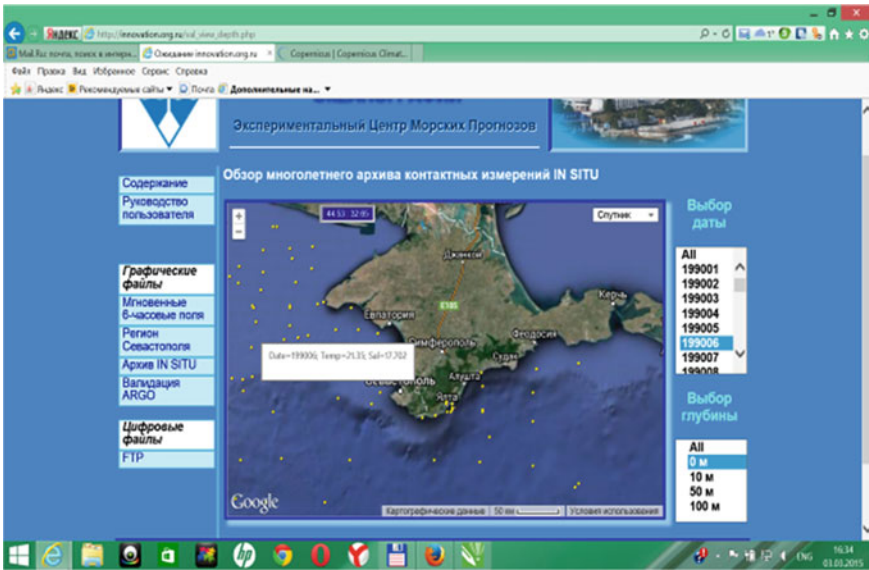


Fig. 4 Display of the values of geophysical parameters on the date with coordinates of the point of contact measurements on the Crimean Black Sea region

any point on the map, scaling) the use of the above software tools makes our work unique and significant.

The described method of geophysical data visualization can be used in every field of scientific activity, one way or another related to the visualization of data linked to geographical coordinates.

In this paper the three ways of data visualization of the results of calculations of operational oceanography tested in practice by authors have been considered. It has evidently demonstrated that only the combined application of modern software graphics products in conjunction with the mapping service Google Maps gives the desired positive results. Therefore, in the near future, in our view, the focus of graphic developments in the field of oceanography (as well as in the fields of science related with geographic mappings) as a whole will concentrate on the mutual use of the local charts and cartographical tools, such as Google Maps, Yandex Maps etc.

Let us say a few words about the possible future application of this “union” graphics with tools Google Maps for validation of marine forecasts. Currently, on the page of the site “Black Sea Marine Forecasting Centre. Validation on ARGO buoys data” (Black sea marine forecasting centre 2010), are uploaded the data with the results of the forecasts validation on Argo buoys. The similar page with validation, but only for the Crimean region and we are creating within the site CEMF, Fig. 5 shows the test example.

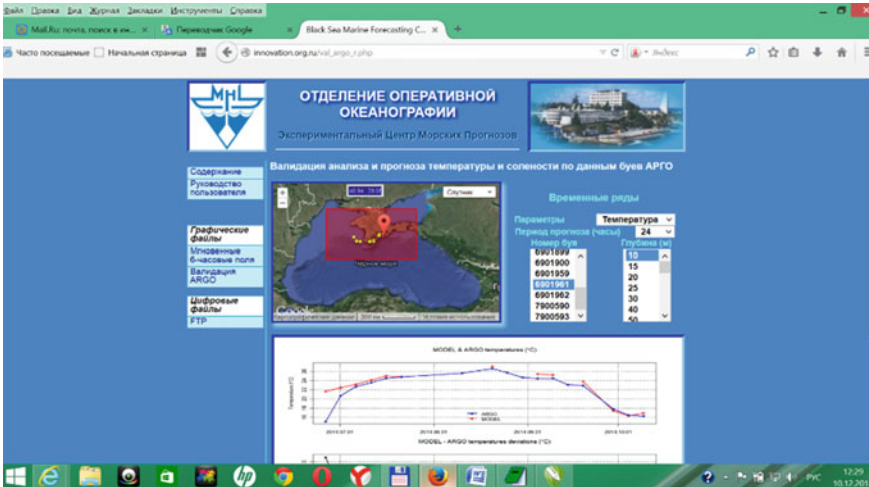


Fig. 5 Display of the trajectories of the Argo buoys moving on the Crimean Black Sea region for defined for validation the point of time

Now the page with validation of prognostic data has two images:

- map showing the path of the buoys with tooltips parameter values in some point of the location of the buoy;
- deviations graphics of the really measured values of geophysical parameters from prognostic values.

Figure 6 shows an example for comparison of the same validation, but already with the use on the map not only trajectories buoys, but also overlay on Google Maps display the local forecast, made on the same date on which the measurements were made of any buoy. That is, when navigating is along the path of a particular buoy then the imposition of a local forecast will change too.

However, the implementation of such approach to validation will require much greater technical and time resources, as it will be about storing large amounts of data necessary for participation in the validation. But that’s already a topic for a separate research, planned for the future.

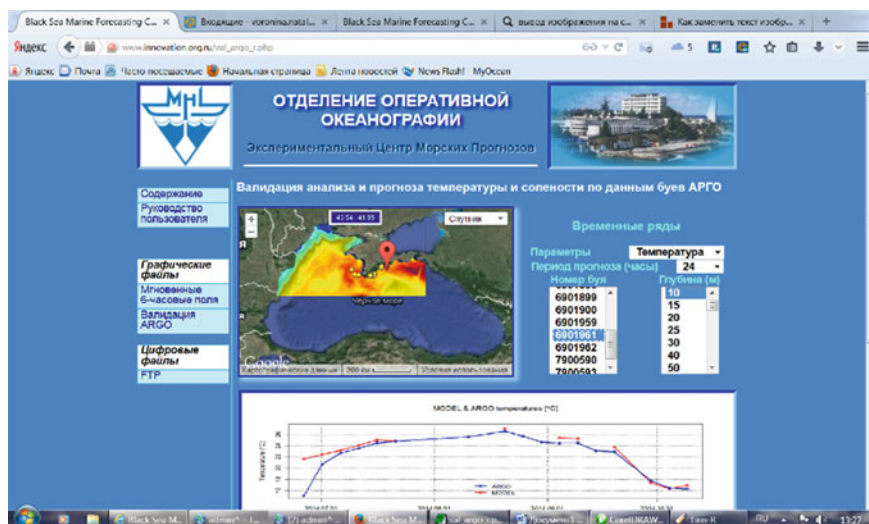


Fig. 6 The path of the ARGO buoys moving on the Crimean Black Sea region with the display of the temperature parameter forecast at the relevant date

Acknowledgements The work was carried out as part of a state assignment on the topic 0555-2021-0004 “Fundamental studies of oceanological processes which determine the state and evolution of the marine environment influenced by natural and anthropogenic factors, based on observation and modeling methods”.

References

- Akinshin A (2013) Funktsii v R. <http://aakinshin.net/ru/blog/r/functions/> (in Russian)
- Armand NA, Tishchenko YuG, Savorskiy VP, Smirnov MT, Ablyazov VS, Khaldin AA (2010) Promising space projects with L-band microwave radiometric systems. *Issl Zemli Iz Kosmosa* 1:20–26 (in Russian)
- Black sea marine forecasting centre. <http://bsmfc.net>
- Black sea marine forecasting centre (2010) Validation on ARGO buoys data. http://bsmfc.net/val_argo_prof.php
- Copernicus Marine service (2018). <https://marine.copernicus.eu/>
- Dincer A (2013) *Balkan uraz google maps javaScript API cookbook*. Packt Publishing, Birmingham-Mumbai
- Ekspertimetal'nyy tsentr morskikh prognozov (2015) [Experimental Center of marine forecasts] http://innovation.org.ru/instan_param.php (in Russian)
- Glazman RE, Greysukh A (1993) Satellite altimeter measurements of surface wind. *J Geoph Res* 98(C2):2475–2483
- Google Maps JavaScript API (2009). <https://developers.google.com/maps/documentation/javascript/examples/>

- Lishaev PN, Knysh VV, Korotaev GK (2020) Reconstructing the black sea hydrophysical fields including assimilation of the sea surface temperature, and the temperature and salinity pseudo-measurements in the model. *Phys Oceanogr* 27(5):445–459. <https://doi.org/10.22449/1573-160X-2020-5-445-459>
- Lawrence MF, Verzani J (2012) *The R series, programming graphical user interfaces in R*. CRC Press, London
- Shipunov AB, Baldin EM, Volkova PA, Korobeinikov AI, Nazarova SA, Petrov SV, Sufianov VG (2020) *Naglyadnaya statistika. Ispol'zuyem R!* <http://ashipunov.info/shipunov/school/books/rbook.pdf> (in Russian)
- Zapevalov AS (2012) Effect of skewness and kurtosis of sea-surface elevations on the accuracy of altimetry surface level measurements. *Izv Atm Ocean Phys* 48(2):200–206. <https://doi.org/10.1134/S0001433812020120>
- Zaryadov IS (2010) *Vvedeniye v statisticheskiy paket R: tipy peremennykh, struktury dannykh, chteniye i zapis' informatsii, grafika*. Izdatel'stvo Rossiyskogo universiteta druzhby narodov, Moscow (in Russian)

Destruction of Rocky Coastes of Cold Seas



V. V. Afanas'ev  and A. V. Uba 

Abstract In 2011, in the area of Nevelsk, Sakhalin Oblast, we started instrumental observations along a network of 100 benchmarks concreted into the surface of a mudstone-siltstone bench coseismically raised as a result of the earthquake on August 2, 2007 in the area of Nevelsk, Sakhalin region. The minimum rates of destruction of the bench surface (up to 25 mm/year) are observed in areas covered by debris washed away from the seaward part with a superposition of the maximum sea levels and waves. The bench was most actively destroyed at the northwestern border, where the mean annual breakdown rates of the edge exceeded 5 cm/year. In areas periodically flooded with water, the rate of destruction of the bench surface reaches 43.7 mm/year. As shown by a comparative analysis of the rates of destruction of benches and coastal scarps in rocks of weak and medium stability, the destruction of the latter occurs at rates about an order of magnitude higher than the rates of destruction of the surface of a coseismically raised bench. The maximum contribution to the destruction of the bench is made by frost weathering at subzero air temperatures during the open sea period. The number of freezing and thawing cycles during this period in a tidal sea reaches 100–150 cycles.

Keywords Sakhalin Island · Coseismic coastal uplift · Shore platform · Sea cliff · Erosion rates

1 Introduction

The destruction of rocky shores is a function of bedrock characteristics, wave climate, tidal regime and weathering patterns. The relative contribution of marine and subaerial processes, as well as the geological properties of the rocks being destroyed, has been discussed and discussed in many tens of studies. A detailed analysis of the state of affairs in this direction of coastal geomorphology is presented in analytical reviews (Stephenson et al. 2018; Sunamura 2015; Trenhaile 2018).

V. V. Afanas'ev (✉) · A. V. Uba
Institute of Marine Geology and Geophysics, FEB RAS, Yuzhno-Sakhalinsk, Russia
e-mail: vvasand@mail.ru

Currently, it is believed that the wave impact is decisive in the development of such shores in areas with high wave energy, while the role of weathering is more significant in warm temperate and tropical regions (Cruslock 2010). Nevertheless, the nature and relative efficiency of physicochemical and biological processes on the bench, the influence of climate, wave regime, tidal range, rock characteristics and the spatio-temporal development of the process of destruction of coastal platforms cannot be unambiguously characterized until now (Trenhaile 2019).

We have found that the seas of the North Pacific are characterized by a significant contribution to the destruction of rocky shores by the processes of physical weathering at negative air temperatures during the open sea. The number of freezing and thawing cycles during this period reaches several dozen. The study of the destruction of coastal platforms—benches, and coastal ledges—cliffs formed on rocky shores (Fig. 1) allows differentiating wave effects and factors of subaerial weathering.

2 Overview of the Problem

Approximately the length of the coastline of the world ocean is made up of rocky shores, the morpholithodynamic specificity of which is determined by the processes of destruction (Emery and Kuhn 1982). Continuous monitoring of the destruction of bedrock shores is practically impossible, therefore, when determining the abrasion rate, the average values for the periods of field observations and data from repeated cartographic and remote sensing surveys are used (Sunamura 1992).

However, the long-term average abrasion rates of abrasive shores should be used with extreme caution in hazard determination and coastal zoning. There is a well-known case when, during one month, storms in California washed away about 14 m of a cliff, composed of siltstones, which retreated from 1931 to 1982 at an average speed of 0.2 m/year (Griggs and Savoy 1985).

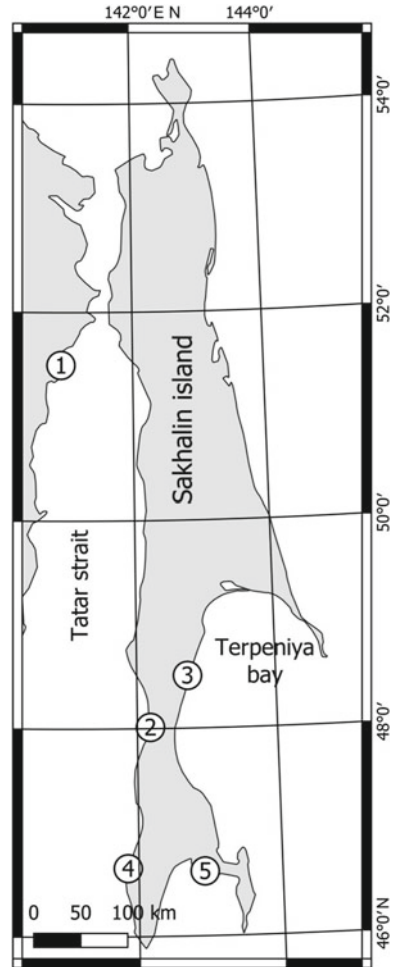
A similar case was noted by us recently in the area of the Prigorodnoye LNG plant, located on a basement terrace composed of weakly cemented mudstones and siltstones of the Bykovskaya suite (K2bk) of the third resistance class (Polunin 1984). In a few days in the fall of 2017, the coast retreated by 4–7 m, while over more than a ten-year observation period, the ledge destruction rate was 0.1–0.15 m/year.

Field observations of the rate of retreat of the bedrock shores of the Terpeniya Bay and the Tatar Strait were also carried out in the period from 1999 to 2007 by the Center for State Monitoring of the Geological Environment at FSUE SakhGRE (Afanasyev 2020).

The average rate of retreat of the coastal scarp in Terpeniya Bay, composed of Neogene siltstones of the Kurasi Formation N1Cr, over the observation period was 0.26 m/year per linear meter of the coastline. However, one storm in 2006 accounted for 77% of the total coastal retreat during the observation period.

Monitoring of the retreat of the shores of western Sakhalin composed of lithified sandstone-siliceous rocks of the Kholmsk lithotype of the fourth resistance class

Fig. 1 Map of the factual material of the study of rocky shores: 1—high coastal scarp in the De Kastri bay, 2—the Tatar Strait cliff, 3—the scarp of the basement terrace of the Terpeniya Bay, 4—bench in the area of Nevelsk, 5—coastal scarp in the LNG area “Prigorodnoye”



showed that the mean annual rates of retreat of the cliff edge approximately correspond to the rates of destruction of the cliff worked out in rocks of II and III lithotypes (Polunin 1984). At the same time, the average annual rate of retreat of the cliff edge in the areas exposed to direct wave impact was 0.25 m/year -0.32 m/year, and the average annual rate of retreat of the coastal scarp, which is located in the wave shadow of a small port facility, was 0.05 m/year (Afanasyev 2020).

As we noted earlier, the study of the processes of destruction of coastal platforms—benches formed on rocky shores with weak rock stability—allows us to clarify the role and contribution of wave effects and factors of subaerial weathering to the destruction of rocky shores. An exceptional opportunity in this regard is provided by studies of the failure of a bench composed of siltstones and thin layers of more

durable calcitized fine-grained sandstones, which was raised by 0.8–1.0 m as a result of the Nevelskoye earthquake on August 2, 2007 (Afanasev 2007).

3 Methodology

The development of geospatial technologies has now made available high-precision photogrammetric digital multi-temporal models of the relief of abrasion-denudation shores of cold seas, which make it possible to determine the rate and nature of destruction of bedrock rocks of weak and medium stability.

In 2011, at a bench near the town of Nevelsk, Sakhalin Oblast, we started instrumental observations over a network of concreted 100 benchmarks.

The distance between the profiles is 25 m, the distance between the benchmarks along the profile is 10 m. The first benchmark is located on the seaward edge of the bench. In 2019, only 32 benchmarks were measured (Fig. 2).

Some of the benchmarks were lost as a result of ice impact in the winter of 2019, some benchmarks were covered with man-made soil or destroyed.

As an example of changes, Figure 3 shows a visual series of the dynamics of the bench surface in one of the sections (target No. 5/benchmark No. 2).

Since July 2016, measurements have been made by subtracting different-time maps of the field of heights of sections measuring 2.25 m^2 with a benchmark in the center. A step-by-step procedure for constructing maps using a digital photogrammetric method in Agisoft Photoscan software using an accurately oriented aluminum frame measuring 1.5×1.5 meters is shown in Fig. 4.

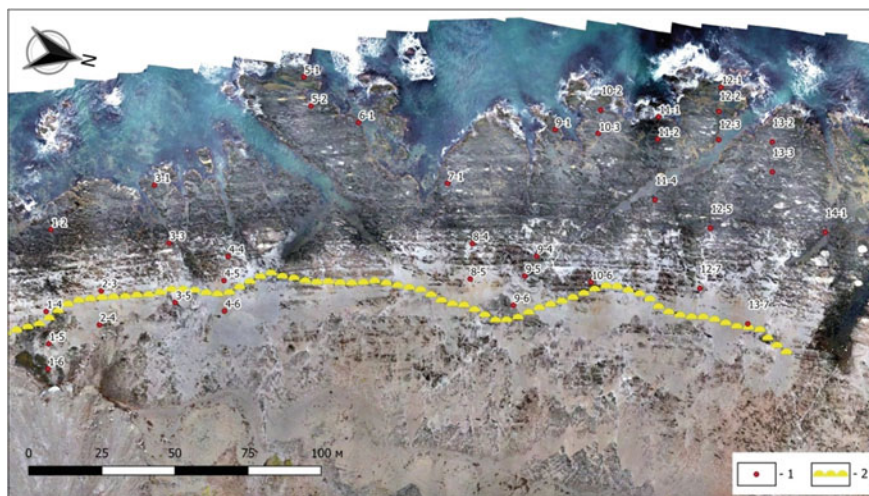


Fig. 2 Snapshot from UAV in 2018: 1—position of benchmarks used before 2019; 2—a shaft formed at the edge of the ice in 2019

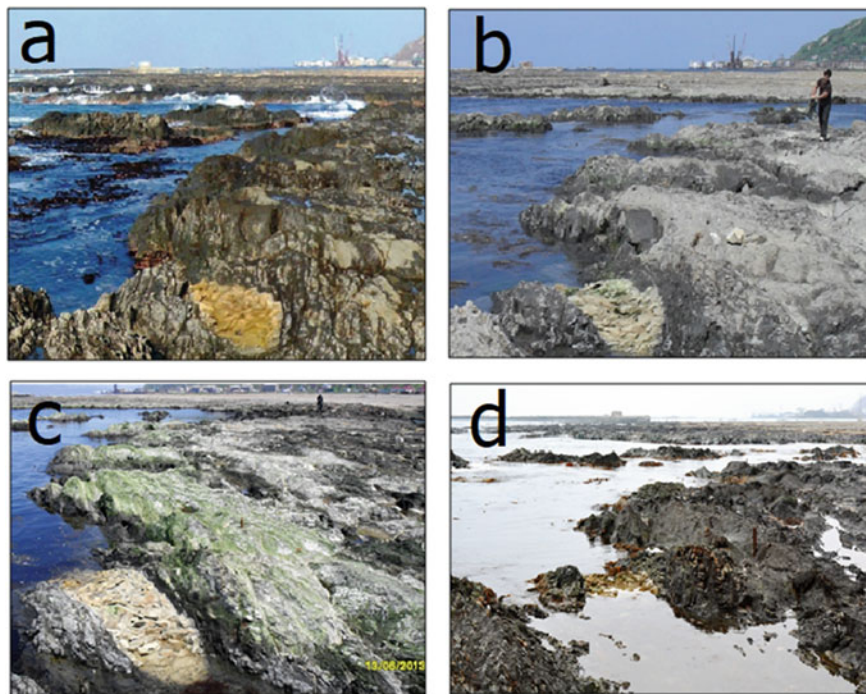


Fig. 3 Visual series of the dynamics of the surface of the bench with calcitized nodule in one of the sites (section No. 5/benchmark 2): **a**—30.10.2010; **b**—19.06.2012; **c**—13.06.2013; **d**—11.08.2018

As a result of comparing the models of the field of heights with a planned resolution of 0.001 m for the periods between surveys, the average rates of destruction were calculated for the measuring site as a whole and for individual differences in rocks.

4 Results and Discussion

The most obvious result of the features of the collapse of a coseismically raised bench is undoubtedly a map of deformations of the bench surface over a five-year period, compiled from the results of photogrammetric measurements (Fig. 5).

Calcitized nodules with a smooth undisturbed surface at a distance of 40 meters from the edge of the bench collapse at a rate of 1–2 mm/yr, which corresponds approximately to the middle of the interval of previously measured values in other regions of the world (Trenhaile 2018; Trenhaile and Porter 2018). Special attention should be paid to the conclusion that the maximum rates of destruction at high hypsometric levels are probably associated with frost weathering, the effect of ice and other mechanisms (Trenhaile and Porter 2018).

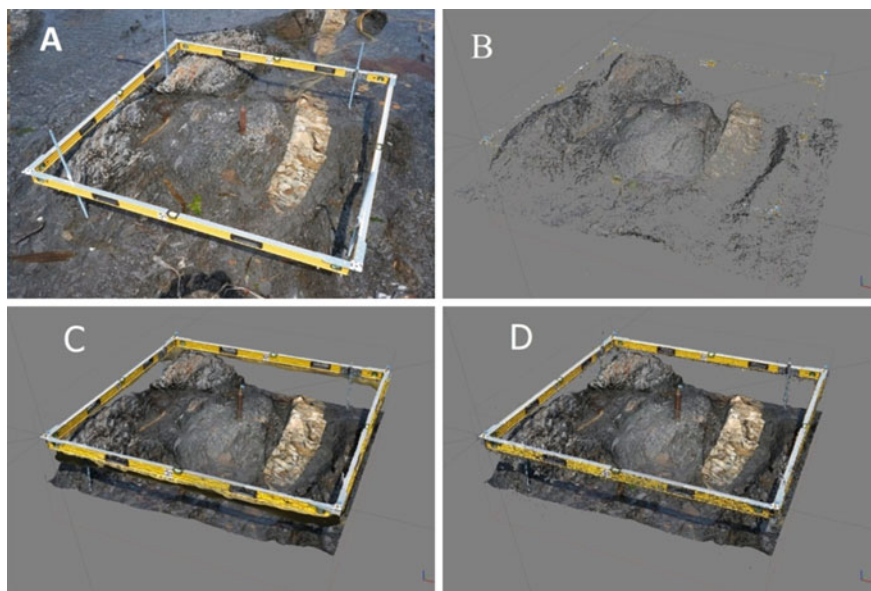


Fig. 4 The sequence of building a polygonal model; **A**—photo of the reference frame with the set frame, **B**—tie points, **C**—polygonal elevation model, **D**—dense cloud of points

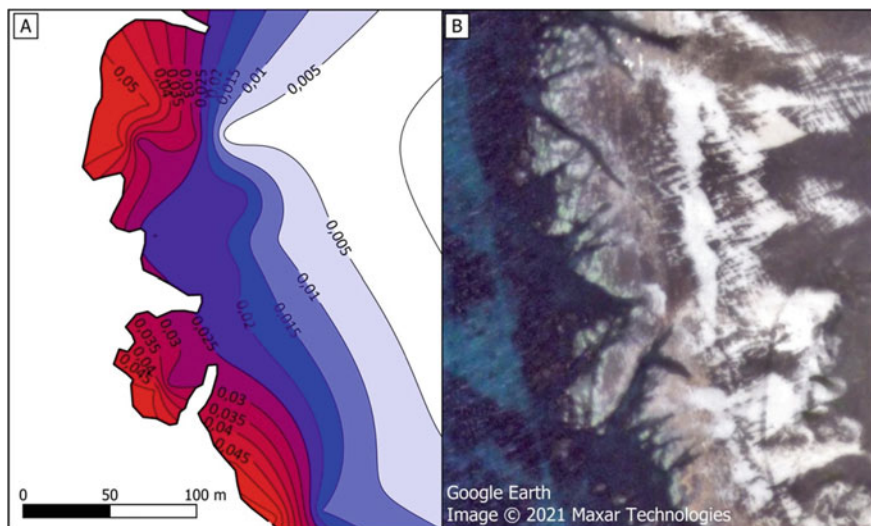


Fig. 5 Average annual rates of destruction of the bench surface; **A**—diagram of deformations (isolines are drawn through 0.005 m), **B**—visualization of the site

The maximum rates of destruction of the bench were noted at the northwestern border of the raised bench, in the area of gates 11–13, where already in 2018 some of the benchmarks deepened by 35 cm were washed out, i.e., the average long-term rates of destruction of the edge of the bench exceeded 5 cm/year. In areas periodically flooded with water, the rate of destruction of the bench surface reaches 4.37 cm/year.

It was also found that the rate of destruction of siltstones is approximately 2 times higher than the rate of destruction of calcified nodules.

At the same time, laboratory experiments using rocks from eastern Canada showed that erosion rates for different types of rocks were maximum at the level of low syzygy tide (which experiences two wetting cycles every day (Porter et al. 2010)).

The features of surface destruction by years and seasons will be presented in the next, more complete work. Figure 6 shows an example of a bench failure in an area subject to intense direct sea impact.

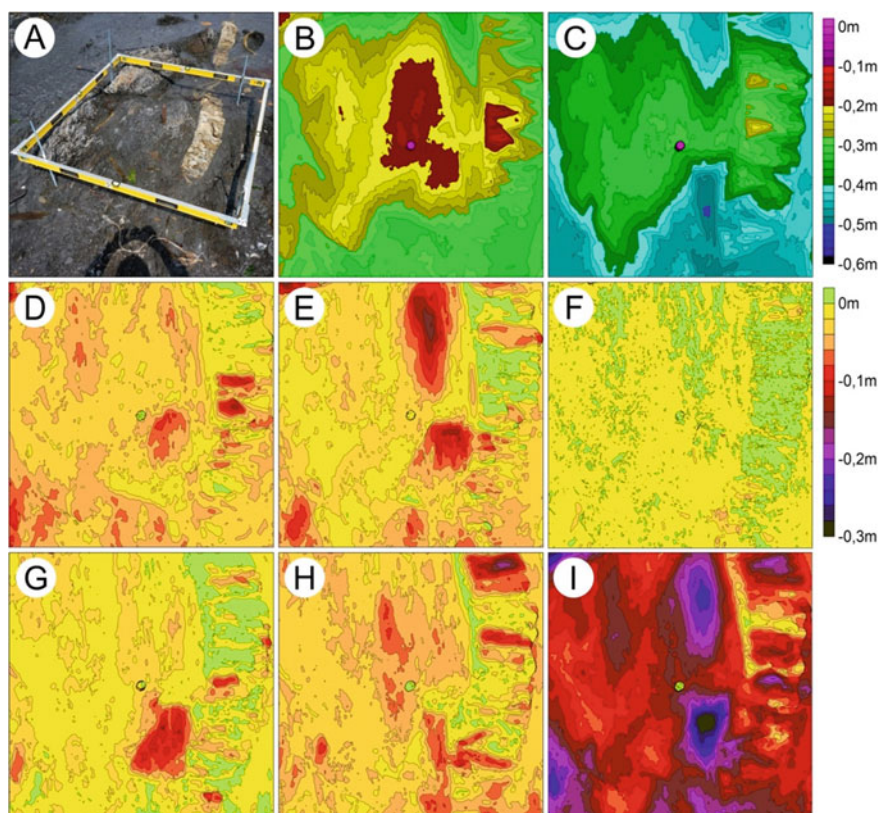


Fig. 6 Maps of the field of heights and differences in the fields of heights by years (benchmark 14/1): **A**—Photo of a site with calcified nodules. 2016; **B**—Elevation map of the site 2016; **C**—Elevation map of the site 2020; Height difference maps: **D**—2016–2017, **E**—2017–2018, **F**—2018–2018, **G**—2018–2019, **H**—2019–2020, **I**—2016–2020

Figure 7 characterizes an area located 50 meters from the edge of the raised bench, which is destroyed mainly due to weathering, provided that its products are removed during the superposition of surges and tides. Areas located outside the zone from which clastic material is washed away at a superposition of the maximum sea levels and waves are destroyed at the minimum, up to 0.25 cm/year, rates.

The high, approximately an order of magnitude higher than those measured in a temperate climate, destruction rates of layered, highly fractured bench rocks are explained, in our opinion, by frost weathering. The average long-term duration of the period with the average daily soil temperature below 0 °C, according to the data of the HMS Nevelsk, is 138 days. Considering that fast ice and continuous ice cover are practically not observed in this area, the average long-term number of freezing and thawing cycles at negative air temperatures during the open sea period in the flooded part of the bench is at least 100.

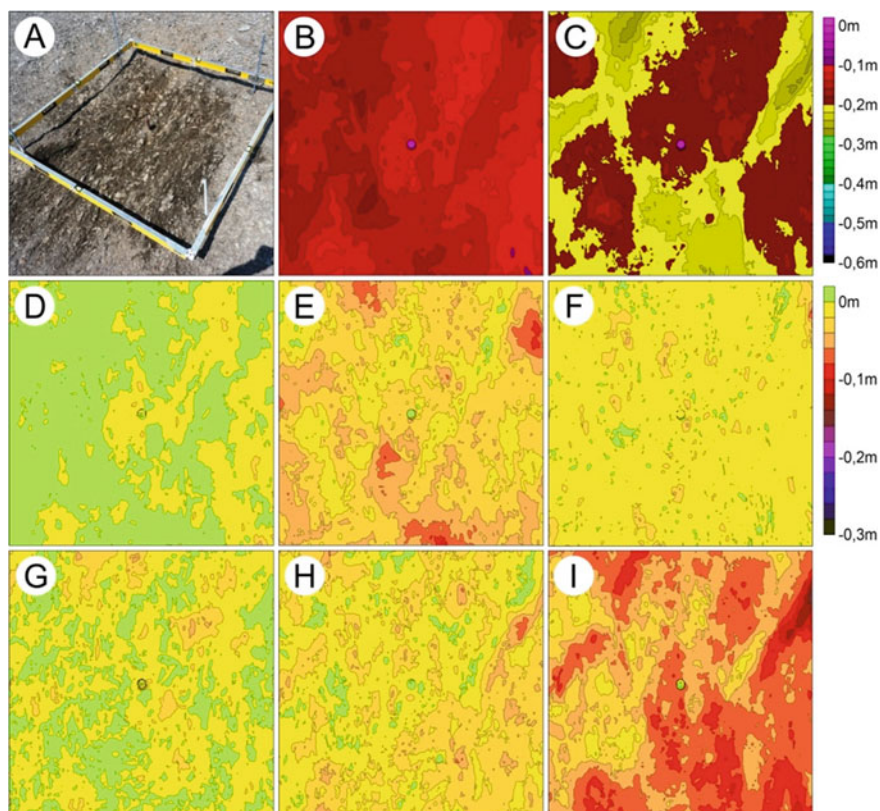


Fig. 7 Maps of the field of heights and differences of fields of heights by years (benchmark (9/5): **A**—Photo of the site July 2016, **B**—Map of heights of the site 2016; **C**—Map of heights of the site 2020; Maps of the difference in heights: **D**—2016–2017, **E**—2017–2018, **F**—2018–2018, **G**—2018–2019, **H**—2019–2020, **I**—2016–2020

Thus, as a result of the study, it was established that the destruction of subvertical coastal scarps in rocks of weak and medium stability under wave action occurs at rates about an order of magnitude higher than the rates of destruction of subhorizontal surfaces of a bench composed of similar rocks. The measured rates of retreat of the coastal scarp without direct wave action approximately correspond to the rates of destruction of rocks similar in terms of the stability class of rocks on the bench. In both cases, there are practically no shock wave loads with the abrasive effect of beach deposits. And if the weathering products are removed from the bench by seawater, then in the case of the cliff this is due to slope processes, mainly gravitational processes.

5 Conclusions

The development of geospatial technologies has now made available high-precision photogrammetric digital multi-temporal models of the relief of abrasion-denudation shores of cold seas, which make it possible to determine the rate and nature of destruction of bedrock rocks of weak and medium stability.

As a result of the study of the bench raised by 1 m as a result of the 2007 earthquake, it was found that the intensity of destruction of the bench surface approximately corresponds to the rates of destruction of the cliff in rocks of similar class of weak and medium stability in the absence of direct wave action. The role of the marine impact under bench conditions is mainly reduced to the intensification of weathering processes and the removal of its products from the surface. The number of cycles of freezing and thawing of the bench surface during the period of non-freezing sea air at subzero temperatures reaches several tens.

The longest study (43 years) of mudstone bench fracture performed in New Zealand using micro-erosion counters showed that the erosion rates obtained from short-term observations are quite consistent with the data of the full series (Stephenson et al. 2019). In 2016, the bench at the monitoring site in New Zealand was raised 1.01 m (Stephenson et al. 2017). Thus, the conditions for the development of the platform changed and a number of observations were interrupted. However, the observations were continued under new conditions and it is hoped that, as in our case, they will improve the understanding of the processes of development of coastal platforms (Stephenson et al. 2017; Afanasyev and Bogomolov 2007).

References

- Afanasev VV, Uba AV (2007) The Erosion of the shore platform raised by the coseismic coastal uplift as a result of the Nevelsk Earthquake of 2007, Mw = 6. 2. In: 9th International conference on geomorphology. – New Delhi, India, Indian institute of geomorphologists, November 6–11, 2017, p 226
- Afanasyev VV (2020) Morpholithodynamic processes and development of the coast of the contact zone of the subarctic and temperate seas of the North Pacific. Yuzhno-Sakhalinsk: IMGIG FEB RAS, 234 p. ISBN 978-5-6040621-8-0, <https://doi.org/10.30730/978-5-6040621-8-0.2020-1>
- Afanasyev VV, Bogomolov LM (2007) Processes of destruction of the newly formed sea coast at Mw = 6, 2 Nevelskoy earthquake in 2007. Trigger effects in geosystems: abstracts. report Second All-Russia. seminar-meeting. - Moscow, IDG RAS, June 18–21, 201, pp 5–6
- Cruslock EM (2010) Geomorphologic equifinality: a comparison between shore platforms in Höga Kusten and Fårö, Sweden and the Vale of Glamorgan, South Wales, UK. *Geomorphology* 114(1–2):78–88
- Emery KO, Kuhn GG (1982) Sea cliffs: their processes, profiles, and classification. *Geol Soc Am Bull* 93(7):644–654
- Griggs G, Savoy L (1985) Sea cliff erosion. *Living with the California Coast*. – Durham: Duke University Press, pp 27–34
- Polunin GV (1984) Map of lithological complexes and manifestations of exogenous processes in Sakhalin: scale 1: 500000/GV Polunin, VA Buzlaev. M: GUGK.
- Porter NJ, Trenhaile AS, Prestanski K, Kanyaya JI (2010) Patterns of surface downwearing on shore platforms in eastern Canada. *Earth Surf Process Landfs* 35(15):1793–1810
- Stephenson WJ, Dickson ME, Denys PH (2017) New insights on the relative contributions of coastal processes and tectonics to shore platform development following the Kaikōura earthquake. *Earth Surf Process Landfs* 42(13):2214–2220
- Stephenson WJ, Kirk RM, Hemmingsen MA (2019) Forty three years of micro-erosion meter monitoring of erosion rates on shore platforms analysis; Trenhaile AS (2018) *Marine Geology* 403:80–92; at Kaikōura Peninsula, South Island, New Zealand; *Geomorphology* 344:1–9
- Stephenson WJ, Kirk RM, Hemmingsen MA (2019) Forty three years of micro-erosion meter monitoring of erosion rates on shore platforms at Kaikōura Peninsula, South Island, New Zealand. *Geomorphology* 344:1–9
- Sunamura T (1992) *Geomorphology of rocky coasts*. Wiley, New York, 302 p
- Sunamura T (2015) Rocky coast processes: with special reference to the recession of soft rock cliffs. *Proc Jpn Acad Ser B* 91(9):481–500
- Trenhaile AS (2018) Shore platform erosion and evolution: Implications for cosmogenic nuclide analysis. *Marine Geology* 403:80–92
- Trenhaile AS, Porter NJ (2018) Shore platform downwearing in eastern Canada A 9–14 year micro-erosion meter record. *Geomorphology*. 311:90–102
- Trenhaile AS (2019) Hard-rock coastal modelling: past practice and future prospects in a changing world. *J Mar Sci Eng* 7(2):34

Bottom Sediments of the Kazantip Nature Reserve Coastal Water Area (Azov Sea) as an Indicator of the Water Area Wellbeing



E. A. Tikhonova, O. V. Soloveva, and N. V. Burdiyan

Abstract An assessment of the physical–chemical (pH, Eh), some chemical (content of chloroform-extractable substances and total petroleum hydrocarbons) and microbiological (hydrocarbon-oxidizing, thionic and sulfur-reducing bacteria) parameters of the bottom sediments of the coastal water area of the Kazantip Nature Reserve (Azov Sea) was done in the period from 2013 to 2016. According to the results obtained, the bottom sediments of the coastal water area of Kazantip Cape were conditionally clean, with the exception of the lake—Neftyanikov Lake, located in the center of the Reserve. The concentrations of chloroform-extractable substances in this lake fluctuated from 70 to 170 mg/100 g air-dry bottom sediments. The number (cell/g) of heterotrophic bacteria ranged from 10^5 to 10^7 , respectively, hydrocarbon-oxidizing—from 1.0 to 10^4 , thionic—from $4.5 \cdot 10^2$ to $2.5 \cdot 10^5$, sulfur-reducing—from 1.0 to $1.5 \cdot 10^3$. This evidenced of the high degree of development of the heterotrophic bacterial community, including hydrocarbon-oxidizing bacteria in shallow stations of the water area.

Keywords Physical–chemical parameters · Organic matter · Bacteriobenthos · Sea bottom sediments · Kazantip Nature Reserve · Azov Sea

1 Introduction

One of the topical tasks facing humanity is the protection of wildlife as a whole and constant monitoring of the state of specially protected natural territories, in particular (Grummo et al. 2018). On the territory of the Crimean Peninsula there is only one reserve adjacent to the water area of the Azov Sea—Kazantip Nature Reserve. The Reserve is located in the north of the Kerch Peninsula, on Kazantip Cape in 2 km from the city of Schelkino. Cape protrudes on 2 km in the southern part of the Azov Sea. The territory is part of the North-east subarea of the Kerch geomorphological area. The total area of the Reserve is 450.1 ha, of which 394.1 ha—land and 56 ha—the

E. A. Tikhonova (✉) · O. V. Soloveva · N. V. Burdiyan
A.O. Kovalevsky Institute of Biology, Southern Seas of RAS, Sevastopol, Russian Federation
e-mail: tihonova@mail.ru

water area of the Azov Sea (bandwidth of 50 m) (Boltachev et al. 2016; Litvinyuk 2016; Ryabushko and Bondarenko 2016). From the West, the North and East, the territory of the Reserve is limited by the water area of the Azov Sea (the outer border passes at a distance of 50 m from the coast), from the south borders—with the lands of the Misovsky rural settlement. The overall length of the borders of the Reserve is approximately 20 km, including land—10 km (of which inland—7 km, external—3 km), sea—about 10 km. The water area of the Reserve (56 ha) is part of the wetland of the international significance “Aquatic-rock complex Kazantip Cape” with a total area of 251 ha (certificate No. 1393 of July 29, 2004, Iran, Ramsar) and the nature monument of regional importance (240 ha) “Coastal aquatic complex near Kazantip Cape” (security obligation No. MPP-008 dated 01.06. 2012) (Litvinyuk 2016; Ryabushko and Bondarenko 2016).

The protection of the territory of Kazantip Cape and the coastal assembly complex is due to the presence of unique marine and coastal landscapes, which are the places of bird's accumulation. There is a great interest to the coast of Cape as a sample of the coast dynamics in the places of exit of ancient bryozoa reefs. Flora and fauna of the Reserve is characterized by a significant zoological value and the presence of endemic species. For example, 15 types of fauna and 12 species of the Nature Reserve are listed in the Red Book of the Russian Federation. In the Red Book of the Crimean Republic, 83 types of fauna and 55 types of flora are recorded. Underwater meadows of marine herbs in the water area of the reserve serve as a spawning point of aboriginal species of the Azov Sea. The migration path of birds lies through the Reserve (Boltachev et al. 2016; Litvinyuk 2016; Oradovskogo 1977; Ryabushko and Bondarenko 2016).

Precipitous, abrasive shores of Kazantip Cape are composed of meotianbryozoya limestones (Klyukin et al. 1987; Litvinyuk 2016; Zenkevich 1963). Bryozoya limestones are sufficiently loose and porous. As a result, emissions of the large number of petroleum products contribute to the its accumulation and chronic pollution for several years, providing a negative effect on algae vegetation.

A lot of domestic garbage is thrown into the Kerch Strait with ships. The course of the Kerch Strait is directed along the coast from the East to the West and is formed from the merger in the area of the Kerch Strait of the Azov stream and the jet of the North-West direction, which goes along the coast of the Caucasus (Litvinyuk 2016; Vylkanov et al. 1983). At the same time, in the cold period, when the river stock decreases sharply with the additional influence of winds, the Black Sea Water comes through the strait in the Azov Sea (Aksyonov 1962; Ereemeev et al. 2003). The coast of Kazantip Cape and similar territorial-aquatic complexes (on the capes Zyuk, Chagan, Kiten, Krasnyy Kut, etc.) have a small-bay character. The areas of accumulative pebble, shell-pebble and gravel-pebble small beaches become a trap for the thrown garbage. Employees of the Reserve repeatedly found in the bays ship mops, mooring ends, plastic plates, Turkish grocery containers, etc. The active development of the Azov Sea offshore oil and gas producing companies, elevate the risk of pollution of the marine environment in the coastal waters Kazantip Cape very seriously. This may affect the state of coastal biocenoses extremely negatively.

The coastal zone of the natural and aquatic complex (NAC) is influenced by anthropogenic-accumulative processes, which are characteristic of the coast of the Arabat foreland and Kazantip Cape bays bordering it. This is basically unregulated recreational activities (ignition of fires, installation of tents, vehicles, dump of garbage, etc.), which usually is most influenced anthropogenic factor in this region.

In the 2000s, the study of landscapes of the Azov Sea were conducted. According to the results obtained, their condition was attributed to the four levels: from satisfactory to critical. In the area of Kazantip coast, it is estimated as conflict (2 level) (Bespalova 2007). The main anthropogenic effects in this area were the search and mining of minerals. So, chloroform-extractable substances (CES) and total petroleum hydrocarbons (TPH) are the chemical parameters which should control on this region. The main environmental problems: the introduction of alien species, a decrease in benthos biodiversity and biomass. At the same time, the integral assessment of the quality of the Azov Sea of NAC allowed to characterize this area of the sea as weakly polluted—dirty (Bespalova 2007). This indicated a sufficiently high level of anthropogenic load in the study area. An important indicator of the ecological state of the water area is also its self-cleaning ability for anthropogenic load (Burdıyan 2011). Therefore, the number and distribution of physiological groups of bacteria—the main destructors of an organic substance of autochthonic and allochronic origin in marine ecosystems should be assessed.

Thus, the conduction of systematic environmental control over the state of the Reserve environment is an objective necessity. The purpose of this work was to study the physical–chemical (pH, EH), some chemical (the content of CES and TPH) and the microbiological characteristic (number and distribution of hydrocarbon-oxidizing (HB), thionic (TB) and sulfur-reducing bacteria (SRB)) in the bottom sediments of the most vulnerable parts of the NAC (coastal zone and mineral mining places) at Kazantip Cape.

2 Material and Methods

Samples of bottom and coastal sediments were collected in the coastal water area of Kazantip Reserve with a hand sampler. In freshly collected samples, pH and Eh were determined. To determine the TPH in the bottom sediments, it was preliminarily prepared as follows: bottom sediments were freed from large shells of mollusks and scraps of algae. The nit was dried to an air-dry state under natural conditions in a special dish. Dry samples were ground in a specially prepared mortar with a pestle and sifted through sieves with a mesh diameter of 0.25 mm. After grinding, they were weighed on a balance. The resulting air-dry mixture was extracted with chloroform until the wash portions were discolored. The extracts were collected in a conical flask with a volume of 100 ml, the solvent was distilled off in a water bath to a residual volume of 2–3 ml and transferred to weighing bottles. After the evaporation of chloroform, the weighing bottles were weighed, and thus the weight value of CES in the test material was obtained. After dissolving of CES in carbon tetrachloride, it

was applied to a column with aluminum oxide for subsequent determination of TPH was held by means of IR-spectrophotometer (Oradovskogo 1977).

For microbiological analysis, the samples were placed in sterile containers. In the collected samples of bottom and coastal sediments, the number of heterotrophic bacteria was determined: HB—destructors of oil hydrocarbons, SRB—the main producers of hydrogen sulfide and TB—the active oxidizing agents of sulfur and its inorganic reduced compounds. The number of bacteria in the sample was determined by the method of limiting dilutions using elective environments (Burdiyan 2011; Mironov et al. 2003; Netrusova 2005). The determination of the number of bacteria was performed using the following liquid nutrient media. For HB was used medium with peptone (Mironov et al. 2003) of the following composition (g): peptone—10.0; yeast extract—1.0; sea water—1 l. For HB was used Dianova-Voroshilova media (Romanenko V and Kuznecov 1974) with the following composition (g): NaCl—18.0; $MgSO_4 \times 7H_2O$ —0.2; KCl—0.7; KH_2PO_4 —1.0; K_2HPO_4 —1.0; $CaCl_2$ —0.02; $FeCl_3$ —2 drops; distilled water—1.0 l. pH 7.2—7.4. 1% of sterile oil was introduced as the only source of carbon and energy into each test tube after sowing. The number of SRB was determined on the Postgate medium (Romanenko and Kuznecov 1974). A 3% sodium sulfide solution was added to the medium as a reducing agent. The number of TB was studied on the Sorokina media (Sorokin 1970). The water salinity was taken into account. The most likely number of microorganisms in a unit of volume was calculated according to the Mac-Credit table, based on the method of variation statistics (Netrusova 2005). Incubation of all sowings was carried out at room temperature (Fig. 1).

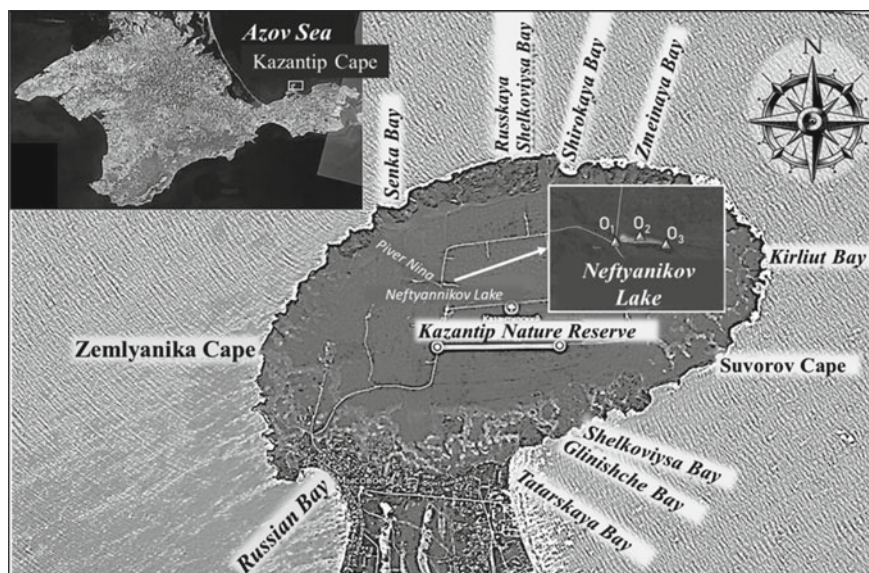


Fig. 1 The scheme of sampling of bottom and coastal sediments

3 Results and Discussion

Bottom sediments in the coastal zone of Kazantip Natural Reserve were represented by small sand of gray-yellow color, sometimes with an admixture of shells. The bottom sediments of a small lake (Neftyanikov Lake) in the central part of the Cape (Sampling Station O₁, O₂, O₃) were presented by semi-liquid gray-brown-colored silt with relevant physicochemical indicators.

For sands pH, hesitated in the range of 7.86–8.73 (Fig. 2A). Previously, in the silts of the Neftyanikov Lake, lower pH rates (7.0–7.35) were noted (Boltachev et al. 2013). The red-ox potential was positive (up to +295 mV) (Fig. 2B), with the exception of coastal sediments of the Russkaya Shelkoviysa, Russian, Senka bays and Neftyanikov Lake (when the minimum values were marked: Eh: –282 mV).

In general, the Azov Sea had elevated levels of organic, including oil, pollution. So, the bottom sediments of the Azov Sea (on the 83th cruise data of the research vessel “Professor Vodjanitsky”) had a weak-reducing environmental conditions (Eh = +1 ... +44 mV), except, of the northern part of the sea. In this part Eh was lowered to –165 mV. The pH in these areas of the water area ranged from 7.54 to 7.63 (Tikhonova et al. 2016, 2019). These conditions may contribute to the accumulation of organic substances, because low red-ox potential of the environment could cause slowdown of the bitumoid conversion. That is, if we compare the obtained indicators with other sites of the Azov Sea, the environmental condition of bottom sediments of the coastal water area of the Kazantip Reserve was favorable for the development of bottom biocenoses, with the exception of the indicators of Neftyanikov Lake.

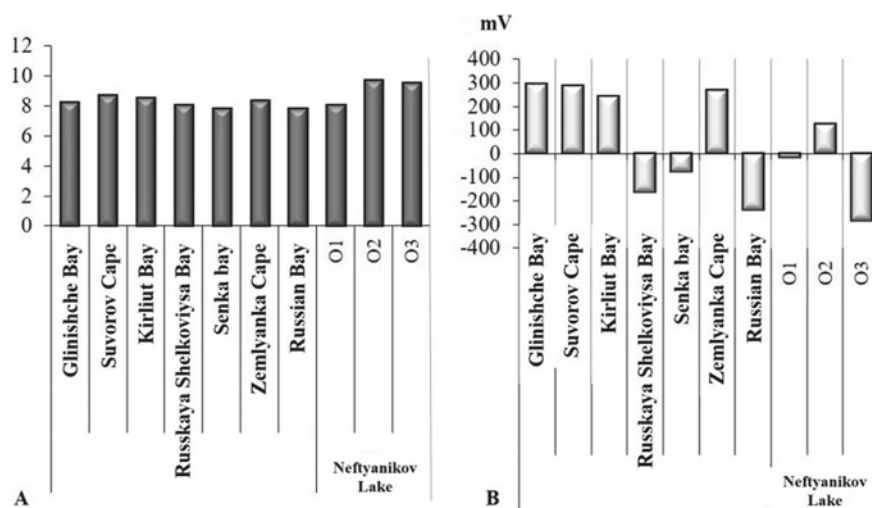


Fig. 2 Physical–chemical indicators (A—pH, B—Eh, mV) of the bottom and coastal sediments of Kazantip Natural Reservoir

In the coastal sediments of the Kazantip Nature Reserve, the trace amounts of CES were found. Its concentration ranged from 5.0 to 13.5 mg/100 g of the air-dry bottom sediments (a.-d. b.s.). These values indicated a low level of organic contamination and a small accumulation capacity of sediments, which was based on the size of their particles. TPH in all samples were marked in trace amounts (0.2–1.1 mg/100 g a.-d. b.s.). The share of TPH from CES in average amounted to 4.6%. Low indicators of the CES concentration the sea bottom sediments of the Kazantip Natural Reserve could be associated with minimal anthropogenic load. For instance, their content in other water areas of the Azov Sea were ten of times more. For example, in 2016th, the CES concentration in sea bottom sediments ranged from 107 to 187 mg/100 g a.-d. b.s., in 2020—from 85 to 125 mg/100 g a.-d. b.s. (Tikhonova et al. 2015, 2019) Indicators in the 2010th, 2016th corresponded to the III level of pollution (Mironov et al. 1986) in 100% samples, and in 2020th—it was in 67% of the samples. 33% of the samples corresponded to II level. However, oil hydrocarbons pollution throughout the water area of the Azov Sea was low, as well as in the coastal zone of Kazantip Reserve. In the sea bottom sediments of the Azov Sea in 2010, only in 65% of the surveyed stations concentration of TPH in bottom sediments amounted less than 5 mg/100 g a.-d. b.s. (Tikhonova and Guseva 2012), while in 2016 the quantities were above the tracks per 100% of the stations (Tikhonova et al. 2016).

The concentration of CES in the bottom sediments of the Nevtyanikov Lake compare to the rest of the coastal water area was significantly higher. Earlier it was shown (Boltachev et al. 2013) that at the stations O1, O2 and O3, the CES indicators were 170.0, 70.0 and 80.0 mg/100 g a.-d. b.s. respectively. Our studies had shown that in the silts of the Nevtyanikov Lake, located in the center of the Kazantip Cape, the concentration of CES was already 439.3 mg/100 g a.-d. b.s., which indicated the level of pollution V—described in Mironov et al. (1986). The distribution of TPH was similar CES: the minimum number was noted at the O2 station (2.7 mg/100 g a.-d. b.s.), and the maximum—at O1 station (57.0 mg/100 100 g a.-d. b.s.). The share of TPH ranged from 3.8 to 33.5%. Thus, the results had been obtained indicated an increase of the concentration of TPH in the Nevtyanikov Lake. It should be noted, that in addition to the production of petroleum hydrocarbons at the Cape, an equally important factor affecting the speed and the level of concentrating of organic pollutants was the granulometric composition of bottom sediments (Alemov et al. 2018; Boltachev et al. 2013). So, the finely dispersed silts of the lake have a greater accumulative ability, than the sands of the coastal water area of the Reserve.

It was noticed (Boltachev et al. 2013; Litvinyuk 2016) that in the coastal zone of the Kazantip Reserve, was revealed a segment with an almost complete absence of benthic macrofauna. In our opinion, the possible reason of a sharp decrease in the species diversity and the quantitative characteristics of the benthos in the specified area of the water area was the periodic flow of water from the small lake located in the central part of the peninsula when its overflowing with flood waters. The water of the lake, due to oil production carried out on the peninsula, may contain increased concentrations of hydrocarbons, both as a result of primary and secondary pollution, when petroleum products fall into water from bottom sediments. The results of our studies showed a fairly high level of organic pollution of the lake bottom sediments.

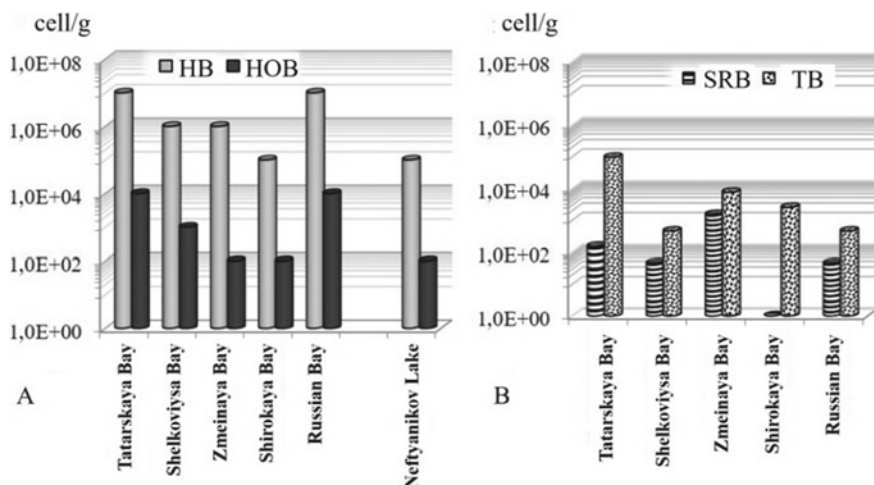


Fig. 3 Number (cell/g) **A**—heterotrophic (GB) and hydrocarbon-oxidizing bacteria (HB); **B**—sulphur-reducing (SRB) and thionic (TB) bacteria in the bottom sediments of the water area Kazantip Cape

The number of heterotrophic bacteria (GB) in the bottom sediments of shallow water stations Kazantip Cape varied from 10⁵ to 10⁷ cell/g (Fig. 3A), on more marine stations the number of GB ranged within the fourth-fifth order.

The greatest amount of GB was found in the bottom sediments of the Russian and Tatarskaya Bays, which undergone intensive recreational load. High indicators of GB indicated the saturation of the bottom sediments of these bays with an easily dismissed organic matter.

Bacteria that carry out the destruction of oil hydrocarbons were isolated from all samples of bottom sediments from Kazantip Cape (Fig. 3A). The number of HB in shallow water stations ranged from 10² to 10⁴ cell/g. In the samples of bottom sediments from deep-sea stations, the number of HB was significantly lower and varied from 1.0 to 10 cell/g. The high HB population was defined in shallow stations in Tatarskaya and Russian bays, demonstrates the high potential ability of the water area to self-cleaning from oil hydrocarbons.

SRB in the Kazantip Cape were isolated from all the samples (Fig. 3B). The number of SRB varied in a wide range from 1.0 to 1.5·10³ cell/g. The greatest SRB indicators were defined in Zmeinaya bay, respectively, the smallest—in Shirokaya bay. In other samples, the number of SRB ranged from 45 to 150 cell/g. The high number of SRB in the waters of Zmeinaya bay, indicated the active processes for the restoration of sulfates leading to the deterioration of the ecological state of the bay, due to the high toxicity of sulfuretted hydrogen for hydrobionts.

TB in the bottom sediments were determined everywhere. The number of TB varied from 4.5·10² to 2.5·10⁵ cell/g (Fig. 3B). The smallest number of TB was defined in samples selected in Russian Shelkovitza bay. The number of TB in all

the samples of bottom sediments exceeded the quantitative indicators of the SRB, thereby assuming the presence of a bacterial filter that prevents the penetration of hydrogen sulfide into the nearby layers of water and soil.

For comparison, in 2010–2011 SRB, TB and denitrifying bacteria in the bottom sediments were isolated everywhere around the polygon. The quantity of SRB varied from $1.5 \cdot 10^2$ to $9.5 \cdot 10^3$ cell/g of wet sediment, maximal number ($9.5 \cdot 10^3$ cell/g) was registered on stations 5 and 6. The fluctuation of TB abundance was from $7.5 \cdot 10^2$ up to $2.0 \cdot 10^4$ cell/g, thus in most samples a number of TB was within the limits of 10^3 – 10^4 cell/g. The number of denitrifying bacteria varied from $1.5 \cdot 10^2$ up to $2.5 \cdot 10^4$ cell/g, the least number of these bacteria was registered on st. 1. On other stations fluctuation of denitrifying bacteria number was one or two orders. In general, the quantity of anaerobic bacteria on the western and eastern coast of Kazantip Cape considerably did not differ from such of the northern coast (Boltachev et al. 2013).

It could be stated that during the period between the studies, the state of the microbial community did not change significantly, which indicates the relative stability of the ratio of natural processes and anthropogenic load on the researched site.

Thus, the ecosystem of the Kazantip National Reserve is a fragile and exposed to the anthropogenic press. In this regard, it seemed to be necessary to carry out environmental protection and conservation activities. To reduce the influence of various pollutants on the development of benthic communities in the coastal zone of the Reserve, it is possible to carry out work on an increase in the self-cleaning potential of the water area, for example, the installation of artificial reefs or hydrobiological cleaning systems. First of all, this work is necessary at the sections of the Reserve with an increased anthropogenic load (in particular, the berths of fishing vessels and the water area of Senka bay). It should also be completely eliminated or minimized any mining near the Reserve territories and water areas.

4 Conclusions

The bottom sediments of the coastal water area of the Kazantip Natural Reserve were generally conditionally clean. The concentrations of CES and TPH in the bottom sediments of indicated a low level of organic pollution and bottom sediments low cumulative ability, with the exception of the Neftyanikov Lake, where the indicators were significantly higher.

The studied groups of bacteria were isolated all around the study sight. The number (cell/g) of GB from 10^5 to 10^7 , HB—from 1.0 to 10^4 , TB—from $4.5 \cdot 10^2$ to $2.5 \cdot 10^5$, SRB—from 1.0 to $1.5 \cdot 10^3$. The high degree of development of the GB community, including HB, was noted in shallow stations of the water area.

To reduce the influence of various pollutants on the development of benthic communities in the coastal zone of the Reserve, it is possible to carry out work on an increase in the self-cleaning potential of the water area, for example, the installation of artificial reefs or hydrobiological cleaning systems. First of all, this work is necessary at the sections of the reserve with an increased anthropogenic load (in

particular, the berths of fishing vessels and the water area of Senka bay). It should also be completely eliminated or minimized any mining near the reserve.

Acknowledgements The work was performed as part of the state assignment, of IBSS on the theme “Molismological and biogeochemical foundations of the marine ecosystems homeostasis” (№ 121031500515-8).



References

- Aksyonov AA (1962) Hydrometeorological reference book of Azov Sea. Gidrometeoizdat, Leningrad (in Russian)
- Alemov S V, Burdiyan N V, Viter T V, Guseva E V, Tihonova E A, Soloveva O V, Alyomova A S (2018) The results of comprehensive sanitary - biological research of the coastal water area of the Kazantip nature reserve (Crimea). In: Proc sci-pract school-conferences “Terrestrial and marine ecosystems of the Black Sea region and their protection”. Novorossiysk, pp 7–9 (in Russian)
- Bespalova LA (2007) Ecological diagnostics and assessment of the stability of the landscape structure of the Sea of Azov. PhD Thesis. Sankt-Peterburg (in Russian)
- Boltachev AR, Alemov SV, Zagorodnyaya YA, Karpova EL, Manzhos LA, Gubanov VV, Litvinyuk NA (2016) Podvodnyj mir Kazantipskogo prirodnogo zapovednika: k 15-letiyu Kazantipskogo prirodnogo zapovednika [The underwater world of the Kazantip Natural Reserve] Business-Inform, Simferopol. (in Russian)
- Boltachev AR, Alyomov SV, Zagorodnyaya YA, Karpova EP, Manzhos LA, Gubanov VV, Burdiyan NV, Tikhonova EA, Popova LA (2013) Integral assessment of the environment, species diversity and ecological structure of coastal marine biocenoses of Kazantip nature reserve (the Sea of Azov). In: Proceedings of 5th IWA Eastern European «Young and Senior Water Professionals» Conferences. Part 1 (English version), pp 32–39
- Burdiyan NV (2011) Sulfate-reducing, thiobacteria and denitrifying bacteria in the coastal zone of the Black Sea and their role in oil hydrocarbon transformation. Sevastopol (in Russian)
- Eremeev VN, Boltachev AR, Aleksandrov BG, Alyomov SV (2012) Biological diversity of the coastal zone of the Crimean Peninsula: problems, preservation and restoration pathways. In: Sevastopol: NAS Ukraine, Institute of Biology of the Southern Seas, 2012. 92 p.
- Eremeev VN, Ivanov VA, Ilyin YP (2003) Oceanographic conditions and ecological problems in the Kerch strait. *Mar Environ J* 3(2):27–40 (in Russian)
- Grummo D, Korobushin D, Malashenkova E (2018) Monitoring of specially protected natural areas. *Nauka i innovacii*. 10(188):63–69 (in Russian)
- Klyukin AA, Korzhenevsky VV, Shchepinsky AA (1987) Kazantip (guide). Simferopol: Tavriya, 112 pp (in Russian)
- Litvinyuk NA (2016) State budgetary establishment of the Republic of Crimea Kazantip nature reserve. Cadastral documentation of the, Scientific notes of the “Cape Martyan” Nature Reserve, vol 8, pp 27–55 (in Russian)
- Mironov OG, Yu MN, Kiryuhina LN (1986) About the maximum permissive concentrations of oil product in the sea bottom sediments of the Black Sea coastal zone. *Hydrobiol J* 22(6):76–78 (in Russian)
- Mironov OG, Kirjukhina LN, Alyomov SV (2003) Sanitary-biological aspects of the Sevastopol bays ecology in XX century. Sevastopol: NAS Ukraine, Institute of Biology of the Southern Seas, 185 p (in Russian)
- Netrusova AI (ed) (2005) Practical guidelines for microbiology. M.: Akademiya, 608 p (in Russian)
- Oradovskogo SG, Gidrometeoizdat L (eds) (1977) Manual by methods of chemical analysis of sea water. 208 p. (in Russian)

- Romanenko VI, Kuznecov SI (1974) *Ekologiya mikroorganizmov presnyh vodoemov*. L.: Nauka, 194 pp
- Ryabushko LI, Bondarenko AV (2016) The qualitative and quantitative characteristics of the benthic diatoms near Kazantip cape of the sea of Azov. *J Black Sea Mediterranean Environ* 22(3):237–249
- Sorokin DY (1970) Study of the number, production and functional activity of bacteria in the Black Sea. *Biology of the Sea* 19:34–41 (in Russian).
- Tikhonova EA, Burdiiyan NV, Soloveva OV, Doroshenko YuV (2015) Chemical and microbiological parameters of the Kerch strait sea bottom sediments after the accident of «Volgoneft-139» ship. *Environ Prot Oil Gas Complex* 4:12–16 (in Russian)
- Tikhonova EA, Guseva EV (2012) The dynamics of oil pollution in sea bottom sediments and coastal sediments of the Kerch Strait after the emergency oil spill in November 2007. In: *Proceedings of the 7th international scientific conference «Modern fisheries management and ecological problems of the Azov-Black Sea region»*, vol 1, pp 253–255 (in Russian).
- Tikhonova E, Kotelyanets E, Soloveva O (2016) Evaluation of the contamination level of sea bottom sediments on the Crimean coast of the Black and Azov Seas. *Principy Èkologii* 5:56–70
- Tikhonova E, Kotelyanets E, Soloveva O (2019) Sea bottom sediments as a pollution level indicator of the Crimean coast (the Black and Azov Seas). In: Pešić V (ed) *8th International symposium Ecologists (ISEM 8)*, book of abstr. Budva, Podgorica, p 87
- Vylkanov A, Danov H, Marinov H, Vladev P (1983) *The black sea*. Gidrometeoizdat, Leningrad (in Russian)
- Zenkevich LA (1963) *Biology of the USSR seas*. Akademiya nauk SSSR, Moscow

The Assessment of the Multifunctional Center Construction Impact on the Surrounding Buildings Within Megapolis Limits



D. L. Neguritsa , G. V. Alekseev, E. A. Medvedev, A. A. Tereshin , and K. M. Slobodin

Abstract The results of modeling changes in the stress–strain state of the soil massive during the construction of a multifunctional center by the finite element method using an elastic and hardening soil model in the spatial formulation of the Plaxis 3D software package are presented. The zone of construction influence is determined and the expected values of displacements and deformations for buildings and structures falling into this construction influence zone are specified. This data will later be used in the program formulation and during geomechanical monitoring establishment. Recommendations for deformation processes monitoring throughout construction process and the pattern to operate the underground complex with objects and structures that fall into the zone of construction influence are developed.

Keywords Modeling · Deformation processes · Hardening soil model · Soil-rock mass · Building structures · Surrounding buildings · Geomonitoring

D. L. Neguritsa (✉)

Sergo Ordzhonikidze Russian State University for Geological Prospecting, 23 Miklukho-Maklaya str, 117997 Moscow, Russia
e-mail: neguritsadl@mgri.ru

G. V. Alekseev · E. A. Medvedev · A. A. Tereshin · K. M. Slobodin
National Research Moscow State University of Civil Engineering, 26 Yaroslavskoe, 129337 Moscow, Highway, Russia
e-mail: alexeev_german@bk.ru

E. A. Medvedev
e-mail: MedvedevEA@mgsu.ru

A. A. Tereshin
e-mail: TereshinAA@mgsu.ru

K. M. Slobodin
e-mail: SlobodinKM@mgsu.ru

1 Introduction

In the process of the development of the city of Moscow, the construction of multifunctional centers is taking place, aiming the complex use of the existing territories (Merkin and Konjuhov 2017; Trubeckoj and Iofis 2007; Kartoziya 2015). The Multifunctional Center under consideration is a complex architectural and planning solution combined with engineering facility with an underground part located on the area of 1.071 ha. The 33-story building has a plan size of 82×38 m, the underground part of the complex is up to 15 m deep and occupies the entire underground space of the construction site—the total area of 18,371 m². The height of the office part equals 36 m, the height of the connecting 4-story part is 21 m. All around the perimeter of the projected facility, an underground structure “soil mix wall” with a depth of up to 27 m is mounted. During the construction of the high-rise part of the complex, a piled foundation is implemented into the ground-rock massif to a depth of more than 50 m.

The site of the planned construction is geomorphologically confined to the third (Khodynskaya) ancient alluvial terrace of the Moscow River. Modern physical and geological processes that can significantly affect the decision-making of the design concept are not revealed at the construction site.

Seven stratigraphic-genetic complexes (SGC) take part in the geological structure of the site up to a depth of 63 m:

- modern technogenic formations (tQ_{IV});
- Upper Quaternary alluvial deposits (aQ_{III});
- Upper Jurassic deposits of the Volga stage (J3v);
- Upper Jurassic deposits of the Oxford stage (J3ox);
- Upper Carboniferous deposits of the Kasimov stage (C₃ks), represented by rocks of the Dorogomilovskaya (C₃dgm), Khamovnicheskaya (C₃hm) and Krevyakin-skaya series (C₃kg).

The hydrogeological conditions of the site are characterized by the distribution of two aquifers:

- (I) the Over Jurassic aquifer complex,
- (II) Upper Carboniferous carbonate aquiferous complex, confined to the fractured limestones of the Perkhurov and Ratmirov formations.

In the explored thickness, 18 engineering-geological elements (EGE) lie to identify:

–	1	–	tQ _{IV}	–	Fill-up soil: sand with inclusions of crushed stone and construction debris, covered with asphalt up to 0.4 m thick
–	2	–	aQ _{III}	–	Sand of medium size, medium density
–	2a	–	aQ _{III}	–	Sand of medium size, high density
–	2b	–	aQ _{III}	–	Sand of medium size, low density

(continued)

(continued)

–	1	–	tQ _{IV}	–	Fill-up soil: sand with inclusions of crushed stone and construction debris, covered with asphalt up to 0.4 m thick
–	3	–	aQ _{III}	–	Sand of small size, medium density
–	3a	–	aQ _{III}	–	Sand of small size, high density
–	3b	–	aQ _{III}	–	Sand of small size, low density
–	4	–	aQ _{III}	–	Sandy silt, medium density, water-saturated
–	4a	–	aQ _{III}	–	Sandy silt, high density, water-saturated
–	4b	–	aQ _{III}	–	Sandy silt, low density, water-saturated
–	5	–	J3v	–	Refractory loam
–	6	–	J3v	–	Semi-hard clay
–	7	–	J3ox	–	Semi-hard clay
–	8	–	C ₃ msc	–	Solid marlaceous clay
–	9	–	C ₃ pr	–	Medium-strength limestone
–	10	–	C ₃ nvr	–	Solid marlaceous clay
–	11	–	C ₃ zt	–	Dolomite, medium-strength limestone
–	12	–	C ₃ vs	–	Solid marlaceous clay

The construction area is not dangerous in karst-suffusion terms, since the thickness of the regional Jurassic clays water barrier here is more than 10 m.

Large caverns and voids in the Upper Carboniferous limestones are not revealed during drilling wells. The average fracture modulus M_f of limestones equals 8, and the rock quality index RQD is 70% (Gattinoni et al. 2014).

The principal determining factors of the possible impact of the new construction on the surrounding building development are:

- change in the stress–strain state of the foundation soil caused by the nearby construction of the foundation pit;
- change in the stress–strain state of the foundation soil caused by an additional load;
- changes in hydrogeological conditions;
- technological factors, such as dynamic impacts, the influence of deep foundations mounting and enclosing structures of the foundation pit, the influence of special types of activities;
- adverse processes in the ground massif associated with the geotechnical labor performance: suffusion processes, the quicksand formation, thixotropic decompression, etc.

In the process of construction in areas with a heterogeneous structure, disrupted by anthropogenic activity, the soil-rock layer often changes its properties at the base of the building structure, which complicates construction, causes the deformation processes progress and can lead to emergency situations (Kulikova 2018; Glozman 2016; Neguritsa 2018; Broere 2013).

The assessment of the impact of construction on the state of the surrounding building development can be comprehensively carried out by mathematical modeling of changes in the stress–strain state of the soil massif by the finite element method with account of geomechanical soil models. Mathematical modeling is performed in a spatial statement in the PLAXIS 3D software package.

To determine the adverse impact of new construction on the surrounding buildings and structures, a geomechanical model in the Plaxis 3D software package is created. Plaxis 3D is a specialized computing complex based on the finite element method in the conditions of three-dimensional problem statement.

To model the mechanical behavior of excavation wall structures, existing building structures, reinforcement piles, new building structures, and engineering-geological elements during their stress–strain state changes the following mathematical models are applied:

- elastic model;
- Hardening-Soil model.

The elastic model is used to model the operation of structural materials such as concrete, rubble stone or brickwork, metal, elements of the foundation pit fencing, and structures of existing buildings.

The functioning of the soil in the PLAXIS 3D software package is set by the Hardening-Soil model. The undeniable advantage of the hardening soil model is the dependence of the soil stiffness on stresses, as well as the ability to distinguish between the soil stiffness during loading and the stiffness during unloading, which best describes the actual behavior of the soil-rock massif under operational conditions (Sidorin et al. 2017).

When constructing the operation model, the following characteristics are set:

- (1) Fracture parameters as in the Coulomb-Mohr model: c —effective cohesion; φ —effective angle of internal friction; ψ —dilatancy angle.
- (2) Basic parameters of soil compressibility: E_{50}^{ref} —secant modulus in standard drained triaxial tests; E_{oed}^{ref} —tangent modulus under primary virgin compression; m —the stress level on the strain modulus dependence index.
- (3) Additional parameters are assigned: E_{ur}^{ref} —module during unloading/reloading; p^{ref} —initial stress for modules in kPa; K_0^{nc} —the coefficient of lateral pressure at normal solidification is given by the following expression:

$$K_0^{nc} = 1 - \sin \varphi$$

The results of modeling for the construction stages are presented in following illustrations (Figs. 1 and 2).

An assessment of the impact of construction over the surrounding buildings for the object “Multifunctional Complex” is made as the result of the simulation.

During the simulation, the choice of the calculated parameters of the soil is made on the basis of engineering and geological surveys. A three-dimensional finite

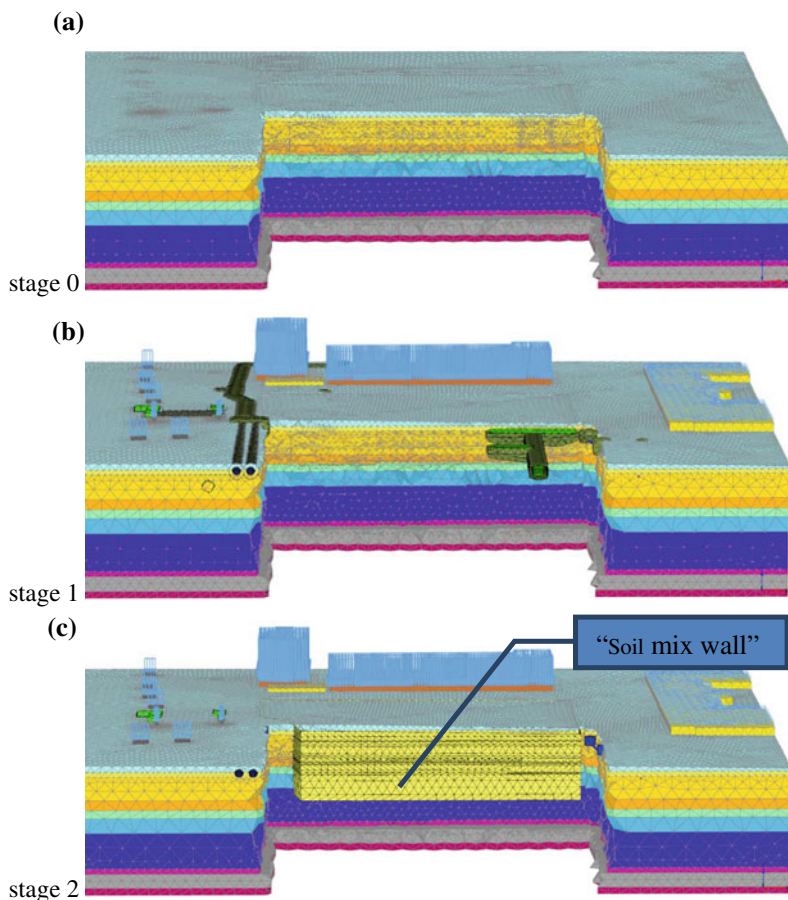


Fig. 1 Stages of the construction modelling: **a** loading the calculated area with the natural weight of the soil and determining the initial stress–strain state of the soil massif; **b** modeling the surrounding development; **c** zero setting for the displacements, modeling of the “soil mix wall” structure in the ground

element geomechanical model of the soil mass is constructed. The designed model includes also the projected object and the surrounding buildings (Figs. 3 and 4).

The assessed size of the impact zone, taking into account the modeling results and recommendations of the SR 22.13330.2011, is 42–47 m.

According to the results of calculations of the construction impact that the projected building deliver to the surrounding buildings, the estimated range of the impact zone lies between 18 and 47 m (Fig. 5).

The calculated changes in the state of the listed below buildings and structures falling into estimated area of influence are:

* Existing building 1—maximum calculated additional foundation settlement—10.9 mm, relative settlement difference 0.0008. The additional provisioned settlement

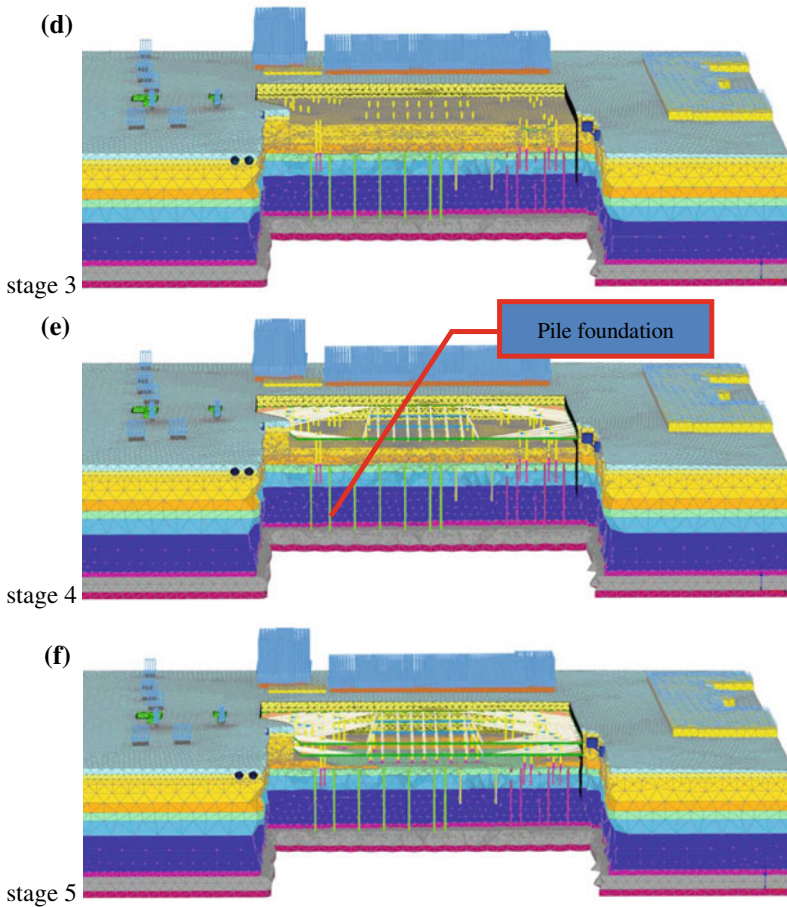


Fig. 2 Stages of the construction modelling: **d** zero setting for the displacements, modeling of the pile foundation design and temporary supports for the spacer system release, the pit development down to the mark 51.6; **e** modeling of the first tier spacer system design at the mark 52.6; **f** the pit development down to the mark 47.6

of the building is calculated to not exceed the maximum permissible values (max. 30.0 mm, rel. diff. 0.001), permitted by regulatory documents (SR 2003).

* Existing building 2—maximum calculated additional foundation settlement—3.4 mm, relative settlement difference 0.0003. The additional calculated settlement of the building does not exceed the maximum permissible values (max. 30.0 mm, rel. diff. 0.001) (SR 2003).

* Existing building 3—maximum calculated additional foundation settlement—3.2 mm, relative settlement difference 0.0001. The additional calculated settlement of the building does not exceed the maximum permissible values (max. 10.0 mm, rel. diff. 0.0006) (SR 2003).

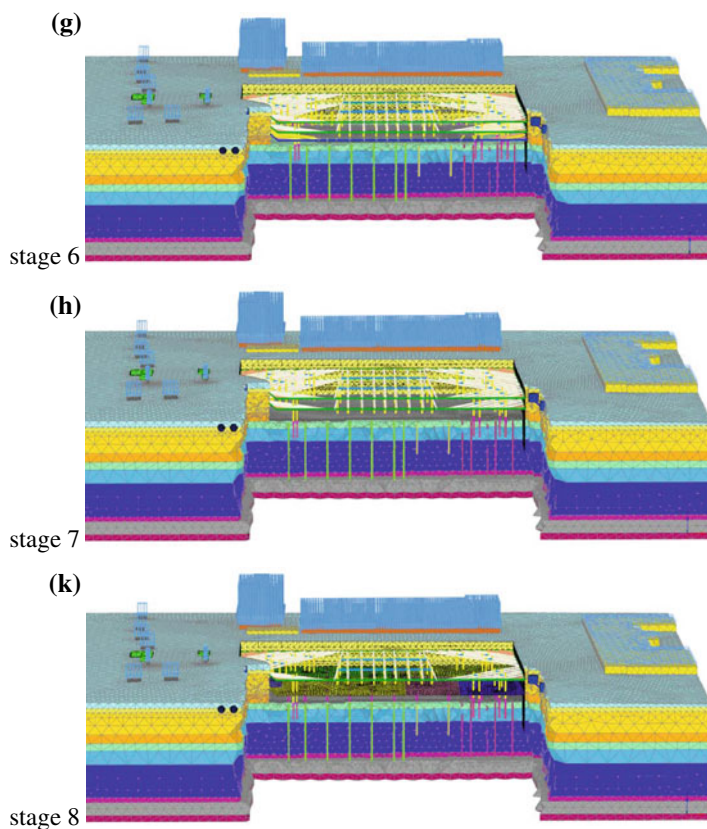


Fig. 3 Stages of the construction modelling: **g** modeling of the second tier spacer system design at the mark 48.6, the pit development down to the mark 41.3–41.6 in the central part with the ground prisms by the contour; **h** modeling of the construction of the foundation slabs central part for the buildings, arrangement of the third tier spacer (struts) system design at the mark 45.6, final pit development to the mark 41.3–41.6; **k** finalization of the foundation slabs, demounting of the third tier of the strut system at mark 45.6

* Tunnel of the underground pedestrian passage T1—maximum calculated additional settlement of the foundation is 28.9 mm, the relative difference in settlement is 0.0006. The additional settlement of the structure prognosticated by calculations does not exceed the maximum permissible values (max. 30.0 mm, rel. diff. 0.001) (SR 2003).

* Tunnel of the underground pedestrian passage T2—maximum predicted additional foundation settlement is 3.3 mm, the relative difference in settlement is 0.0003. The additional calculated settlement of the facility does not exceed the maximum permissible values (max. 30.0 mm, rel. diff. 0.001) (SR 2003).

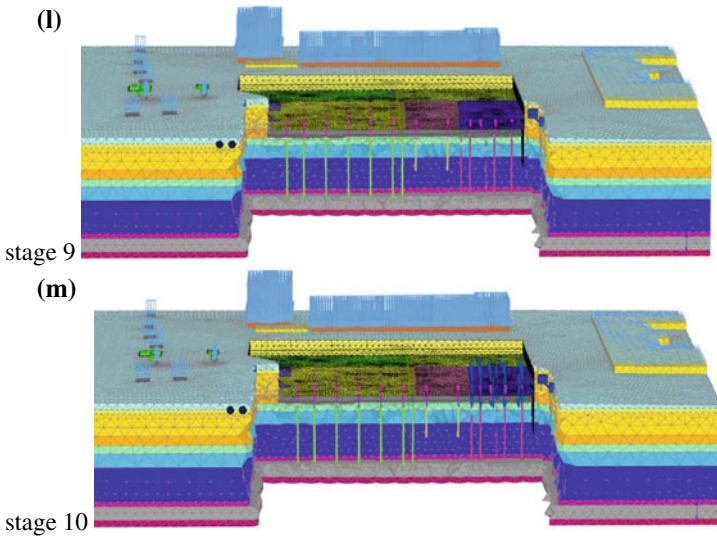


Fig. 4 Stages of the construction modelling: **l** modeling of vertical structures construction of the underground part and floor overlap at mark 46.8, demounting of the second tier of the strut system at mark 48.6; **m** modeling of vertical structures construction of the underground part and floor overlap at mark 50.9, demounting of the second tier of the strut system at mark 52.6

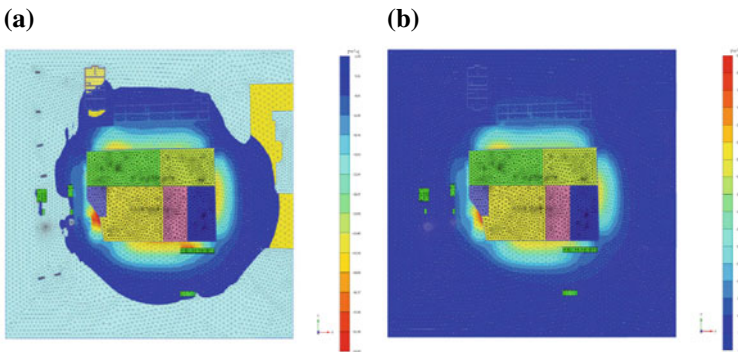


Fig. 5 At the time of construction completion isofields: **a** of the ground massif settlement; **b** of additional general deformations of the ground massif

Additional deformations of the foundations bases of buildings and structures falling into the zone of influence will not affect the operational suitability. Strength and safety are provided, additional measures to ensure safety are not required.

If the priority and technology of construction works are kept, the new construction does not have adverse impact on the existing engineering communications.

During the new construction process and after its completion, geomechanical monitoring of the ground and rock mass and the surrounding buildings located in the influence zone should be carried out.

References

- Broere W (2013) Urban problems – Underground solutions. In: Proceedings of 13th world conferences of ACUUS: advances in underground space development, 1528–1539.
- Gattinoni P, Pizzarotti E, Scesi L (2014) Engineering geology for underground works. *Eng Geol Undergr Work* 9789400778504:1–305. https://doi.org/10.1007/978-94-007-7850-4_1
- Gluzman OS (2016) Podzemnoe planirovanie Moskvy. *Zhilishhnoe stroitel'stvo* 11:14–19 (in Russian)
- Kartozija BA (2015) Osvoenie podzemnogo prostranstva krupnyh gorodov. *Novye tendencii. Gornyj informacionno-analiticheskij bjulleten'* S1:615–630 (in Russian)
- Kulikova EY (2018) Defects of urban underground structure and their prediction. *IOP Conf Ser: Mater Sci Eng* 012108. <https://doi.org/10.1088/1757-899X/451/1/012108>
- Lehmann R, Neitzel F (2013) Testing the compatibility of constraints for parameters of a geodetic adjustment model. *J Geodesy* 87(6):555–566
- Merkin VE, Konjuhov DS (2017) Osnovnye problemy, zadachi i perspektivy osvoenija podzemnogo prostranstva Moskvy. *Metro Tunnels* 1–2:18–23 (in Russian)
- Neguritsa D (2018) The problems of monitoring the deformation processes in the integrated development of the underground space of metropolitan cities. *E3S Web of Conf* 56:02027. <https://doi.org/10.1051/e3sconf/20185602027>
- Sidorin YuV, Ustinov KB, Kovalenko YuF, Stepanova EV (2017) Experimental study of sedimentary rocks deformation properties dependence on loading history. *Processy v Geosredah* 3(12):632–637 (in Russian)
- SR (2003) 13-102-2003 Rules of inspection of load-bearing building structures of buildings and structures (in Russian)
- Trubeckoj KN, Iofis MA (2007) Sostojanie i problemy osvoenija podzemnogo prostranstva goroda Moskvy. *Markshejderskij Vestnik* 4(62):27–30 (in Russian)